Optimized Filter Design for Non-Differential GPS/IMU Integrated Navigation

Heft 46
Schriftenreihe der Fachrichtung Geodäsie
Fachbereich Bau- und Umweltingenieurwissenschaften
Technische Universität Darmstadt
ISBN 978-3-935631-35-8

Darmstadt, Mai 2015

TECHNISCHE
UNIVERSITÄT
DARMSTADT

Heft 46

Darmstadt, Mai 2015

Yingwei Zhao

Optimized Filter Design for Non-Differential GPS/IMU Integrated Navigation

Schriftenreihe
Fachrichtung Geodäsie
Fachbereich Bau- und Umweltingenieurwissenschaften
Technische Universität Darmstadt

ISBN 978-3-935631-35-8

Schriftenreihe Fachrichtung Geodäsie der Technischen Universität Darmstadt
Zugl.: Darmstadt, Technische Universität, Dissertation, 2015
D17

Online unter: http://tuprints.ulb.tu-darmstadt.de

Verantwortlich für die Herausgabe der Schriftenreihe:

Der Sprecher der Fachrichtung Geodäsie
im Fachbereich Bau- und Umweltingenieurwissenschaften
der Technischen Universität Darmstadt

Bezugsnachweis:

Technische Universität Darmstadt
Fachgebiet Physikalische Geodäsie und Satellitengeodäsie
Franziska-Braun-Straße 7
64287 Darmstadt

ISBN: 978-3-935631-35-8

Optimized Filter Design for Non-Differential GPS/IMU Integrated Navigation

Vom Fachbereich Bau- und Umweltingenieurwissenschaften
der Technischen Universität Darmstadt
zur Erlangung des akademischen Grades eines
Doktor-Ingenieurs (Dr.-Ing.) genehmigte Dissertation

vorgelegt von
M.Sc. Yingwei Zhao
aus Zhengzhou, China

Referent: Prof. Dr.-Ing. Matthias Becker
Korreferent: Prof. Dr.-Ing. Andreas Eichhorn
Tag der Einreichung: 19. Mai 2015
Tag der mündlichen Prüfung: 07. Juli 2015

Darmstadt, Mai 2015
D17

Acknowledgement

I am sincerely grateful to my supervisor Prof. Matthias Becker for his constant support, encouragement, constructive criticism, and unwavering guidance. I am truly appreciated for all the time he spent in helping me despite he is so busy as always. I would also like to thank my co-supervisor, Prof. Andreas Eichhorn for offering me his advice on how to improve my dissertation. Special thanks go to Dr. Stefan Leinen for his valuable advices of my PhD study. His broad knowledge in the navigation fields helps me a lot.

I would like to extend my gratitude to Mr. David Becker and Ms. Sha Liu for the helpful and fruitful discussions on scientific matters. I appreciate Mrs Angelika Klinkrad for her kind help in my living and working in Germany and the introduction to the German culture. Many thanks go to all the colleagues in the Physical and Satellite Geodesy group for providing such a wonderful environment for research.

I would like to acknowledge to China Scholarship Council (CSC) for awarding me scholarship and allowing me to enjoy this challenging but interesting research work. My gratitude is also extended to the U.S. Institute of Navigation (ION) for awarding me the best student paper award and fully supporting my attendance at the 27th ION GNSS+ Conference in Tampa, Florida, USA, 2014.

Last, but not least, I would like to thank my parents, Xizhong Zhao and Juni Wang, for giving me life, taking care of me, and supporting my education. I am grateful to all my friends I met at Technical University of Darmstadt. You guys make my life in Germany become colourful.

Zusammenfassung

Diese Arbeit befasst sich damit, die Forschungen zur Leistungsverbesserung eines konventionellen, nicht-differenzialen GPS/MEMS IMU eng gekoppeltes Navigationssystems durch Filter-Design darzustellen, einschließlich nicht-linearer Filtermethoden, der stochastischen Fehlermodellierung für die Inertial-Sensoren und der Umsetzung der Trägerphase.

Zunächst wird die Leistungsauswertung einer jüngst entwickelten nicht-linearen Filtermethode, dem Cubature Kalman-Filter (CKF), gemäß der Taylorentwicklung analysiert. Die theoretische Analyse deutet darauf hin, dass die nicht-lineare Filtermethode CKF ihre Vorteile nur dann ausspielt, wenn sie in einem nicht-linearen System umgesetzt wird. Entsprechend wird ein nicht-linearer Ausdruck für die Ausrichtung mit Ausrichtungskosinus-Matrix (Direction Cosine Matrix, DCM) in ein eng verknüpftes Navigationssystem eingebaut, um den Ausrichtungsfehler zwischen dem wahren und geschätzten Navigationsrahmen darzustellen. Die Ergebnisse aus Simulation und Experiment zeigen, dass der CKF eine bessere Leistung als der Erweiterter Kalman-Filter (EKF) bei nicht beobachtbarem, großem Ausrichtungsfehler bietet und auch in Fällen, bei denen das GPS ausfällt und sich Ausrichtungsfehler schnell ansammeln können, so dass der Ausdruck des Psi-Winkels ungültig wird, wodurch ein gewisses Maß an Nicht-Linearität zum Ausdruck kommt.

Zum Zweiten präsentiert diese Arbeit die Shaping-Filter-Theorie, um die stochastischen Fehler in den Inertial-Sensoren eines Navigations-Kalman-Filters zu modellieren. Die Koeffizienten des Rauschens der Inertial-Sensoren werden aufgrund des Allan-Varianzgraphen bestimmt. Die Transferfunktion des Shaping-Filters wird aufgrund der Spektralleistungsdichte (Power Spectral Density, PSD) des Rauschens bei sowohl stationären als auch nicht-stationären Prozessen abgeleitet. Das gesamte farbige Rauschen wird zusammen in dem Navigations-Kalman-Filter modelliert, gemäß der Äquivalenztheorie. Die Freilaufleistung zeigt, dass die Modellierungsmethode auf Grundlage eines Shaping-Filters eine ähnliche und sogar kleinere Maximaldrift aufweist, als die konventionelle Modellierungsmethode mit Markov-Ketten erster Ordnung während GPS-Ausfällen; damit deutet sie ihre Wirksamkeit an.

Drittens, gemäß den Methoden, wie mit Mehrdeutigkeiten in der Trägerphase umzugehen ist, werden eng verknüpfte Navigationssysteme mit Time Differenced Carrier Phase (TDCP) und Total Carrier Phase (TCP) zur Messung der Kalman-Filter abgeleitet. Die Ergebnisse aus Simulation und Experiment zeigen, dass TDCP die Schätzgenauigkeit für die Geschwindigkeit ebenso wie glatte Trajektorien verbessern kann, aber die Positionsgenauigkeit kann nur das Niveau der Einzelpunktbeschreibung (Single Point Positioning, SPP) erreichen, sofern das TDCP mit der Pseudo-Entfernung verstärkt wird, während die Positionsgenauigkeit der TCP-basierten Methode unter einem Meter liegt. Um die Positionsgenauigkeit der TDCP-basierten Methode weiter zu verbessern, wird ein Partikel-Filter (PF) mit modifizierter TDCP-Beobachtung innerhalb eines TDCP/IMU eng verknüpften Navigationssystems umgesetzt. Die modifizierte TDCP wird als der Unterschied in der Trägerphase zwischen den Referenz- und den Beobachtungs-Epochen definiert. Die absolute Positionsgenauigkeit wird durch die Positionsgenauigkeit der Referenz bestimmt. Stammt die Referenzposition aus DGPS, so kann die absolute Positionsgenauigkeit bis unter einem Meter liegen.

Da die Umsetzung von TCP in dem Navigations-Kalmanfilter dem Zustandsvektor zusätzliche Zustände zufügt, wird bei TCP/IMU eng verknüpften Navigationssystemen eine hybride CKF+EKF-Filtermethode vorgeschlagen, bei welcher der CKF nicht-lineare Zustände und der EKF lineare Zustände schätzt, um die Vorteile des CKFs zu bewahren, aber gleichzeitig die benötigte Rechenleistung zu verringern. Die Navigationsergebnisse weisen auf die Wirksamkeit der Methode hin.

Nach Anwendung der Verbesserungsmaßnahmen kann die Leistung eines nicht-differenzialen GPS/MEMS IMU eng verknüpften Navigationssystems stark gesteigert werden.

Abstract

The endeavours in improving the performance of a conventional non-differential GPS/MEMS IMU tightly-coupled navigation system through filter design, involving nonlinear filtering methods, inertial sensors' stochastic error modelling and the carrier phase implementation, are described and introduced in this thesis. The main work is summarised as follows.

Firstly, the performance evaluation of a recently developed nonlinear filtering method, the Cubature Kalman filter (CKF), is analysed based on the Taylor expansion. The theoretical analysis indicates that the nonlinear filtering method CKF shows its benefits only when implemented in a nonlinear system. Accordingly, a nonlinear attitude expression with direction cosine matrix (DCM) is introduced to tightly-coupled navigation system in order to describe the misalignment between the true and the estimated navigation frames. The simulation and experiment results show that the CKF performs better than the extended Kalman filter (EKF) in the unobservable, large misalignment and GPS outage cases when attitude errors accumulate quickly, rendering the psi-angle expression invalid and subsequently showing certain nonlinearity.

Secondly, the use of shaping filter theory to model the inertial sensors' stochastic errors in a navigation Kalman filter is also introduced. The coefficients of the inertial sensors' noises are determined from the Allan variance plot. The shaping filter transfer function is deduced from the power spectral density (PSD) of the noises for both stationary and non-stationary processes. All the coloured noises are modelled together in the navigation Kalman filter according to equivalence theory. The coasting performance shows that the shaping filter based modelling method has a similar and even smaller maximum position drift than the conventional 1st-order Markovian process modelling method during GPS outages, thus indicating its effectiveness.

Thirdly, according to the methods of dealing with carrier phase ambiguities, tightly-coupled navigation systems with time differenced carrier phase (TDCP) and total carrier phase (TCP) as Kalman filter measurements are deduced. The simulation and experiment results show that the TDCP can improve the velocity estimation accuracy and smooth trajectories, but position accuracy can only achieve the single point positioning (SPP) level if the TDCP is augmented with the pseudo-range, while the TCP based method's position accuracy can reach the sub-meter level. In order to further improve the position accuracy of the TDCP based method, a particle filter (PF) with modified TDCP observation is implemented in the TDCP/IMU tightly-coupled navigation system. The modified TDCP is defined as the carrier phase difference between the reference and observation epochs. The absolute position accuracy is determined by the reference position accuracy. If the reference position is taken from DGPS, the absolute position accuracy can reach the sub-meter level.

For TCP/IMU tightly-coupled navigation systems, because the implementation of TCP in the navigation Kalman filter introduces additional states to the state vector, a hybrid CKF+EKF filtering method with the CKF estimating nonlinear states and the EKF estimating linear states, is proposed to maintain the CKF's benefits while reducing the computational load. The navigation results indicate the effectiveness of the method.

After applying the improvements, the performance of a non-differential GPS/MEMS IMU tightly-coupled navigation system can be greatly improved.

Contents

List of Figures

List of Tables

1 Introduction and background

1.1 Introduction

Owing to the complementary natures of global positioning system (GPS) and inertial measurement unit (IMU), their integration has been researched for several decades. GPS errors have long-term stability, which do not diverge unlimitedly over time (Kaplan and Hegarty, 2005). Nonetheless, as a radio navigation system, GPS is easy to be affected by surroundings such as high buildings or forests. IMU errors, especially for MEMS IMU, usually grow and accumulate very quickly in a stand-alone mode. However, IMU is not sensitive to surroundings. When the GPS signal is blocked and unavailable, IMU can help maintain the positioning accuracy and thus serves as a GPS backup in the short term (Titterton and Weston, 2004). A GPS/IMU integrated navigation system is proposed based on the error properties of these two systems (Groves, 2008). In such a system, GPS sensors can bound navigation errors and calibrate the inertial sensors, while IMU can interpolate the GPS positioning result and consequently improve the output frequency. Furthermore, the attitude is estimated from the IMU raw data, which is not possible for a single GPS receiver alone (Farrell, 2008). A GPS/IMU integrated navigation system makes the best use of the properties of the GPS sensor and the inertial sensors to construct a long-term stable, self-contained and high output frequency position-velocity-attitude navigation system.

1.1.1 Integration architectures

According to the types of GPS measurements implemented and how a GPS receiver is aided by the IMU in the integration algorithm, the architectures of GPS/IMU integrated navigation systems can be divided into loosely-coupled, tightly-coupled and deeply-coupled navigation systems (Groves, 2008). The definition and properties of each integration strategy can be summarised as below.

1. Loosely-coupled integration

In a GPS/IMU loosely-coupled navigation system, the position and velocity estimated by the GPS receiver are used as measurements in the integrated navigation Kalman filter. The integration scheme is simpler than tightly- and deeply- coupled navigation systems and accordingly requires a lower computational load. However, this kind of integrated navigation system has a cascaded architecture with two separate Kalman filters. The GPS navigation Kalman filter output errors are time-correlated (Groves, 2008). The direct implementation of GPS solutions in the IMU navigation Kalman filter may affect the estimation of IMU errors. The loosely-coupled navigation system works only when the number of observed GPS satellites is greater than three, which is the basic requirement of the GPS positioning.

2. Tightly-coupled integration

In a GPS/IMU tightly-coupled navigation system, GPS raw observations, such as pseudorange (PR), carrier phase and Doppler, will be integrated directly with the inertial navigation system. GPS-related states are also estimated in the navigation Kalman filter and fed back to correct GPS observations. Tightly-coupled navigation systems can still work when the number of the observed GPS satellites is less than four. Full GPS solutions are not necessary, either. The cascaded filtering problem in the loosely-coupled navigation system is also avoided. Further more, the handover of GNSS positioning and velocity covariance, due to satellite geometry and availability, to the integration algorithm is done implicitly in a tightly-coupled navigation system (Groves, 2008).

3. Deeply-coupled integration

In a deeply-coupled, also referred to as ultra-tightly coupled, GPS/IMU integrated navigation system, the GPS receiver accumulated correlator outputs: in-phase sample (Is) and quadraphase samples (Qs), serve as direct inputs into the integration algorithm. The code and carrier numerical controller oscillator (NCO) commands are generated using corrected inertial navigation solutions. Since the IMU measurements are not affected by jamming or spoofing, the robustness of the integrated navigation system can be greatly enhanced. Deep integration enables lower tracking bandwidth and increased noise resistance. It can work at lower C/N_0 levels (Groves, 2008).

1.1.2 Tightly-coupled integration strategies

The loosely-coupled integration is easy to accomplish and has been researched in many works (Godha, 2006; Ramanandan, 2011; Schmidt, 2011). For which reason, it will not be discussed in this thesis. Deeply-coupled navigation systems are mainly implemented with a software GPS receiver, due to the hardware limit. The implementation of a GPS/IMU deeply-coupled navigation system has been described in Sun (2010); Li (2012); Wang et al. (2009). In this work, the research focuses on improving the performance of a non-differential GPS/MEMS IMU tightly-coupled navigation system. According to GPS observations implemented in a navigation Kalman filter and how to deal with carrier phase observations, GPS/IMU tightly-coupled navigation systems can be categorized as:

1. pseudorange+Doppler tightly-coupled navigation system

A pseudorange+Doppler GPS/IMU tightly-coupled navigation represents a conventional strategy. Many researchers dealing with tightly-coupled navigation systems adapt this integration strategy (Godha, 2006; Angrisano, 2010; Zhou, 2013; Jiang, 2010; Miller et al., 2008; Yi, 2007). This kind of system is relatively easy to accomplish and can be applied in real time, because there is no need to deal with the inherent ambiguity problem of carrier phase observations and because there are no requirements for precise orbit and precise clock, which usually have a time delay. However, this method only achieves single point positioning (SPP) accuracy.

2. Time differenced carrier phase tightly-coupled navigation system

Due to the difficulty in dealing with carrier phase ambiguities, the time differenced carrier phase (TDCP) method is proposed to form an observation without GPS carrier phase ambiguity terms through differencing between two GPS epochs. This method is based on a fact that the ambiguity maintains as a constant while there are no GPS blockages or cycle slips (Moafipoor et al., 2004; Wendel et al., 2006a; Wendel and Trommer, 2004). The TDCP measurements, derived from GPS carrier phase observations, can achieve centimeter or even millimeter accuracy, thus leading to an accurate delta-position observation and further a high accuracy velocity estimation (Serrano et al., 2004; Ding and Wang, 2011; Ding, 2007). The TDCP system is suitable for real-time applications. However, implementing TDCP measurements only in integrated navigation systems will cause large position drift, because of the fast position error accumulation through the TDCP (Han and Wang, 2012; Ding, 2008). Accordingly, pseudorange measurements are usually augmented as observations to bound position drift but with SPP accuracy. The measurement matrix related with TDCP measurements is difficult to compute, since it involves several matrix adding and multiplying operations (Zhao et al., 2015).

3. Total carrier phase tightly-coupled navigation system

In order to further improve the positioning accuracy of the integrated navigation system, total carrier phase (TCP) observations can be implemented as measurements in the navigation Kalman filter. The TCP method estimates carrier phase parameters such as ambiguities in the navigation Kalman filter, considering them as extra states augmented by a conventional state vector (Zhang and Gao, 2005b,a; Ascher et al., 2011; Du and Gao, 2010; Du, 2010; Roesler and Martell, 2009; Rabbou and El-Rabbany, 2014b). Applying the TCP in a tightly-coupled navigation system can improve positioning accuracy to the sub-meter level. However, carrier phase observations must be preprocessed based on precise

point positioning (PPP) technique, with all possible errors corrected by relevant models before applied in the integrated navigation system or estimated as extra states in the navigation Kalman filter. The computational load is greatly increased accordingly. The TCP based tightly-coupled navigation system is not suitable for real-time applications, due to the requirement for precise orbit and precise clock.

If the reference station is available, the differential GPS positioning technique can also be applied to correct GPS observations and improve positioning accuracy (Ramanandan, 2011; Karamat, 2014). In this work, non-differential GPS/IMU tightly-coupled navigation systems are the main concern. Differential GPS/IMU integration systems will not be discussed any further.

1.2 Previous work

This thesis aims at improving the navigation performance of conventional non-differential GPS/MEMS IMU tightly-coupled navigation systems. The work mainly concentrates on three aspects: nonlinear filter application, inertial sensors' stochastic error modelling and the implementation of the carrier phase as measurements. The previous work of each aspect is summarized below.

1.2.1 Nonlinear filter application

Estimation techniques are important in the GPS/IMU tightly-coupled navigation system design. A robust, effective and optimal state estimator is helpful in improving not only navigation accuracy but also fault detection and integrity monitoring for a time-varying system like a GPS/IMU integrated navigation system (Groves, 2008). The artificial neural network (ANN) technique can be implemented in a GPS/IMU integrated navigation system (Chiang et al., 2003; El-Sheimy et al., 2006; Abdel-Hamid, 2005). ANN consists of a set of adaptive weights and is capable of approximating non-linear functions of their inputs.

As an optimal, linear and Guassian estimation technique, the Kalman filter has also been widely applied in tightly-coupled navigation systems. GPS/IMU tightly-coupled navigation systems feature some nonlinearity in their measurement and state transition functions, so the extended Kalman filter (EKF), generating a first order Taylor approximation to nonlinear functions, is proposed and applied (Angrisano, 2010; Jiang, 2010). Due to that the higher order terms are neglected, the EKF appears to have a degraded computation performance in high nonlinear cases. In order to further improve the navigation performance, nonlinear Kalman filtering methods, e.g. the sigma-point Kalman filter (SPKF), the Unscented Kalman filter (UKF) and the Cubature Kalman filter (CKF), are implemented in integrated navigation systems, which are expected to show better performance than the EKF and Kalman filter (Van Der Merwe, 2004; Zhou, 2013; Yi, 2007; Julier et al., 2007). These nonlinear filtering methods are proposed and categorized according to how to compute the integral of nonlinear function times Gaussian density through some transformations such as Unscented transformation or Cubature transformation (Julier and Uhlmann, 2004; Arasaratnam, 2009; Arasaratnam and Haykin, 2009). Some researchers implement the particle filter (PF) and its relevant extensions, e.g. the extended particle filter (EPF) and the Unscented particle filter (UPF), in tightly-coupled navigation systems, because multipath effects behave like a non-Gaussian noise (Zhou, 2013; Yi, 2007; Georgy et al., 2010). The implementation of nonlinear filtering methods can also avoid calculating Jacobian matrices.

However, the effectiveness of nonlinear filtering methods in integrated navigation systems is controversial. In some research works, the authors reported that nonlinear filtering methods can improve the navigation performance (Bistrovs and Kluga, 2013; Wang et al., 2008; Crassidis, 2006; Van Der Merwe, 2004; Julier et al., 2007), while other researchers argue that nonlinear filtering methods are useless in this regard (Rhudy et al., 2013). The merits of nonlinear filtering methods are shown when the system's nonlinearity is high. If nonlinear filtering methods are implemented in a linear system or nonlinear system with a linearised state transition function and measurement function, they should have a similar or

even worse performance than the EKF or Kalman filter, because nonlinear filtering methods themselves are suboptimal estimators, while the Kalman filter is an optimal estimator.

With regard to the error state space form of a GPS/IMU tightly-coupled navigation system, its nonlinearity is not so high when observations are available and all the states are observable under specific motions (Becker et al., 2010). In these cases, a nonlinear filtering method degrades into a linear method with a similar and even worse navigation performance than the KF. In other cases, for example, in a large misalignment or large initialisation position error case when integrated navigation systems present high nonlinearity, the merits of nonlinear filtering methods can be better shown (Wendel et al., 2005, 2006b; Ali and Ullah Baig Mirza, 2011). Similar nonlinear filtering performance improvements can also be seen in GPS outages and unobservable cases when observations have no benefits in the state estimation and inertial sensor errors cannot be well compensated or estimated. In an error state Kalman filter, the error state transition function is valid only when the estimation error is small. For example, the attitude error should be smaller than 5 deg. In large misalignment, GPS outage and unobservable cases, the large attitude error from the bad attitude initialisation or the fast attitude error accumulation can render the psi-angle attitude expression invalid. The fact that the small error assumption in a psi-angle expression cannot hold true leads to the system's nonlinearity. Nonlinear filtering methods working with nonlinear attitude error expression are able to overcome this kind of nonlinearity, because they have no requirements in small attitude error assumption. In Chapter 3, the CKF will be taken as an example to further examine the performance of nonlinear filtering methods in integrated navigation systems through theoretical analysis, simulation and experiment results.

The particle filter is a sampling based filtering method. It uses N independent samples from the *a priori* density to approximate the expectation of a system by sample average (Arulampalam et al., 2002). One of the largest advantages of the particle filter is its capability of dealing with nonlinear and non-Gaussian problems such as the object-tracking, map-aided navigation, robot applications and so on (Arulampalam et al., 2002; Okuma et al., 2004; Hafner et al., 2014; Vlassis et al., 2002). The particle filter and its relative extensions, the EPF, the UPF and the Gaussian sum particle filter (GSPF) have been successfully applied in GPS/IMU tightly-coupled navigation systems (Yi, 2007; Zhou, 2013; Giremus et al., 2005; Yi and Grejner-Brzezinska, 2006; Zhou et al., 2011). However, the non-Gaussian property of pseudorange observations is obvious only in the multipath surroundings such as buildings or forests. Besides this, most researchers implement Gaussian particle filter in the GPS/IMU tightly-coupled navigation system on the assumption that all the noises are Gaussian distributed, because of the difficulty of determining the actual noise distribution of states and observations. So the benefits of the particle filtering methods in dealing with nonlinear and non-Gaussian problems cannot be fully shown in integrated navigation systems (Zhou, 2013; Zhou et al., 2011). Actually, the introduction of the particle filter to a Gaussian system will add extra noise to the estimation results, which seems to be harmful and increases the computational load.

1.2.2 Inertial sensors' stochastic error modelling

The inertial sensors' error can be roughly divided into two parts: deterministic errors and stochastic errors (Groves, 2008; Yi, 2007). Deterministic errors include scale factor error, constant bias, misalignment effects and so on, which can be reduced or eliminated through calibration. Stochastic errors include inertial sensors' random noises, which cannot be reduced or eliminated through calibration (IEEE Std 952TM-1997, 2008). How to calibrate inertial sensors and eliminate deterministic errors has been described and introduced in many works (Hall et al., 2000; Buschmann et al., 2001; Syed et al., 2007; Syed, 2009). This thesis primarily delas with the modelling of inertial sensors' stochastic errors in the navigation Kalman filter.

The prerequisite of stochastic error modelling is how to determine the coefficients of inertial sensors' noises. Considering calculation principles and processes, there are mainly three methods that can be used

here: Allan variance, power spectral density (PSD) and Wavelet moment (IEEE Std 952TM-1997, 2008; Zhao et al., 2011; Guerrier, 2013; Stebler, 2013). All the three methods are equivalent in mathematics. They can be converted into each other through relevant mathematical transformations. For example, as a time-domain method, the Allan variance can be treated as a Fourier pair of PSD, which is calculated in the frequency domain. The recently developed Wavelet moment based method creates a relationship between the stochastic errors' coefficients and the coefficients of wavelet terms. If a Haar filter is applied, this method is equivalent to the Allan variance according to Guerrier (2013); Stebler (2013). In other words, the Allan variance technique can be treated as a special case of the Wavelet moment based methods. The Allan variance is now the primary method used in determining inertial sensors' stochastic errors (IEEE Std 952TM-1997, 2008; Hou, 2004; El-Sheimy et al., 2008) and is also applied in many other fields such as different GPS positioning methods' residual analysis and a GPS/IMU integrated navigation system evaluation (Niu et al., 2014; Zhang et al., 2013a).

The inertial sensors' noise is usually modelled as a 1st-order Markovian process or a random walk in the navigation Kalman filter. In Schwarz and Wei (2001); Xing and Gebre-Egziabher (2008), the researchers apply the Allan variance technique to first sort out and determine the stochastic errors' coefficients and then model the inertial sensor noise as a 1st-order Markovian process or a random walk. The ignoring in other noises determined from the Allan variance plot is not scientific and may produce some negative effects to the final navigation results, although a simpler implementation can help reduce the computational load. In order to further improve the modelling accuracy of the inertial sensors' stochastic errors, some researchers model the inertial sensors' noises as high order auto-regressive moving average (ARMA) processes (Park, 2004; Wang et al., 2012; Park and Gao, 2008). The order and coefficients of the ARMA processes are determined by applying Yule-Walker or Burger estimation methods (Zelinker and Taylor, 1994). However, the ARMA process is model sensitive as introduced in IEEE Std 952TM-1997 (2008). In order to determine the order of the inertial sensors' ARMA process, Seong et al. (2000) applies Allan variance technique to identify inertial sensors' noise types. The order of the ARMA process is determined according to the combination of different kinds of noise, while the coefficients are estimated based on the relevant ARMA parameters estimation methods. A differential equation is also used to model inertial sensors' stochastic errors. In Han and Wang (2011); Saini et al. (2010); Zhao (2013), an equivalent differential equation is implemented in the navigation Kalman filter to describe all the coloured noises. This leads to an improvement in the navigation performance.

1.2.3 Carrier phase application

Implementing carrier phase observations in GPS/IMU tightly-coupled navigation systems brings some benefits to the navigation results estimation. The TDCP is one of the most popular carrier phase related observations, which can eliminate the ambiguities through differencing between two GPS epochs. Thus, there is no need in fixing carrier phase ambiguities. TDCP observations can help improve the relative positioning accuracy and velocity estimation accuracy (Moafipoor et al., 2004; Wendel et al., 2006a; Wendel and Trommer, 2004). A conventional pseudorange+TDCP/IMU tightly-coupled navigation system can only achieve SPP accuracy. In order to improve the performance of the TDCP based system, several enhancing methods have been developed. In Tang et al. (2007), a reduced Kalman filter is applied to a TDCP based integration navigation system and can help reduce the computational load. Han and Wang (2012) design a dual-rate Kalman filter where pseudorange and TDCP measurements work in one Kalman filter with different updating rates to reduce the pseudorange but increase the TDCP effects in the final position estimation, which shows a relatively higher positioning accuracy than the pseudorange-only method. The idea behind the dual-rate Kalman filter is trying to separate the pseudorange observation noise from the TDCP to make use of the TDCP's higher relative positioning accuracy. Although a dual-rate or reduced Kalman filter is applied, the reported pseudorange+TDCP positioning accuracy can only reach SPP accuracy.

The integration of the TCP observations with low-cost MEMS IMU can improve the positioning accuracy to the sub-meter level in kinematic cases when the ambiguities are convergent (Ascher et al., 2011; Du and Gao, 2010; Du, 2010; Roesler and Martell, 2009; Rabbou and El-Rabbany, 2014b). IMU can also enhance the GPS performance. In Du (2011); Du and Gao (2012), a MEMS IMU is used as an aiding sensor with wide lane (WL) and extra wide lane (EWL) phase combinations to determine unique cycle slips in L1 and L2 frequencies. The reported cycle slip detection and PPP re-convergence speed can be improved by applying IMU aiding. In Karaim et al. (2013); Figueiredo e Silva (2012), inertial sensors are proved to be useful in real-time cycle slip detection, which is helpful for the carrier phase positioning technique. However, TCP observations will introduce some GPS related states to the navigation Kalman filter, which increases the computational burden, especially when implemented with nonlinear filtering methods.

1.3 Thesis organisation and contribution

1.3.1 Thesis organisation

This thesis mainly introduces the author's effort in improving the performance of a non-differential GPS/MEMS IMU tightly-coupled navigation system through nonlinear filtering methods' application, inertial sensors' stochastic modelling and the implementation of carrier phase observations. This thesis is accordingly divided into eight chapters. The main work of each chapter is summarised as below.

Chapter 1 gives a brief introduction to the integration architectures of GPS/IMU integrated navigation systems and tightly-coupled strategies. The previous work is then summarised. Finally, this thesis' organisation and the author's contribution are presented.

Chapter 2 summarises the working principles and error budgets of GPS and IMU navigation systems separately. The conventional GPS/IMU tightly-coupled navigation system and its relevant state transition and measurement functions are also derived. Owing to the high noise level and biases of MEMS gyroscopes, a brief summary on determining initial yaw angle using aiding information is also provided.

Chapter 3 evaluates the performance of the CKF in a GPS/IMU tightly-coupled navigation system. The estimation accuracy and working principle of the CKF is firstly analysed through Taylor expansion. A nonlinear attitude error expression is introduced and implemented in the navigation Kalman filter. The benefits of the CKF in an integrated navigation system are further examined in the unobservable, large misalignment and GPS outage cases. The CPF (Cubature Particle Filter) is also derived and tested in this chapter.

Chapter 4 describes how to use the shaping filter theory to model inertial sensors' stochastic errors in the navigation Kalman filter. Shaping filter theory is introduced at first. Each IMU stochastic error's shaping filter transfer function is deduced from its relevant PSD. An equivalence theory is proposed to find an equivalent shaping filter transfer function for all the inertial sensors' coloured noises. State space forms are further deduced from the s-domain transfer function using inverse Laplace transformation or Z-transformation. The simulation and experiment results indicate that this method is helpful in improving the navigation performance.

Chapter 5 makes a comparison between TDCP and TCP/IMU tightly-coupled navigation systems. Their relevant measurement functions are derived. The performance comparison is evaluated through the simulation and experiment.

Chapter 6 describes how to apply the particle filter in a TDCP/IMU tightly-coupled navigation system to improve the positioning accuracy. A modified TDCP, which is defined as the carrier phase measurements' difference between reference and current epochs, is proposed to weight the particles. The positioning accuracy of the PF based TDCP/IMU tightly-coupled navigation system can achieve sub-meter level, if the initial reference position is determined from the phase DGPS.

Chapter 7 introduces a CKF+EKF hybrid filtering method to the TCP/IMU tightly-coupled navigation system, which applies a nonlinear filtering method (the CKF) to the estimated IMU related states, while a linear filtering method (the EKF) to estimate GPS related states. Proposing this hybrid filtering method aims at maintaining the advantage of nonlinear filtering methods while reducing the computational load. The CFK+EKF hybrid filtering method is compared with EKF+EKF, EKF-only and CKF-only methods through simulation and experiments.

Chapter 8 summarises the author's work and presents recommended future work.

1.3.2 Contribution

The contribution of this thesis is summarised as below.

1. The performance of a nonlinear filtering method (the CKF) in a GPS/IMU tightly-coupled navigation system is examined and researched in detail. The CKF estimation accuracy is analysed through Taylor expansion. The mathematical derivation shows that the CKF's advantage is only fully presented when the system's nonlinearity is high. Several simulations and trajectories with different yaw angle observability are conducted to check the attitude estimation accuracy difference between the CKF and EKF. When the yaw angle is unobservable in the stationary and constant velocity cases, the CKF performs better than the EKF. In large misalignment case and GPS outages, the CKF converges faster than the EKF. If the GPS signal is always available and all the states are observable, the benefit of the CKF is not obvious.
2. This work introduces and develops the use of a shaping filter to model inertial sensors' stochastic errors. The method describes how to implement coloured noise in a navigation Kalman filter after determining the stochastic errors' coefficients from the Allan variance plot. The shaping filters for both stationary and nonstationary processes are deduced and approximated from their PSD. From the state space form, it can be seen that the differential equation and the ARMA process modelling methods are mathematically equivalent. They show a similar performance because they can be derived from the same shaping filter transfer function. The navigation performance can also be improved with the shaping filter based method.
3. The implementation of the carrier phase in a GPS/IMU tightly-coupled navigation system is introduced. Applying high accuracy carrier phase observations can improve velocity and position estimation accuracy, whether the carrier phase is implemented as TDCP or TCP. A more accurate TDCP measurement matrix is deduced in this thesis. The TCP based method can improve the positioning accuracy of an integrated navigation system to the sub-meter level.
4. A modified TDCP, defined as the carrier phase difference between the reference and observation epochs, is proposed to bound position drift caused by conventional TDCP measurements. It is further implemented with the particle filter to improve positioning accuracy, based on the position uncertainty of pseudorange being larger than the carrier phase. If some particles are generated around the position estimated by the pseudorange measurements, there is a considerable possibility that several particles will lie close to the carrier phase position result. A modified TDCP with a particle filter can lead to sub-meter positioning accuracy, which is impossible for a conventional KF-based PR+TDCP tightly-coupled strategy.
5. For a TCP/IMU tightly-coupled navigation system, a CKF+EKF hybrid filtering method is proposed to reduce the computational load. The hybrid filtering method creates a balance between maintaining the advantage of the CKF in dealing with nonlinear problems and reducing the computational burden. The simulation and experiment results show that the CKF+EKF filtering method performs better than the EKF based methods. Considering the computational load, the hybrid filtering method is more efficient than the CKF-only method.

2 Basic concepts of integrated navigation

In this chapter, some basic concepts related to GPS/IMU tightly-coupled navigation systems will be introduced. The GPS and IMU principles and errors are briefly described. The model of the conventional GPS/IMU tightly-coupled navigation system is deduced subsequently. Several yaw determination methods are compared regarding their effectiveness in a MEMS IMU application, due to the difficulty in determining the yaw angle from the MEMS gyroscope outputs.

2.1 GPS principles and errors

2.1.1 GPS system

GPS is an all-weather, passive, worldwide, continuous coverage, satellite-based radio navigation system (Kaplan and Hegarty, 2005). It consists of three major segments: space, control and user. The space segment consists of GPS satellites. The control segment mainly monitors the health and status of the space segment and determines the navigation messages including orbital model and clock correction parameters for each satellite. The user segment mainly relates to antennas and receivers. For a specific GPS user, GPS observations and navigation messages are the most important elements for positioning. The geometric distance between satellite and receiver is contained in GPS observations, while the navigation messages provide the satellites' position and velocity (Kaplan and Hegarty, 2005). When the number of observed satellites and observation time meet positioning requirements, the GPS system can determine the user's position through state estimation methods.

1. GPS observations

GPS observations include pseudorange, carrier phase and range rate. Range rate is usually derived from Doppler, which can be used to estimate the user's velocity. The user's position is determined from pseudorange and carrier phase. pseudorange, carrier phase and range rate observations are expressed as (Kaplan and Hegarty, 2005)

$$\begin{aligned} \rho_m &= r_m + c\delta t_r - c\delta t_{s,m} + I_m + T_m + \varepsilon_{\rho,m} \\ l_m &= r_m + c\delta t_r - c\delta t_{s,m} - I_m + T_m + \lambda N + \varepsilon_{l,m} \\ \dot{\rho}_m &= \dot{r}_m + c\delta \dot{t}_r - c\delta \dot{t}_{s,m} + \delta f + \varepsilon_{\dot{\rho},m} \end{aligned} \tag{2.1}$$

where ρ_m represents pseudorange from the m-th satellite, l_m represents carrier phase expressed in meters and $\dot{\rho}_m$ represents Doppler (or range rate). r_m and $\dot{r}_m$ are the true range and range rate between the receiver antenna at receiving time and the m-th GPS satellite at transmission time, δt_r is the receiver clock offset, $\delta t_{s,m}$ is the m-th satellite clock offset, $\delta \dot{t}_r$ is the receiver clock drift, $\delta \dot{t}_{s,m}$ is the m-th satellite clock drift. δf is the frequency correction of the relativistic effects (Xu, 2007). I_m is ionospheric delay, T_m is tropospheric delay, N is the carrier phase ambiguity, which is an unknown constant if there is no cycle slip. $\varepsilon_{\rho,m}$, $\varepsilon_{l,m}$ and $\varepsilon_{\dot{\rho},m}$ are the errors in pseudorange, carrier phase and Doppler, due to receiver noise and other errors such as multipath effects and orbit prediction errors.

2. Navigation message

The navigation message provides the necessary information for the position computation. It includes ephemeris for the calculation of the satellite coordinates, time parameters and clock corrections, satellite health information and so on. The navigation message is generated in the control segment. The control segment uploads all the information to the satellites several times every day.

2.1.2 GPS positioning methods

According to the implemented observations and the availability of base stations, the GPS positioning techniques can be roughly divided into three categories: single point positioning (SPP), precise point positioning (PPP), and differential GPS (DGPS). SPP and PPP are non-differential GPS positioning methods without base stations, while DGPS needs corrections from the base stations to achieve a greater positioning accuracy. The properties and working principles of the three positioning methods can be summarised as below.

1. SPP

The SPP method performs the positioning based on pseudorange observations from a single GPS receiver. After applying all the relevant corrections to pseudorange observations, the SPP technique is applied to estimate the receiver position and clock offset with the satellite position calculated from the navigation message. The positioning accuracy of the SPP method cannot exceed 13 m (95%) horizontally, 22 m (95%) vertically, which fits a low-accuracy requirement (Kaplan and Hegarty, 2005). Since the SPP method can resolve position in one epoch, it is suitable for real-time applications.

2. PPP

PPP is a single-receiver GPS positioning method using pseudorange and carrier phase as observations. PPP utilizes precise obit and precise clock provided by international GNSS service (IGS) to calculate satellite position and clock offset and then corrects all the possible errors, such as phase center offset, atmospheric delay, etc., through relevant models or products from IGS for a greater positioning accuracy. The PPP technique converges more slowly (usually 30 minutes) than the differential GPS positioning method (Martin, 2013; Carcanague, 2013). When PPP is convergent, its positioning accuracy can reach to the centimeter level in static cases and the sub-meter level in kinematic cases. The PPP method relies on the precise orbit published by IGS stations, which features some time delay. PPP is now mainly used for post-processing (Martin, 2013; Carcanague, 2013). However, with the ultra-rapid (predicted half) orbit provided by IGS, PPP can perform real-time positioning. Trimble and Fugro begin to provide their own commercial real-time PPP service like RTX (Real Time eXtended) and Starfix G2 at present.

3. DGPS

In DGPS mode, the roving receiver works with common mode errors (ionospheric delay, tropospheric delay, satellite ephemeris and clock error) estimated and broadcasted by one base receiver with a fixed known position to improve positioning accuracy. The rover position is determined relative to the reference position. If that reference position is known, the absolute position can be computed. The effect of eliminating the common mode errors is related to the baseline length. Increasing the baseline length will enlarge positioning error. The pseudorange DGPS positioning accuracy can reach 1 m with a baseline less than 10 km, while the carrier phase DGPS achieves the centimeter level (Misra and Enge, 2006). DGPS can meet real-time positioning requirements.

A popular DGPS technique is the real-time kinematic (RTK) positioning method. In RTK mode, the observations of base stations are transmitted to the rover receiver via radio link in real time. The rover receiver determines the difference between measurements from the reference receivers in order to eliminate measurement errors and thus achieve a greater positioning accuracy. The key to the RTK technique is fixing carrier phase ambiguities in real time (Ueno et al., 1997). On the fly (OTF) initialization can help determine ambiguities, which can be initialized in 30-60 seconds. The RTK technique's static positioning accuracy is within millimetres, while the kinematic positioning accuracy is within centimetres.

In order to overcome baseline limitations, a network RTK technique is proposed to solve the problem of RTK positioning accuracy decreasing as baseline increases. In the network RTK technique, several reference stations need to be established to cover the local area (Han and Rizos, 1996; Rizos, 2003; Rizos and Han, 2003). During the positioning process, the stations work together to form a virtual

reference station, which can send corrections to the user's receiver by radio to improve positioning accuracy. Applying network RTK technique can extend the baseline to 100 km (Rizos, 2003; Rizos and Han, 2003).

2.1.3 GPS error sources and properties

GPS observation can be represented as the summation of the geometric range from the GPS antenna to the satellite and various error terms. According to error properties, GPS errors are generally categorized into navigation message errors, transmission errors and receiver errors. The first are the parameter errors from navigation messages including satellite orbit and clock errors. The second set consists of transmission errors caused by the atmosphere when GPS signals propagate from satellite to receiver, for example, tropospheric delay and ionospheric delay. The third group is produced by the GPS receiver when the GPS signal is tracked, consisting of receiver clock offset, multipath effects, receiver noise, etc.

1. Navigation message errors

The navigation message errors contain the satellite calculation-related errors including satellite clock error and ephemeris error. Satellite clock correction parameters are computed using a curve-fitting method. Some residual errors arise from predicted estimates of actual satellite clock errors. However, the range error due to residual clock errors is relatively smaller. It is expected that this kind of error will continue to decrease as newer satellites are launched with more accurate clocks and improvements on the control segment side.

The ephemeris error or residual satellite position error represents the position difference between the true satellite position and the control segment's best prediction of each satellite's position. The effective GPS observation error, due to ephemeris errors, is on the order of 0.8 m (1σ) (Kaplan and Hegarty, 2005). The satellite clock error and ephemeris error have strong spatially correlated characteristics, which allows them possible to be completely eliminated by applying differential positioning techniques.

2. Transmission errors

During the propagation of GPS signal from satellite to receiver, the atmosphere will slow down the propagation speed of electromagnetic wave signal when it enters to the Earth atmosphere. Since GPS works with the speed of light in vacuum, the speed change caused by atmosphere effects adds an extra delay to the GPS positioning system, specifically tropospheric delay and ionospheric delay.

Tropospheric delay includes both a dry part and a wet part. 90% of the dry part can be corrected using relevant models such as the Hopfield model, Saastamoinen model and Black model (Kaplan and Hegarty, 2005). The wet part can be estimated as an extra state in the Kalman filter, which is modelled as equal for all the satellites in the zenith path direction. However, for a low-accuracy application like SPP, the estimation of the wet tropospheric delay is neither necessary nor required. Tropospheric delay has strong spatial and temporary correlation properties.

Ionospheric delay is calculated to first-order as

$$I = \frac{40.3 \cdot TEC}{f^2} \tag{2.2}$$

where TEC is total electron count along the path, and f is the carrier phase frequency. Ionosphere has opposite effects on the phase and group refractive indices, wherefore phase ionospheric delay acts in the opposite way than pseudorange ionospheric delay. The two frequency receivers can utilize the frequency dependence of ionospheric delay to eliminate its effect as shown in equation (2.3). The single frequency receiver must rely on differential operations or the ionospheric model such as the Klobuchar model, to correct ionospheric delay (Kaplan and Hegarty, 2005).

$$\rho_{IF} = \frac{f_1^2}{f_1^2 - f_2^2}\rho_{1,m} - \frac{f_2^2}{f_1^2 - f_2^2}\rho_{2,m}$$
$$l_{IF} = \frac{f_1^2}{f_1^2 - f_2^2}l_{1,m} - \frac{f_2^2}{f_1^2 - f_2^2}l_{2,m} \tag{2.3}$$

where ρ_{IF} and l_{IF} are the ionosphere free pseudorange and carrier phase combinations. $\rho_{1,m}$ and $\rho_{2,m}$ represent the pseudorange observations of the m-th satellite in L1 and L2 carrier frequencies. $l_{1,m}$ and $l_{2,m}$ represent the carrier phase observations of the m-th satellite in L1 and L2 carrier frequencies. f_1 and f_2 are the L1 and L2 carrier frequencies.

3. Receiver errors

Receiver errors contain receiver noise, multipath effects and receiver clock error. Receiver noise and multipath effects have different influences on pseudorange and carrier phase observations. Receiver errors are spatially and temporarily independent.

Receiver noise comes from thermal fluctuations, extraneous RF signals, cross correlation between the code division multiple access (CDMA) codes, signal quantization and sampling effects. This noise is usually modelled as white and independent noise between both satellites and channels. The multipath effects are caused by the satellite signal reaching the receiver antenna via multiple paths due to multiple signal reflections. The multipath effect is usually modelled as a non-Gaussian noise. According to Misra and Enge (2006), in the positioning application, the receiver noise will cause a 0.25-0.5 m error to pseudorange observations and 1-2 mm to carrier phase observations. The multipath effects can cause a 0.5-1 meter error to pseudorange observations and 5-10 mm error to carrier phase observations.

The receiver clock error can be eliminated by introducing a reference satellite. The user equipment bias introduced by the receiver hardware is often ignored since they are relatively smaller than the other error sources.

4. Summary

From the analysis above, it can be seen that GPS errors have the following properties: long-term stability, environment-dependence, strong spatial and temporary correlation.

In long-term observations, unlike self-contained sensors, GPS errors will not grow divergent. So in a GPS/IMU integrated navigation system, GPS observations or navigation results can help bound IMU navigation error accumulation.

As a radio signal, the GPS signal can easily be blocked by surroundings such as high buildings or forests. In heavily reflective environments, the multipath effects will be enlarged. Accordingly, GPS errors have environment-dependent properties. The integration with an IMU can help reduce the environment dependence errors.

GPS transmission errors also have spatial and temporary correlation characteristics. The correlation characteristics can be exploited to improve the over-all performance of the GPS system especially in differential mode, which is helpful in eliminating most of the transmission and common mode errors.

2.2 IMU principle and errors

Inertial navigation is a dead-reckoning navigation system that works by continuously measuring a vehicle's accelerations and angle rates in its pointing directions to compute navigation solutions through inertial navigation mechanization. Three orthogonally configured accelerometers and gyroscopes constitute an IMU carrying out navigation tasks. Given the previously known initial position, velocity and

attitude, the inertial sensors' output can be integrated to deduce position, velocity and attitude. IMU principles, related basic concepts and errors will be discussed and analysed as follows.

2.2.1 IMU principles of operation

A strapdown IMU comprises three mutually orthogonal accelerometers and gyroscopes. The accelerometer triad can sense the vehicle's acceleration, which can be further integrated to compute the velocity and position. The gyroscope triad can sense the vehicle's turn rate, including attitude information. An IMU works in the continuous self-contained mode with high output rates. Unlike radio based positioning systems, an inertial navigation system does not suffer from signal transmission problems such as signal blockages, since it does not rely on signal transmission (Titterton and Weston, 2004). Due to the initial uncertainty and imperfections of inertial sensors, aiding sensors should be applied to correct the inertial navigation system (INS) state estimation in a complementary filter.

2.2.2 Reference frames

In strapdown mechanizations, the following seven frames are involved: inertial frame, Earth frame, local-level frame, navigation frame, computer frame, body frame and platform frame. In this section, the definitions of and the transformation among the frames will be analysed and discussed (Titterton and Weston, 2004; Groves, 2008; Farrell, 2008).

1. Inertial frame

The inertial frame noted as *i*-frame, is a non-accelerating and non-rotating reference frame which is at rest or may be in uniform linear motion. The Newton's laws of motion are applied to an inertial frame. The origin of the inertial coordinate system is arbitrary. For discussion convenience, an Earth centred inertial (ECI) frame is defined with its origin coinciding with the Earth's center of mass and the x and z axes pointing toward the vernal equinox and along the Earth's spin axes in respect. The y-axis is defined to complete the right-handed coordinate system. The inertial frame is the reference for the strapdown inertial navigation system.

2. Earth frame

The Earth frame noted as *e*-frame, originates at the Earth's center of mass with the x and z axes pointing toward the Greenwich meridian and in the mean direction of the rotation axis of Earth. The y-axis completes the right-handed coordinate system. The Earth frame is also called as Earth centred Earth fixed (ECEF) frame. In an ECEF frame, a point can be expressed both in terms of Cartesian or ellipsoidal coordinates with longitude, latitude and height (LLH).

3. Local-level frame

The local-level frame noted as *l*-frame, usually serves as a direct reference to geodetic observations, which can be defined anywhere on the surface of Earth. The origin of the local-level frame is arbitrary such that the x axis points to the east, the y axis to the north and the z axis to the up directions. The east-north-up (ENU) frame is more suitable for vehicle applications, while north-east-down (NED) frame suits airborne applications.

4. Navigation frame

The navigation frame is usually denoted as *n*-frame. A navigation frame refers to the coordinate frame in which the INS is mechanized. In this thesis, the *l*-frame is chosen as *n*-frame for the mechanization of the strapdown INS.

5. Computer frame

The computer frame noted as *c*-frame, is a frame which the navigation computer assumes to be the true frame. The computer frame differs from the true navigation frame in its definition of the attitude errors. The difference from the platform frame to the true navigation frame is usually defined as ϕ angle (Scherzinger, 1996), while the difference from platform frame to computer frame is defined as ψ angle (Benson, 1975; Pham, 1991). Inertial error state navigation functions can be both expressed in ϕ and ψ angles.

6. Platform frame

The platform frame noted as *p*-frame, is determined by the real physical platform for a platform inertial navigation system. For a strapdown INS, the platform is determined by the direction cosine matrix (DCM). The origin of *p*-frame can be anywhere in the platform, while its axes are defined to be mutually orthogonal and right-handed along the application-dependent directions. In strapdown inertial mechanisation, *p*-frame always coincides with the navigation frame. In the inertial navigation error analysis, the difference between *p*-frame and *c*-frame or *n*-frame represents the orientation error. The difference between *p*-frame and *c*-frame is used in this study.

7. Body frame

The body frame noted as *b*-frame, is rigidly connected with moving objects. The *b*-frame's origin is the mass center of objects. Three axes are defined as the roll axis pointing toward front, the pitch axis pointing toward right and the yaw axis completing the right-handed coordinates. The transformation between *b*-frame and *n*-frame is usually described by three rotation angles: roll, pitch and yaw.

2.2.3 Inertial navigation error sources and properties

Based on their properties, inertial navigation errors are divided into mathematical model errors, inertial sensor errors, initialisation errors, computational errors and motion-dependence errors. These errors will affect strapdown INS performance and should be analysed and discussed in detail before modelling.

1. Mathematical model errors

Mathematical model errors mainly refer to Earth shape and gravitational errors in this study. In order to determine a position in the Earth surface, it is necessary to know the shape of the Earth, which is approximated by a reference ellipsoid. Gravity, usually computed from a gravity model, should be subtracted from specific forces sensed by accelerometers to calculate the acceleration of objects.

World geodetic system 84 (WGS 84) established in 1984 by Defense Mapping Agency, provides an ellipsoidal model of the Earth shape with two parameters: semimajor axis and eccentricity. WGS 84 is the coordinate system of reference for GPS. The shape difference between the Earth's true shape and WGS 84 contributes to the Earth shape error (Torge, 1991). However, for a low-cost MEMS IMU, the effect of the Earth shape error can be safely neglected.

Normal gravity can be computed using the International Gravity Formula 1980. The formula implies that normal gravity is determined by local latitude (Torge, 1991; Moritz, 1980). Gravitational errors refer to the difference between the computed and true gravities. Gravitational errors can be further subdivided into gravity anomaly and vertical deflection. Gravity anomaly is the difference between observed gravity and a value predicted from a model, while vertical deflection is a measure of how far the direction of the local gravity field has been shifted by local anomalies. Gravitational errors will affect final navigation results especially in high-precision inertial navigation mechanisation, which should be carefully modelled and calculated. However, for a low-cost MEMS IMU application, the effect of gravitational errors is not obvious, either.

2. Inertial sensor errors

Table 2.1: Accelerometer and gyroscope biases for different IMU grades (Groves, 2008)

IMU Grade	Accelerometer bias (m/s^2)	Gyroscope Bias (deg $/h$)
Marine	10^{-4}	0.001
Aviation	$3 \cdot 10^{-4} - 10^{-3}$	0.01
Intermediate	$10^{-3} - 10^{-2}$	0.1
Tactical	$10^{-2} - 10^{-1}$	1-100
Automotive	$> 10^{-1}$	> 100

Inertial sensor errors are the most significant error sources in inertial navigation systems. Inertial sensor errors are mainly attributed to imperfections in principle, manufacturing, assembly technique and so on. Although the accuracy is different, all types of inertial sensors (accelerometers and gyroscopes) exhibit biases, scale factors, cross-coupling errors and random noise (Groves, 2008). Inertial sensor errors can be categorized into deterministic and stochastic errors.

Deterministic errors have four components: a fixed contribution, a temperature-dependent variation, a run-to-run variation and an in-run variation. These mainly include constant bias, scale factor errors, temperature effects and so on. The effects of systematic errors can be eliminated or reduced through pre-calibration in the laboratory (Groves, 2008).

Stochastic errors refer to the stochastic aspect of inertial sensor errors including white noise, bias instability, quantization noise, rate random walk, rate ramp and so on. Stochastic errors can not be eliminated through calibration. In theory, they can be corrected through integration with other sensors and estimated simultaneously in a navigation Kalman filter (IEEE Std 952TM-1997, 2008).

The typical accelerometer and gyroscope biases for different IMU grades are shown in Table 2.1 (Groves, 2008).

3. Initialisation errors

Initialisation errors include initial position, velocity and alignment errors. A large initialisation error causes the nonlinearity of the integrated navigation system (Wendel et al., 2005, 2006b; Ali and Ullah Baig Mirza, 2011). The initial position can be resolved through GPS positioning or surveying techniques. Initial velocity can always be assumed to be zero, because INS usually navigates from still stand. Initial position and velocity errors have relatively smaller effects on the final navigation results.

Alignment errors originate from IMU alignment progress, which will affect navigation initialisation time and accuracy. The alignment process itself can result in the correlation between attitude errors and sensor biases. IMU alignment can be further divided into stationary alignment and in-motion alignment according to its motion statues.

In stationary alignment, the initial attitude is calculated from inertial measurements. Roll and pitch (levelling) angles are initialized by outputs of accelerometers. An accurate yaw angle initialisation requires aviation-grade gyros or even better. For a low-cost MEMS IMU, the initial yaw angle should be determined using other aiding sensors such as magnetometers, GPS attitude system and transfer alignment. Sensor biases are the main source of stationary alignment errors.

In-motion alignment is aided by other observations via Kalman filtering. For a MEMS IMU, yaw angle estimation accuracy can be improved by applying in-motion alignment technique (Kubo et al., 2006; Shin and El-Sheimy, 2004). In-motion alignment errors come from observation errors aside from sensor biases.

4. Computational errors

Computational errors are mainly attributed to bandwidth limitations, truncated mathematical functions implemented in strapdown navigation algorithms and numerical integration limitations. Due to the limited sensor bandwidth, the dynamic mismatch between sensors and insufficient computational speed prevents the systems from interpreting oscillatory motions correctly, giving rise to coning and sculling errors. Coning and sculling errors can lead to significant navigation errors. They can be compensated through Miller's and Savage's procedures (Miller, 1983; Savage, 1998a,b; Roscoe, 2001). However, with the performance improvements of modern computer hardware, the effects of coning and sculling errors on the final navigation results can be ignored as well. The navigation errors arising from computational imperfections are small compared with the contributions from other errors (Titterton and Weston, 2004).

5. Motion-dependence errors

The strapdown INS performance depends on the motion of the host vehicle. The motion-dependence error refers to system imperfections caused by vehicle motion. According to motion types, motion-dependence errors can be further divided into maneuver-dependent and vibration-dependent errors (Titterton and Weston, 2004). Vehicle maneuvering can trigger a number of error sources within an on-board strapdown INS such as Schuler pumping and cycling errors. Vibration-dependent errors deal with the effects of vibratory and oscillatory motions on the strapdown INS performance. A strapdown INS can not interpret this vibration correctly, due to its high-frequency properties. Vibration-dependent errors consist of instrument rectification errors, coning errors, sculling errors, size effect errors and pseudo-motion errors. As discussed in Zhang et al. (2013b), the motion-dependence errors' contribution to MEMS IMU navigation accuracy is smaller than inertial sensor and alignment errors.

6. Summary

The analysis above implies that strapdown INS errors mainly stem from inertial sensor and alignment errors. The INS error propagation of these two errors is briefly summarized as follows (Groves, 2008; Flenniken et al., 2005).

1) *Navigation errors from gyroscope biases*: Gyroscope biases will produce a quadratically increasing position error over time in short-term error propagation. In medium- and long-term error propagation, the equivalent eastern gyroscope bias will cause a latitude error oscillating around zero-mean over time and a longitude error oscillating around nonzero-mean over time; the equivalent northern and heading gyroscope biases will cause a latitude error oscillating around nonzero-mean over time and a disconvergent longitude error over time.

2) *Navigation errors from accelerometer biases*: Accelerometer biases will produce a quadratically increasing position error over time in short-term error propagation. In medium- and long-term error propagation, the equivalent eastern accelerometer bias will cause a latitude error oscillating around zero-mean over time and a longitude error oscillating around nonzero-mean over time; the equivalent northern accelerometer bias will cause a latitude error oscillating around nonzero-mean over time and a longitude error oscillating around zero-mean over time.

3) *Navigation errors from alignment errors*: Alignment errors will produce a quadratically increasing position error over time in short-term error propagation. In medium- and long-term error propagation, the initial pitch error will cause a latitude and longitude error oscillating round zero-mean over time; the initial roll and yaw errors will cause a latitude error oscillating around zero-mean over time and a longitude error oscillating around nonzero-mean over time.

2.3 Pseudorange+Doppler GPS/IMU tightly-coupled navigation system

A GPS/IMU tightly-coupled navigation system outperforms a loosely-coupled navigation system in that it can work fluently even when the observed GPS satellites' number is less than four. Besides this,

there is no need to design two separate Kalman filters for GPS and IMU. The cascaded Kalman filtering problem in loosely-coupled navigation systems can be avoided. Unlike loosely-coupled navigation using position and velocity as observations, a tightly-coupled navigation system directly estimates states and the covariance matrix from GPS raw observations such as pseudorange, carrier phase and Doppler.

The observations of a conventional PR+Doppler GPS/IMU tightly-coupled navigation system are pseudorange and Doppler. The state vector, state transition function and measurement function are given in the following sections.

2.3.1 State vector and transition function

The state vector of a conventional PR+Doppler GPS/IMU tightly-coupled navigation Kalman filter is

$$\mathbf{x} = \left[\delta\alpha, \delta\beta, \delta\gamma, \delta v_e, \delta v_n, \delta v_u, \delta\lambda, \delta\varphi, \delta h, \epsilon_x, \epsilon_y, \epsilon_z, \nabla_x, \nabla_y, \nabla_z, c\delta t, c\dot{\delta} t\right]^T \tag{2.4}$$

where $\delta\alpha, \delta\beta, \delta\gamma$ are attitude errors expressed as Ψ, $\delta v_e, \delta v_n, \delta v_u$ are velocity errors expressed as $\delta\mathbf{v}$ in ENU navigation frame, $\delta\lambda, \delta\varphi, \delta h$ are position errors expressed in longitude, latitude and height, $\epsilon_x, \epsilon_y, \epsilon_z$ are gyroscope biases in body frame, $\nabla_x, \nabla_y, \nabla_z$ are accelerometer biases, and $c\delta t, c\dot{\delta} t$ are receiver clock offset expressed in meters and drift in m/s.

IMU state transition functions are (Groves, 2008; Titterton and Weston, 2004)

$$\begin{cases} \dot{\Psi} = -\tilde{\omega}_{in}^n \times \Psi + \delta\omega_{in}^n - \mathbf{C}_b^n \epsilon \\ \delta\dot{\mathbf{v}}^n = -\left[\mathbf{f}^n\times\right]\Psi + \mathbf{C}_b^n \nabla - (2\delta\omega_{ie}^n + \delta\omega_{en}^n) \times \mathbf{v}^n - (2\tilde{\omega}_{ie}^n + \tilde{\omega}_{en}^n) \times \delta\mathbf{v}^n + \delta\mathbf{g}^n \\ \delta\dot{\varphi} = \dfrac{\delta v_N^n}{R_m + h} - \dfrac{\delta h v_N^n}{(R_m + h)^2} \\ \delta\dot{\lambda} = \dfrac{\delta v_E^n \sec\varphi}{R_n + h} + \dfrac{\delta\varphi v_E^n \tan\varphi \sec\varphi}{R_n + h} - \dfrac{\delta h v_E^n \sec\varphi}{(R_n + h)^2} \\ \delta\dot{h} = \delta v_U^n \\ \dot{\epsilon} = -\beta_\epsilon \epsilon \\ \dot{\nabla} = -\beta_\nabla \nabla \end{cases} \tag{2.5}$$

where ϵ are gyroscopes' biases, ∇ are accelerometers' biases and β_ϵ and β_∇ are the time constants of 1st-order Markovian processes for gyroscope and accelerometer biases, R_n is the normal radius, R_m is the median radius. $\tilde{\omega}_{in}^n$ is the estimated turn rate of navigation frame with respect to inertial frame expressed in navigation frame, $\delta\omega_{in}^n$ is the estimated turn rate error, and $\mathbf{C}_b^n$ is the DCM from the body frame to the navigation frame. $\mathbf{f}^n$ represents the specific forces in navigation frame, ω_{ie}^n is the turn rate of the Earth with respect to inertial frame expressed in navigation frame, ω_{en}^n represents the turn rate of navigation frame with respect to Earth frame expressed in navigation frame, $\delta\omega_{ie}^n$ and $\delta\omega_{en}^n$ are the relevant estimation errors defined as $\tilde{\omega}_{ie}^n - \omega_{ie}^n$ and $\tilde{\omega}_{en}^n - \omega_{en}^n$, and $\delta\mathbf{g}^n$ represents the gravitational error expressed in navigation frame. λ, φ, h represent Longitude, Latitude and Height.

Equation (2.5) can be further simplified in low-cost MEMS IMU and short distance navigation applications to save computational time (Zhou, 2013). The gyroscope biases usually significantly exceed the Earth rate and the accelerometer biases are much larger than the centripetal forces caused by the Earth rotation. Therefore, the Earth rate and its related terms and gravitational error can be assumed to be zero. In the short distance navigation applications, the turn rate of the navigation frame with respect to the Earth frame is negligible. So ω_{en}^n and its related terms can also be assumed to be zero. According the above analysis, the second term in the first equation and the Coriolis terms (the third and fourth terms) and the fifth term in the second equation of (2.5) can be eliminated for simplification. In this thesis, this kind of simplification is not applied.

GPS state transition matrix is

$$\mathbf{T}_{GPS} = \begin{bmatrix} 1 & \Delta t \\ 0 & 1 \end{bmatrix} \tag{2.6}$$

where Δt is the time interval.

The state transition functions will be implemented in a navigation Kalman filter to propagate states and the covariance matrix.

2.3.2 pseudorange measurement equation

As introduced in Section 2.1.1, the pseudorange for the m-th satellite observed by the GPS receiver is

$$\rho_m = r_m + c\delta t_r - c\delta t_{s,m} + I_m + T_m + \varepsilon_{\rho,m} \tag{2.7}$$

The geometric range between the m-th satellite position and the antenna position estimated from IMU is

$$\rho_I = \sqrt{(x_{s,m} - x_r)^2 + (y_{s,m} - y_r)^2 + (z_{s,m} - z_r)^2} \tag{2.8}$$

where ρ_I is the estimated pseudorange, $[x_{s,m}, y_{s,m}, z_{s,m}]$ is the m-th satellite's position in the ECEF frame and $[x_r, y_r, z_r]$ is the antenna position estimated by the IMU. If the true position of antenna is $[x, y, z]$, the estimated range ρ_I can be extended to the first-order Taylor term around the true antenna position $[x, y, z]$, which is

$$\begin{aligned} \rho_I &= r_m + \frac{\partial \rho_I}{\partial x}\delta x + \frac{\partial \rho_I}{\partial y}\delta y + \frac{\partial \rho_I}{\partial z}\delta z \\ &= r_m + e_{x,m}\delta x + e_{y,m}\delta y + e_{z,m}\delta z \end{aligned} \tag{2.9}$$

where

$$\begin{aligned} e_{x,m} = \frac{\partial \rho_I}{\partial x} &= -\frac{x_{s,m} - x_r}{\sqrt{(x_{s,m} - x_r)^2 + (y_{s,m} - y_r)^2 + (z_{s,m} - z_r)^2}} \\ e_{y,m} = \frac{\partial \rho_I}{\partial y} &= -\frac{y_{s,m} - y_r}{\sqrt{(x_{s,m} - x_r)^2 + (y_{s,m} - y_r)^2 + (z_{s,m} - z_r)^2}} \\ e_{z,m} = \frac{\partial \rho_I}{\partial z} &= -\frac{z_{s,m} - z_r}{\sqrt{(x_{s,m} - x_r)^2 + (y_{s,m} - y_r)^2 + (z_{s,m} - z_r)^2}} \end{aligned}$$

and $\delta x, \delta y, \delta z$ is the difference between the true and estimated positions. $\overrightarrow{e_m}$ denotes $[e_{x,m}, e_{y,m}, e_{z,m}]$.

The difference between the GPS observed pseudorange and the IMU estimated range, after compensating for the satellite clock offset, tropospheric delay and ionospheric delay, is

$$\delta\rho = \rho_m - \rho_I = c\delta t_r - e_{x,m}\delta x - e_{y,m}\delta y - e_{z,m}\delta z + \varepsilon_{\rho,m} \tag{2.10}$$

In this thesis, position is expressed in longitude, latitude and height. The measurement matrix should be converted from the ECEF frame to the LLH frame. When n satellites are observed, the measurement function is

$$\mathbf{z}_\rho = \mathbf{H}_\rho \mathbf{x} \tag{2.11}$$

where

$$\mathbf{z}_\rho = [\delta\rho_1 \quad \delta\rho_2 \quad ... \quad \delta\rho_n]^T$$

$$\mathbf{H}_\rho = [\mathbf{0}_{n\times 6} \quad -\overrightarrow{e_n}\cdot\mathbf{C}_e \quad \mathbf{0}_{n\times 6} \quad \mathbf{1}_{n\times 1} \quad \mathbf{0}_{n\times 1}]$$

$$\mathbf{C}_e = \begin{bmatrix} -(R_n+h)\cos\varphi\sin\lambda & -(R_n+h)\sin\varphi\cos\lambda & \cos\varphi\cos\lambda \\ (R_n+h)\cos\varphi\cos\lambda & -(R_n+h)\sin\varphi\sin\lambda & \cos\varphi\sin\lambda \\ 0 & [R_n(1-e^2)+h]\cos\varphi & \sin\varphi \end{bmatrix}$$

and $\mathbf{C}_e$ converts the position from ECEF frame to LLH frame, $\overrightarrow{e_n}$ represents the unit line of sight of n satellites and e is the Earth eccentricity.

2.3.3 Range rate measurement equation

The range rate can be calculated through the time derivative of (2.9) as

$$\dot{\rho}_I = \dot{r}_m + g_{x,m}\delta x + g_{y,m}\delta y + g_{z,m}\delta z + e_{x,m}\delta\dot{x} + e_{y,m}\delta\dot{y} + e_{z,m}\delta\dot{z} \tag{2.12}$$

where

$$\begin{aligned} \dot{r}_m &= e_{x,m}(\dot{x}_{s,m}-\dot{x}) + e_{y,m}(\dot{y}_{s,m}-\dot{y}) + e_{z,m}(\dot{z}_{s,m}-\dot{z}) \\ g_{x,m} &= \frac{1}{r_m}(\dot{x}_{s,m}-\dot{x}_r-\dot{r}_m e_{x,m}) \\ g_{y,m} &= \frac{1}{r_m}(\dot{y}_{s,m}-\dot{y}_r-\dot{r}_m e_{y,m}) \\ g_{z,m} &= \frac{1}{r_m}(\dot{z}_{s,m}-\dot{z}_r-\dot{r}_m e_{z,m}) \end{aligned}$$

where $\dot{r}_m$ is the true range rate from the GPS receiver to the m-th satellite, $[\dot{x}_r, \dot{y}_r, \dot{z}_r]$ is the velocity of the GPS receiver in the ECEF frame, $[\dot{x}_{s,m}, \dot{y}_{s,m}, \dot{z}_{s,m}]$ is the GPS satellite velocity, and $[\delta\dot{x}, \delta\dot{y}, \delta\dot{z}]$ is the velocity error in ECEF frame. $\overrightarrow{g_m}$ denotes $[g_{x,m}, g_{y,m}, g_{z,m}]$.

The pseudorange rate from the GPS antenna to the m-th satellite tracked by the GPS receiver is

$$\dot{\rho}_m = \dot{r}_m + c\delta\dot{t}_r - c\delta\dot{t}_{s,m} + \varepsilon_{\dot{\rho},m} \tag{2.13}$$

where $\dot{\rho}_m$ is the range rate derived from Doppler, $\delta\dot{t}_{s,m}$ is the satellite clock drift and $\delta\dot{t}_r$ is the receiver clock drift (Xu, 2007).

For the m-th satellite, the difference between the observed and IMU estimated range rates after correcting for tropospheric and ionospheric effects is

$$\begin{aligned} \delta\dot{\rho}_m &= \dot{\rho}_m - \dot{\rho}_I \\ &= c\delta\dot{t}_r - g_{x,m}\delta x - g_{y,m}\delta y - g_{z,m}\delta z - e_{x,m}\delta\dot{x} - e_{y,m}\delta\dot{y} - e_{z,m}\delta\dot{z} \end{aligned} \tag{2.14}$$

When n satellites are observed, considering the LLH coordinate system, the range rate measurement equation is

$$\mathbf{z}_{\dot{\rho}} = \mathbf{H}_{\dot{\rho}}\mathbf{x} \tag{2.15}$$

where

$$\mathbf{z}_{\dot{\rho}} = [\delta\dot{\rho}_1 \quad \delta\dot{\rho}_2 \quad \cdots \quad \delta\dot{\rho}_n]^T$$

$$\mathbf{H}_{\dot{\rho}} = [\mathbf{0}_{n\times 3} \quad -\overrightarrow{e_n}\cdot\mathbf{C}_e^n \quad -(\overrightarrow{e_n}\cdot\mathbf{C}_a + \overrightarrow{g_n}\cdot\mathbf{C}_e) \quad \mathbf{0}_{n\times 6} \quad \mathbf{0}_{n\times 1} \quad \mathbf{1}_{n\times 1}]$$

$$\mathbf{C}_e^n = \begin{bmatrix} -\sin\lambda & -\sin\varphi\cos\lambda & \cos\varphi\cos\lambda \\ \cos\lambda & -\sin\varphi\sin\lambda & \cos\varphi\sin\lambda \\ 0 & \cos\varphi & \sin\varphi \end{bmatrix}$$

$$\mathbf{C}_a = \begin{bmatrix} -v_e\cos + v_n\sin\varphi\sin\lambda - v_u\cos\varphi\sin\lambda & -v_n\cos\varphi\cos\lambda - v_u\sin\varphi\cos\lambda & 0 \\ -v_e\sin - v_n\sin\varphi\cos\lambda + v_u\cos\varphi\cos\lambda & -v_n\cos\varphi\sin\lambda - v_u\sin\varphi\sin\lambda & 0 \\ 0 & -v_n\sin\varphi + v_u\cos\varphi & 0 \end{bmatrix}$$

and $\mathbf{C}_a$ is the time derivative of $\mathbf{C}_e$, $\mathbf{C}_e^n$ is the transition matrix from ECEF frame to ENU frame.

In PR+Doppler GPS/IMU tightly-coupled navigation systems, the pseudorange is mainly for the position estimation, while the range rate is mainly for the velocity estimation.

2.3.4 Kalman filter

A Kalman filter is widely applied in sensor fusion problems such as GPS/IMU integrated navigation systems and multi-sensor applications. In a stochastic process framework, a Kalman filter is an unbiased, minimum variance and linear stochastic process (Särkkä, 2006). A Kalman filter itself can be derived as an extension of the weighted least squares approach from linear sets of algebraic to linear systems. So the Kalman filter works with a system when the process and measurement noises are white and Gaussian, the initial state is Gaussian and the system is linear. Nonlinear problems can be processed using the suboptimal nonlinear Kalman filters, for instance, the EKF, the UKF and the CKF, which aim to compute integrals like nonlinear function times Gaussian density. The PF can be applied to solve non-Gaussian problems, while the coloured noise can be augmented as extra states in the Kalman filter though a shaping filter or pre-whitening techniques.

The Kalman filter has the following properties (Farrell, 2008).

1. The Kalman filter estimate is unbiased and the maximum likelihood estimate. It is also the minimum mean-squared error estimate under Gaussian distribution assumptions.
2. The conditional mean is the minimum of any positive definite quadratic error cost function.
3. The Kalman filter is the optimal state estimation algorithm for a linear system, while the nonlinear Kalman filter is a suboptimal estimator.
4. The Kalman filter residual state error is orthogonal to all previous measurements, because it is an extension of the least squares method.
5. If a state is controllable and observable, the Kalman filter estimation error dynamics are asymptotically stable, which indicates that initial conditions do not affect the solutions over time. However, a good state and covariance initialisation is beneficial for filter convergence.

The state transition and measurement functions of a GPS/IMU tightly-coupled navigation system are nonlinear. As a time-varying system, the nonlinearity of integrated navigation systems changes over time and under different conditions. So the EKF is applied by linearising relevant state transition and measurement functions. However, the negligibility in higher-order nonlinear terms sometimes appear to lead to performance degradation, because the accumulation of estimation errors has the possibility in rendering the implemented linearised model invalid. In this case, nonlinear filtering methods should be applied, for instance, the UKF, the CKF and so on.

2.4 Initial yaw angle determination

It is impossible to determine the initial yaw angle directly from MEMS gyroscopes' outputs during stationary alignment, due to the large noise and bias. Therefore, some aiding sensors or methods are utilized to calculate the initial yaw angle for MEMS IMU, such as heading from a moving GPS receiver, GPS heading, magnetometer, transfer alignment and rotation modulation. In this section, all these methods mentioned above are introduced and compared to determine their effects on estimating the initial yaw angle.

1. Heading from a moving GPS receiver

This method uses one GPS antenna to determine yaw angle from the north and east velocities, expressed in the ENU frame as

$$\gamma = -\arctan(\frac{v_e}{v_n}) \tag{2.16}$$

This expression works only when the absolute velocity is large enough. On the contrary, a lower velocity causes a computational problem in the heading calculation. For example, when the vehicle is stationary, the north and east velocities are zero, and it is impossible to calculate the division mathematically.

2. GPS heading

The GPS heading contains at least two GPS antennas. The yaw angle is accordingly calculated from the position difference between these two antennas. The attitude accuracy is related to the baseline between two GPS antennas as

$$\gamma = \arcsin(\frac{\Delta_e}{L}) \tag{2.17}$$

where L is the baseline length and Δ_e is the position difference between two GPS antennas in eastern direction. From this expression, it can be seen that a longer baseline leads to a better attitude accuracy, because the position uncertainty is constant for a specific GPS positioning method. However, a GPS heading system is always far more expensive than the heading system with a single moving GPS receiver. So when the price is taken into consideration, for example, the low-cost application, the heading from a moving GPS receiver method is a better choice.

3. Magnetometer

A magnetometer measures the three components of the local magnetic field to calculate the yaw angle. Unlike GPS based methods, it works fluently even when the GPS signal is blocked, which makes it suitable for indoor positioning. In the pedestrian dead reckoning (PDR) application, a magnetometer is usually used to estimate yaw angle (Rahim, 2012). The magnetometer working principle is

$$\gamma = -\arctan(\frac{M_e}{M_n}) \tag{2.18}$$

where M_e and M_n are the eastern and northern components of the magnetometer's output. Although the magnetometer shows its advantage in GPS denied environments, it is still affected by other disturbances such as hard iron and soft iron distortions. Hard iron distortions caused by permanent magnets and magnetized iron or steel in a fixed location on the compass platform, will add a constant magnetic field component to the true magnetic measurements in each axis of magnetometer. Similarly, soft iron from materials near the magnetometer distorts the Earth's magnetic field lines. Unlike hard iron, the amount of distortion from soft iron depends on the magnetometer orientation, which appears to vary in

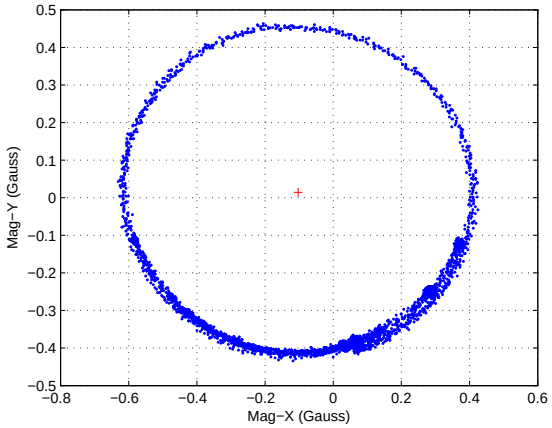

Figure 2.1: Hard iron distortions of a magnetometer

different directions. Hard iron can be calibrated in static case, while the calibration of soft iron is rather difficult because it varies in different directions. In this section, how to calibrate hard iron distortions in magnetometers will be introduced in brief.

If there are no hard iron or soft iron distortions, rotating a magnetometer at least one round will result in a circle centred at $(0, 0)$, when the outputs from the magnetometer are plotted as y-axis vs x-axis. If the hard iron distortions from surroundings are present, the centre of the circle will have a small offset from origin. If soft iron distortions are detected, the circle will degrade into an ellipse. The pre-calibration of the magnetometer is based on this property. With the magnetometer in the MEMS IMU MTi-G-700 as an example, after rotating the IMU, magnetometer measurements in horizontal plane is shown in Figure 2.1.

It can be seen that hard iron distortions are mainly present on the x-axis and soft iron distortions don't exist because the plot is nearly a circle. Hard iron distortions determined from this plot should be compensated to calculate the yaw angle. The magnetometer distortions are more environment-specific. For example, there may be some unknown magnetized iron in an unknown environment, which leads to a change in pre-calibrated hard iron distortions and subsequently affects the yaw angle determination. So the pre-calibration doesn't show the best performance in this case. Therefore, the posteriori calibration is utilized to compensate magnetometer outputs (Rahim, 2012; Ali, 2013).

4. Transfer alignment

Transfer alignment transfers the attitude estimated by a high-graded IMU to a low-cost MEMS IMU. According to the implemented observations, transfer alignment can be divided into three categories in general: attitude matching, velocity matching as well as attitude and velocity matching (Titterton and Weston, 2004). The attitude and velocity matching method is proved to have the best performance. In this thesis, the attitude from a ring laser gyroscope (RLG) IMU is simply set as the initial attitude of the MEMS IMU, because the misalignment between them is almost zero.

5. Rotation modulation

Rotation modulation is based on the observability analysis. The observability degree of the yaw angle is improved when it is experiencing some changes (Rahim, 2012; Du et al., 2014). During the rotation, neglecting the effects of the inner lever arm, the linear velocity is 0 m/s, which can be implemented as the observation of the fine alignment Kalman filter to estimate inertial sensor errors (Li et al., 2012b). For the roll and pitch estimation, rotating an IMU improves the observability of the x/y-accelerometer biases. According to the roll and pitch estimation accuracy evaluation as shown below (Titterton and Weston, 2004)

$$\delta\alpha = \frac{\nabla_x}{g}$$
$$\delta\beta = \frac{\nabla_y}{g} \tag{2.19}$$

a higher roll and pitch estimation accuracy can be expected by applying this technique.

Rotation modulation is mainly applied in high accuracy inertial navigation systems. How to apply rotation modulation in MEMS IMU applications to improve the yaw estimation accuracy in PDR and vehicle navigation systems have been described in Rahim (2012); Du et al. (2014).

3 Cubature Kalman filter for GPS/IMU tightly-coupled navigation

In a GPS/IMU tightly-coupled navigation system, the EKF is widely used to estimate navigation states, due to its simpler implementation and lower computational load. However, the EKF is a first order approximation to the nonlinear system. When the nonlinearity of the system is high, the ignoring in higher order terms will decrease the estimation accuracy and subsequently result in a suboptimal performance. So nonlinear filtering methods like the UKF, the PF and their extensions, can be applied in integrated navigation systems to improve the navigation performance. In this chapter, a recently proposed nonlinear filtering method: the CKF and its related particle filter extension the CPF will be introduced and analysed. The performance comparison between the CKF and the EKF will be tested and examined in different scenarios.

3.1 Introduction and background

Since R. E. Kalman proposed his famous recursive method to solve discrete linear filtering problems in 1960 (Kalman, 1960), the Kalman filter has been widely used in many applications. However, the KF's basic requirements in linearity and Gaussian-distributed noise are hard to meet in real world implementations. To make the KF applicable to nonlinear systems, the EKF, based on the first order Taylor term of nonlinear functions, is proposed. Although the EKF maintains the computationally efficient updated form of the KF, it suffers some drawbacks, one of which is the degradation in the estimation accuracy, due to neglecting the higher-order terms of nonlinear system functions (Lee, 2005). The 2nd-order EKF and iterated EKF (IEKF) can improve the estimation accuracy by considering the higher order terms and iterative updating. However, the 2nd-order EKF is more complicated, because it requires the higher-order linearised state space model (Sadeghi and Moshiri, 2007). The IEKF is less effective in real-time processing because of its requirement in iterative measurement updating (Kerr, 1991; Zhan and Wan, 2007).

Based on the deterministic sampling framework, the UKF and the central difference Kalman filter (CDKF) use a series of sigma-points to propagate the states and covariance matrix (Julier and Uhlmann, 2004, 1997). The sigma-points are deterministically calculated from the mean and square-root decomposition of the covariance matrix of the *a priori* random variable (Van Der Merwe, 2004). Both the UKF and the CDKF belong to the sigma-point Kalman filter family. The main difference between them is the sigma-points generation methods (Van Der Merwe, 2004; Julier and Uhlmann, 2002). The UKF generates sigma-points through the unscented transformation, while the CDKF uses the Stirling's interpolation formula to produce sigma-points (Van Der Merwe, 2004). The UKF and the CDKF can be treated as a second-order approximation to a nonlinear system. So in theory they have higher estimation accuracy than the EKF. The UKF and the CDKF have been applied in the GPS/IMU integrated navigation system and perform better than the EKF as introduced in Bistrovs and Kluga (2013); Wang et al. (2008); Crassidis (2006); Van Der Merwe (2004); Julier et al. (2007).

The CKF is a recently developed nonlinear filtering method based on the spherical-radial Cubature rule, which is developed to compute integrals like nonlinear function times Gaussian density (Arasaratnam and Haykin, 2009; Arasaratnam, 2009; Arasaratnam et al., 2010). The CKF can be treated as a second-order approximation to a nonlinear system. The higher-order CKF is also proposed as a more accurate approximation to a nonlinear system (Jia et al., 2013; Zhang et al., 2014b). Unlike the UKF using $2n+1$ unscented points to propagate the state and covariance matrix, the CKF propagates the state and covariance matrix with $2n$ Cubature points, due to which the CKF has a relatively lower computational load than the UKF. Although the Cubature points are applied, the CKF still belongs to the sigma-point Kalman filter family. The CKF shows better performance than the UKF in stability and accuracy, especially

when the dimension of the system is higher than three as suggested in Arasaratnam and Haykin (2009); Arasaratnam (2009); Arasaratnam et al. (2010). The CKF and its extension have been implemented in many application fields. The CKF is applied to a GNSS/INS tightly-coupled navigation system and the navigation estimation is enhanced as shown in Liu et al. (2010); Benzerrouk (2014). Li and Jia (2012) use an interactive multi model- (IMM-)CKF method to estimate the mobile station's location. In Tang et al. (2012), a square-root adaptive CKF is applied in the spacecraft attitude estimation. In Chandra et al. (2014); Zhang et al. (2014a), a Cubature $H\infty$ filter and its square-root version are proposed and verified in a continuous stirred tank reactor and a permanent magnet synchronous motor as examples. The CKF can also be applied to the simultaneous localisation and mapping (SLAM) problem as reported in Chandra et al. (2011).

Compared with deterministic sampling filtering methods, the PF is a sample sequential Monte Carlo filtering method based on Bayesian state estimation. The PF outperforms the KF in that it can process non-Guassian and nonlinear problems (Okuma et al., 2004). However, the PF is easy to experience the curse of dimensionality, which means the number of particles increases exponentially with the number of states (Okuma et al., 2004). This property will increase the PF computational load significantly. To avoid the curse of dimensionality, the *a posteriori* estimation of other filtering methods such as the EKF and the UKF is commonly used as the importance probability density function of the PF to ensure most of particles fall in the high likelihood area (Van Der Merwe et al., 2000). Following this logic, the CKF can be combined with the PF to generate particles. The performance of the CPF will be further tested in GPS/IMU tightly-coupled navigation systems.

In this chapter, the performance of the CKF and the CPF in GPS/IMU tightly-coupled navigation systems is the main concern.

3.2 Filtering algorithms

This section briefly introduces the CKF and the CPF algorithms. The conventional EKF filtering method is implemented as a comparison. Considering a discrete nonlinear system as

$$\begin{aligned} \mathbf{x}_k &= \mathbf{f}(\mathbf{x}_{k-1}) + \mathbf{w}_{k-1} \\ \mathbf{z}_k &= \mathbf{h}(\mathbf{x}_k) + \mathbf{v}_k \end{aligned} \tag{3.1}$$

where $\mathbf{x}_k \in \Re^{\mathbf{n_x}}$ is the system's state vector at time epoch k, $\mathbf{z}_k \in \Re^{\mathbf{n_z}}$ are the measurements, $\mathbf{w}_{k-1} \in \Re^{\mathbf{n_w}}$ and $\mathbf{v}_k \in \Re^{\mathbf{n_v}}$ represent independent process and measurement Gaussian noise sequences assumed to be independent, white and with covariance $\mathbf{Q}$ and $\mathbf{R}_k$ in respect.

3.2.1 Extended Kalman Filter

The EKF solves nonlinear problems by approximating nonlinear functions using the first order Taylor term. The Jacobian matrices calculated from the nonlinear state transition and measurement functions are implemented in the EKF as state transition and measurement matrices. The EKF algorithm is summarised as:

i) Time Update

$$\begin{aligned} \mathbf{x}_{k|k-1} &= \Phi \mathbf{x}_{k-1|k-1} \\ \mathbf{P}_{k|k-1} &= \Phi \mathbf{P}_{k-1|k-1} \Phi^T + \mathbf{Q} \end{aligned} \tag{3.2}$$

ii) Measurement Update

$$\begin{aligned} \mathbf{K}_k &= \mathbf{P}_{k|k-1}\mathbf{H}^T(\mathbf{H}\mathbf{P}_{k|k-1}\mathbf{H}^T + \mathbf{R}_k)^{-1} \\ \mathbf{x}_{k|k} &= \mathbf{x}_{k|k-1} + \mathbf{K}_k(\mathbf{z} - \mathbf{H}\mathbf{x}_{k|k-1}) \\ \mathbf{P}_{k|k} &= \mathbf{P}_{k|k-1} - \mathbf{K}_k\mathbf{H}\mathbf{P}_{k|k-1} \end{aligned} \tag{3.3}$$

where Φ is the state transition matrix, which is the Jacobian matrix of the nonlinear state transition function $\mathbf{f}(\cdot)$, and $\mathbf{H}$ is the measurement matrix, which is the Jacobian matrix of the nonlinear measurement function $\mathbf{h}(\cdot)$. $\mathbf{K}_k$ is the Kalman gain.

3.2.2 Cubature Kalman Filter

The CKF uses a series of Cubature points to propagate the *a priori* and *a posteriori* statistical characteristics. The core of the CKF is the Cubature transformation based on the spherical-radial rule (Arasaratnam and Haykin, 2009). The CKF algorithm is summarized as:

i) Time Update

$$\begin{aligned}
\mathbf{S}_{k-1|k-1} &= SVD(\mathbf{P}_{k-1|k-1}) \\
\chi_{k-1|k-1} &= \mathbf{S}_{k-1|k-1}\xi + \mathbf{x}_{k-1|k-1} \\
\chi^*_{k|k-1} &= \mathbf{f}(\chi_{k-1|k-1}) \\
\mathbf{x}_{k|k-1} &= \frac{1}{m}\sum_{i=1}^{m}\chi^*_{i,k|k-1} \\
\mathbf{P}_{k|k-1} &= \frac{1}{m}\sum_{i=1}^{m}\chi^*_{i,k|k-1}\chi^{*T}_{i,k|k-1} - \mathbf{x}_{k|k-1}\mathbf{x}^T_{k|k-1} + \mathbf{Q}
\end{aligned} \tag{3.4}$$

ii) Measurement Update

$$\begin{aligned}
\mathbf{S}_{k|k-1} &= SVD(\mathbf{P}_{k|k-1}) \\
\chi_{k|k-1} &= \mathbf{S}_{k|k-1}\xi + \mathbf{x}_{k|k-1} \\
\mathbf{Z}_{k|k-1} &= \mathbf{h}(\chi_{k|k-1}) \\
\mathbf{z}_{k|k-1} &= \frac{1}{m}\sum_{i=1}^{m}\mathbf{Z}_{i,k|k-1} \\
\mathbf{P}_{\mathbf{zz},k|k-1} &= \frac{1}{m}\sum_{i=1}^{m}\mathbf{Z}_{i,k|k-1}\mathbf{Z}^T_{i,k|k-1} - \mathbf{z}_{k|k-1}\mathbf{z}^T_{k|k-1} + \mathbf{R}_k \\
\mathbf{P}_{\mathbf{xz},k|k-1} &= \frac{1}{m}\sum_{i=1}^{m}\chi_{i,k|k-1}\mathbf{Z}^T_{i,k|k-1} - \mathbf{x}_{k|k-1}\mathbf{z}^T_{k|k-1} \\
\mathbf{K}_k &= \mathbf{P}_{\mathbf{xz},k|k-1}\mathbf{P}^{-1}_{\mathbf{zz},k|k-1} \\
\mathbf{x}_{k|k} &= \mathbf{x}_{k|k-1} + \mathbf{K}_k(\mathbf{z}_k - \mathbf{z}_{k|k-1}) \\
\mathbf{P}_{k|k} &= \mathbf{P}_{k|k-1} - \mathbf{K}_k\mathbf{P}_{\mathbf{zz},k|k-1}\mathbf{K}^T_k
\end{aligned} \tag{3.5}$$

where SVD is the matrix singular value decomposition, $\mathbf{S}$ is the square-root of the covariance matrix $\mathbf{P}$, $m = 2n$, $\xi = \sqrt{\frac{m}{2}}[1]_i$, χ_i is the Cubature point generated from states and $\mathbf{Z}_i$ represents the Cubature point generated from measurements. If $n = 2$, $[1]_i$ represents the following set of points:

$$\left\{\begin{pmatrix} 1 \\ 0 \end{pmatrix}, \begin{pmatrix} 0 \\ 1 \end{pmatrix}, \begin{pmatrix} -1 \\ 0 \end{pmatrix}, \begin{pmatrix} 0 \\ -1 \end{pmatrix}\right\}$$

The CKF uses $2n$ Cubature points to propagate state and covariance matrix. The calculation of the Jacobian matrix is avoided.

3.2.3 Cubature Particle Filter

Due to the curse of dimensionality, the number of particles in the PF increases exponentially with the dimensionality of states (Bengtsson et al., 2008; Li et al., 2005; Quang et al., 2010). In order to reduce the amount of particles without degrading the estimation accuracy, the EKF and UKF can be combined with the PF to form either the EPF or the UPF in respect (Zhou et al., 2011; Yi, 2007; Van Der Merwe et al., 2000). The *a posteriori* mean and covariance matrix from the KFs are used to specify the importance density function to generate particles, ensuring that most of the particles are located in the high likelihood area. The conventional EPF and UPF are time-consuming, because every particle is propagated by the Kalman filter before the particle filtering algorithm (Lee, 2005). Thus, a bank of KFs (one for each particle) are implemented for the particles' propagation. In the CPF, after the CKF measurement update, the *a posteriori* covariance matrix is employed as an importance density function to generate particles. The CKF is executed only once in one filtering loop. Aside from this, particles are regenerated in each recursion and will not be propagated to the next filtering loop. Therefore, the sample impoverishment problem can be avoided because of the non-recursive process.

It is usually very hard to correctly obtain the real system's noise statistics. Therefore, some researchers proposed the Gaussian particle filter (GPF) as an alternative to the particle filter (Kotecha and Djuric, 2003a,b). The GPF assumes the *a posteriori* probability distribution and the *a priori* probability distribution as Gaussian distributed. Although the multipath effects behave like a non-Gaussian noise, it is difficult to measure its statistics in real time. Therefore, to simplify, the GPF is combined in serial with the CKF to construct the CPF in this chapter. Following the CKF, the particle filter is implemented as shown below.

According to the CKF *a posteriori* estimation $\mathbf{x}_{k|k}$, particles can be generated from the importance density distribution $N(0,\mathbf{P}_{k|k})$ as

$$\mathbf{X}_{k,i} = \mathbf{x}_{k|k} + \Delta\mathbf{x}_{k|k,i}, \Delta\mathbf{x}_{k|k,i} \sim N(0,\mathbf{P}_{k|k}) \tag{3.6}$$

where $i = 1,2,...N$, and N is the number of particles. This particle generation method ensures most of the particles fall in the high likelihood area.

The importance weights can be calculated as

$$w(\mathbf{X}_{k,i}) = \frac{p(\mathbf{z}_k|\mathbf{X}_{k,i})N(\mathbf{X}_{k,i}|\mathbf{x}_{k|k-1},\mathbf{P}_{k|k-1})}{N(\mathbf{X}_{k,i}|\mathbf{x}_{k|k},\mathbf{P}_{k|k})} \tag{3.7}$$

with

$$p(\mathbf{z}_k|\mathbf{X}_{k,i}) = \frac{1}{\sqrt{(2\pi)^m\|\mathbf{R}_k\|}}\exp(-\frac{[\mathbf{z}_k-\mathbf{h}(\mathbf{X}_{k,i})]^T\mathbf{R}_k^{-1}[\mathbf{z}_k-\mathbf{h}(\mathbf{X}_{k,i})]}{2})$$

$$N(\mathbf{X}_{k,i}|\mathbf{x}_{k|k-1},\mathbf{P}_{k|k-1}) = \frac{1}{\sqrt{(2\pi)^n\|\mathbf{P}_{k|k-1}\|}}\exp(-\frac{[\mathbf{X}_{k,i}-\mathbf{x}_{k|k-1}]^T(\mathbf{P}_{k|k-1})^{-1}[\mathbf{X}_{k,i}-\mathbf{x}_{k|k-1}]}{2})$$

$$N(\mathbf{X}_{k,i}|\mathbf{x}_{k|k},\mathbf{P}_{k|k}) = \frac{1}{\sqrt{(2\pi)^n\|\mathbf{P}_{k|k}\|}}\exp(-\frac{[\mathbf{X}_{k,i}-\mathbf{x}_{k|k}]^T(\mathbf{P}_{k|k})^{-1}[\mathbf{X}_{k,i}-\mathbf{x}_{k|k}]}{2})$$

where m and n denote the dimensions of observation vector and state vector. $p(\mathbf{z}_k|\mathbf{X}_{k,i})$ is the likelihood density function. The measurements of the CPF are the same as the CKF when implemented in GPS/IMU tightly-coupled navigation systems (Zhou et al., 2011; Zhou, 2013). $N(\mathbf{X}_{k,i}|\mathbf{x}_{k|k-1},\mathbf{P}_{k|k-1})$ is the *a priori* density function, which is taken from the CKF prediction. $N(\mathbf{X}_{k,i}|\mathbf{x}_{k|k},\mathbf{P}_{k|k})$ is the importance density function taken from the CKF *a posteriori* estimation.

The *a posteriori* mean and covariance matrix can be computed as

$$\begin{aligned}\mathbf{x}_{k|k}^{+} &= \sum_{i=1}^{N} w(\mathbf{X}_{k,i})\mathbf{X}_{k,i} \\ \mathbf{P}_{k|k}^{+} &= \sum_{i=1}^{N} w(\mathbf{X}_{k,i})[\mathbf{X}_{k,i} - \mathbf{x}_{k|k}^{+}][\mathbf{X}_{k,i} - \mathbf{x}_{k|k}^{+}]^{T}\end{aligned} \tag{3.8}$$

The noise statistics is assumed to be Gaussian distributed, which is an approximation to the real probability density function. When the statistics of non-Gaussian distributed measurement errors is already known, they should be implemented in the CPF.

3.3 CKF performance analysis

The links among the EKF, the UKF and the CKF have been demonstrated from the discrete Riccati equation and the formula on conditional expectations that does not involve an explicit Riccati equation in Gustafsson and Hendeby (2012). In this section, the CKF estimation accuracy will be evaluated mathematically through Taylor expansion. Using Taylor expansion to evaluate the estimation accuracy of the sigma-point Kalman filter's *a posteriori* mean and covariance matrix has been discussed in Van Der Merwe (2004). However, the author does not show the other terms' accuracy of the SPKF such as the Kalman gain, the *a priori* estimation, etc. The analysis of these terms is helpful in understanding the working principle of nonlinear filtering methods. Unlike the analysis in Van Der Merwe (2004), the CKF performance is analysed considering all the CKF related terms. The internal relationship between the CKF and the EKF is also shown in the following analysis.

3.3.1 Analysis of the CKF estimation accuracy

i) Time update

In order to evaluate the estimation accuracy, the CKF is expanded into its related Taylor terms. Considering a random variable $\mathbf{x}_{k-1|k-1}$ with mean $\overline{\mathbf{x}}_{k-1|k-1}$ and covariance matrix $\mathbf{P}_{k-1|k-1}$ obeying a Gaussian distribution $\mathbf{x}_{k-1|k-1} \sim \mathbf{N}(\overline{\mathbf{x}}_{k-1|k-1}, \mathbf{P}_{k-1|k-1})$ and defining $\Delta\mathbf{x}_{k-1|k-1}$ as $\mathbf{x}_{k-1|k-1} - \overline{\mathbf{x}}_{k-1|k-1}$ with the Gaussian distribution $\Delta\mathbf{x}_{k-1|k-1} \sim \mathbf{N}(0, \mathbf{P}_{k-1|k-1})$, the state transition function $\mathbf{f}(\mathbf{x}_{k-1|k-1})$ can be expanded into a Taylor series around $\overline{\mathbf{x}}_{k-1|k-1}$ as

$$\begin{aligned}\mathbf{f}(\mathbf{x}_{k-1|k-1}) &= \mathbf{f}(\overline{\mathbf{x}}_{k-1|k-1} + \Delta\mathbf{x}_{k-1|k-1}) \\ &= \mathbf{f}(\overline{\mathbf{x}}_{k-1|k-1}) + D_{\Delta\mathbf{x}_{k-1|k-1}}\mathbf{f} + \frac{D^2_{\Delta\mathbf{x}_{k-1|k-1}}\mathbf{f}}{2!} + \frac{D^3_{\Delta\mathbf{x}_{k-1|k-1}}\mathbf{f}}{3!} + \frac{D^4_{\Delta\mathbf{x}_{k-1|k-1}}\mathbf{f}}{4!} + \ldots\end{aligned} \tag{3.9}$$

where $D_{\Delta\mathbf{x}}\mathbf{f} = [(\Delta\mathbf{x}^T\nabla)\mathbf{f}(x)^T]^T|_{\mathbf{x}=\overline{\mathbf{x}}}$ and ∇ represents the differential of $\mathbf{f}(\mathbf{x})$.

Substituting the Cubature points $\chi_{i,k-1|k-1} = \overline{\mathbf{x}}_{k-1|k-1} + \sqrt{n\mathbf{P}_{k-1|k-1}}[1]_i$ into the equation (3.9), the state transition function's predicted value of each Cubature point is

$$\begin{aligned}\chi^{*}_{i,k|k-1} &= \mathbf{f}(\chi_{i,k-1|k-1}) = \mathbf{f}(\overline{\mathbf{x}}_{k-1|k-1} + \Delta\mathbf{x}_{k-1|k-1}) \\ &= \mathbf{f}(\overline{\mathbf{x}}_{k-1|k-1}) + D_{\Delta\mathbf{x}_{k-1|k-1}}\mathbf{f} + \frac{D^2_{\Delta\mathbf{x}_{\mathbf{k-1|k-1}}}\mathbf{f}}{2!} + \frac{D^3_{\Delta\mathbf{x}_{k-1|k-1}}\mathbf{f}}{3!} + \frac{D^4_{\Delta\mathbf{x}_{k-1|k-1}}\mathbf{f}}{4!} + \ldots\end{aligned} \tag{3.10}$$

The predicted estimation mean is

$$\begin{aligned}\mathbf{x}_{k|k-1} &= \frac{1}{2n}\sum_{i=1}^{2n}\chi^*_{i,k|k-1} \\ &= \frac{1}{2n}\sum_{i=1}^{2n}\mathbf{f}(\overline{\mathbf{x}}_{k-1|k-1}+\Delta\mathbf{x}_{k-1|k-1}) \\ &= \frac{1}{2n}\sum_{i=1}^{2n}(\mathbf{f}(\overline{\mathbf{x}}_{k-1|k-1})+D_{\Delta\mathbf{x}_{k-1|k-1}}\mathbf{f}+\frac{D^2_{\Delta\mathbf{x}_{k-1|k-1}}\mathbf{f}}{2!}+\frac{D^3_{\Delta\mathbf{x}_{k-1|k-1}}\mathbf{f}}{3!}+\frac{D^4_{\Delta\mathbf{x}_{k-1|k-1}}\mathbf{f}}{4!}+...)\end{aligned} \tag{3.11}$$

Considering $\Delta\mathbf{x}_{k|k-1}$ is symmetrically distributed, all the odd moments sum up to zero. Therefore, $\mathbf{x}_{k|k-1}$ is computed as

$$\mathbf{x}_{k|k-1} = \mathbf{f}(\overline{\mathbf{x}}_{k-1|k-1})+\frac{1}{2n}\sum_{i=1}^{2n}(\frac{D^2_{\Delta\mathbf{x}_{k-1|k-1}}\mathbf{f}}{2!}+\frac{D^4_{\Delta\mathbf{x}_{k-1|k-1}}\mathbf{f}}{4!}+...) \tag{3.12}$$

It is complex to calculate equation (3.12) directly because of the higher order terms. To simplify, equation (3.12) is rewritten by keeping the second order term and neglecting higher order terms,

$$\mathbf{x}_{k|k-1} = \mathbf{f}(\overline{\mathbf{x}}_{k-1|k-1})+E[\frac{D^2_{\Delta\mathbf{x}_{k-1|k-1}}\mathbf{f}}{2!}] \tag{3.13}$$

where $\frac{D^2_{\Delta\mathbf{x}_{k-1|k-1}}\mathbf{f}}{2!} = \frac{D_{\Delta\mathbf{x}_{k-1|k-1}}(D_{\Delta\mathbf{x}_{k-1|k-1}}\mathbf{f})}{2!} = \frac{\nabla^T\Delta\mathbf{x}_{k-1|k-1}\Delta^T\mathbf{x}_{k-1|k-1}\nabla}{2!}\mathbf{f}$. According to the definition of the covariance matrix that $E[\Delta\mathbf{x}\Delta\mathbf{x}^T]=\mathbf{P}$, the second order term in the Taylor expansion is

$$E[\frac{D^2_{\Delta\mathbf{x}_{k-1|k-1}}\mathbf{f}}{2!}] = \frac{\nabla^T\mathbf{P}_{k-1|k-1}\nabla\mathbf{f}}{2!} \tag{3.14}$$

The CKF predicted state is

$$\mathbf{x}_{k|k-1} = \mathbf{f}(\overline{\mathbf{x}}_{k-1|k-1})+\frac{\nabla^T\mathbf{P}_{k-1|k-1}\nabla\mathbf{f}}{2!} \tag{3.15}$$

As shown in the CKF algorithm (3.4), $\mathbf{P}_{k|k-1}$ is given as

$$\mathbf{P}_{k|k-1} = E[(\chi^*_{i,k|k-1}-\mathbf{x}_{k|k-1})(\chi^*_{i,k|k-1}-\mathbf{x}_{k|k-1})^T]+\mathbf{Q} \tag{3.16}$$

After neglecting the terms higher than three, $\chi^*_{i,k|k-1}-\mathbf{x}_{k|k-1}$ can be calculated as

$$\chi^*_{i,k|k-1}-\mathbf{x}_{k|k-1} = D_{\Delta\mathbf{x}_{k|k-1}}\mathbf{f}+\frac{D^2_{\Delta\mathbf{x}_{k|k-1}}\mathbf{f}}{2!}+\frac{D^3_{\Delta\mathbf{x}_{k|k-1}}\mathbf{f}}{3!}-E[\frac{D^2_{\Delta\mathbf{x}_{k|k-1}}\mathbf{f}}{2!}] \tag{3.17}$$

Considering the symmetry of $\Delta\mathbf{x}_{k|k-1}$, the mean value of all odd order terms of $\Delta\mathbf{x}_{k|k-1}$ equals zero and the true covariance matrix is

$$\begin{aligned}\mathbf{P}_{k|k-1} = E[&D_{\Delta\mathbf{x}_{k|k-1}}\mathbf{f}(D_{\Delta\mathbf{x}_{k|k-1}}\mathbf{f})^T + \frac{D_{\Delta\mathbf{x}_{k|k-1}}\mathbf{f}(D^3_{\Delta\mathbf{x}_{k|k-1}}\mathbf{f})^T}{3!} + \frac{D^2_{\Delta\mathbf{x}_{k|k-1}}\mathbf{f}(D^2_{\Delta\mathbf{x}_{k|k-1}}\mathbf{f})^T}{2\times 2!} \\ &+ \frac{D^3_{\Delta\mathbf{x}_{k|k-1}}\mathbf{f}(D_{\Delta\mathbf{x}_{k|k-1}}\mathbf{f})^T}{3!}] - E[\frac{D^2_{\Delta\mathbf{x}_{k|k-1}}\mathbf{f}}{2!}]E[\frac{D^2_{\Delta\mathbf{x}_{k|k-1}}\mathbf{f}}{2!}]^T + \mathbf{Q}\end{aligned} \tag{3.18}$$

If the following relationship is valid,

$$D_{\Delta\mathbf{x}}\mathbf{f} = \Phi\Delta\mathbf{x} \tag{3.19}$$

where Φ is the Jacobian matrix of $\mathbf{f}(\cdot)$, equation (3.18) can be rewritten as

$$\begin{aligned}\mathbf{P}_{k|k-1} = \Phi\mathbf{P}_{k-1|k-1}\Phi^T + E[&\frac{D_{\Delta\mathbf{x}_{k-1|k-1}}\mathbf{f}(D^3_{\Delta\mathbf{x}_{k-1|k-1}}\mathbf{f})^T}{3!} + \frac{D^2_{\Delta\mathbf{x}_{k-1|k-1}}\mathbf{f}(D^2_{\Delta\mathbf{x}_{k-1|k-1}}\mathbf{f})^T}{2\times 2!} \\ &+ \frac{D^3_{\Delta\mathbf{x}_{k-1|k-1}}\mathbf{f}(D_{\Delta\mathbf{x}_{k-1|k-1}}\mathbf{f})^T}{3!}] - [(\frac{\nabla^T\mathbf{P}_{k-1|k-1}\nabla}{2!})\mathbf{f}][(\frac{\nabla^T\mathbf{P}_{k-1|k-1}\nabla}{2!})\mathbf{f}]^T + \mathbf{Q}\end{aligned} \tag{3.20}$$

From equations (3.15) and (3.20), it can be found that the CKF can capture and propagate at least the second order terms of a nonlinear system. However, when applied in a linear or linearised system, the higher-order terms including the second order terms are zero. As a result, (3.15) and (3.20) will be identical to the EKF.

ii) Measurement update

Considering the random variable $\mathbf{x}_{k|k-1}$ with mean $\overline{\mathbf{x}}_{k|k-1}$ and covariance matrix $\mathbf{P}_{k|k-1}$ of Gaussian distribution $\mathbf{x}_{k|k-1} \sim \mathbf{N}(\overline{\mathbf{x}}_{k|k-1}, \mathbf{P}_{k|k-1})$ and define $\Delta\mathbf{x}_{k|k-1}$ as $\mathbf{x}_{k|k-1} - \overline{\mathbf{x}}_{k|k-1}$, with the Gaussian distribution $\Delta\mathbf{x}_{k|k-1} \sim \mathbf{N}(0, \mathbf{P}_{k|k-1})$ as shown in the analysis before, the measurement function $\mathbf{h}(\mathbf{x}_{k|k-1})$ can be expanded into a Taylor series around $\overline{\mathbf{x}}_{k|k-1}$ as

$$\begin{aligned}\mathbf{h}(\mathbf{x}_{k|k-1}) &= \mathbf{h}(\overline{\mathbf{x}}_{k|k-1} + \Delta\mathbf{x}_{k|k-1}) \\ &= \mathbf{h}(\overline{\mathbf{x}}_{k|k-1}) + D_{\Delta\mathbf{x}_{k|k-1}}\mathbf{h} + \frac{D^2_{\Delta\mathbf{x}_{k|k-1}}\mathbf{h}}{2!} + \frac{D^3_{\Delta\mathbf{x}_{k|k-1}}\mathbf{h}}{3!} + \frac{D^4_{\Delta\mathbf{x}_{k|k-1}}\mathbf{h}}{4!} + \ldots\end{aligned} \tag{3.21}$$

Substituting the Cubature points $\chi_{i,k|k-1} = \overline{\mathbf{x}}_{k|k-1} + \sqrt{n\mathbf{P}_{k|k-1}}[1]_i$ into the equation (3.21), the measurement function's predicted value of each Cubature point is

$$\begin{aligned}\mathbf{Z}_{i,k|k-1} = \mathbf{h}(\chi_{i,k|k-1}) &= \mathbf{h}(\overline{\mathbf{x}}_{k|k-1} + \Delta\mathbf{x}_{k|k-1}) \\ &= \mathbf{h}(\overline{\mathbf{x}}_{k|k-1}) + D_{\Delta\mathbf{x}_{k|k-1}}\mathbf{h} + \frac{D^2_{\Delta\mathbf{x}_{k|k-1}}\mathbf{h}}{2!} + \frac{D^3_{\Delta\mathbf{x}_{k|k-1}}\mathbf{h}}{3!} + \frac{D^4_{\Delta\mathbf{x}_{k|k-1}}\mathbf{h}}{2!} + \ldots\end{aligned} \tag{3.22}$$

Like the calculation in predicted value of state transition function, neglecting the higher order terms, the mean value of measurement Cubature points is

$$\mathbf{z}_{k|k-1} = \mathbf{h}(\overline{\mathbf{x}}_{k|k-1}) + \frac{\nabla^T\mathbf{P}_{k|k-1}\nabla\mathbf{h}}{2!} \tag{3.23}$$

By definition, $\mathbf{P}_{\mathbf{zz},k|k-1}$ is given as

$$\mathbf{P}_{\mathbf{zz},k|k-1} = E[(\mathbf{Z}_{k|k-1} - \mathbf{z}_{k|k-1})(\mathbf{Z}_{k|k-1} - \mathbf{z}_{k|k-1})^T] + \mathbf{R}_k \tag{3.24}$$

$\mathbf{Z}_{k|k-1} - \mathbf{z}_{k|k-1}$ can be calculated as

$$\mathbf{Z}_{k|k-1} - \mathbf{z}_{k|k-1} = D_{\Delta\mathbf{x}_{k|k-1}}\mathbf{h} + \frac{D^2_{\Delta\mathbf{x}_{k|k-1}}\mathbf{h}}{2!} + \frac{D^3_{\Delta\mathbf{x}_{k|k-1}}\mathbf{h}}{3!} - E[\frac{D^2_{\Delta\mathbf{x}_{k|k-1}}\mathbf{h}}{2!}] \tag{3.25}$$

Applying the symmetry of $\Delta\mathbf{x}_{k|k-1}$, the mean value of all odd order terms of $\Delta\mathbf{x}_{k|k-1}$ equals zero and the covariance matrix is calculated as

$$\begin{aligned}\mathbf{P}_{\mathbf{zz},k|k-1} = E[D_{\Delta\mathbf{x}_{k|k-1}}\mathbf{h}(D_{\Delta\mathbf{x}_{k|k-1}}\mathbf{h})^T + \frac{D_{\Delta\mathbf{x}_{k|k-1}}\mathbf{h}(D^3_{\Delta\mathbf{x}_{k|k-1}}\mathbf{h})^T}{3!} + \frac{D^2_{\Delta\mathbf{x}_{k|k-1}}\mathbf{h}(D^2_{\Delta\mathbf{x}_{k|k-1}}\mathbf{h})^T}{2\times 2!} \\ + \frac{D^3_{\Delta\mathbf{x}_{k|k-1}}\mathbf{h}(D_{\Delta\mathbf{x}_{k|k-1}}\mathbf{h})^T}{3!}] - E[\frac{D^2_{\Delta\mathbf{x}_{k|k-1}}\mathbf{h}}{2!}]E[\frac{D^2_{\Delta\mathbf{x}_{k|k-1}}\mathbf{h}}{2!}]^T + \mathbf{R}_k\end{aligned} \tag{3.26}$$

If the following relationship is valid,

$$D_{\Delta\mathbf{x}}\mathbf{h} = \mathbf{H}\Delta\mathbf{x} \tag{3.27}$$

where $\mathbf{H}$ is the Jacobian matrix of $\mathbf{h}(\cdot)$, equation (3.26) can be rewritten as

$$\begin{aligned}\mathbf{P}_{\mathbf{zz},k|k-1} = \mathbf{H}\mathbf{P}_{k|k-1}\mathbf{H}^T + E[\frac{D_{\Delta\mathbf{x}_{k|k-1}}\mathbf{h}(D^3_{\Delta\mathbf{x}_{k|k-1}}\mathbf{h})^T}{3!} + \frac{D^2_{\Delta\mathbf{x}_{k|k-1}}\mathbf{h}(D^2_{\Delta\mathbf{x}_{k|k-1}}\mathbf{h})^T}{2\times 2!} \\ + \frac{D^3_{\Delta\mathbf{x}_{k|k-1}}\mathbf{h}(D_{\Delta\mathbf{x}_{k|k-1}}\mathbf{h})^T}{3!}] - E[\frac{\nabla^T\mathbf{P}_{k|k-1}\nabla}{2!}\mathbf{h}]E[\frac{\nabla^T\mathbf{P}_{k|k-1}\nabla}{2!}\mathbf{h}]^T + \mathbf{R}_k\end{aligned} \tag{3.28}$$

By definition, $\mathbf{P}_{\mathbf{xz},k|k-1}$ is given by

$$\begin{aligned}\mathbf{P}_{\mathbf{xz},k|k-1} &= E[(\chi_{k|k-1} - \mathbf{x}_{k|k-1})(\mathbf{Z}_{k|k-1} - \mathbf{z}_{k|k-1})^T] \\ &= E[\Delta\mathbf{x}_{k|k-1}(D_{\Delta\mathbf{x}_{k|k-1}}\mathbf{h} + \frac{D^2_{\Delta\mathbf{x}_{k|k-1}}\mathbf{h}}{2!} + \frac{D^3_{\Delta\mathbf{x}_{k|k-1}}\mathbf{h}}{3!})^T]\end{aligned} \tag{3.29}$$

Applying equation (3.27) to equation (3.29), the following equation can be deduced

$$\mathbf{P}_{\mathbf{xz},k|k-1} = \mathbf{P}_{k|k-1}\mathbf{H}^T + E[\Delta\mathbf{x}_{k|k-1}\frac{D^3_{\Delta\mathbf{x}_{k|k-1}}\mathbf{h}}{3!}]^T \tag{3.30}$$

The Cubature Kalman gain is then expressed as

$$\mathbf{K}_k = \frac{\mathbf{P}_{\mathbf{xz},k|k-1}}{\mathbf{P}_{\mathbf{zz},k|k-1}} \tag{3.31}$$

The *a posteriori* state and covariance matrix are calculated as

$$\begin{aligned}\mathbf{x}_{k|k} &= \mathbf{x}_{k|k-1} + \mathbf{K}_k(\mathbf{z}_k - \mathbf{z}_{k|k-1}) \\ \mathbf{P}_{k|k} &= \mathbf{P}_{k|k-1} - \mathbf{K}_k\mathbf{P}_{\mathbf{zz},k|k-1}\mathbf{K}_k^T\end{aligned} \tag{3.32}$$

From the analysis of the CKF estimation accuracy, it is found that the CKF is not only related to the first order but also the second (or even higher) order terms of the covariance matrix, showing the CKF's ability to capture higher order terms of nonlinear functions. However, if the nonlinearity of the system is not so high or the system is a linear system, the higher-order terms evaluate to be zero and the CKF degrades to match the EKF, while the EKF is the same as KF, which is an optimal estimator. As shown in Li et al. (2006); Yi and Grejner-Brzezinska (2006); Zhou (2013), nonlinear filtering methods like UKF do not show any estimation accuracy enhancement when applied in a GPS/IMU integrated navigation system with a linear model, although they mention the improvement in robustness by applying nonlinear filtering methods. Rhudy et al. (2013) and Rhudy (2013) analyse the sensitivity of the EKF and UKF and point out that the UKF has a similar estimation accuracy as the EKF. However, the model implemented in his analysis is linear. Therefore, the linear and nonlinear filtering methods are expected to have a similar performance. In this thesis, a nonlinear attitude expression will be introduced into the state transition function to better examine the advantage of the CKF in a tightly-coupled navigation system.

3.3.2 Comparison between the EKF, UKF and CKF

Compared with the EKF, the UKF and CKF can be categorized as deterministic filtering methods using a series of centrally distributed weighted sampling sigma points to approximate the *a posteriori* distribution of nonlinear states.

The UKF is more applicable to lower-dimensional nonlinear systems ($n \leq 3$). As indicated in the UKF algorithm, since the choice of κ in the UKF must satisfy $n + \kappa = 3$, if the dimensionality or number of nonlinear equations is higher than three, κ is negative, which may render the covariance matrix negative definite. The CKF will not suffer from such a problem because all the weights in the CKF are positive, guaranteeing the positive definiteness of the covariance matrix. Therefore, the CKF is applicable to all nonlinear problems, no matter how large the dimensionality is (Arasaratnam and Haykin, 2009; Arasaratnam, 2009).

Due to the possibility of negative weights, the UKF covariance matrix can not be guaranteed to be positive-definite, which causes some difficulties in obtaining the square-root of the covariance matrix, too. So another two parameters α and β are introduced to prevent this from happening. Therefore, a balance among the three parameters is an art and a science, which also limits the flexibility of the UKF.

When the scale factor κ in the UKF is set to zero, the UKF will have the same form as the CKF. In this sense, the CKF can be treated as a special case of the UKF with the zero-point weight w_0 being zero. However, according to Arasaratnam and Haykin (2009) and Arasaratnam (2009), the Cubature transformation is deduced mathematically in theory. On the contrary, the unscented transformation is based on a certain assumption and is not yet proved mathematically.

The EKF utilizes the first order Taylor term to approximate a nonlinear system. The precise computation of the Jacobian matrix is not an easy task, and the approximation works under a certain assumption. For example, the GPS/IMU error state space EKF works when the error is small enough. On the other hand, both the UKF and the CKF make a second order approximation to a nonlinear system, which can not only improve the filtering accuracy, but also reduce the effect in computing the Jacobian matrix.

3.4 Application of the CKF in tightly-coupled navigation

3.4.1 Nonlinear attitude expression

From the estimation accuracy evaluation, it can be found that if a nonlinear filtering method like the CKF is applied to a linear system, the estimation accuracy will not be improved due to the CKF's failure to capture higher order terms of nonlinear functions. According to this, the conventional psi-angle expression in equation (2.5) is revised by treating the attitude error as the misalignment angle between the true and estimated frames according to Kong et al. (1999). The direction cosine matrix can then be applied to describe the misalignment.

$$\mathbf{C}_{\tilde{n}}^{n} = \begin{bmatrix} c\delta\beta c\delta\gamma - s\delta\beta s\delta\alpha s\delta\gamma & c\delta\beta s\delta\gamma + s\delta\beta s\delta\alpha c\delta\gamma & -s\delta\beta c\delta\alpha \\ -c\delta\alpha s\delta\gamma & c\delta\alpha c\delta\gamma & s\delta\alpha \\ s\delta\beta c\delta\gamma + c\delta\beta s\delta\alpha s\delta\gamma & s\delta\beta s\delta\gamma - c\delta\beta s\delta\alpha c\delta\gamma & c\delta\beta c\delta\alpha \end{bmatrix} \tag{3.33}$$

where c, s represent the cos and sin calculations. The expression related to roll and pitch errors in (3.33) can be further simplified by applying $c\delta\beta \approx 1$ and $s\delta\beta \approx \delta\beta$. Unlike the yaw angle, roll and pitch angles are always observable, so the CKF should be expected to have a similar or sometimes even worse roll and pitch estimation accuracy than the EKF even if implemented with the nonlinear attitude expression (Farrell, 2008). Considering the different degrees of observability between the yaw angle and roll, pitch angles, equation (3.33) is implemented with the CKF to show the effects of the observability to the performance of nonlinear filtering methods.

The psi-angle expression can be approximated as (Groves, 2008)

$$[\Psi\times] = \mathbf{I}_{3\times 3} - \mathbf{C}_{\tilde{n}}^{n} \tag{3.34}$$

This expression is widely used in solving in-motion alignment problems (Li et al., 2013). The conventional psi-angle approximation works only when the attitude error is small enough (Groves, 2008). However, when a vehicle is standing still or there are no observations, attitude errors especially yaw angle error accumulate very quickly, since the observations have no benefits in the state estimation (Georgy et al., 2010). In these cases, the psi-angle expression's requirement of small attitude errors cannot always be met, leading to some truncation errors in the attitude estimation. According to the inertial navigation mechanization, if the attitude is not well estimated, navigation estimations like position and velocity will be degraded, too. The expression (3.33) transforms the attitude error into a misalignment direction cosine matrix, which has no the small attitude error requirement. So even if the attitude error is very large, the expression can still work fluently (Ali and Ullah Baig Mirza, 2011). The state transition functions of the attitude and velocity errors should be revised as (Kong et al., 1999):

$$\dot{\Psi} = (\mathbf{I} - \mathbf{C}_{\tilde{n}}^{n})\tilde{\omega}_{in}^{\tilde{n}} + \delta\omega_{in}^{n} - \mathbf{C}_{b}^{n}\epsilon \tag{3.35}$$

$$\delta\dot{\mathbf{v}}^{n} = \left[\mathbf{I} - \mathbf{C}_{\tilde{n}}^{n}\right]\mathbf{C}_{b}^{\tilde{n}}\mathbf{f}^{b} + \mathbf{C}_{b}^{n}\nabla - (2\delta\omega_{ie}^{n} + \delta\omega_{en}^{n}) \times \mathbf{v}^{n} - (2\tilde{\omega}_{ie}^{n} + \tilde{\omega}_{en}^{n}) \times \delta\mathbf{v}^{n} + \delta\mathbf{g}^{n} \tag{3.36}$$

As shown in equations (3.35) and (3.36), if the attitude error is small enough, the attitude and velocity error state transition functions are the same as the psi-angle expression in (2.5). For a high-grade IMU like a RLG IMU with lower gyro drift, the EKF and the CKF can be expected to show a similar performance.

Table 3.1: Observability degree of different states under different maneuvering

Observability	linear motion			Angular motion				Linear and angular motion	
	Uniform motion	North acc.	East acc.	Roll axis	Pitch axis	Yaw axis	Triaxial rotation	Tri. rot.+ linear mot.	Uni. cir. mot.
$\delta\alpha$	Ob	Ob	Ob	Ob	Ob	Ob	Ob	Ob	Ob
$\delta\beta$	Ob	Ob	Ob	Ob	Ob	Ob	Ob	Ob	Ob
$\delta\gamma$	Un	WOb	WOb	WOb	WOb	Ob	Ob	Ob	Ob

Ob: Observable; WOb: Weakly Observable; Un: Unobservable
Tri. rot.+ linear mot.: Triaxial rotation and linear motion; Uni. cir. mot.: Uniform circular motion

3.4.2 Observability analysis

As a time varying system, the states of an integrated navigation system have different degrees of observability under different motion scenarios. Using a complex trajectory to examine the filtering method's performance is too general. If states become totally observable in some specific scenarios, it is hard to point out that nonlinear filtering methods like the CKF must be superior to the EKF even when implemented with a nonlinear model (Yi and Grejner-Brzezinska, 2006; Yi, 2007). So it will be beneficial and suggestive to compare the filtering methods' performance under different scenarios according to observability analysis.

Observability analysis has been discussed in many papers. In Goshen-Meskin and Bar-Itzhack (1992, 1990), the piece wise constant system (PWCS) method is used to analyse the observability of a time variant system. The global observability is applied to analyse navigation states' observability of integrated navigation systems (Tang et al., 2009) and non-holonomic constraints (Rothman et al., 2014; Niu et al., 2012). According to Niu et al. (2012); Hong et al. (2005); Becker et al. (2010), under different maneuvering, unobservable states will become observable. Li et al. (2012a); Han and Wang (2008) and Rhee et al. (2004) introduce the concept of degree of observability, which reflects the effect of maneuvering to state estimation. According to the navigation states' degree of observability under different maneuvering, Table 3.1 is given.

In Table 3.1, Ob represents observable, Un represents unobservable and WOb represents weakly observable. In tri-axial rotation maneuvering, although $\delta\gamma$ becomes observable as indicated in Table 3.1, the yaw observability degree improvement is still smaller than the other states. But compared with the yaw angle in other scenarios, its observability degree is improved significantly. How to improve the yaw angle estimation accuracy in unobservable cases is always a hard task because the measurements have no benefits in yaw estimation in such cases. The unobservability will lead to a fast accumulation of estimation error and make the linear expression become invalid. The nonlinear filtering method can be expected to have a superior performance to the linear method in such a case. On the contrary, if the states are always observable, the error accumulation will be slower (the linear psi-angle expression is still valid), indicating a similar performance of the linear and nonlinear filtering methods. The navigation accuracy improvement will be zero even if applying nonlinear filtering methods with nonlinear attitude expression in such scenarios.

3.5 Simulation

In this section, several scenarios are designed with specific maneuvering to examine the performance difference between the EKF and the CKF under different degrees of observability. Since the position and velocity of the integrated navigation system are usually determined directly from GPS and they are

Table 3.2: Attitude comparison between the CKF and the EKF methods in constant velocity simulation

Filtering methods	Roll RMS (deg)	Pitch RMS (deg)
EKF	0.834	0.927
CKF	0.871	0.947

always observable, the attitude estimation is taken as the main indicator to show the performance difference between these two filtering methods in different scenarios, including constant velocity, accelerating and turning.

Some noises are introduced to simulate a low-cost MEMS IMU. It is assumed that the constant bias of the gyroscopes is 1.146 deg/s, the bias instability is 1.146 deg/s, which is generated by combining two independent 1st-order Markovian processes, the rate random walk is 0.458 $deg/s/\sqrt{s}$, generated by integrating a white noise, and the sensor noise is a white noise with standard derivation 1.146 $deg/\sqrt{s}$. Like a gyroscope, the accelerometers' bias and noise can be summarized as: constant bias 0.02 m/s^2, bias instability 0.02 m/s^2, rate random walk 0.008 $m/s^2/\sqrt{s}$ and white noise 0.02 $m/s/\sqrt{s}$. When implemented in the Kalman filter, the inertial sensors' noises are modelled as 1st-order Markovian processes plus white noise in this chapter.

In order to reduce the effect of parameter tuning on the noise covariance matrices such as $\mathbf{P}_0, \mathbf{Q}, \mathbf{R}$, all the parameters are identically tuned in all scenarios. The vehicle starts from a stationary state with good position and attitude initialization. So the initial standard deviation of attitude, position and velocity can be set to 0. The gyroscope and accelerometer biases are modelled as 1st-order Markovian processes with a time constant of 40 h. The initial standard deviations of the gyroscope and accelerometer biases are 10 $''/s$ and 2×10^{-4} m/s^2. In the simulation, in order to better show the effect of observability on filtering methods' performance, the GPS observation is simulated as error free. Considering the computational error, the measurement standard deviation is assumed as 1 $cm/\sin(\theta_{ele})$, where θ_{ele} is the satellite elevation angle. The system matrix $\mathbf{Q}$ is determined from the inertial sensors' stochastic errors. The standard deviation related to the gyroscope and accelerometer biases in $\mathbf{Q}$ are 1 deg/s and 0.01 m/s^2 respectively. The attitude, velocity and position standard deviations are set as 3.6 $''$, 0.03 m/s, 1 m. The position related elements in $\mathbf{P}_0, \mathbf{Q}$ should be converted to the LLH frame.

The simulation is executed 10 times to examine the performance difference between the CKF and the EKF. The inertial sensors' noises are regenerated in each simulation run, and the same simulation data will be implemented with the CKF and the EKF separately. The simulation result is the average of the absolute estimation errors of the 10 simulation runs. Since the yaw angle's observability changes under different scenarios, the yaw estimation error comparison is emphasized. For all the simulations and experiments in this thesis, the root mean square (RMS) value over the whole trajectory will be used to indicate the performance of different methods.

1. Constant velocity

In this simulation, after an accelerating period, the vehicle is at a constant velocity without any attitude change as shown in Figure 3.1. The simulation time is 600 s. During the first 30 s, the vehicle accelerates from 0 to 30 m/s. And then the velocity will be kept as a constant in the following 570 s. According to observability analysis, the yaw angle is unobservable in stationary or constant velocity cases (no acceleration). Since the unobservable yaw angle drifts very quickly over time, especially for the EKF, only the first 300 seconds' navigation result is shown. The roll, pitch and yaw estimation errors between the CKF and the EKF are shown in Figures 3.2, 3.3, 3.4 and Table 3.2.

It can be seen from the figures and table that after applying the CKF and the nonlinear attitude expression, the yaw angle drift is far slower than the EKF in the constant velocity case. During the acceleration

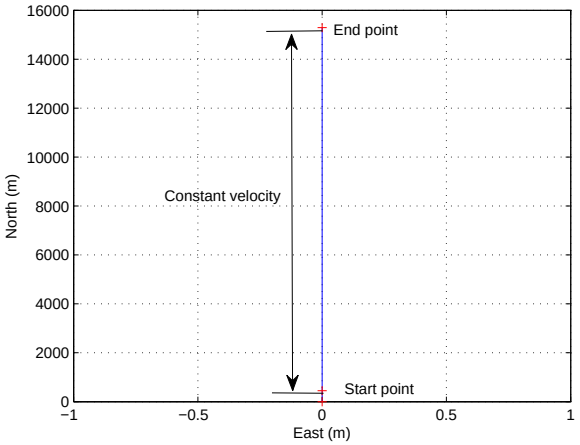

Figure 3.1: Trajectory of constant velocity simulation

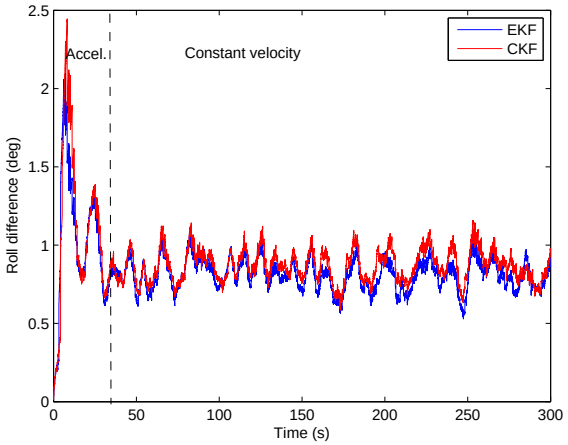

Figure 3.2: Roll error of the EKF and the CKF in constant velocity simulation

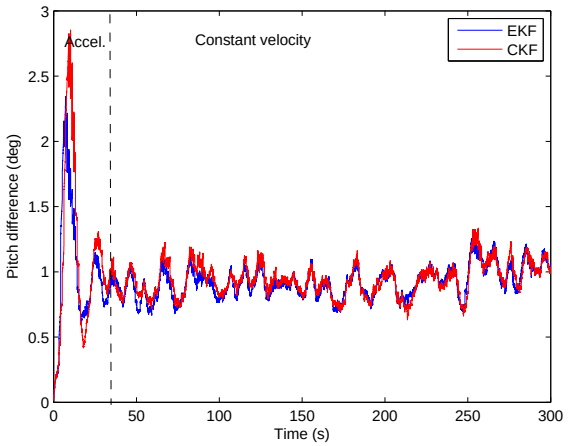

Figure 3.3: Pitch error of the EKF and the CKF in constant velocity simulation

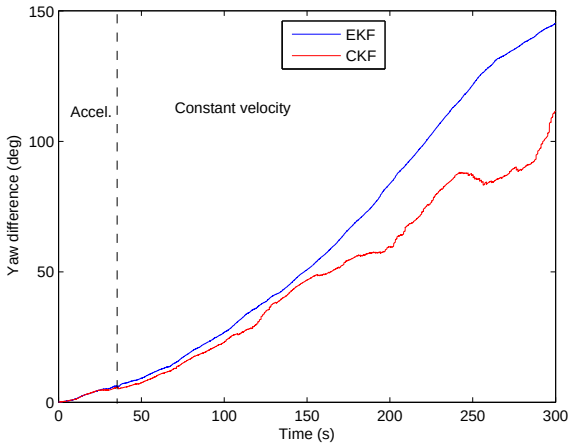

Figure 3.4: Yaw error of the EKF and the CKF in constant velocity simulation

period, the CKF and the EKF have the similar performance, due to the yaw angle becoming weakly observable. Since the yaw angle drifts very quickly, only the pitch and roll estimation errors are given in Table 3.2. From Table 3.2, it can be seen that the CKF shows no improvements in the roll and pitch estimation which are always observable.

2. Accelerating

In the accelerating simulation, the velocity changes as shown in Figure 3.5. The vehicle heads for the north. There are no attitude and velocity changes in the eastern and up directions in the simulation. According to the observability analysis, the yaw angle is weakly observable when accelerating. The roll, pitch and yaw estimation error comparisons between the CKF and the EKF are shown in Figures 3.6, 3.7, 3.8 and Table 3.3.

During the acceleration process, the yaw angle is weakly observable. As shown in Figure 3.8, the yaw estimation accuracy differences between the CKF and the EKF are much smaller than in the constant velocity case. However, it still can be seen that the CKF performs better than the EKF in the yaw angle estimation.

3. Turning

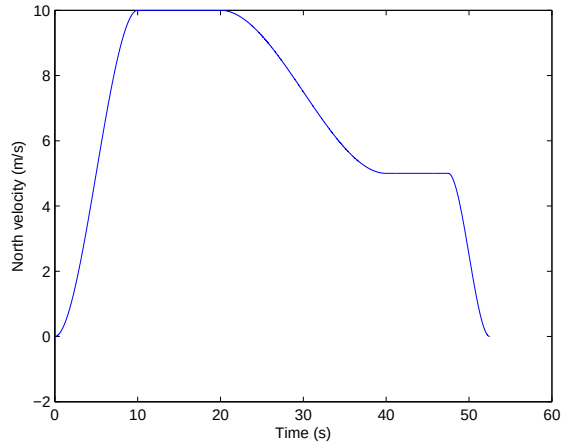

Figure 3.5: Velocity change of accelerating simulation

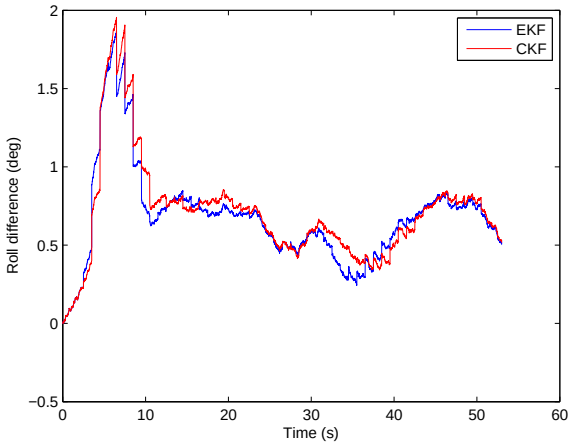

Figure 3.6: Roll error of the EKF and the CKF in accelerating simulation

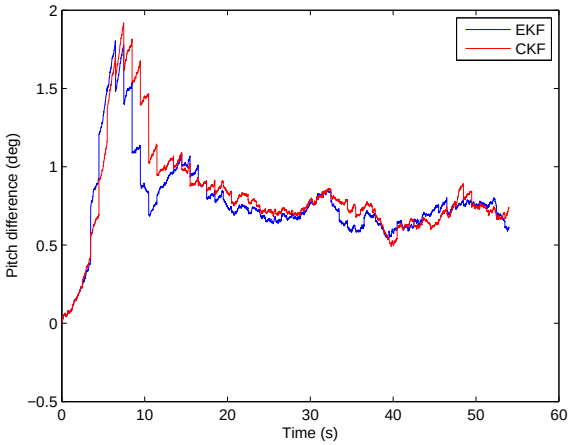

Figure 3.7: Pitch error of the EKF and the CKF in accelerating simulation

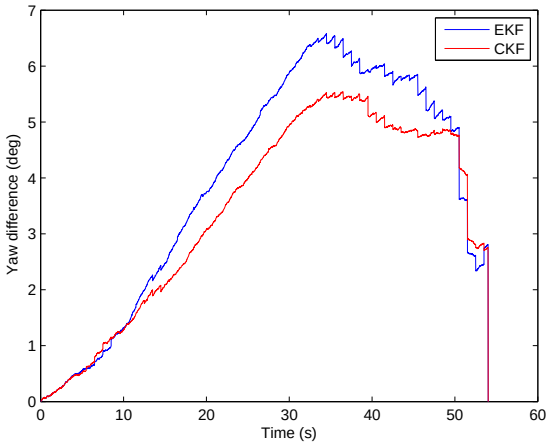

Figure 3.8: Yaw error of the EKF and the CKF in accelerating simulation

Table 3.3: Attitude comparison between the CKF and the EKF in the accelerating simulation

Filtering methods	Roll RMS (deg)	Pitch RMS (deg)	Yaw RMS (deg)
EKF	0.771	0.831	4.401
CKF	0.764	0.839	3.816

In this simulation, the vehicle experiences a turn after a straight acceleration process as shown in Figure 3.9. According to the observability analysis, the yaw angle is observable when undergoing a change. The roll, pitch and yaw estimation errors between the CKF and the EKF are shown in Figures 3.10, 3.11, 3.12 and Table 3.4. It can be seen that in observable cases, the CKF and the EKF have similar accuracy in the attitude estimation. However, the benefit of the CKF in the yaw estimation still can be seen as shown in Figure 3.12.

The attitude comparison of the three simulation scenarios shows that the CKF clearly presents its advantage when the state's degree of observability is low. When the vehicle is experiencing constant velocity (no acceleration), the yaw angle is completely unobservable. The observations have no benefits in the state estimation in such a case. The fast accumulation of the yaw angle error makes the psi-angle ex-

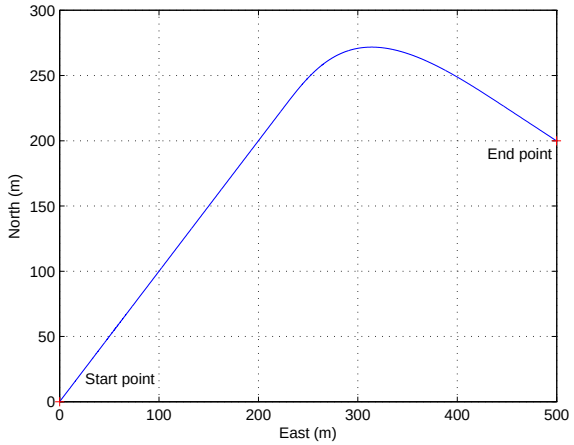

Figure 3.9: Trajectory of turning simulation

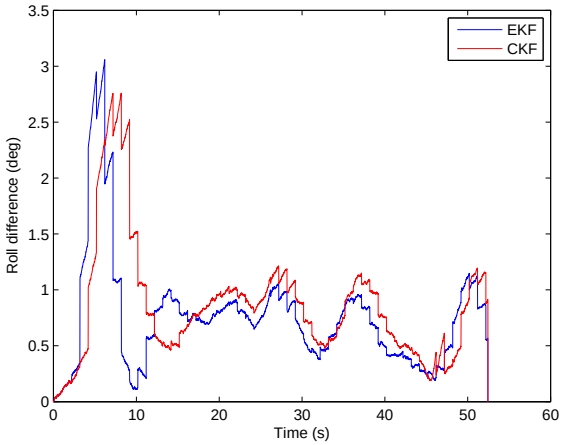

Figure 3.10: Roll error of the EKF and the CKF in turning simulation

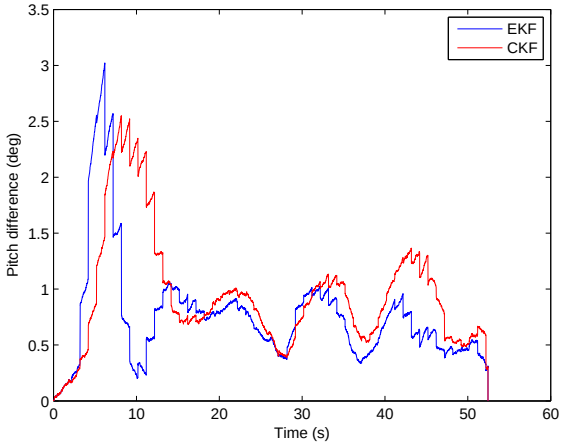

Figure 3.11: Pitch error of the EKF and the CKF in turning simulation

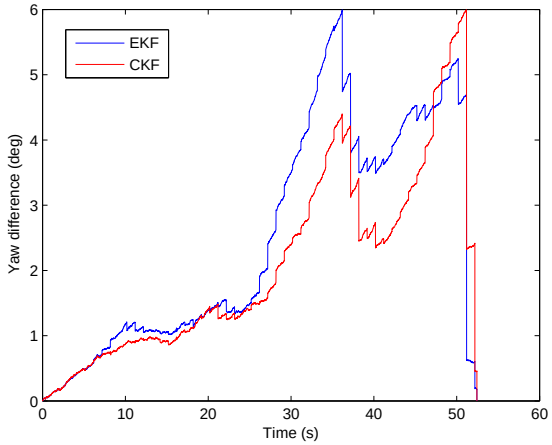

Figure 3.12: Yaw error of the EKF and the CKF in turning simulation

Table 3.4: Attitude comparison between the CKF and the EKF in turning simulation

Filtering methods	Roll RMS (deg)	Pitch RMS (deg)	Yaw RMS (deg)
EKF	0.988	0.982	3.034
CKF	1.018	1.075	2.541

pression invalid. When the CKF with a nonlinear attitude model is applied to the integrated navigation system, the yaw angle drift in the constant velocity case is smaller than the EKF, because this nonlinear model has no requirement of small angle approximation and is always valid. When the state's observability degree is high such as in turning or acceleration cases, the yaw estimation accuracy improvement is not as obvious as in the constant velocity case as shown in Figures 3.8 and 3.12. The roll and pitch have similar performances in all the scenarios, due to always being observable. The attitude estimation accuracy improvement by applying the CKF varies with the degree of observability, which is shown by the varying estimation accuracy of the yaw angle and the similar estimation accuracy of roll and pitch angles in the various scenarios.

Table 3.5: Specification of the RLG IMU

	Gyroscope	Accelerometer
Scale factor	5 ppm	100 ppm
Random walk	0.002 $deg/\sqrt{h}$	8 $\mu g/\sqrt{Hz}$
Bias instability	0.003 deg/h	25 μg

Table 3.6: Attitude comparison between the CKF and the EKF in stationary experiment

Filtering methods	Roll RMS (deg)	Pitch RMS (deg)	Yaw RMS (deg)
EKF	0.047	0.125	8.231
CKF	0.049	0.125	7.669

3.6 Experiments

Due to the high noise and bias of the MEMS gyroscope, the initial yaw angle can not be directly determined from its outputs. As introduced in Chapter 2, there are several methods used to determine the initial yaw angle. In this section, to simplify, the yaw angle calculated from a RLG IMU is taken as the initial yaw angle for the MEMS IMU. Due to the low noise and bias of the RLG IMU, its attitude estimation is much more accurate than the MEMS IMU, which also allows it to be the attitude reference to the MEMS IMU. The parameters of the RGL IMU are shown in Table 3.5.

3.6.1 Filtering performance comparison under different maneuvering

In this part, several land vehicle tests are designed to test the filtering performance difference between the CKF and the EKF. The filtering methods' performance comparison is based on the observability analysis as well. Three experiments including stationary, acceleration and 8 shape figure driving, are designed. During the experiments, the assumption can not always be kept as true because it is much more difficult to control a real drive than a simulation. In order to reduce the effect of parameter tuning, all parameters are tuned identically in all experiments for the EKF and the CKF. The initial attitude standard deviation is 20 $''$, because the initial attitude is taken from the RLG IMU. Considering vibration, the initial velocity standard deviation is 1 cm/s, because the vehicle starts from a static state. The initial position is determined from the SPP method, so the initial position standard deviation is 3 m. The initial standard deviations of the gyroscopes and accelerometers are 1 $''/s$ and 0.003 m/s^2. The receiver clock offset and drift standard deviations are 10 m and 1 m/s. In the measurement matrix $\mathbf{R}$, the standard deviations for the pseudorange and Doppler are set as 3 $m/\sin(\theta_{ele})$ and 0.1 $m/s/\sin(\theta_{ele})$. In the system matrix $\mathbf{Q}$, the standard deviations of the elements related to attitude, velocity, position, gyroscope biases, accelerometer biases, receiver clock offset and drift are set as 3 $''$, 0.14 m/s, 1 m, 10 $''/s$, 0.001 m/s^2, 5 m, 0.5 m/s.

1. Stationary case

According to the observability analysis, the yaw angle is completely unobservable in a stationary case. The simulation results also indicate that yaw errors accumulate very quickly without acceleration. The experiment trajectory is shown in Figure 3.13, where the moving period is about 2 minutes long and the subsequent stationary period is about 15 minutes long. The experiment can be used to examine the filtering performance difference between the EKF and the CKF filtering methods in the unobservable case. The attitude comparisons are shown in Figures 3.14, 3.15, 3.16 and Table 3.6.

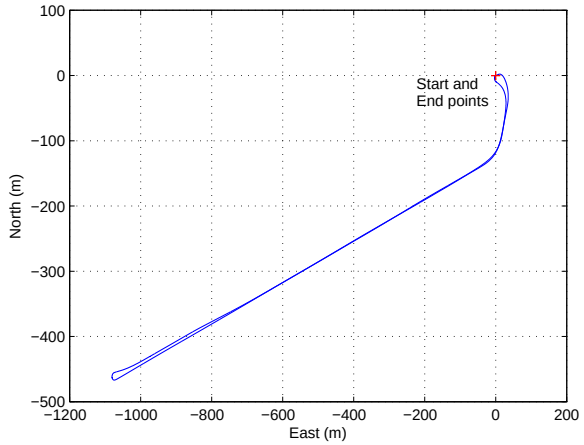

Figure 3.13: Trajectory of stationary experiment's moving period

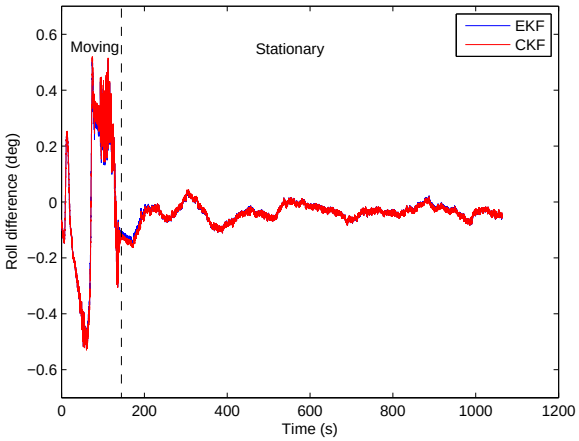

Figure 3.14: Roll error of the EKF and the CKF in stationary experiment

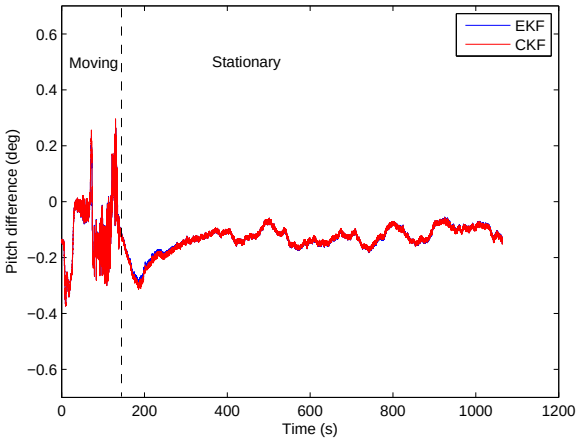

Figure 3.15: Pitch error of the EKF and the CKF in stationary experiment

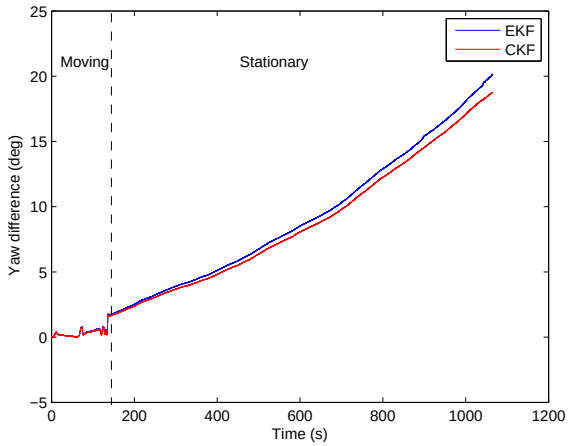

Figure 3.16: Yaw error of the EKF and the CKF in stationary experiment

It can be seen that roll and pitch have a similar estimation accuracy by applying the EKF and the CKF filtering methods due to that they are always observable. For the yaw angle estimation, since it is unobservable in a stationary case, it drifts much faster than the roll and pitch angles. However, the CKF still seems to have a lower yaw drift than the EKF, due to its capability of dealing with nonlinear problems from the yaw angle error accumulation.

2. Accelerating+Turning

According to observability analysis, the yaw angle is weakly observable in the accelerating case and completely observable when it experiences a change. As shown in the simulation part, the yaw estimated in this case seems to have a higher estimation accuracy than in the non-accelerating cases. The accuracy improvement by applying the CKF is also relatively smaller than in non-accelerating cases. The experimental trajectory is shown in Figure 3.17, covering an accelerating process and a turning process. The attitude comparisons between the CKF and the EKF are shown in Figures 3.18, 3.19, 3.20 and Table 3.7.

It can be seen that the CKF and the EKF have a similar roll, pitch and yaw estimation accuracy in such a case, since all the attitude components become observable (roll and pitch) or weakly observable (yaw). The measurements have the capability in bounding estimation error accumulation and reduce the nonlinearity of the system.

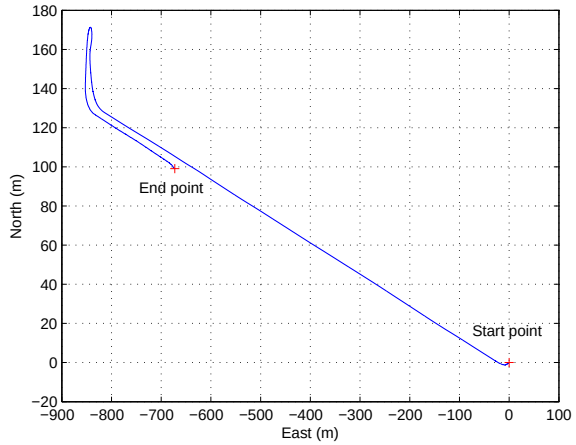

Figure 3.17: Trajectory of accelerating+turning experiment

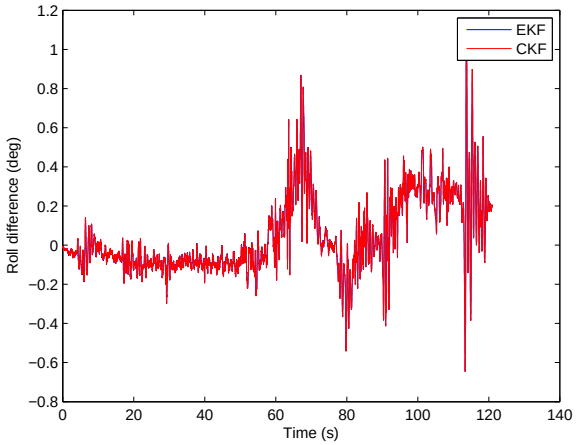

Figure 3.18: Roll error of the EKF and the CKF in accelerating+turning experiment

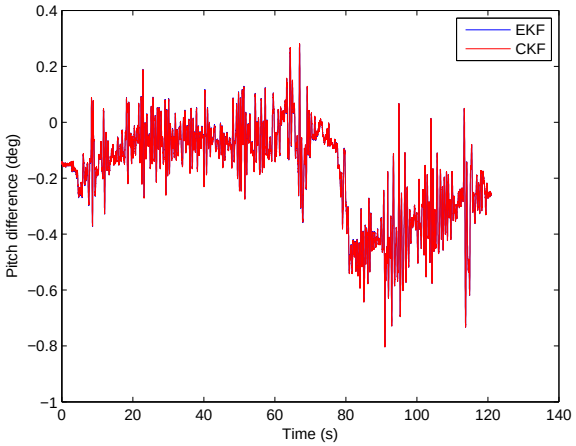

Figure 3.19: Pitch error of the EKF and the CKF in accelerating+turning experiment

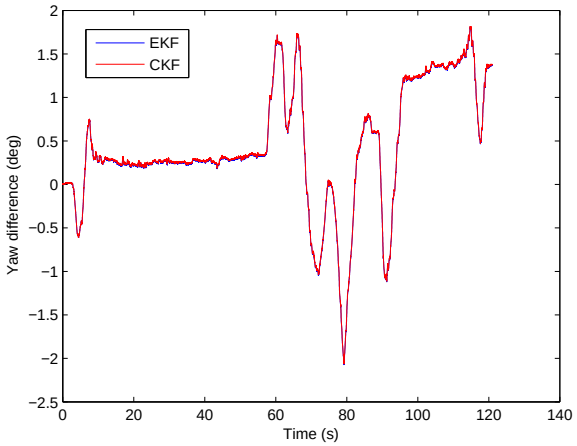

Figure 3.20: Yaw error of the EKF and the CKF in accelerating+turning experiment

Table 3.7: Attitude comparison between the CKF and the EKF in accelerating+turning experiment

Filtering methods	Roll RMS (deg)	Pitch RMS (deg)	Yaw RMS (deg)
EKF	0.244	0.198	0.828
CKF	0.243	0.198	0.824

3. 8 shape figure driving

Observability analysis shows that the change of the yaw angle can make it observable. Therefore, an 8 shape figure driving experiment is constructed to examine the performance difference between the CKF and the EKF in the observable case. The 8 shape figure driving trajectory is shown in Figure 3.21. The attitude comparisons between the CKF and the EKF in the 8 shape figure driving case are shown in Figures 3.22, 3.23, 3.24 and Table 3.8.

It can be seen that when the yaw angle becomes observable, the CKF and the EKF have a similar attitude estimation accuracy. According to the CKF estimation accuracy evaluation, implementing the CKF in a linear system will not be productive. In a GPS/IMU tightly-coupled navigation system, if the yaw angle

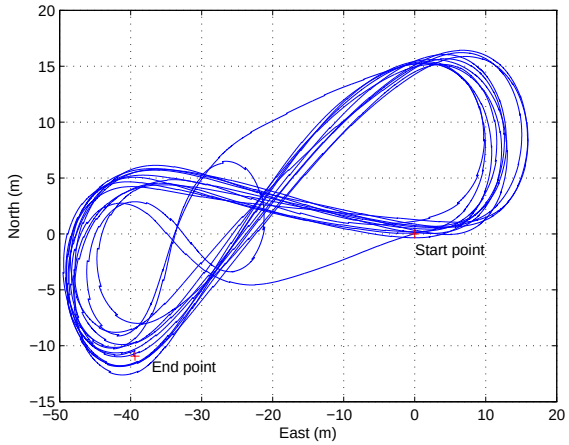

Figure 3.21: Trajectory of 8 shape figure driving experiment

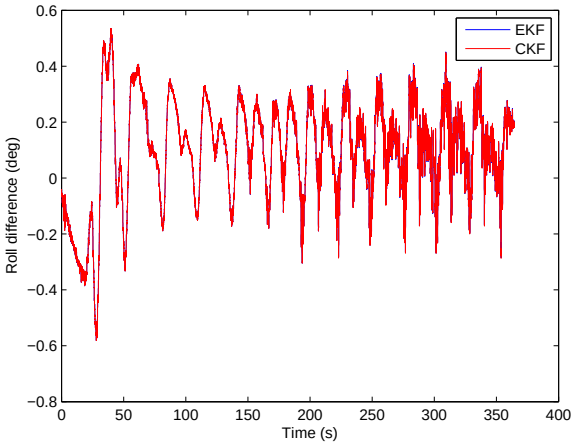

Figure 3.22: Roll error of the EKF and the CKF in 8 shape figure driving experiment

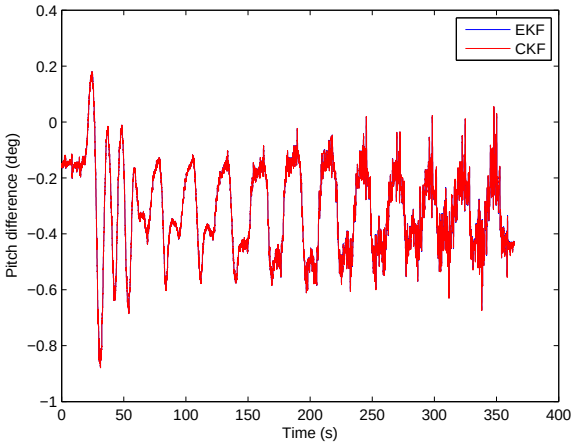

Figure 3.23: Pitch error of the EKF and the CKF in 8 shape figure driving experiment

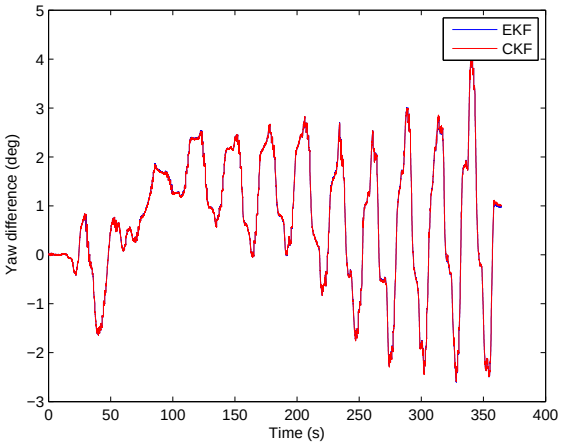

Figure 3.24: Yaw error of the EKF and the CKF in 8 shape figure driving experiment

Table 3.8: Attitude comparison between the CKF and the EKF in 8 shape figure driving experiment

Filtering methods	Roll RMS (deg)	Pitch RMS (deg)	Yaw RMS (deg)
EKF	0.207	0.351	1.550
CKF	0.207	0.351	1.548

is observable, its estimation error accumulates slowly. The linear psi-angle expression is always valid. Thus, the application of the CKF in the observable cases does not show an accuracy improvement.

From the attitude comparisons between the CKF and the EKF in different scenarios, it can be seen that the application of the CKF in tightly-coupled navigation system can improve the yaw angle accuracy in unobservable cases when the prediction accuracy dominates the accuracy of the Kalman filter. According to observability analysis, the yaw angle's degree of observability varies in different kinds of motion. The lower the observability, the more obvious the merit of the CKF is. For example, in a stationary case, the yaw accuracy improvement is very obvious after applying the CKF. On the contrary, in the 8 shape figure driving case, the improvement is quite small. Since roll and pitch are always observable, it can be seen that they have an almost identical estimation accuracy in all the experiments. The application of the

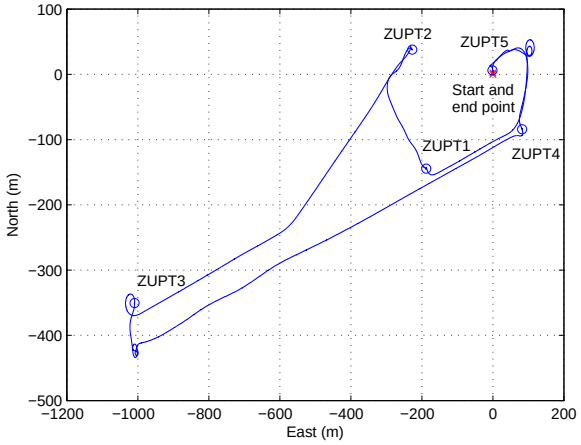

Figure 3.25: Trajectory of Griesheim airport experiment

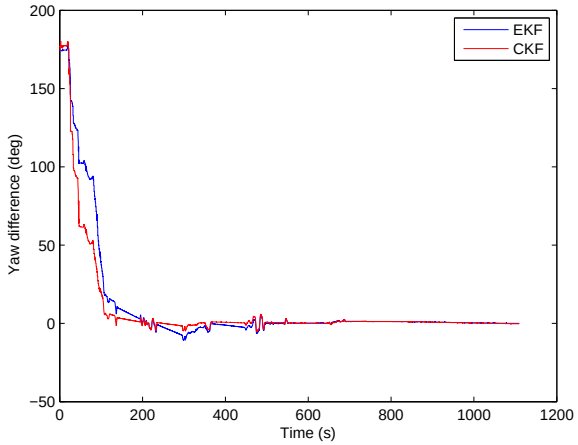

Figure 3.26: Yaw angle comparison between the EKF and the CKF in large misalignment case

CKF only eliminates the work in deducing the Jacobian matrix. The same trend can also be found in the simulation results. The nonlinearity of a GPS/IMU tightly-coupled navigation system is also affected by sensor quality. A lower sensor quality with high noise and bias leads to faster error accumulation in unobservable cases, which renders the linear psi-angle expression invalid and consequently leads to an increased degree of nonlinearity in the system.

3.6.2 Filtering performance comparison in a large misalignment case

In the experiments above, the initial yaw angle of the MEMS IMU is assumed to be already known, as it is taken directly from a high-grade RLG IMU. However, when aiding sensors like magnetometers and GPS attitude systems are not available, MEMS gyroscopes' outputs in the stationary case cannot be used to correctly calculate the initial yaw angle. Therefore, the MEMS IMU experiences a large misalignment problem, which makes the psi-angle expression invalid and inserts some nonlinearity into the integrated navigation system according to Crassidis (2006); Rhudy et al. (2013); Li et al. (2013). Wendel et al. (2006b, 2005) show that a large initial position error, for example 30 km, also causes some nonlinearity and that the UKF has superior performance to the EKF. So it can be concluded that a large initialization error (position or attitude) inserts a degree of nonlinearity into the integrated navigation system. However, unlike the large misalignment problem, the large position error problem seldom appears in integrated systems because the initial position can be determined by GPS. Considering this, the filtering methods' performance comparison is only examined in the large misalignment case.

The experimental trajectory is shown in Figure 3.25. This trajectory is complex and contains several stationary, straight driving and turning parts, which will also be used to examine the algorithms' performance in the following sections and chapters. The initial yaw angle is calculated from the MEMS gyroscopes' outputs, which is neither accurate nor trustworthy. The large azimuth angle error problem arises. A large initial attitude standard deviation has the possibility in causing the Kalman filter to become divergent, while a small attitude standard deviation will make the Kalman filter converge to a wrong value. Considering both the aspects, the initial attitude standard deviations are 5 deg for roll and pitch angles, 17 deg for the yaw angle. The other parameters are identical to the parameters in the previous section. The yaw angle comparison is shown in Figure 3.26.

From Figure 3.26, it can be seen that the CKF converges faster than the EKF in the yaw angle estimation when the initial yaw angle error is very large. When the yaw angle is already convergent, the CKF estimation error still seems to be smaller than the EKF. A large initial yaw error renders the psi-angle

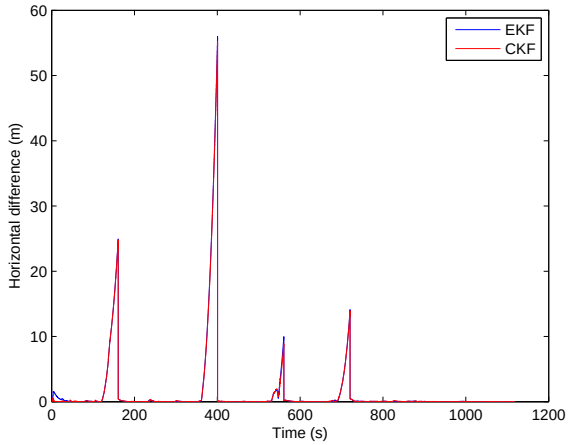

Figure 3.27: Horizontal position drift of the EKF and the CKF in coasting period

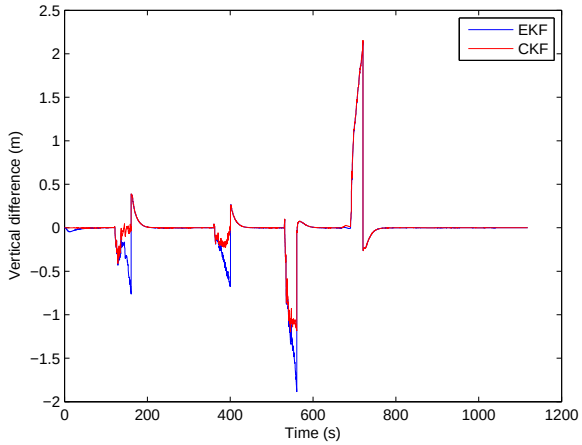

Figure 3.28: Vertical position drift of the EKF and the CKF in coasting period

expression implemented in the EKF less effective, while the nonlinear attitude expression in the CKF is still valid. Thus, a faster convergence speed and smaller estimation error can be expected from the CKF. In the large misalignment case, the CKF is superior to the EKF.

3.6.3 Coasting performance comparison

The coasting performance can also be used to examine the performance difference among various filtering methods. During the coasting periods, the GPS signal is blocked artificially, and the integrated navigation system turns into the IMU-only navigation. Due to that there is no aiding sensors, the estimation errors accumulate very quickly, rendering small angle approximation invalid as well. The trajectory of the experiment is shown in Figure 3.25 with initial attitude determined from the RLG IMU. The time lengths of the first and second coasting periods are 40 s, while the third and fourth coasting periods are 30 s. The horizontal and vertical position drifts during coasting periods are shown in Figures 3.27, 3.28 and Table 3.9.

It can be found that the EKF drifts faster than the CKF in both horizontal and vertical directions. During the coasting periods, since the observations are unavailable, all the states can accordingly be treated as unobservable, which leads to the estimation errors accumulating very quickly. According to the inertial navigation mechanisation, a large attitude error causes a false velocity estimation and subsequently a

Table 3.9: Maximum position drift of the EKF and the CKF in coasting periods

Methods	1st GPS outage		2nd GPS outage	
	Horizontal drift (m)	Vertical drift (m)	Horizontal drift (m)	Vertical drift (m)
EKF	24.48	0.76	36.76	0.67
CKF	24.41	0.40	36.17	0.22
Methods	3rd GPS outage		4th GPS outage	
	Horizontal drift (m)	Vertical drift (m)	Horizontal drift (m)	Vertical drift (m)
EKF	6.80	1.88	9.64	2.14
CKF	6.26	1.20	9.63	2.14

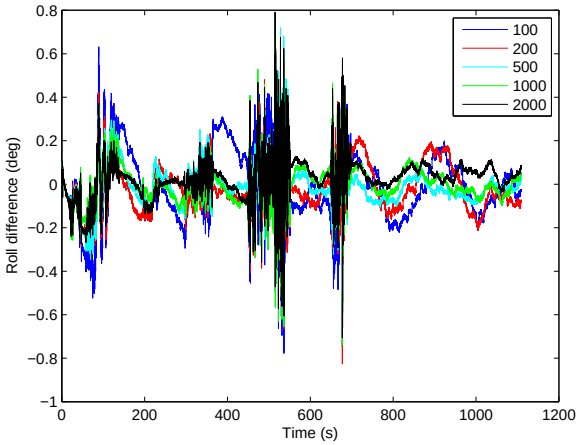

Figure 3.29: Roll error of the CPFs with different numbers of particles

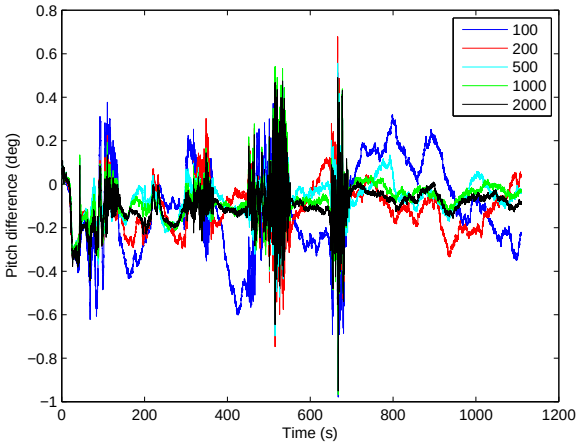

Figure 3.30: Pitch error of the CPFs with different numbers of particles

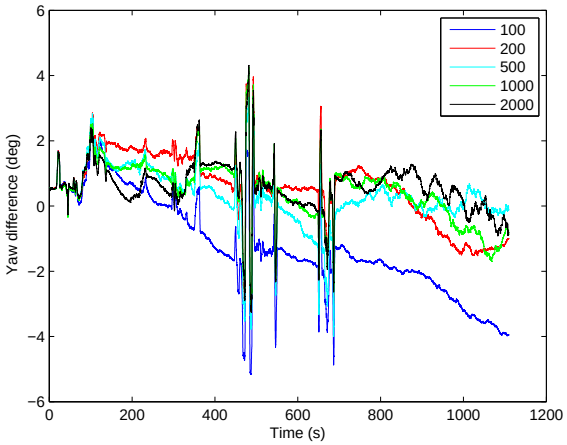

Figure 3.31: Yaw error of the CPFs with different numbers of particles

large position drift. The nonlinear attitude expression implemented in the CKF can bound the attitude error accumulation and then lead to a relatively smaller position drift. Considering the maximum horizontal and vertical position drifts, the nonlinear filtering method (the CKF) performs better than the EKF during coasting periods.

3.6.4 CPF performance

In this section, the CPF performance is examined in a GPS/IMU tightly-coupled navigation system.

1. Effect of the number of particles

The first comparison is the CPF performance with different numbers of particles. The attitude comparison is taken as an indicator to evaluate the CPF filtering methods' performance. 100, 200, 500, 1000 and 2000 particles are implemented in the CPF. The trajectory is shown in Figure 3.25. The attitude estimation accuracy in roll, pitch and yaw angles is shown in Figures 3.29, 3.30 and 3.31. The navigation results are the average of 10 CPF runs.

It can be seen that the CPF estimation accuracy increases with the number of particles. More particles show a higher attitude estimation accuracy. On the contrary, less particles reveal the random properties

Table 3.10: Attitude comparison of the CPFs with different numbers of particles

Particle number	Roll RMS (deg)	Pitch RMS (deg)	Yaw RMS (deg)
100	0.156	0.232	1.946
200	0.114	0.153	1.252
500	0.093	0.110	0.990
1000	0.088	0.108	1.012
2000	0.089	0.114	0.942

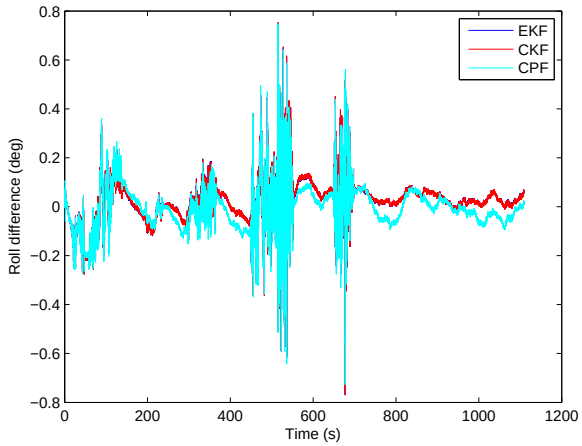

Figure 3.32: Roll estimation error of the EKF, CKF and CPF

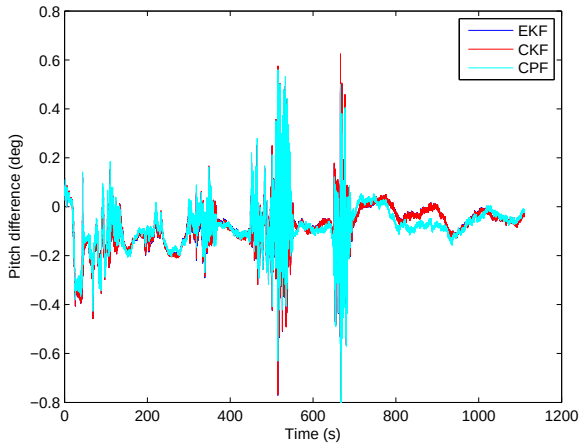

Figure 3.33: Pitch estimation error of the EKF, CKF and CPF

Table 3.11: Attitude comparison among the EKF, CKF and CPF

Particle number	Roll RMS (deg)	Pitch RMS (deg)	Yaw RMS (deg)
EKF	0.085	0.117	1.080
CKF	0.085	0.117	1.075
CPF	0.088	0.110	1.001

of particles, as shown by the attitude estimated by the CPF with 100 particles being much worse than the other CPFs with more particles. In the following comparison, the CPF with 1000 particles will be implemented for the comparison with the EKF and the CKF filtering methods.

2. Comparison with the CKF and the EKF

In this comparison, the trajectory shown in Figure 3.25 is used to examine the attitude estimation accuracy of the three filtering methods. The roll, pitch and yaw angle comparisons are shown in Figures 3.32, 3.33, 3.34 and Table 3.11. The attitude computed from the CPF is the average of 15 CPF runs.

It can be seen from the comparison that the EKF, CKF and CPF have similar roll and pitch estimation accuracy. In the yaw estimation, the nonlinear filtering methods (the CKF and the CPF) perform a little better than the EKF especially when the vehicle is stationary (the vehicle stops for five minutes at the end of the trajectory). And the CPF seems to have better yaw angle estimation accuracy than the CKF. However, due to the random properties of the particles, the CPF should be executed several times and the average of the attitude estimation will be similar to the CKF as suggested in Zhou et al. (2010). A single

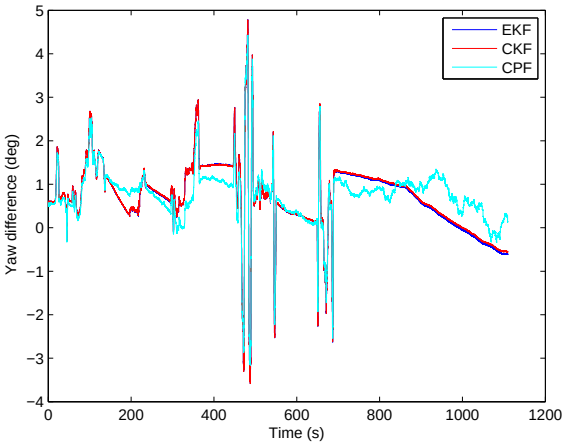

Figure 3.34: Yaw estimation error of the EKF, CKF and CPF

run of the CPF cannot show too much attitude estimation accuracy improvement. Therefore, considering the attitude comparison and the computational load of the CPF, it can be concluded that the CPF can be considered as a method when designing a tightly-coupled navigation system, but its benefits in dealing with nonlinear and non-Gaussian problems may bot be fully shown in an integrated navigation system.

3.7 Conclusion

In this chapter, the performance of the Cubature Kalman filter is evaluated in a conventional GPS/IMU tightly-coupled navigation system through mathematical derivation, simulation and experiments. The estimation accuracy of the CKF is examined through a Taylor expansion, proving that the CKF has a similar estimation accuracy as the EKF, when implemented with linear or linearised systems. Based on this conclusion, a nonlinear attitude expression is introduced into the navigation system to better show the CKF's benefits. The observability of the yaw angle varies under different dynamics. Thus the CKF's filtering performance under different maneuvering is further investigated according to the observability analysis. From the simulation and experiment results, it can be seen that the CKF performs better than the EKF especially for a low-cost MEMS IMU applied in unobservable cases. The large misalignment and coasting performance show that the CKF performs better than the EKF and can be treated as a better choice when designing an integrated navigation system.

A Cubature particle filter based on the CKF is developed. The CKF *a posteriori* mean and covariance matrix are applied to generate particles. The CPF performance improves with the increase in the number of particles, although too many particles will not further improve the estimation accuracy of the CPF. The attitude comparison among the EKF, CKF and CPF shows that the CPF can not achieve too much estimation accuracy improvement because the non-Gaussian property of tightly-coupled navigation systems is weaker, thus also concluding that the CPF and the other related particle filters can be taken into consideration in designing a GPS/IMU tightly-coupled navigation system, but their benefits cannot be shown fully in such an integrated navigation system.

4 Shaping filter modelling of inertial sensors' stochastic errors

In this chapter, the application of the shaping filter theory to model inertial sensors' stochastic errors will be described. The shaping filter theory describes how to use a unit white noise to generate a coloured noise (also named as $1/f^{\alpha}$ noise). According to shaping filter theory, the transfer function of each inertial sensor's coloured noise can be deduced from its PSD, which will be converted into the state space form and then augmented in a GPS/IMU integrated navigation Kalman filter. The shaping filter-based method will be compared with the conventional 1st-order Markovian process modelling method to determine its effectiveness through simulation and experiments.

4.1 Introduction and background

A MEMS IMU is more attractive for its low cost, mass and size. However, it also suffers from a higher error level, which together with the integration of the inertial data very quickly causes the navigation solution to drift, especially when aiding measurements are unavailable. So the inertial sensors' errors modelling is one of the key issues in improving the performance of a GPS/MEMS IMU integrated navigation system. According to the errors' properties, inertial sensors' errors can be divided into roughly two segments: deterministic errors and stochastic errors. Deterministic errors contain scale factor errors, constant biases, misalignment effects, temperature related variations, nonlinearity errors and so on (Yi, 2007). These errors are normally reduced using prior calibration before operation. The inaccuracies of deterministic errors can be further estimated using the Kalman filter technique. Stochastic errors include white noise, quantization noise, rate random walk, rate ramp, bias instability and some other forms of noise (IEEE Std 952TM-1997, 2008). Stochastic errors cannot be reduced through calibration methods. But they can be modelled as some random processes and then estimated in the navigation Kalman filter (Flenniken et al., 2005).

Power spectral density (PSD) and Allan variance (AV) are the two main methods used to identify inertial sensors' stochastic errors. They describe a same process from frequency and time domains separately (IEEE Std 952TM-1997, 2008). Considering the inconsistency of the Allan variance technique, some researchers proposed a wavelet-based (WV) method in determining stochastic errors, which creates a connection between the WV coefficients and the stochastic errors' parameters (Stebler, 2013; Guerrier, 2013; Guerrier et al., 2013).

After determining the coefficients of stochastic errors, it is also important to estimate them in a Kalman filter. Van Dierendonck et al. (1984) tries to establish a relationship between the Allan variance and the Kalman filter parameters. Seong et al. (2000) carefully describe the selection of an ARMA process according to the combination of different stochastic errors. The coefficients of the ARMA process can be estimated using the prediction error method (PEM), Yule-Walker or Burg estimation methods (Zelinker and Taylor, 1994). The authors share similar goals but model stochastic errors as an AR(4) process, which is a fourth order auto-regressive process (Park, 2004; Wang et al., 2012; Park and Gao, 2008). Guerrier (2013) uses the generalized method of wavelet moments (GMWM) to model the stochastic errors as a summation of three 1st-order Markovian processes, and each 1st-order Markovian process is converted to its related ARMA process and estimated separately. The authors also suggest the possibility of modelling all the three 1st-order Markovian processes together. Unlike with the ARMA process, the researchers model all the coloured noise of the stochastic errors together using differential equations with a unit white noise as input (Han and Wang, 2011; Saini et al., 2010; Zhao, 2013). The state space form is then deduced from modern control theory.

In this chapter, a shaping filter will be used to model inertial sensors' stochastic errors in the navigation Kalman filter. The transfer function of the shaping filter is determined from the PSD of relevant stochastic

errors. The ARMA process and the differential equation are deduced from the shaping filters' transfer function using Z-transformation and inverse Laplace transformation separately (Ogata and Yang, 1970). It can be seen that they are equivalent and describe the same errors using two different expressions. The ARMA process' coefficients also can be calculated from the shaping filter without using the ARMA process coefficients determination methods like the Yule-Walker or Burg estimation methods. The relationship between the Allan variance and the ARMA process's coefficients can be established.

4.2 Allan variance

The Allan variance technique was initially developed for studying the frequency stability of precision oscillators in 1966 by David Allan (Allan, 1966). In the 1990s, the Allan variance method was adapted by institute of electrical and electronics engineers (IEEE) to estimate stochastic errors of a fibre optic gyroscope (FOG) (IEEE Std 952TM-1997, 2008). The AV method is also used to evaluate MEMS IMU stochastic errors as discussed in Hou (2004); El-Sheimy et al. (2008); Zhao et al. (2011). The AV method can be summarized as follows in brief.

1. Take a long sequence of discrete data $\Omega(t)$ with length N and sampling time T_s, and then divide it into n clusters with duration τ. Integration of $\Omega(t)$ in each cluster is

$$\theta(t) = \int_{t_k}^{t_k+\tau} \Omega(t)dt \tag{4.1}$$

2. Average each cluster over time period τ

$$\overline{\Omega_k}(\tau) = \frac{1}{\tau}\theta(t) \tag{4.2}$$

3. Allan variance is defined as

$$\sigma^2(\tau) = \frac{1}{2}\langle(\overline{\Omega_{k+n}}(\tau) - \overline{\Omega_k}(\tau))^2\rangle = \frac{1}{2\tau^2}\langle(\theta_{k+2n} - 2\theta_{k+n} + \theta_k)^2\rangle \tag{4.3}$$

where $\langle\rangle$ denotes an infinite time average. In practical application, the AV is estimated from a finite number of samples by

$$\sigma^2(\tau) = \frac{1}{2\tau^2(N-2n)}\sum_{k=1}^{N-2n}(\theta_{k+2n} - 2\theta_{k+n} + \theta_k)^2 \tag{4.4}$$

The Allan deviation's characteristic curve of each error term can be derived by a log-log calculation on the Allan variance equation, which is also called as Allan variance plot. Figure 4.1 is a typical Allan variance plot, taken from (Stebler, 2013). It can be seen that after applying Allan variance technique, different stochastic processes appear in different segments of Allan variance plot with different slopes. The relationship between the Allan deviation of each noise and time is shown in Table 4.1 (IEEE Std 952TM-1997, 2008; Zhang et al., 2008; Vágner et al., 2012; Zhao et al., 2011).

Allan variance is a time domain method widely used to specify and determine the coefficients of the inertial sensors' stochastic errors. Unlike Allan variance, the PSD method identifies the inertial sensors' stochastic errors from the frequency domain. PSD can be treated as a Fourier pair of Allan variance as shown in equation (4.5) (IEEE Std 952TM-1997, 2008).

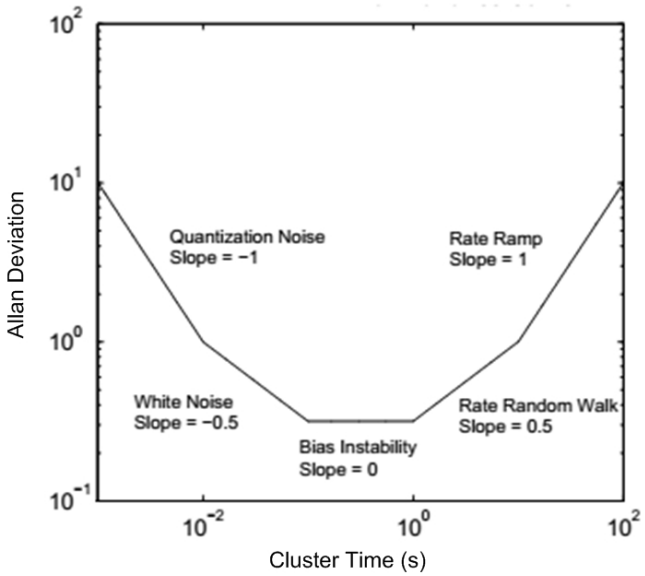

Figure 4.1: A typical Allan variance plot (Stebler, 2013)

$$\sigma^2(\tau) = 4\int_0^{\infty} S_\Omega(f)\frac{\sin^4(\pi f\tau)}{(\pi f\tau)^2}df \tag{4.5}$$

where $S_\Omega(f)$ is the two-sided PSD of $\Omega(t)$.

The recently developed generalized wavelet-based method transfers the coefficients of stochastic errors to the coefficients of wavelet terms. The stochastic errors' coefficients are further determined using least square method. As suggested by the authors, when the Haar filter is chosen as the base function of the wavelet, the generalized wavelet is the same as Allan variance (Stebler, 2013; Guerrier, 2013; Guerrier et al., 2013). In this sense, the three methods are equivalent and can change mutually through relevant mathematical transformation. If all the three methods are applied to determine the coefficients of stochastic errors, a similar estimation accuracy should be expected in theory.

According to IEEE Std 952TM-1997 (2008), inertial sensors mainly contain five stochastic errors: angle/velocity random walk, quantization noise, rate random walk, rate ramp, and bias instability as shown in Table 4.2. It can be seen that quantization noise is a high-frequency noise, angle/velocity random walk is a white noise and the other three stochastic errors are low-frequency noises. Allan variance is applied

Table 4.1: Allan deviation vs time

Stochastic error	Relationship	Curve slope	Coefficient value
Angle/Velocity random walk*	$\log(\sigma) = -\frac{1}{2}\log(\tau) + \log(N)$	$-\frac{1}{2}$	$N = \sigma(1)$
Quantization noise	$\log(\sigma) = -\log(\tau) + \log(\sqrt{3}Q)$	-1	$Q = \sigma(\sqrt{3})$
Rate random walk	$\log(\sigma) = \frac{1}{2}\log(\tau) + \log(\frac{K}{\sqrt{3}})$	$\frac{1}{2}$	$K = \sigma(3)$
Rate ramp	$\log(\sigma) = \log(\tau) + \log(\frac{R}{\sqrt{2}})$	1	$R = \sigma(\sqrt{2})$
Bias instability	$\log(\sigma) = \log(\sqrt{\frac{2\ln 2}{\pi}}B) = \log(0.664B)$	0	$B = \frac{\sigma}{0.664}$

*This kind of stochastic error is not a random walk (or Weiner process). According to IEEE Std 952TM-1997, it behaves more like a white noise.

to determine the coefficients of the inertial sensors' stochastic errors in this thesis. The relevant PSD is deduced from the Allan variance coefficients according to Table 4.2.

4.3 Shaping filter theory

The Kalman filter is only driven by white noise. Only the angle/velocity random walk can be treated as a white noise, which can be processed directly without any modelling. In order to compensate for the effect of the other four stochastic errors, it is necessary to model them using a white noise and then estimate them as augmented states in the Kalman filter (Bartosch, 2001). Shaping filter theory introduces a method of how to generate a coloured noise using a unit white noise.

Considering an arbitrary continuous stationary stochastic process $x(t)$ with mean μ, its auto-correlation function is calculated as

$$C_x(\tau) = E\{x(t)x(t-\tau)\} \tag{4.6}$$

Its PSD is the Fourier transformation of $C_x(\tau)$, which is

$$S_x(\omega) = \int_{-\infty}^{\infty} C_x(\tau)\exp(-j\omega\tau)d\tau \tag{4.7}$$

If $x(t)$ is non-stationary, its PSD does not exist, but its sampled PSD (or generalized PSD), which is the spectral estimate with a rectangular window as defined in Kasdin (1995), matches (4.7), too. In the following analysis, the non-stationary process' PSD refers to its sampled PSD.

If $S_x(\omega)$ is assumed to be real and matches the Paley-Wiener criterion,

$$\int_{-\infty}^{\infty} \frac{\log(S_x(\omega))}{1+\omega^2} d\omega < \infty \tag{4.8}$$

which indicates a causal system, $S_x(\omega)$ can be factorized as

$$S_x(\omega) = |H(j\omega)|^2 = H(j\omega)H(j\omega)^* \tag{4.9}$$

Table 4.2: Stochastic errors in inertial sensors

Stochastic error	Coefficient	Allan Variance	Power Spectral Density	Noise type
Angle/Velocity random walk	N	$\sigma_N^2(\tau) = \frac{N^2}{\tau}$	$S_N(f) = N^2$	White noise
Quantization noise	Q	$\sigma_Q^2(\tau) = \frac{3Q^2}{\tau^2}$	$S_Q(f) = (2\pi f)^2 Q^2 T_s$	Violet noise
Rate random walk	K	$\sigma_K^2(\tau) = \frac{K^2\tau}{3}$	$S_K(f) = \frac{K^2}{(2\pi f)^2}$	Red noise
Rate ramp	R	$\sigma_R^2(\tau) = \frac{R^2\tau^2}{2}$	$S_K(f) = \frac{R^2}{(2\pi f)^3}$	Power-law noise
Bias instability	B	$\sigma_B^2(\tau) = \frac{2B^2\ln 2}{\pi}$	$S_B(f) = \frac{B^2}{2\pi f}$	Pink noise

If the transfer function $H(j\omega)$ is a rational function, it can be decomposed into the 'zero-poles' format. If all the poles are on the left side of the s plane, $H(j\omega)$ is the transfer function of a stable linear time-invariant (LTI) system to generate $x(t)$ from a white noise. In this case, a linear time-invariant system (shaping filter) is constructed to simulate $x(t)$ as

$$\widehat{x}(t) = F^{-1}\{H(j\omega)\} * w(t) + \mu \tag{4.10}$$

where $w(t)$ is a white noise with the following first and second moments as

$$\begin{aligned} E\{w(t)\} &= 0 \\ E\{w(t)w(t-\tau)\} &= C_w(\tau) = \delta(\tau) \end{aligned} \tag{4.11}$$

and then $\widehat{x}(t)$ will have the same mean and PSD as $x(t)$.

4.4 Inertial sensors' stochastic errors modelling

The derivation above introduces how to generate a coloured noise by inputting a white noise to a shaping filter. The shaping filter transfer function can be deduced by the factorization of the relevant PSD, see equation (4.9). The PSD is rewritten by applying $\omega = 2\pi f$ in the following analysis. The transfer function and modelling of each noise are deduced as shown below.

4.4.1 Bias instability

Bias instability is usually a primary parameter used to classify the gyroscope performance (Schmidt, 2011). The PSD of bias instability is represented as

$$S_B(\omega) = \frac{B^2}{\omega} \tag{4.12}$$

From equations (4.12) and (4.9), the shaping filter transfer function of the bias instability is deduced as

$$H_B(j\omega) = \frac{B}{\sqrt{j\omega}} \tag{4.13}$$

Obviously, $H_B(j\omega)$ is an irrational function, which cannot describe a LTI system directly. So a rational function should be applied to approximate the irrational function. The PSD of the bias instability indicates that it can be treated as a flicker noise (also named as $1/f$ noise or pink noise). In Ninness (1998), flicker noise is generated using a wavelet-based method, which is only consistent for spectral exponents γ in the range $\gamma \in (0, 1)$. Flicker noise is generated by cascading a pole/zero pair for each decade of the frequency of interest using white noise as the input in Keshner (1982). In this case, the transfer function works more like a low-pass filter. Since flicker noise behaves like a low frequency noise, it is possible to be generated through low-pass filtering. However, the order of the transfer function is very high, which increases the computational burden when implemented in a Kalman filter.

Flicker noise can also be approximated as a sum of 1st-order Markovian processes. The 1st-order Markovian process is stationary, which can be used to model many stochastic processes and even non-stationary processes. As mentioned in Stebler et al. (2012), the researchers use three 1st-order Markovian processes to model IMU stochastic errors. One 1st-order Markovian process plus white noise is also adapted to model the inertial sensors' stochastic errors as introduced in Schwarz and Wei (2001); Hammon (1960);

Xing and Gebre-Egziabher (2008). Pittelkau (2013) has investigated how to model the gyroscope bias instability using the summation of 1st-order Markovian processes. He models the flicker noise as a summation of several independent 1st-order Markovian processes. In this thesis, bias instability is modelled as the summation of several 1st-order Markovian processes with an identical white noise according to the method introduced in Granger and Morris (1976); Teräsvirta (1977).

The spectrum of flicker noise can be represented as the weighted sum of many exponentially correlated processes as

$$\int_0^\infty \frac{2B^2}{\pi(\omega^2+\lambda^2)}d\lambda = \frac{2B^2}{\pi\omega}\tan^{-1}(\frac{\lambda}{\omega})|_0^\infty = \frac{B^2}{\omega} \tag{4.14}$$

After applying equation (4.15) to (4.14)

$$\lambda = \exp(\beta) \Rightarrow \frac{B^2}{\omega} = \int_{-\infty}^{\infty} \frac{2B^2\exp(\beta)}{\pi(\omega^2+\exp(2\beta))}d\beta \tag{4.15}$$

The integration (4.14) can be approximated as an infinite sum:

$$\frac{B^2}{\omega} = \lim_{\Delta\beta\to 0}\sum_{k=-\infty}^{\infty} \frac{2B^2\exp(k\Delta\beta)\Delta\beta}{\pi(\omega^2+\exp(2k\Delta\beta))} \tag{4.16}$$

Each component in the summation term corresponds to the spectrum of the following process:

$$H_{GM}(j\omega) = \frac{\tau\sigma_{GM}}{\tau+j\omega} \tag{4.17}$$

which is the transfer function of the 1st-order Markovian process with time constant $\tau = \exp(k\Delta\beta)$ and covariance $\sigma_{GM}^2 = \frac{B^2\exp(-k\Delta\beta)\Delta\beta}{\pi}$.

Therefore, the transfer function of the bias instability can be roughly approximated as a summation of a series of 1st-order Markovian processes. In this chapter, two 1st-order Markovian processes are used to model bias instability, which is

$$y_B(t) = F^{-1}\{\frac{q_{c_1}T_{c_1}}{1+j\omega T_{c_1}}\} * w_1(t) + F^{-1}\{\frac{q_{c_2}T_{c_2}}{1+j\omega T_{c_2}}\} * w_2(t) \tag{4.18}$$

According to the method introduced in Granger and Morris (1976); Teräsvirta (1977), which describes how to find an equivalent process for the summation of two AR(1) processes, a transfer function $H_B(j\omega)$ equivalent to the summation of two independent 1st-order Markovian processes can be determined to shape a white noise to be $y_B(t)$ as

$$y_B(t) = F^{-1}\{H_B(j\omega)\} * w(t) \tag{4.19}$$

If $(\tau_{peak}, \sigma_{peak})$ is set as the peak point in the AV plot of the 1st-order Markovian process as shown in Figure 4.2, q_c, T_c in (4.18) are computed as (IEEE Std 952TM-1997, 2008)

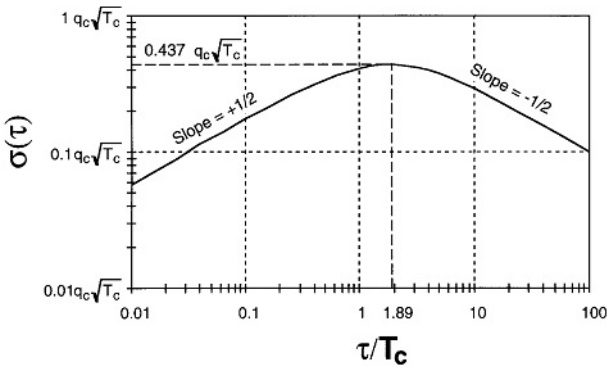

Figure 4.2: Allan variance plot for 1st-order Markovian process (IEEE Std 952TM-1997, 2008)

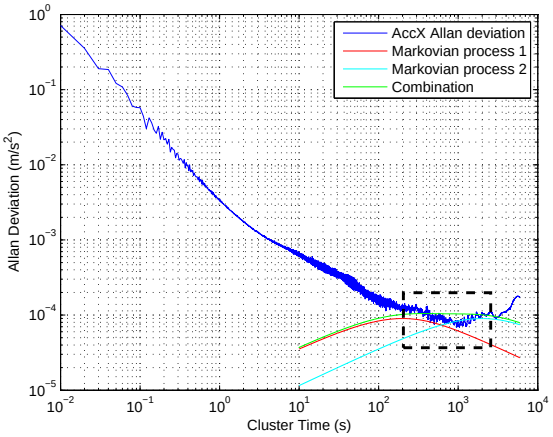

Figure 4.3: Using two 1st-order Markovian processes to approximate bias instability

$$
\begin{aligned}
T_c &= \tau_{peak}/1.89 \\
q_c &= \frac{\sigma_{peak}}{0.437\sqrt{T_c}}
\end{aligned}
\tag{4.20}
$$

However, that does not mean that all the inertial sensors' bias instability should be modelled as a summation of two 1st-order Markovian processes. The number of Markovian processes is determined by the length of the flat segment in the AV plot. If the length of slope 0 is short, only one 1st-order Markovian process is enough to approximate the bias instability, which is widely used in many applications (Hammon, 1960).

Figure 4.3 shows how a summation of two independent 1st-order Markovian processes approximates the X-accelerometer's bias instability. The flat segment in Figure 4.3 is long. So two 1st-order Markovian processes (red and light blue lines) are utilized to describe bias instability. As shown in the dashed box, their combination (green line) is quite similar as the measured X-accelerometer's bias instability (blue line), which indicates the effectiveness of the method in using several independent 1st-order Markovian processes to approximate bias instability. It is not necessary to use too many 1st-order Markovian processes for the approximation, as that increases the computational load without too much estimation accuracy improvement.

4.4.2 Rate random walk

The PSD of rate random walk is represented as

$$S_K(\omega) = \frac{K^2}{\omega^2} \tag{4.21}$$

From equations (4.21) and (4.9), the shaping filter transfer function is deduced as

$$H_K(j\omega) = \frac{K}{j\omega} \tag{4.22}$$

This transfer function is rational and it describes an integration process. Some people treat rate random walk as a Wiener process, because both of them can be generated by integrating a white noise (Stebler, 2013). Wiener process is non-stationary without PSD (Itô, 1974). But its related sampled PSD can be calculated by applying a window to its auto-correlation function as introduced in Kasdin (1995).

According to the definition of a sampled PSD (or generalized PSD) in Kasdin (1995), the sampled PSD of Wiener process is calculated as

$$\begin{aligned} S(\omega) = &\int_{-T}^{0} [\frac{1}{T} \int_{t_0-\frac{\tau}{2}}^{t_0+T+\frac{\tau}{2}} R(t,\tau)dt] e^{-j\omega\tau} d\tau \\ &+ \int_{0}^{T} [\frac{1}{T} \int_{t_0+\frac{\tau}{2}}^{t_0+T-\frac{\tau}{2}} R(t,\tau)dt] e^{-j\omega\tau} d\tau \end{aligned} \tag{4.23}$$

where $R(t,\tau)$ is the auto-correlation function of a non-stationary process. Equation (4.23) is also applicable to stationary processes. The sampled PSD of the stationary processes is the same as its true PSD. The auto-correlation function of Wiener process is

$$R(t,\tau) = t - \frac{|\tau|}{2} \tag{4.24}$$

The PSD of Wiener process cannot be computed directly from (4.24) through a Fourier transformation, because it is not absolutely integrable which does not meet the Dirichlet condition. The PSD directly calculated from $R(t,\tau)$ using a Fourier transformation has no meaning as such, although it is possible to use the Fourier transformation table to find a relevant transformation for $R(t,\tau)$. In the sense of a sampled PSD, $R(t,\tau)$ becomes absolutely integrable after applying a rectangular window. The spectral estimate for Wiener process by substituting (4.24) into (4.23), can be further computed as

$$S(\omega) = 2(1+\frac{t_0}{T})\frac{1}{\omega^2} - 2(\frac{t_0}{T})\frac{\cos\omega T}{\omega^2} - \frac{2}{T\omega^3}\sin\omega T \tag{4.25}$$

If T is much larger than t_0, $S(\omega)$ matches the following relationship

$$S(\omega) \propto \frac{1}{\omega^2} \tag{4.26}$$

which is similar to the PSD of rate random walk. In this sense, a rate random walk in the Allan variance can be represented as a segment of an infinite Wiener process.

4.4.3 Rate ramp

Generally speaking, a rate ramp seldom appears in the AV plot of a low-cost MEMS inertial sensor, since it behaves more like a deterministic error. If a segment with a slope greater than one is found, the compensation for temperature, stability of power source and readout circuit should be checked to eliminate their effects. If necessary, the IMU needs to be recalibrated. However, this does not mean that rate ramp will never appear in an AV plot. So it is still necessary to deduce a transfer function for rate ramp and compensate it in a navigation Kalman filter in case this error actually occurs.

The PSD of a rate ramp is

$$S_R(\omega) = \frac{R^2}{\omega^3} \tag{4.27}$$

The transfer function deduced from the PSD is

$$H_R(j\omega) = \frac{R}{(j\omega)^{1.5}} \tag{4.28}$$

Equation (4.28) is an irrational function, which should be approximated using a rational function. A 2nd order Markovian process can be used to describe rate ramp as

$$\hat{H}_R(j\omega) = \frac{R}{(j\omega)^2 + j\sqrt{2}\omega_0\omega + \omega_0^2} \tag{4.29}$$

where ω_0 is the natural frequency of the 2nd order Markovian process.

The following analysis will state how to roughly determine ω_0 in equation (4.29). The magnitude error between the true and estimated transfer functions can be defined as (Han and Wang, 2011)

$$\begin{aligned} \varepsilon_R &= 10 \cdot \log\left|\frac{|\hat{H}_R(j\omega)| - |H_R(j\omega)|}{|H_R(j\omega)|}\right| \\ &= 10 \cdot \log\left|\frac{\sqrt{\omega^3}}{\sqrt{\omega^4 + \omega_0^4}} - 1\right| \end{aligned} \tag{4.30}$$

Since rate ramp is a low-frequency noise, its frequency range can be set from 0.005 Hz to 0.01 Hz. In this frequency range, if $\omega_0 = 0.05 rad/s$, the magnitude error is below -3dB as indicated in Han and Wang (2011).

4.4.4 Quantisation noise

According to the outputs of inertial sensors, the quantisation noise can be modelled using two different methods. If the inertial sensor's output is delta velocity or delta angle, the quantisation noise will not accumulate and can be modelled as a white noise. In this case, navigation functions should be revised, and the effects of quantisation noise can be absorbed by enlarging the system noise covariance matrix (Savage, 2002). So even if a segment with slope -2 is detected in an AV plot, this kind of quantisation noise can be completely and safely neglected. If the output is acceleration or angle rate, the quantisation noise can be modelled as the differential of a white noise. However, unlike the other four noises, quantisation noise is a high-frequency noise. Therefore, its effect can be reduced or even eliminated by filtering the

inertial sensors' raw data using a low pass filter especially when the vehicle is in a low-dynamic motion (Hou, 2004). In this case, the effect of the quantisation noise can be ignored as well.

The transfer function of the quantisation noise is

$$H_Q(j\omega) = j\omega Q\sqrt{T_s} \tag{4.31}$$

where T_s is sampling interval.

4.5 Equivalence theory

The discussion above indicates that the inertial sensor's stochastic error modelling is mainly the modelling of coloured noises. After deriving the transfer function of each coloured noise (or $1/f^{\alpha}$ noise) including bias instability, rate random walk and rate ramp, their relevant state space forms can be deduced and then implemented separately in a Kalman filter, which is adapted in many applications and achieves some satisfactory results (Yi, 2007; Guerrier, 2013; Li et al., 2014).

In this thesis, it is investigated whether it is possible to use one single transfer function to model all coloured noises together. The summation of all the independent noises can eliminate states estimated in the Kalman filter compared with the independent noise modelling method. The possibility of modelling two separate ARMA processes together has been discussed in Granger and Morris (1976); Teräsvirta (1977). In Seong et al. (2000), the researchers introduce the equivalence theory to use one single ARMA process to model the combination of inertial sensor noise and the coefficients of the relevant ARMA processes are determined using the PEM method to find the best fit. In Han and Wang (2011); Zhao (2013), the equivalence theory is deduced from the differential equation aspect. The authors also describe how to calculate the coefficients of the equivalent differential equation. However, the equivalence theory deduced in former works is only valid for the stationary processes. For nonstationary processes, the equivalence theory is not applicable, since their PSDs don't exist. In this chapter, the equivalence theory is deduced from the s-domain transfer function aspect. The sampled PSD (or generalized PSD) will also be introduced to make it suitable for the nonstationary process application.

Notice that the transfer function of each coloured noise only has poles without zeros in the application. To simplify, the coefficients of the summation of the transfer functions without zeros are determined, which is sufficient for the stochastic error modelling application.

Considering two independent stochastic processes $y_1(t)$, $y_2(t)$ shaped by white noises $w_1(t)$, $w_2(t)$ as

$$\begin{aligned} y_1(t) &= F^{-1}\{H_1(j\omega)\} * w_1(t) + \mu_1 \\ y_2(t) &= F^{-1}\{H_2(j\omega)\} * w_2(t) + \mu_2 \end{aligned} \tag{4.32}$$

where $H_1(j\omega)$ and $H_2(j\omega)$ are the transfer functions of the relevant shaping filters, which can be represented as

$$\begin{aligned} H_1(j\omega) &= \frac{1}{a_1 \cdot (j\omega)^m + a_2 \cdot (j\omega)^{m-1} + \cdots + a_{m+1}} \\ H_2(j\omega) &= \frac{1}{b_1 \cdot (j\omega)^n + b_2 \cdot (j\omega)^{n-1} + \cdots + b_{n+1}} \end{aligned} \tag{4.33}$$

μ_1 and μ_2 are the mean values of two stochastic processes. $w_1(t)$ and $w_2(t)$ are two independent unit white noises. They meet the following relationship

$$\begin{aligned} E\{w_1(t)w_1^*(t)\} = \delta(t), E\{w_2(t)w_2^*(t)\} = \delta(t) \\ E\{w_1(t)w_2^*(t)\} = 0, E\{w_2(t)w_1^*(t)\} = 0 \end{aligned} \tag{4.34}$$

Considering another stochastic process $y'(t)$ shaped by a white noise $w'(t)$ as

$$y'(t) = F^{-1}\{H(j\omega)\} * w'(t) + \mu_1 + \mu_2 \tag{4.35}$$

where $H(j\omega) = \frac{A(j\omega)}{B(j\omega)}$ and $\mu_1 + \mu_2$ is the mean value of $y'(t)$.

If $y'(t)$ and $y_1(t) + y_2(t)$ are equivalent when implemented in the Kalman filter, they should have the same mean value and PSD or sampled PSD, which consequently causes a same auto-covariance (Han and Wang, 2011; Zhao, 2013; Kasdin, 1995; Granger and Morris, 1976; Teräsvirta, 1977). Considering that $E\{w_1(t)\} = 0, E\{w_2(t)\} = 0, E\{w'(t)\} = 0$, it is easy to prove that $E\{y'(t)\} = E\{y_1(t) + y_2(t)\}$.

In the following part, the expression of $H(j\omega)$ will be determined to ensure that $y'(t)$ and $y_1(t) + y_2(t)$ have a same PSD.

According to equations (4.7), (4.9) and (4.11), if $y'(t)$ and $y_1(t) + y_2(t)$ have the same PSD, the following relationship is established

$$|H(j\omega)|^2 = |H_1(j\omega)|^2 + |H_2(j\omega)|^2 \tag{4.36}$$

According to the amplitude frequency characteristic definition of the transfer function, if $B(j\omega)$ is written as

$$\begin{aligned} B(j\omega) = (a_1 \cdot (j\omega)^m + a_2 \cdot (j\omega)^{m-1} + \cdots + a_{m+1}) \cdot \\ (b_1 \cdot (j\omega)^n + b_2 \cdot (j\omega)^{n-1} + \cdots + b_{n+1}) \end{aligned} \tag{4.37}$$

and $A(j\omega) = f_1 \cdot (j\omega)^l + f_2 \cdot (j\omega)^{l-1} + \cdots + f_{l+1}$ meets the following relationship

$$\begin{aligned} |f_1 \cdot (j\omega)^l + f_2 \cdot (j\omega)^{l-1} + \cdots + f_{l+1}|^2 = |a_1 \cdot (j\omega)^m + a_2 \cdot (j\omega)^{m-1} + \cdots + a_{m+1}|^2 \\ + |b_1 \cdot (j\omega)^n + b_2 \cdot (j\omega)^{n-1} + \cdots + b_{n+1}|^2 \end{aligned} \tag{4.38}$$

where $l \leqslant \max(n, p)$, $H(j\omega)$ has the same amplitude frequency characteristic as $H_1(j\omega) + H_2(j\omega)$. In other words, if the coefficients f_i in $A(j\omega)$ match equation (4.38) and $B(j\omega)$ is written as equation (4.37), $y'(t)$ and $y_1(t) + y_2(t)$ will have the same PSD. $y'(t)$ is equivalent to $y_1(t) + y_2(t)$ when implemented in the Kalman filter. This conclusion can be extended to the summation of several shaping filters' transfer functions.

After substituting $s = j\omega$ into equations (4.19), (4.22) and (4.29), according to equations (4.36), (4.37) and (4.38), the transfer function of coloured noises in s-domain should meet

$$|H_c(s)|^2 = |H_B(s)|^2 + |H_K(s)|^2 + |H_R(s)|^2 \tag{4.39}$$

which can be written as

$$H_c(s) = \frac{a_1 s^4 + a_2 s^3 + a_3 s^2 + a_4 s + a_5}{(1 + q_{c_1} T_{c_1} s)(1 + q_{c_2} T_{c_2} s) s (s^2 + \sqrt{2}\omega_0 s + \omega_0^2)} \tag{4.40}$$

How to calculate the coefficients a_i will be discussed in the following sections.

The transfer function of quantisation noise can be treated as a differentiator. Some people may argue whether it is possible to model quantisation noise together with the other three coloured noises, although it is not necessary to model quantisation noise especially for a low-cost MEMS IMU in low-dynamic cases. According to automatic control theory, a system is causal only when the number of zeros is smaller than the number of poles in the s-plane, indicating that the current state is only determined by the former states and will not be affected by future states. If the quantisation noise is modelled together with the other coloured noise, the number of zeros of the equivalent transfer function will be larger than that of poles, which does not meet the causality requirement of a LTI system. Therefore, the shaping filter and equivalence theory method is not applicable to the quantisation noise modelling. However, the quantisation noise effect can be reduced by enlarging the **Q** matrix or pre-filtering as explained in section 4.4.4.

4.6 State space

The s-domain transfer function cannot be implemented directly in the Kalman filter. It should be changed into a state space form when implemented in a navigation Kalman filter. A state space describes a system in modern control theory. Unlike the transfer function describing only the external property of a system, a state space also describes the internal property of a system.

4.6.1 From transfer function to differential equation

The three coloured noises will not always exist at the same time in all inertial sensors. However, in order to obtain a more general form, all the coloured noises are considered together in the following analysis. In case that some noise cannot be observed in the AV plot, its relevant coefficient can be set to zero.

The equivalent transfer function of the coloured noises is

$$H_c(s) = \frac{a_1 s^4 + a_2 s^3 + a_3 s^2 + a_4 s + a_5}{b_1 s^5 + b_2 s^4 + b_3 s^3 + b_4 s^2 + b_5 s + b_6} \tag{4.41}$$

where

$$\begin{aligned}
a_1^2 &= (q_{c_1} T_{c_1} T_{c_2})^2 + (q_{c_2} T_{c_1} T_{c_2})^2 + (K T_{c_1} T_{c_2})^2 \\
a_2^2 - 2a_1 a_3 &= K^2 T_{c_1}^2 + K^2 T_{c_2}^2 + R^2 T_{c_1}^2 T_{c_2}^2 + T_{c_1}^2 q_{c_1}^2 + T_{c_2}^2 q_{c_2}^2 \\
a_3^2 + 2a_1 a_5 - 2a_2 a_4 &= K^2 T_{c_1}^2 T_{c_2}^2 \omega_0^4 + K^2 + R^2 T_{c_1}^2 + R^2 T_{c_2}^2 \\
&\quad + T_{c_1}^2 T_{c_2}^2 q_{c_1}^2 \omega_0^4 + T_{c_1}^2 T_{c_2}^2 q_{c_2}^2 \omega_0^4 \\
a_4^2 - 2a_3 a_5 &= K^2 T_{c_1}^2 \omega_0^4 + K^2 T_{c_2}^2 \omega_0^4 + R^2 \\
&\quad + T_{c_1}^2 q_{c_1}^2 \omega_0^4 + T_{c_2}^2 q_{c_2}^2 \omega_0^4 \\
a_5^2 &= K^2 \omega_0^4 \\
b_1 &= T_{c_1} T_{c_2} \\
b_2 &= T_{c_1} + T_{c_2} + \sqrt{2} T_{c_1} T_{c_2} \omega_0 \\
b_3 &= T_{c_1} T_{c_2} \omega_0^2 + \sqrt{2}(T_{c_1} + T_{c_2}) \omega_0 + 1 \\
b_4 &= (T_{c_1} + T_{c_2}) \omega_0^2 + \sqrt{2} \omega_0 \\
b_5 &= \omega_0^2 \\
b_6 &= 0
\end{aligned} \tag{4.42}$$

From the definition of the transfer function $H_c(s) = \frac{Y(s)}{X(s)}$, the following relationship can be established

$$\begin{aligned} b_1 s^5 Y(s) + b_2 s^4 Y(s) + b_3 s^3 Y(s) + b_4 s^2 Y(s) + b_5 s Y(s) + b_6 Y(s) \\ = a_1 s^4 X(s) + a_2 s^3 X(s) + a_3 s^2 X(s) + a_4 s X(s) + a_5 X(s) \end{aligned} \tag{4.43}$$

After applying an inverse Laplace transformation to equation (4.43), the following differential equation is derived

$$\begin{aligned} b_1 y^{(5)}(t) + b_2 y^{(4)}(t) + b_3 y^{(3)}(t) + b_4 y''(t) + b_5 y'(t) + b_6 y(t) \\ = a_1 x^{(4)}(t) + a_2 x^{(3)}(t) + a_3 x''(t) + a_4 x'(t) + a_5 x(t) \end{aligned} \tag{4.44}$$

According to the definition of the observability canonical form of a system, the system's state space is expressed as (Ogata and Yang, 1970):

$$\begin{cases} \dot{\mathbf{z}}(t) = \mathbf{F}\mathbf{z}(t) + \mathbf{G}\mathbf{w}(t) \\ \mathbf{y}(t) = \mathbf{H}\mathbf{z}(t) \end{cases} \tag{4.45}$$

where $\mathbf{z}(t)$ is a 5×1 vector related with the coloured noise, $\mathbf{y}(t)$ represents the observation and $\mathbf{w}(t)$ is a unit white noise. $\mathbf{F}, \mathbf{G}, \mathbf{H}$ are defined as

$$\mathbf{F} = \begin{bmatrix} 0 & 0 & 0 & 0 & -\frac{b_6}{b_1} \\ 1 & 0 & 0 & 0 & -\frac{b_5}{b_1} \\ 0 & 1 & 0 & 0 & -\frac{b_4}{b_1} \\ 0 & 0 & 1 & 0 & -\frac{b_3}{b_1} \\ 0 & 0 & 0 & 1 & -\frac{b_2}{b_1} \end{bmatrix}, \mathbf{G} = \begin{bmatrix} \frac{a_5}{b_1} \\ \frac{a_4}{b_1} \\ \frac{a_3}{b_1} \\ \frac{a_2}{b_1} \\ \frac{a_1}{b_1} \end{bmatrix}, \mathbf{H} = \begin{bmatrix} 0 \\ 0 \\ 0 \\ 0 \\ 1 \end{bmatrix}^T$$

The process covariance matrix $\mathbf{Q_{zz}}$ satisfies

$$\mathbf{Q_{zz}}\delta(\tau) = E\{\mathbf{G}\mathbf{w}(t)(\mathbf{G}\mathbf{w}(t-\tau))^*\} \tag{4.46}$$

Substituting $\mathbf{G}$ into equation (4.46), $\mathbf{Q_{zz}}$ is

$$\mathbf{Q_{zz}} = \frac{1}{b_1^2} \begin{bmatrix} a_5^2 & a_5 a_4 & a_5 a_3 & a_5 a_2 & a_5 a_1 \\ a_4 a_5 & a_4^2 & a_4 a_3 & a_4 a_2 & a_4 a_1 \\ a_3 a_5 & a_3 a_4 & a_3^2 & a_3 a_2 & a_3 a_1 \\ a_2 a_5 & a_2 a_4 & a_2 a_3 & a_2^2 & a_2 a_1 \\ a_1 a_5 & a_1 a_4 & a_1 a_3 & a_1 a_2 & a_1^2 \end{bmatrix} \tag{4.47}$$

The derivation above can be applied to all the six inertial sensors. If all the inertial sensors' $\mathbf{z}(t)$ are augmented in a navigation Kalman filter's state vector, the system function is

$$\begin{bmatrix} \dot{\mathbf{x}}(t) \\ \dot{\mathbf{z}}(t) \end{bmatrix} = \begin{bmatrix} \mathbf{F_{xx}} & \mathbf{F_{xz}} \\ \mathbf{0} & \mathbf{F_{zz}} \end{bmatrix} \begin{bmatrix} \mathbf{x}(t) \\ \mathbf{z}(t) \end{bmatrix} + \begin{bmatrix} \mathbf{w_x}(t) \\ \mathbf{w_z}(t) \end{bmatrix} \tag{4.48}$$

where $\mathbf{F_{xx}}$ is the system matrix of error-state navigation Kalman filter for attitude, velocity and position errors, $\mathbf{F_{zz}}$ is the same as $\mathbf{F}$, and $\mathbf{F_{xz}}$ is a transfer matrix which converts the coloured noise from the body frame to the navigation frame, which is

$$\mathbf{F_{xz}} = \begin{bmatrix} \mathbf{F}_{Gyro} & \mathbf{0} \\ \mathbf{0} & \mathbf{F}_{Acc} \\ \mathbf{0} & \mathbf{0} \end{bmatrix} \tag{4.49}$$

where

$$\mathbf{F}_{Gyro} = \mathbf{C}_b^n \begin{bmatrix} \mathbf{H}_{GyroX} & \mathbf{0} & \mathbf{0} \\ \mathbf{0} & \mathbf{H}_{GyroY} & \mathbf{0} \\ \mathbf{0} & \mathbf{0} & \mathbf{H}_{GyroZ} \end{bmatrix}, \mathbf{F}_{Acc} = \mathbf{C}_b^n \begin{bmatrix} \mathbf{H}_{AccX} & \mathbf{0} & \mathbf{0} \\ \mathbf{0} & \mathbf{H}_{AccY} & \mathbf{0} \\ \mathbf{0} & \mathbf{0} & \mathbf{H}_{AccZ} \end{bmatrix}$$

The process noise covariance matrix of the new system function is

$$\mathbf{Q} = E\{ \begin{bmatrix} \mathbf{w_x}(t) \\ \mathbf{w_z}(t) \end{bmatrix} \begin{bmatrix} \mathbf{w_x}(t) \\ \mathbf{w_z}(t) \end{bmatrix}^T \} = \begin{bmatrix} \mathbf{Q_{xx}} & 0 \\ 0 & \mathbf{Q_{zz}} \end{bmatrix} \tag{4.50}$$

4.6.2 From transfer function to ARMA process

The ARMA process' Allan Variance has been deduced and discussed in Zhang (2008). In this section, the Allan variance plot (the shaping filter's transfer function) will be used to determine the ARMA process's coefficients. All the coloured noises are still considered together.

After substituting the zero-order holder $s = \frac{1-z^{-1}}{T_s}$ into (4.41) for discretion, its Z-transformation is

$$H_c(z) = \frac{d_1 z^{-4} + d_2 z^{-3} + d_3 z^{-2} + d_4 z^{-1} + d_5}{e_1 z^{-5} + e_2 z^{-4} + e_3 z^{-3} + e_4 z^{-2} + e_5 z^{-1} + e_6} \tag{4.51}$$

where

$$\begin{aligned} d_1 &= a_1 T_s \\ d_2 &= -T_s(4a_1 + T_s a_2) \\ d_3 &= T_s(a_3 T_s^2 + 3a_2 T_s + 6a_1) \\ d_4 &= -T_s(a_4 T_s^3 + 2a_3 T_s^2 + 3a_2 T_s + 4a_1) \\ d_5 &= T_s(a_5 T_s^4 + a_4 T_s^3 + a_3 T_s^2 + a_2 T_s + a_1) \\ e_1 &= -b_1 \\ e_2 &= 5b_1 + T_s b_2 \\ e_3 &= -(b_3 T_s^2 + 4b_2 T_s + 10b_1) \\ e_4 &= b_4 T_s^3 + 3b_3 T_s^2 + 6b_2 T_s + 10b_1 \\ e_5 &= -(b_5 T_s^4 + 2b_4 T_s^3 - 3b_3 T_s^2 - 4b_2 T_s - 5b_1) \\ e_6 &= b_6 T_s^5 + b_5 T_s^4 + b_4 T_s^3 + b_3 T_s^2 + b_2 T_s + b_1 \end{aligned} \tag{4.52}$$

and T_s is the sampling interval.

As a transfer function of a discrete system, $H_c(z)$ is defined as $H_c(z) = \frac{Y(z)}{X(z)}$. Like $H_c(s)$, the following equation can be deduced as

$$\begin{aligned} &e_1Y(z)z^{-5} + e_2Y(z)z^{-4} + e_3Y(z)z^{-3} + e_4Y(z)z^{-2} + e_5Y(z)z^{-1} + e_6Y(z) \\ &= d_1X(z)z^{-4} + d_2X(z)z^{-3} + d_3X(z)z^{-2} + d_4X(z)z^{-1} + d_5X(z) \end{aligned} \tag{4.53}$$

If an inverse Z-transform is applied to equation (4.53), the related difference equation is computed as

$$\begin{aligned} &e_1y_{k-5} + e_2y_{k-4} + e_3y_{k-3} + e_4y_{k-2} + e_5y_{k-1} + e_6y_k \\ &= d_1x_{k-4} + d_2x_{k-3} + d_3x_{k-2} + d_4x_{k-1} + d_5x_k \end{aligned} \tag{4.54}$$

After normalizing the coefficient of y_k and moving all the other terms except y_k to the right side of (4.54),

$$\begin{aligned} y_k = -\frac{1}{e_6}(&e_1y_{k-5} + e_2y_{k-4} + e_3y_{k-3} + e_4y_{k-2} + e_5y_{k-1} \\ &+d_1x_{k-4} + d_2x_{k-3} + d_3x_{k-2} + d_4x_{k-1} + d_5x_{k-1}) \end{aligned} \tag{4.55}$$

y_k has the form of an ARMA process, which is

$$X_t = \sum_{i=1}^{p} \varphi_i X_{t-i} + \sum_{j=0}^{q} \theta_j \varepsilon_{t-j} + \mu_t \tag{4.56}$$

In this sense, the relationship between ARMA process and transfer function (Allan variance plot) can be built. The coefficients of ARMA process are determined from e_j and d_j.

How to deduce ARMA process's state space form has been described in detail in Geist and Pietquin (2011); de Jong and Penzer (2004), which is

$$\begin{cases} \mathbf{z}_k = \mathbf{T}_k\mathbf{z}_{k-1} + \mathbf{G}_k\mathbf{w}_k \\ \mathbf{y}_k = \mathbf{H}_k\mathbf{z}_k \end{cases} \tag{4.57}$$

where $\mathbf{z}_k$ is a 5×1 vector. $\mathbf{F}_k, \mathbf{G}_k, \mathbf{H}_k$ are defined as

$$\mathbf{T}_k = \begin{bmatrix} -\frac{e_5}{e_6} & 1 & 0 & 0 & 0 \\ -\frac{e_4}{e_6} & 0 & 1 & 0 & 0 \\ -\frac{e_3}{e_6} & 0 & 0 & 1 & 0 \\ -\frac{e_2}{e_6} & 0 & 0 & 0 & 1 \\ -\frac{e_1}{e_6} & 0 & 0 & 0 & 0 \end{bmatrix}, \mathbf{G}_k = \begin{bmatrix} \frac{d_5}{e_6} \\ \frac{d_4}{e_6} \\ \frac{d_3}{e_6} \\ \frac{d_2}{e_6} \\ \frac{d_1}{e_6} \end{bmatrix}, \mathbf{H}_k = \begin{bmatrix} 1 \\ 0 \\ 0 \\ 0 \\ 0 \end{bmatrix}^T$$

The process covariance matrix $\mathbf{Q_{zz}}$ satisfies

$$\mathbf{Q_{zz}} = E\{\mathbf{G}_k\mathbf{w}_k(\mathbf{G}_k\mathbf{w}_k)^*\} \tag{4.58}$$

Substituting $\mathbf{G}_k$ into equation (4.58), $\mathbf{Q_{zz}}$ becomes

$$\mathbf{Q_{zz}} = \frac{1}{e_6^2}\begin{bmatrix} d_5^2 & d_5d_4 & d_5d_3 & d_5d_2 & d_5d_1 \\ d_4d_5 & d_4^2 & d_4d_3 & d_4d_2 & d_4d_1 \\ d_3d_5 & d_3d_4 & d_3^2 & d_3d_2 & d_3d_1 \\ d_2d_5 & d_2d_4 & d_2d_3 & d_2^2 & d_2d_1 \\ d_1d_5 & d_1d_4 & d_1d_3 & d_1d_2 & d_1^2 \end{bmatrix} \tag{4.59}$$

However, the direct computation of the coefficients e_j and d_j is very difficult, especially for higher order transfer functions, since it involves several adding and multiplying operations. Besides this, due to discretion, coefficients determined from the shaping filter transfer function sometimes may cause numerical instability. For example, e_6 is not only related to b_1, but also affected by the higher order power of T_s. If T_s is small, e_6 is dominated by b_1, which eliminates the effect of other coefficients and degrades the state space estimation accuracy. The direct implementation of the conventional ARMA state space will introduce some negative effects to the navigation results. Considering the internal relationship among the coefficients of the ARMA process in the specific application, a modified state space form is introduced as shown in Appendix, which is

$$\mathbf{T}_k = \begin{bmatrix} 1-\frac{b_2T_s}{b_1} & T_s & 0 & 0 & 0 \\ -\frac{b_3T_s}{b_1} & 1 & T_s & 0 & 0 \\ -\frac{b_4T_s}{b_1} & 0 & 1 & T_s & 0 \\ -\frac{b_5T_s}{b_1} & 0 & 0 & 1 & T_s \\ -\frac{b_6T_s}{b_1} & 0 & 0 & 0 & 1 \end{bmatrix}, \mathbf{G}_k = \begin{bmatrix} \frac{a_1}{b_1}T_s \\ \frac{a_2}{b_1}T_s \\ \frac{a_3}{b_1}T_s \\ \frac{a_4}{b_1}T_s \\ \frac{a_5}{b_1}T_s \end{bmatrix}, \mathbf{H}_k = \begin{bmatrix} 1 \\ 0 \\ 0 \\ 0 \\ 0 \end{bmatrix}^T$$

The state space from the ARMA process can augment the navigation state vector by

$$\begin{bmatrix} \mathbf{x}_k \\ \mathbf{z}_k \end{bmatrix} = \begin{bmatrix} \mathbf{T_{xx}} & \mathbf{T_{xz}} \\ \mathbf{0} & \mathbf{T_{zz}} \end{bmatrix} \begin{bmatrix} \mathbf{x}_{k-1} \\ \mathbf{z}_{k-1} \end{bmatrix} + \begin{bmatrix} \mathbf{w_x} \\ \mathbf{w_z} \end{bmatrix} \tag{4.60}$$

where $\mathbf{T_{xx}}$ is transition matrix implemented in error-state navigation Kalman filter, $\mathbf{T_{zz}}$ is the same as $\mathbf{T}_k$, and $\mathbf{T_{xz}}$ is a transfer matrix which converts coloured noise from the body frame to the navigation frame.

4.7 Simulation

In the simulation, the accelerometer's stochastic errors include two 1st-order Markovian processes ($T_{c1} = 5.291\ s$, $q_{c1} = 0.01\ m/s^3$, $T_{c2} = 21.164\ s$, $q_{c2} = 0.01\ m/s^3$) approximating bias instability, one rate random walk ($K = 0.008\ m/s^2/\sqrt{s}$), a white noise ($N = 0.02\ m/s/\sqrt{s}$) and constant bias $0.02\ m/s^2$. As with the gyroscopes, the constant bias of gyroscope is $1.146\ \mathrm{deg}/s$, the bias instability is $1.146\ \mathrm{deg}/s$, which will be generated by combining two separate 1st-order Markovian processes, rate random walk is $0.458\ \mathrm{deg}/s/\sqrt{s}$, generated by integrating a unit white noise and white noise with auto-covariance $1.146\ \mathrm{deg}/\sqrt{s}$. Since the random ramp seldom appears in the inertial sensors, it is not simulated for all the inertial sensors. The order of the relevant shaping filters' transfer functions can then be reduced. The Allan variance plot of the simulated inertial sensors' noises is shown in Figures 4.4 and 4.5. All the elements in $\mathbf{P}_0, \mathbf{Q}$ are set identically to the parameters of the simulation section in Chapter 3, except that the gyroscope and accelerometer biases of the conventional modelling method are taken from the system matrix of the shaping filter based method. In the $\mathbf{R}$ matrix, the position standard deviation is set to be 1 cm.

The relevant accelerometers' and gyroscopes' shaping filter transfer functions are

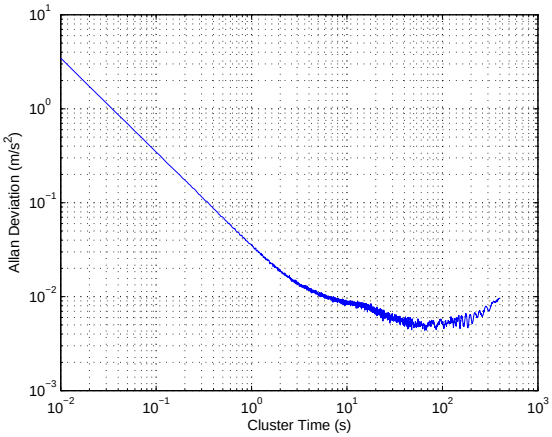

Figure 4.4: Simulated accelerometer's AV plot

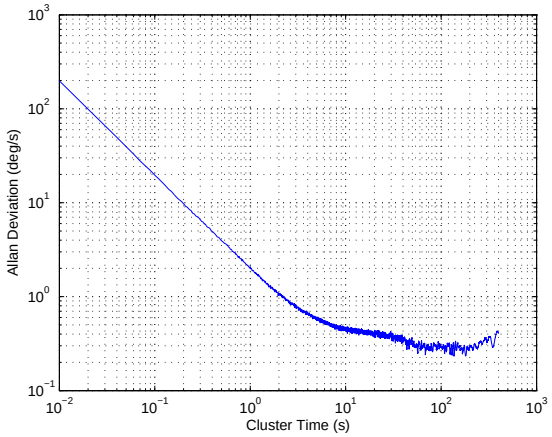

Figure 4.5: Simulated gyroscope's AV plot

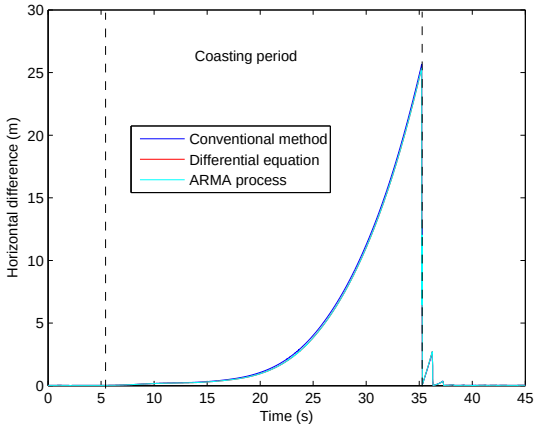

Figure 4.6: Horizontal position drift in simulation

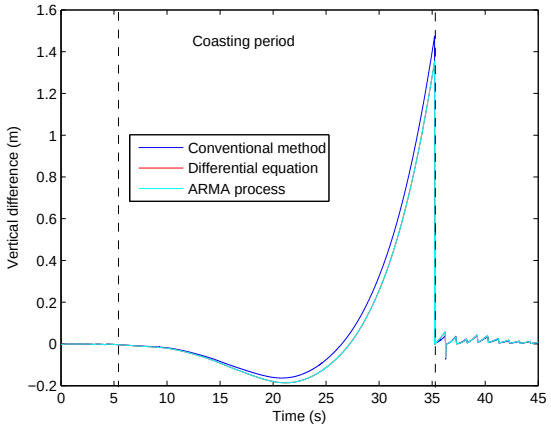

Figure 4.7: Vertical position drift in simulation

$$H_{Acc}(s) = \frac{19.33s^2 + 1.241s + 0.008}{1120s^3 + 116.4s^2 + s}$$
$$H_{Gyro}(s) = \frac{1107.52s^2 + 71.104s + 0.458}{1120s^3 + 116.4s^2 + s} \tag{4.61}$$

After applying an inverse Laplace transformation and a Z-transformation to the transfer function (4.61), their related state space forms can be deduced and then implemented in the navigation Kalman filter. The coasting performance is introduced to indirectly examine the effectiveness of the shaping filter based method. Due to the random property of the simulated noises, the navigation results shown in Figures 4.6 and 4.7 are the average of 10 filter runs.

From Figures 4.6, 4.7 and Table 4.3, it can be found that the shaping filter based methods (Differential equation and ARMA process) are effective in estimating IMU stochastic errors in the Kalman filter, which have similar and even smaller maximum position drifts than the conventional method during GPS outages. However, the shaping filter based methods introduce additional states to the state vector with an increased computational burden. When computational efficiency is considered, the conventional 1st-order Markovian process based method is preferred. As shown in Figures 4.6 and 4.7, after the coasting period, the position estimation seems to have some jumps when the observation is available. This is due

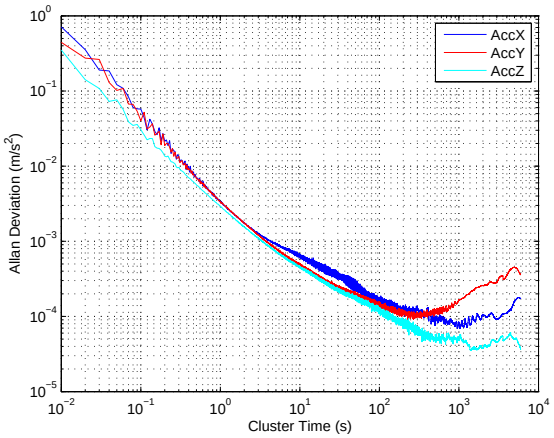

Figure 4.8: Allan variance plot of accelerometers

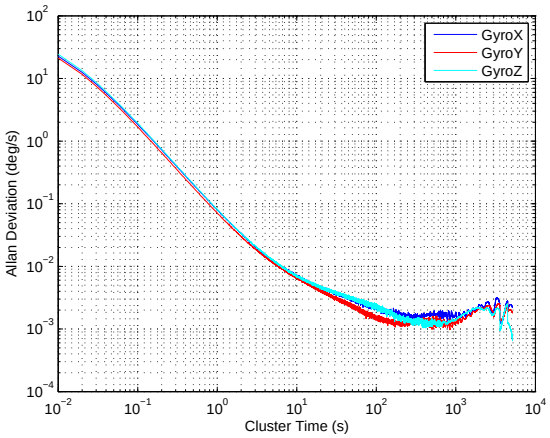

Figure 4.9: Allan variance plot of gyros

to that the state covariance matrix becomes very large during the coasting period and the navigation Kalman filter needs some time to become convergent once the observation is available.

4.8 Experiment

The stochastic error modelling method will be further implemented with the real experiment data. Two experiments including the Allan variance and test experiments are conducted. The Allan variance experiment aims at determining the coefficients of the inertial sensors' stochastic errors, while the test experiment is used to examine the performance and effectiveness of the stochastic error modelling method.

4.8.1 Allan variance experiment

Five hours of raw data is sampled from a stationary MEMS IMU (iMAR VRU) with a sampling rate at 100 Hz. Before sampling, the MEMS IMU was warmed up for 30 minutes. The AV plots of the three gyroscopes and accelerometers are shown in Figures 4.8 and 4.9.

According to the relationship shown in Table 4.1, the coefficients of the relevant stochastic errors can be determined using the curve fitting method. The least squares method can also be used to determine the coefficients of stochastic errors (Quinchia, 2014), while the initial values for the least squares method are still determined directly from the AV plot (Guerrier, 2013; Guerrier et al., 2013; Quinchia et al., 2013).

According to the length of the flat segments in the AV plots, two 1st-order Markovian processes are applied to approximate the bias instabilities of X,Z-accelerometers and X,Y-gyros and one 1st-order Markovian process to approximate bias instabilities of Y-accelerometer and Z-gyro. The coefficients of the relevant inertial sensors' stochastic errors are shown in Table 4.4. The transfer function of each

Table 4.3: Maximum position drift in simulated coasting period

	Horizontal drift (m)	Vertical drift (m)
Conventional method	25.662	1.475
Differential equation	25.355	1.355
ARMA process	25.355	1.355

inertial sensor's coloured noises can be summarized as shown in (4.62). The relevant differential equation and ARMA process are deduced from (4.62). The inertial sensors' coloured noises can then be implemented in the navigation Kalman filter.

$$
\begin{aligned}
H_{AccX}(s) &= \frac{3.5729s^3 + 0.2533s^2 + 0.008948s + 2.673 \cdot 10^{-5}}{1.12 \times 10^5 s^4 + 9082s^3 + 363.3s^2 + 2.981s + 0.0025} \\
H_{AccY}(s) &= \frac{0.005186s + 7.415 \cdot 10^{-6}}{158.7s^2 + s} \\
H_{AccZ}(s) &= \frac{4.805s + 3.963 \cdot 10^{-3}}{4.199 \times 10^5 s^2 + 1852s + 1} \\
H_{GyroX}(s) &= \frac{64.17s^2 + 0.2155s + 8.046 \cdot 10^{-5}}{1.26 \times 10^5 s^3 + 952.4s^2 + s} \\
H_{GyroY}(s) &= \frac{26.20s^2 + 0.1324s + 7.509 \cdot 10^{-5}}{5.599 \times 10^4 s^3 + 634.9s^2 + s} \\
H_{GyroZ}(s) &= \frac{0.06466s + 8.483 \cdot 10^{-5}}{264.6s^2 + s}
\end{aligned}
\tag{4.62}
$$

4.8.2 Test experiment

The Griesheim airport experiment data shown in Figure 3.25, is used to examine the performance of the shaping filter based method. The GPS signal is blocked artificially for 30 seconds to observe the IMU coasting performance. GPS is loosely integrated with IMU in the experiment. During the coasting periods, there is no aiding information, and IMU is only compensated by the biases estimated before coasting. If stochastic errors are modelled and estimated accurately, the IMU position drift is smaller, which can indirectly indicate the effectiveness of stochastic modelling methods (Guerrier, 2013; Guerrier et al., 2013; Han and Wang, 2011). All the elements in $\mathbf{P}_0, \mathbf{Q}$ are set as the parameters of experiment section in Chapter 3, except that the gyroscope and accelerometer biases of the conventional modelling method are taken from the system matrix deduced with the shaping filter based method. The DGPS position standard deviation is implemented in the $\mathbf{R}$ matrix. The coasting performance comparison is shown in Figures 4.10, 4.11 and Table 4.5.

From Figures 4.10, 4.11 and Table 4.5, it can be found that both the differential equation and ARMA process modelling methods outperform the conventional 1st-order Markovian process modelling method.

Table 4.4: Coefficients of MEMS IMU stochastic errors

	Quantisation noise	Angle/Velocity random walk	Bias instability	Rate random walk	Rate ramp
unit	$Q(m/s)$	$N(m/s/\sqrt{s})$	$B(m/s^2)$	$K(m/s^2/\sqrt{s})$	$R(m/s^2/s)$
AccX	$2.175 \cdot 10^{-3}$	$1.799 \cdot 10^{-3}$	$1.370 \cdot 10^{-4}$	N/A	$4.107 \cdot 10^{-8}$
AccY	$1.491 \cdot 10^{-3}$	$1.432 \cdot 10^{-3}$	$1.721 \cdot 10^{-4}$	$9.518 \cdot 10^{-6}$	N/A
AccZ	$1.724 \cdot 10^{-3}$	$1.202 \cdot 10^{-3}$	$0.753 \cdot 10^{-4}$	N/A	N/A
unit	$Q(\text{deg})$	$N(\text{deg}/\sqrt{s})$	$B(\text{deg}/s)$	$K(\text{deg}/s/\sqrt{s})$	$R(\text{deg}/s/s)$
GyroX	0.0491	0.0220	$2.528 \cdot 10^{-3}$	$8.046 \cdot 10^{-5}$	N/A
GyroY	0.0426	0.0199	$1.896 \cdot 10^{-3}$	$7.509 \cdot 10^{-5}$	N/A
GyroZ	0.0485	0.0211	$1.866 \cdot 10^{-3}$	$8.483 \cdot 10^{-5}$	N/A

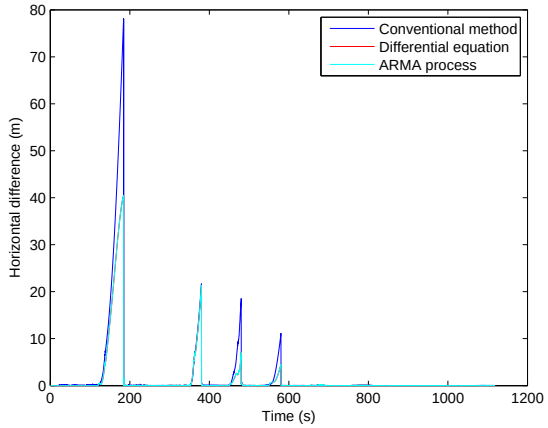

Figure 4.10: Horizontal position drift with experimental data

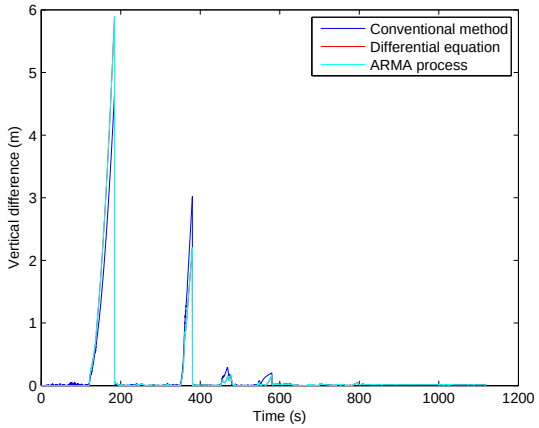

Figure 4.11: Vertical position drift with experimental data

The differential equation and ARMA process both show a similar coasting performance during the GPS outages, because they are deduced from the same shaping filter's transfer function and have the same state space. The comparison also indicates that the maximum position drifts during the four outages become smaller and smaller over time as the stochastic errors are better estimated. As shown in the relevant state space, the shaping filter based method introduces additional states to the state vector, increasing the computational load.

4.9 Conclusion

This chapter introduces how to determine the shaping filter for each inertial sensor's stochastic error based on the Allan variance technique. The differential equation and ARMA process of the inertial sensor's stochastic errors are deduced from the s-domain transfer function by applying an inverse Laplace transformation and a Z-transformation. The relevant state space forms are also established. The discussion and derivation show that the differential equation and ARMA process modelling methods are equivalent, and they describe the same stochastic process from two different aspects. A similar estimation accuracy can be expected from them as indicated in both simulation and experiment results.

Table 4.5: Maximum position drift during coasting periods

Methods	1st GPS outage		2nd GPS outage	
	Horizontal drift (m)	Vertical drift (m)	Horizontal drift (m)	Vertical drift (m)
Conventional method	78.108	4.658	21.674	3.018
Differential equation	40.485	5.894	21.310	2.202
ARMA process	40.485	5.894	21.310	2.202
Methods	3rd GPS outage		4th GPS outage	
	Horizontal drift (m)	Vertical drift (m)	Horizontal drift (m)	Vertical drift (m)
Conventional method	18.534	0.290	11.118	0.200
Differential equation	7.031	0.170	4.167	0.169
ARMA process	7.031	0.170	4.167	0.169

A relationship between the Allan variance and ARMA process is also created, and the coefficients of ARMA process do not need to be estimated using the Yule-Walker or Burg estimation methods and can be determined directly from the shaping filter's transfer function.

5 Carrier phase implementation in GPS/IMU tightly-coupled navigation system

In a conventional GPS/IMU tightly-coupled navigation system, the GPS pseudorange and Doppler are usually implemented as observations in the navigation Kalman filter. Since the pseudorange is applied to absolute positioning, the conventional integrated navigation system can only reach the SPP accuracy. Compared with the pseudorange, the carrier phase is much more accurate and can achieve centimetre positioning accuracy, especially when a differential GPS technique is applied. Therefore, the implementation of the carrier phase in a GPS/IMU tightly-coupled navigation system is beneficial for the position, velocity and attitude estimation.

However, carrier phase observations always suffer from the problem of fixing ambiguities, which is not feasible in non-differential mode. To avoid this problem, the TDCP method is proposed to eliminate carrier phase ambiguities by differencing between two successive GPS epochs based on GPS carrier phase ambiguities staying constant when there are no cycle slips. Although the TDCP technique can improve relative positioning accuracy and smooth trajectory, the absolute positioning accuracy is still determined by the absolute pseudorange observation in pseudorange+TDCP tightly-coupled navigation systems. In the TCP based systems, the carrier phase ambiguities are estimated as additional states in the navigation Kalman filter. The positioning accuracy of integrated navigation systems can be greatly improved compared to the TDCP based methods. This chapter investigates how to implement the GPS carrier phase in a non-differential GPS/IMU tightly-coupled navigation system. A performance comparison between these two carrier phase methods is examined through simulation and experiment.

5.1 Time differenced carrier phase

In order to avoid the difficulty of fixing carrier phase ambiguities for a single GPS receiver in non-differential mode, differencing carrier phase observations between two successive GPS epochs was proposed to eliminate ambiguities since such carrier phase ambiguities will remain constant if there are no cycle slips or blockages (Wendel and Trommer, 2004; Wendel et al., 2006a). Fixing carrier phase ambiguities can then be avoided after applying the TDCP. Since the TDCP is computed directly from carrier phase observations, its accuracy can reach as high as the centimetre or even millimetre level as suggested in Ding and Wang (2011); Serrano et al. (2004); Freda et al. (2014) and can be applied in many fields with satisfactory results. In Soon et al. (2008); Moafipoor et al. (2004); Ding (2007); Steinhardt (2014); Han and Wang (2012), the TDCP is implemented in GPS/INS tightly-coupled navigation systems to improve the navigation performance. The TDCP is also applied to solve the low-cost IMU in-motion alignment problem because of its higher velocity estimation accuracy in Choi et al. (2014). Aside from vehicle applications, a TDCP/IMU integrated navigation system is successfully applied to improve heave compensation as discussed in Blake (2007).

5.1.1 Measurement equation

Compared with Doppler, the TDCP appears to estimate the vehicle's average velocity between two successive GPS epochs (Wendel et al., 2006a). In the following, it will be investigated how to implement the TDCP observation in a GPS/IMU tightly-coupled navigation system.

As shown in equation (2.1), the carrier phase observation from GPS antenna to the m-th satellite tracked by GPS receiver is

$$l_m = r_m + c\delta t_r - c\delta t_{s,m} - I_m + T_m + \varepsilon_{l,m} + \lambda N \tag{5.1}$$

where N is the carrier phase ambiguity. When there are no signal blockages or cycle slips, this value is an unknown constant.

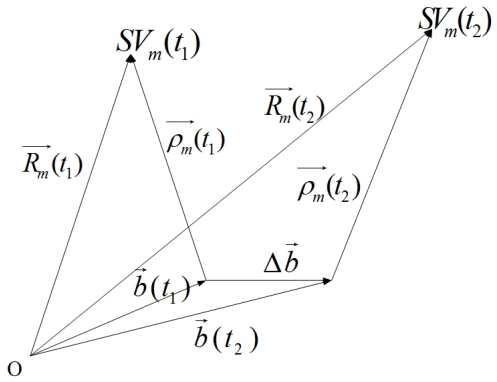

Figure 5.1: Positions of GPS receiver and one satellite at two epochs in ECEF frame (Han and Wang, 2012)

For two successive measurement time epochs t_1 and t_2, the TDCP measurement equation is

$$\Delta l_m = \Delta r_m + c\Delta\delta t_r - c\Delta\delta t_{s,m} - \Delta I_m + \Delta T_m + \Delta\varepsilon_{\delta,m} \tag{5.2}$$

where the ambiguity term in (5.1) is eliminated through differencing. Δr_m represents the change of the distance from antenna to satellite during $t_1 - t_2$ period, equally shown by the time difference operator $\Delta\cdot$. After compensating for the ionospheric and tropospheric delays as well as satellite clock error, equation (5.2) can be revised as

$$\Delta l_m = \Delta r_m + c\Delta\delta t_r + \Delta\varepsilon_{\delta,m} \tag{5.3}$$

In equation (5.3), the calculation of Δr_m is one of the key issues in deducing the TDCP measurement matrix (Wendel and Trommer, 2004; Wendel et al., 2006a; Han and Wang, 2012).

In Figure 5.1, $SV_m(t_1)$ and $SV_m(t_2)$ are positions of the m-th satellite tracked by the GPS receiver at t_1 and t_2 time epochs. $\overrightarrow{R_m}(t_1)$ and $\overrightarrow{R_m}(t_2)$ are the m-th satellite's position vectors at different epochs expressed in ECEF frame. $\overrightarrow{b}(t_1)$ and $\overrightarrow{b}(t_2)$ are the GPS receiver position vectors. $\overrightarrow{\rho_m}(t_1)$ and $\overrightarrow{\rho_m}(t_2)$ are the range vectors from the GPS receiver to the m-th satellite. $\Delta\overrightarrow{b}$ is the GPS receiver's position change from t_1 to t_2. From Figure 5.1, Δr_m is calculated as

$$\begin{aligned}\Delta r_m &= \overrightarrow{\rho_m}(t_2) - \overrightarrow{\rho_m}(t_1) \\ &= (\overrightarrow{R_m}(t_2) - \overrightarrow{b}(t_2))\cdot\overrightarrow{e_m}(t_2) - (\overrightarrow{R_m}(t_1) - \overrightarrow{b}(t_1))\cdot\overrightarrow{e_m}(t_1)\end{aligned} \tag{5.4}$$

where $\overrightarrow{e_m}(t)$ is the unit vector of the line of sight pointing from the GPS receiver to the m-th satellite.

Δr_m can be expanded as

$$\Delta r_m = (\overrightarrow{R_m}(t_2)\overrightarrow{e_m}(t_2) - \overrightarrow{R_m}(t_1)\overrightarrow{e_m}(t_1)) - (\overrightarrow{b}(t_1)\overrightarrow{e_m}(t_2) - \overrightarrow{b}(t_1)\overrightarrow{e_m}(t_1)) - \Delta\overrightarrow{b}\,\overrightarrow{e_m}(t_2) \tag{5.5}$$

The first two terms in (5.5) are usually calculated directly from the navigation messages and results. So both of them can be moved to the left side of equation (5.3), which is

$$\begin{aligned}\Delta\tilde{l}_m &= \Delta l_m - (\overrightarrow{R_m}(t_2)\overrightarrow{e_m}(t_2) - \overrightarrow{R_m}(t_1)\overrightarrow{e_m}(t_1)) + (\overrightarrow{b}(t_1)\overrightarrow{e_m}(t_2) - \overrightarrow{b}(t_1)\overrightarrow{e_m}(t_1)) \\ &= -\Delta\overrightarrow{b}\,\overrightarrow{e_m}(t_2) + c\Delta\delta t_r + \Delta\varepsilon_{\delta,m}\end{aligned} \tag{5.6}$$

A new variable is defined as

$$\begin{aligned} Y &= -\overrightarrow{e_m}(t_2)\Delta\overrightarrow{b} + \Delta\varepsilon_{\delta,m} \\ &= -\overrightarrow{e_m}(t_2)\int_{t_1}^{t_2}\mathbf{v}_n dt + \Delta\varepsilon_{\delta,m} \end{aligned} \tag{5.7}$$

When perturbation is applied to equation (5.7), its error expression is

$$\begin{aligned} \delta Y &= -\overrightarrow{e_m}(t_2)\delta\Delta\overrightarrow{b} + \delta\Delta\varepsilon_{\delta,m} \\ &= -\overrightarrow{e_m}(t_2)\int_{t_1}^{t_2}\delta\mathbf{v}_n dt + \delta\Delta\varepsilon_{\delta,m} \end{aligned} \tag{5.8}$$

The first term in equation (5.8) is related to an integration. An integration term cannot be implemented in the Kalman filter directly, since the measurement function should be of the form as $\mathbf{z} = \mathbf{H}\mathbf{x} + \mathbf{v}$. Therefore this integration should be transformed into a linear form through some approximations. According to the error propagation principle, $\mathbf{x}(t)$ can be expressed as

$$\mathbf{x}(t) = \Phi(t, t_1)\Phi(t_1, t_2)\mathbf{x}(t_2) \tag{5.9}$$

where $\Phi(t_i, t_j)$ is the state transition matrix from time epoch t_j to t_i. Φ is calculated by discretizing the system matrix $\mathbf{F}$. Φ and $\mathbf{F}$ have the following relationship (Wendel and Trommer, 2004)

$$\begin{cases} \Phi(t_i + \delta t, t_i) = \mathbf{I} + \mathbf{F}\delta t \\ \Phi(t_i - \delta t, t_i) = \mathbf{I} - \mathbf{F}\delta t \end{cases} \tag{5.10}$$

where the first equation describes how to use the current state to predict the future state and the second equation describes how to use the current state to deduce the previous state.

The velocity error at epoch t is

$$\delta\mathbf{v} = \mathbf{C}_v\mathbf{x}(t) = \mathbf{C}_v\Phi(t, t_1)\Phi(t_1, t_2)\mathbf{x}(t_2) \tag{5.11}$$

where $\mathbf{C}_v$ is $[\mathbf{0}_{3\times3} \quad \mathbf{I}_{3\times3} \quad \mathbf{0}_{3\times11}]$.

Then the integration in (5.8) can be further expressed as

$$\begin{aligned} \int_{t_1}^{t_2}\delta\mathbf{v}_\mathbf{n} dt &= \int_{t_1}^{t_2}\mathbf{C}_v\Phi(t, t_1)\Phi(t_1, t_2)\mathbf{x}(t_2)dt \\ &= \mathbf{C}_v\int_{t_1}^{t_2}\Phi(t, t_1)dt\Phi(t_1, t_2)\mathbf{x}(t_2) \end{aligned} \tag{5.12}$$

where the two transition matrices related to Φ are calculated as

$$\begin{cases} \displaystyle\int_{t_1}^{t_2}\Phi(t, t_1)dt = \sum_{i=1}^{k}\delta t\Phi(t_1 + i\delta t, t_1) = \delta t\sum_{i=1}^{k}\prod_{j=1}^{i}\Phi(t_1 + j\delta t, t_1 + (j-1)\delta t) \\ \qquad\qquad = \delta t\sum_{i=1}^{k}(\mathbf{I} + \mathbf{F}\delta t)^i \approx \delta t\sum_{i=1}^{k}(\mathbf{I} + i\mathbf{F}\delta t) = k\delta t(\mathbf{I} + \mathbf{F}\delta t(k+1)/2) \\ \Phi(t_1, t_2) = \displaystyle\prod_{i=1}^{k}\Phi(t_1 + (i-1)\delta t, t_1 + i\delta t) = (\mathbf{I} - \mathbf{F}\delta t)^k \end{cases} \tag{5.13}$$

where $k = (t_2 - t_1)/\delta t$, $\mathbf{F}$ is the system matrix at time epoch t_2 and δt is a small sampling period.

The first term in (5.8) can then be rewritten as

$$\int_{t_1}^{t_2} \delta \mathbf{v_n} dt = \mathbf{C}_v(k\delta t(\mathbf{I} + \mathbf{F}\delta t(k+1)/2))(\mathbf{I} - \mathbf{F}\delta t)^k \mathbf{x}(t_2) \tag{5.14}$$

So the matrix relevant to the velocity error integration is

$$\mathbf{H}_v = \mathbf{C}_v(k\delta t(\mathbf{I} + \mathbf{F}\delta t(k+1)/2))(\mathbf{I} - \mathbf{F}\delta t)^k \tag{5.15}$$

The measurement function of the TDCP/IMU tightly-coupled navigation Kalman filter is

$$\mathbf{z} = \mathbf{H}_{TDCP}\mathbf{x} + \delta\Delta\varepsilon_{\delta,m} \tag{5.16}$$

where

$$\mathbf{z} = [\delta\Delta l_1 \quad \delta\Delta l_2 \quad \cdots \quad \delta\Delta l_n]^T$$
$$\mathbf{H}_{TDCP} = [\mathbf{0}_{n\times 3} \quad -\overrightarrow{e_n}(t_2) * \mathbf{C}_e^n.\mathbf{H}_v \quad \mathbf{0}_{n\times 9} \quad \mathbf{0}_{n\times 1} \quad \mathbf{1}_{n\times 1}\cdot\Delta t]$$

and $\mathbf{C}_e^n$ is the transformation matrix from the earth frame to the navigation frame, Δt is the time interval between t_1 and t_2, $\delta\Delta l = \Delta l_m - \Delta l_I$ is the difference between the measured and estimated TDCP, and $\delta\Delta\varepsilon_{\delta,m}$ is TDCP measurement noise.

5.1.2 Discussion of the velocity error integration measurement matrix

The velocity error integration measurement matrix $\mathbf{H}_v$ expressed as equation (5.15) is considered in this section. If $\mathbf{F}\delta t$ is small enough, $\mathbf{H}_v$ can be expanded as

$$\begin{aligned}\mathbf{H}_v &\approx \mathbf{C}_v k\delta t(\mathbf{I} + \mathbf{F}\delta t(k+1)/2)(\mathbf{I} - k\mathbf{F}\delta t) \\ &= \mathbf{C}_v k\delta t(\mathbf{I} - \mathbf{F}\delta t(k-1)/2 - (\mathbf{F}\delta t)^2 k(k+1)/2)\end{aligned} \tag{5.17}$$

If higher order terms in (5.17) are neglected, $\mathbf{H}_v$ is

$$\mathbf{H}_v \approx \mathbf{C}_v k\delta t(\mathbf{I} - \mathbf{F}\delta t(k-1)/2) \tag{5.18}$$

From equation (5.18), it can be seen that if the current system matrix is already known, the measurement matrix can be easily calculated, significantly reducing the computational load, because there is no need to perform several adding and multiplying operations. This form can be treated as a simplified version of the TDCP measurement update equation. In Steinhardt (2014), a similar simplified TDCP observation is adapted to estimate the average velocity between two successive GPS epochs and then implemented in a tightly-coupled navigation system to improve navigation performance.

In equation (5.15), a constant system matrix $\mathbf{F}$ is utilized to calculate the measurement matrix. If the time interval between two successive GPS epochs is small, a constant $\mathbf{F}$ is suitable for calculating the integration of $\delta\mathbf{v}_n$. However, if the time interval between two successive GPS epochs is very large, a constant system matrix appears to produce some computation inaccuracy in deducing the former transition matrices, especially when the vehicle's states change quickly during this time interval. In order to improve the filtering performance, it is beneficial to use a changeable system matrix at each time update instead of a constant one to perform the velocity error integration. Considering that the measurement update is executed only when the GPS observations are available, the state transition matrix in each

time update of IMU sampling rate multiplying the IMU sampling period δt_{IMU} can be stored and then accumulated to calculate the integration of $\delta \mathbf{v}_n$. In this case, there is no need to deduce the former system matrix from the current system matrix using several multiplying and adding operations, which also saves some computational time while reaching a higher estimation accuracy. $\Phi(t, t_1)$ and $\Phi(t_1, t_2)$ can accordingly be rewritten as

$$\begin{cases} \int_{t_1}^{t_2} \Phi(t, t_1) dt = \sum_{i=1}^{k} \delta t_{IMU} \prod_{j=1}^{i} (\mathbf{I} + \mathbf{F}(t_1 + j\delta t_{IMU}) \delta t_{IMU}) \\ \Phi(t_1, t_2) = \prod_{i=1}^{k} (\mathbf{I} - \mathbf{F}(t_1 + i\delta t_{IMU}) \delta t_{IMU}) \end{cases} \tag{5.19}$$

where $\mathbf{F}(t_1 + i\delta t_{IMU})$ is the system matrix at time epoch $t_1 + i\delta t_{IMU}$.

In the error-state EKF, the predicted velocity error is zero in each time update. The velocity error integration will subsequently be zero. However, it is still important to calculate the TDCP measurement matrix, because it is related to the Kalman gain and *a posteriori* covariance matrix calculation, which greatly affects the estimation accuracy.

Implementing TDCP as the only observation in tightly-coupled navigation systems will cause large position drift especially in high-dynamic and large misalignment cases, which are very common for GPS/MEMS IMU tightly-coupled navigation applications. In order to bound the position drift, the pseudorange observation is usually introduced for the absolute positioning thus resulting in SPP accuracy. Hence, some enhanced methods are developed, such as dual-rate Kalman filter (Han and Wang, 2012), reduced Kalman filter (Tang et al., 2007) and delta position aiding (Ding, 2008), in order to improve the positioning accuracy of the pseudorange+TDCP GPS/IMU tightly-coupled navigation system. However, these enhanced methods show limited improvements in the positioning accuracy. Therefore, in this chapter, the pseudorange observations are directly augmented with the TDCP measurements in the navigation Kalman filter. The pseudorange+TDCP GPS/IMU tightly-coupled navigation system will behave similar as the pseudorange+Doppler GPS/IMU tightly-coupled navigation system. The method of improving the positioning accuracy of the TDCP based system will be discussed further in Chapter 6.

5.2 Total carrier phase

As a non-differential positioning technique, the PPP uses the measurements from a single GPS receiver with the improvement from the application of corrections to the observation error sources determined or estimated as additional unknowns to perform positioning, which is a promising technique for a high-accuracy single GPS application. The static PPP accuracy can reach the centimetre level, while the kinematic application can achieve the sub-meter level when the PPP is convergent. The PPP technique is the basis of a TCP/IMU tightly-coupled navigation system. Unlike conventional PR+Doppler GPS/IMU tightly-coupled navigation systems, a TCP/IMU tightly-coupled navigation system implements the total carrier phase as observations in the navigation Kalman filter, which adds more carrier phase related states to the state vector but can improve positioning accuracy to the sub-meter level. Integrating the PPP technique with a high-grade IMU through the tightly-coupled strategy has been discussed preliminarily in Zhang and Gao (2004). The researchers further compare a point positioning based system with a DGPS based system in Zhang and Gao (2005b,a, 2008). The point positioning GPS/IMU integrated navigation system can reach a decimetre level positioning accuracy and a similar attitude accuracy as a DGPS/IMU tightly-coupled navigation system. In Ascher et al. (2011); Du and Gao (2010); Du (2010); Roesler and Martell (2009); Rabbou and El-Rabbany (2014b), the researchers introduce how to implement the PPP observation with a low-cost MEMS IMU, and the reported positioning accuracy can reach to the sub-meter level in kinematic cases when the filter is convergent. In Rabbou and El-Rabbany (2014a); Rabbou (2014), the researchers implement nonlinear filtering methods to further improve the navigation

performance of a PPP/MEMS IMU tightly-coupled navigation system during GPS outages and in large misalignment cases. The integration with an IMU can also enhance the PPP technique. In Du (2011); Du and Gao (2012), a MEMS IMU is used as an aiding sensor with WL and EWL phase combinations to uniquely determine cycle slips in the L1 and L2 frequencies. The reported cycle slip detection and PPP re-convergence speed can be greatly improved by applying this technique. In Karaim et al. (2013); Figueiredo e Silva (2012), inertial sensors are helpful for real time cycle slip detection. A PPP/IMU tightly-coupled navigation system has been applied to many applications like land vehicle navigation (Rabbou and El-Rabbany, 2014b; Ascher et al., 2011), seismic wave motions measurement (Xu et al., 2013), hydro-graphic surveys (El-Diasty), positioning for visually impaired people (Hafner et al., 2014) and so on.

The state vector, transition function and measurement equation of a TCP/IMU tightly-coupled navigation system are deduced as shown in the following sections.

5.2.1 State vector

The state vector of a TCP/IMU tightly-coupled error-state navigation Kalman filter is

$$\mathbf{x} = \left[\delta\alpha, \delta\beta, \delta\gamma, \delta v_e, \delta v_n, \delta v_u, \delta\lambda, \delta\varphi, \delta h, \epsilon_x, \epsilon_y, \epsilon_z, \nabla_x, \nabla_y, \nabla_z, \Delta c\delta t_r, \Delta c\delta \dot{t}_r, \delta T_{zpd}, \delta\lambda N_1 \cdots \delta\lambda N_n\right] \tag{5.20}$$

where $\delta\alpha, \delta\beta, \delta\gamma$ are attitude errors, $\delta v_e, \delta v_n, \delta v_u$ are velocity errors expressed in ENU navigation frame, $\delta\lambda, \delta\varphi, \delta h$ are position errors expressed in longitude, latitude and height, $\epsilon_x, \epsilon_y, \epsilon_z$ are gyro biases, $\nabla_x, \nabla_y, \nabla_z$ are accelerometer biases, $\Delta c\delta t_r, \Delta c\delta \dot{t}_r$ are receiver clock offset and drift errors, δT_{zpd} represents the tropospheric zenith path delay error, and $\delta\lambda N_1 \cdots \delta\lambda N_n$ are ambiguity errors expressed in meters. Ambiguities are estimated as float values in the system.

As shown in equation (5.20), both IMU and GPS states are expressed as errors, defined as the difference between the true and estimated navigation states. So after each Kalman filter measurement update, both GPS and IMU navigation updates should be executed to correct the navigation states by the estimated errors. IMU related error states will be compensated through inertial navigation mechanization, and GPS error states will be accumulated to correct GPS related terms like ambiguities. The IMU state transition function and model have been shown in Chapter 2. The GPS related transition function and error model can be deduced as below.

5.2.2 GPS error state transition function

GPS error states include additional states such as zenith path delay and ambiguity errors, compared with a conventional GPS/IMU tightly-coupled navigation system. The GPS error state transition matrix is,

$$\begin{bmatrix} \Delta c\delta t_{r,k} \\ \Delta c\delta \dot{t}_{r,k} \\ \delta T_{zpd,k} \\ \delta\lambda N_{1,k} \\ \vdots \\ \delta\lambda N_{n,k} \end{bmatrix} = \begin{bmatrix} 1 & \Delta t & 0 & 0 & \cdots & 0 \\ 0 & 1 & 0 & 0 & \cdots & 0 \\ 0 & 0 & 1 & 0 & \cdots & 0 \\ 0 & 0 & 0 & 1 & \cdots & 0 \\ \vdots & \vdots & \vdots & \vdots & \ddots & \vdots \\ 0 & 0 & 0 & 0 & \cdots & 1 \end{bmatrix} \begin{bmatrix} \Delta c\delta t_{r,k-1} \\ \Delta c\delta \dot{t}_{r,k-1} \\ \delta T_{zpd,k-1} \\ \delta\lambda N_{1,k-1} \\ \vdots \\ \delta\lambda N_{n,k-1} \end{bmatrix} \tag{5.21}$$

which is a linear function and can be implemented directly in the Kalman filter.

5.2.3 Measurement equation

The measurement equation difference between the TCP/IMU and the PR+Doppler GPS/IMU tightly-coupled navigation systems mainly lies in whether they augment the carrier phase as observations.

The observation equations of the pseudorange, carrier phase and Doppler from the GPS antenna to the m-th satellite are,

$$\begin{aligned} \rho_m &= r_m + c\delta t_r - c\delta t_{s,m} + I_m + T_m + \varepsilon_{\rho,m} \\ l_m &= r_m + c\delta t_r - c\delta t_{s,m} - I_m + T_m + \lambda N + \varepsilon_{l,m} \\ \dot{\rho}_m &= \dot{r}_m + c\delta \dot{t}_r - c\delta \dot{t}_{s,m} + \dot{I}_m + \dot{T}_m + \varepsilon_{\dot{\rho},m} \end{aligned} \tag{5.22}$$

The ionosphere-free combination is applied to eliminate the ionospheric delay. The dry part of the tropospheric delay is compensated by the Saastamoinen model. The zenith wet path delay is estimated as a state in the navigation Kalman Filter. The implemented mapping function is a global mapping function in this chapter.

After correcting the errors, including phase center offset, phase wind-up, etc., the estimated pseudorange and carrier phase observations between the satellite position and the estimated receiver position are

$$\begin{aligned} \rho_I &= \sqrt{(x_{s,m}-x_r)^2+(y_{s,m}-x_r)^2+(z_{s,m}-z_r)^2} + c\delta t_r + m_{wet}T_{zpd} \\ l_I &= \sqrt{(x_{s,m}-x_r)^2+(y_{s,m}-x_r)^2+(z_{s,m}-z_r)^2} + c\delta t_r + m_{wet}T_{zpd} + \lambda_{IF}N_{IF} \end{aligned} \tag{5.23}$$

where m_{wet} is the mapping function, and T_{zpd} is the tropospheric zenith path delay.

Equation (5.23) can be linearised by expanding to the first order Taylor term around a true receiver position $[x, y, z]$ as

$$\begin{aligned} \rho_I &= r_m + \frac{\partial \rho_I}{\partial x}(x_r - x) + \frac{\partial \rho_I}{\partial y}(y_r - y) + \frac{\partial \rho_I}{\partial z}(z_r - z) + c\delta t_r + m_{wet}T_{zpd} \\ l_I &= r_m + \frac{\partial l_I}{\partial x}(x_r - x) + \frac{\partial l_I}{\partial y}(y_r - y) + \frac{\partial l_I}{\partial z}(z_r - z) + c\delta t_r + m_{wet}T_{zpd} + \lambda_{IF}N_{IF} \end{aligned} \tag{5.24}$$

where the partial derivatives are

$$\begin{aligned} e_{x,m} &= \frac{\partial \rho_I}{\partial x} = \frac{\partial l_I}{\partial x} = -\frac{x_{s,m}-x_r}{\sqrt{(x_{s,m}-x_r)^2+(y_{s,m}-y_r)^2+(z_{s,m}-z_r)^2}} \\ e_{y,m} &= \frac{\partial \rho_I}{\partial y} = \frac{\partial l_I}{\partial y} = -\frac{y_{s,m}-y_r}{\sqrt{(x_{s,m}-x_r)^2+(y_{s,m}-y_r)^2+(z_{s,m}-z_r)^2}} \\ e_{z,m} &= \frac{\partial \rho_I}{\partial z} = \frac{\partial l_I}{\partial z} = -\frac{z_{s,m}-z_r}{\sqrt{(x_{s,m}-x_r)^2+(y_{s,m}-y_r)^2+(z_{s,m}-z_r)^2}} \end{aligned} \tag{5.25}$$

As introduced in Chapter 2, the range rate $\dot{\rho}_m$ from the GPS antenna to the m-th satellite is

$$\dot{\rho}_I = \dot{r}_m + g_{x,m}\delta x + g_{y,m}\delta y + g_{z,m}\delta z + e_{x,m}\delta \dot{x} + e_{y,m}\delta \dot{y} + e_{z,m}\delta \dot{z} + c\delta \dot{t}_r \tag{5.26}$$

The observation equation of a TCP/IMU tightly-coupled navigation system is

$$\begin{aligned} \rho_m - \rho_I &= \Delta c\delta t_r + m_{wet}\delta T_{zpd} - e_{x,m}\delta x - e_{y,m}\delta y - e_{z,m}\delta z \\ l_m - l_I &= \Delta c\delta t_r + m_{wet}\delta T_{zpd} + \delta\lambda N - e_{x,m}\delta x - e_{y,m}\delta y - e_{z,m}\delta z \\ \dot{\rho}_m - \dot{\rho}_I &= \Delta c\delta \dot{t}_r - g_{x,m}\delta x - g_{y,m}\delta y - g_{z,m}\delta z - e_{x,m}\delta \dot{x} - e_{y,m}\delta \dot{y} - e_{z,m}\delta \dot{z} \end{aligned} \tag{5.27}$$

The observation model can be further expressed as $\mathbf{z} = \mathbf{H}_{TCP}\mathbf{x} + \mathbf{v}$, where

$$\mathbf{z} = \begin{bmatrix} \delta\rho_{n\times 1} & \delta\mathbf{l}_{n\times 1} & \delta\dot{\rho}_{n\times 1} \end{bmatrix}^T \tag{5.28}$$

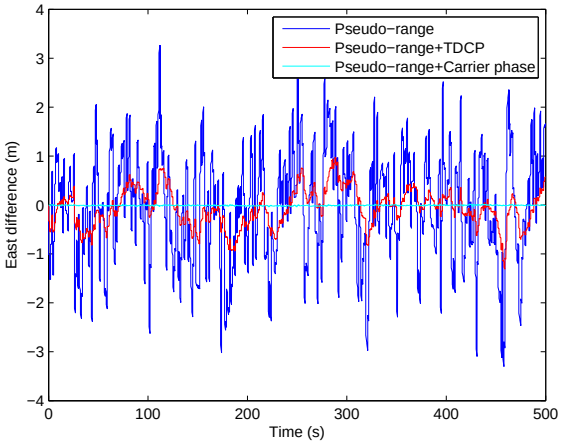

Figure 5.2: Eastern position error in the carrier phase simulation

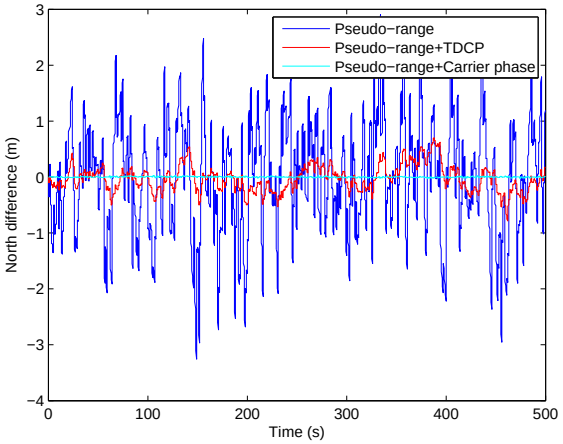

Figure 5.3: Northern position error in the carrier phase simulation

$$\mathbf{H}_{TCP} = \begin{bmatrix} \mathbf{0}_{n\times3} & \mathbf{0}_{n\times3} & -\overrightarrow{e_n}\cdot\mathbf{C}_e & \mathbf{0}_{n\times6} & \mathbf{1}_{n\times1} & \mathbf{0}_{n\times1} & \mathbf{m}_{wet,n\times1} & \mathbf{0}_{n\times n} \\ \mathbf{0}_{n\times3} & \mathbf{0}_{n\times3} & -\overrightarrow{e_n}\cdot\mathbf{C}_e & \mathbf{0}_{n\times6} & \mathbf{1}_{n\times1} & \mathbf{0}_{n\times1} & \mathbf{m}_{wet,n\times1} & \mathbf{1}_{n\times n} \\ \mathbf{0}_{n\times3} & -\overrightarrow{e_n}\cdot\mathbf{C}_n^e & -(\overrightarrow{e_n}\cdot\mathbf{C}_a + \overrightarrow{g_n}\cdot\mathbf{C}_e) & \mathbf{0}_{n\times6} & \mathbf{0}_{n\times1} & \mathbf{1}_{n\times1} & \mathbf{0}_{n\times1} & \mathbf{0}_{n\times n} \end{bmatrix} \tag{5.29}$$

Position is expressed in longitude, latitude and height in this work. The relevant elements in the measurement matrix should be transferred from the ECEF frame to the LLH frame, while velocity should be transferred from the ECEF frame to the navigation frame. The transition matrices related to the position and velocity transformations are defined in Chapter 2.

After deducing the measurement equations of a TDCP/IMU and a TCP/IMU tightly-coupled navigation system, simulation and experiment data will be applied to check the performance of these two methods.

5.3 Simulation

Only white noise is introduced to the geometric distance between the satellite and receiver positions to simulate GPS observations: pseudorange and carrier phase. All other errors like tropospheric delay, ionospheric delay and so on are assumed to be well corrected. The errors of GPS observations are white noise. Considering the real noise property of the pseudorange and carrier phase observation, white noises with 3 m and 1 cm standard deviation are added to the true range to separately simulate the pseudorange and carrier phase observations, which are subsequently implemented in the measurement matrix $\mathbf{R}$. To better show the carrier phase's effect in an integrated navigation system, the IMU is simulated as error free. The elements in $\mathbf{P}_0$ and $\mathbf{Q}$ are identical to the simulation in Chapter 3. The carrier phase ambiguities' standard deviation in $\mathbf{P}_0$ is set to be 1 cm, since the vehicle starts from an already known position and the other errors like tropospheric delay, receiver clock offset and so on are neglected. The carrier phase observations are simulated as cycle slip free. The performance comparison with the constant velocity simulation data among the pseudorange only, the pseudorange+TDCP and the pseudorange+carrier phase measurement update methods is shown in Figures 5.2, 5.3, 5.4, 5.5, 5.6, 5.7, 5.8 and Table 5.1.

From the position comparison in Figures 5.2, 5.3 and 5.4, it can be seen that the pseudorange+TDCP measurement update method has a higher positioning accuracy than the pseudorange only method (less noisy), while the implementation of the total carrier phase in tightly-coupled navigation systems has the highest positioning accuracy among all the three methods. The less noisy carrier phase observation is

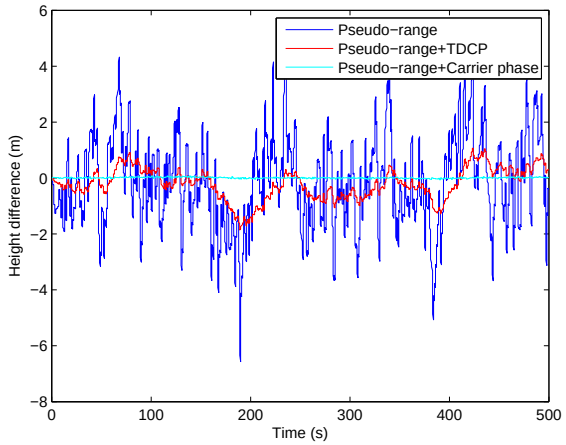

Figure 5.4: Height error in the carrier phase simulation

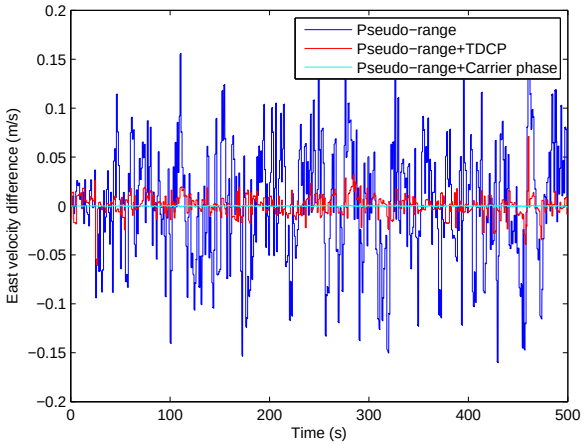

Figure 5.5: Eastern velocity error in the carrier phase simulation

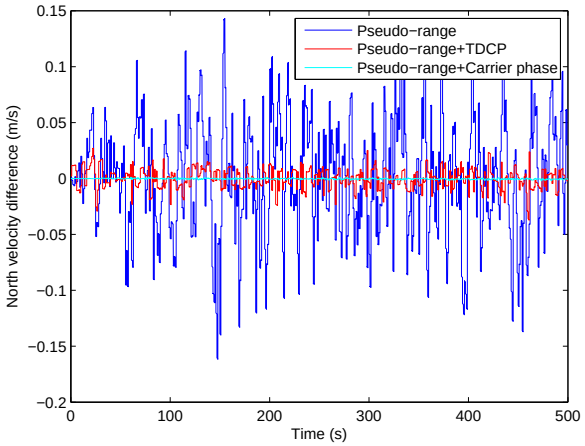

Figure 5.6: Northern velocity error in the carrier phase simulation

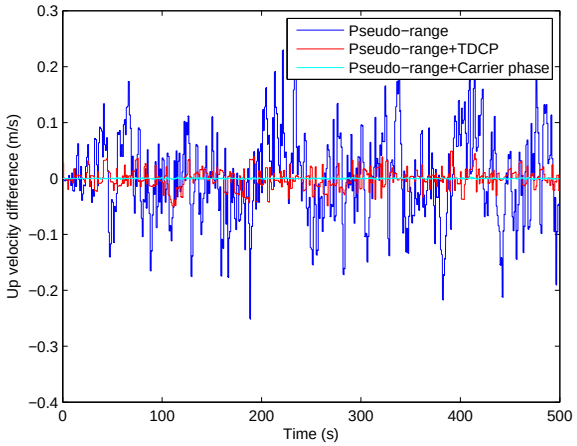

Figure 5.7: Up velocity error in the carrier phase simulation

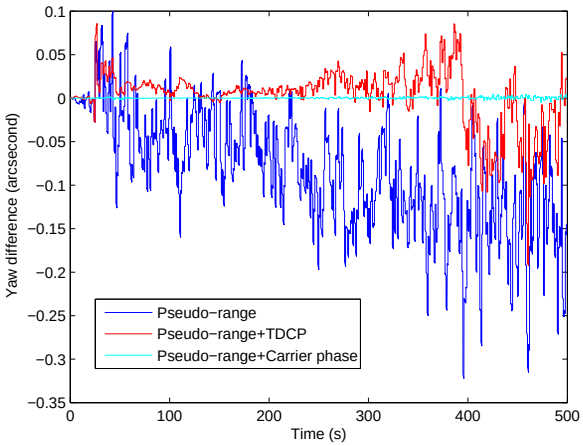

Figure 5.8: Yaw comparison in the carrier phase simulation

helpful to smooth the position estimation as shown in the comparison. From the velocity comparison in

Figures 5.5, 5.6 and 5.7, it can be seen that the TDCP observation can improve the velocity estimation to the cm/s level, which will consequently enhance the yaw estimation as shown in Figure 5.8. The velocity and yaw estimation accuracy of the total carrier phase method is also higher than the pseudorange only and pseudorange+TDCP methods. From the simulation and analysis, it can be concluded that the implementation of the carrier phase observation is beneficial to a GPS/IMU tightly-coupled navigation system no matter whether the carrier phase is applied as TDCP or TCP. The total carrier phase method achieves greater positioning accuracy enhancements than TDCP.

5.4 Experiment

The pseudorange, pseudorange+TDCP and pseudorange+carrier phase methods are implemented with the Griesheim airport experimental data to examine their position estimation difference. The phase DGPS is utilized as the position reference. The initial attitude is taken from a RLG IMU. $\mathbf{P}_0$ and $\mathbf{Q}$ of the three methods are set as the same as the experiment with good attitude initialisation in Chapter 3, except that the carrier phase ambiguities' standard deviation of $\mathbf{P}_0$ in the TCP based method is 1 m, because initial ambiguities are calculated with positioning by executing the PPP during the fine alignment, which is not yet convergent. The ambiguities' related parameters in the $\mathbf{Q}$ matrix are set to be 0.0001 m. The TDCP standard deviation is the same as the Doppler observation, because they have similar accuracies. For the TDCP based method, the relevant observations will be abandoned once cycle slips are detected. For the TCP based method, ambiguities will be reinitialised for estimation in the Kalman filter when cycle slips happen. The position comparison is shown in Figures 5.9, 5.10, 5.11 and Table 5.2. From the position comparison above, it can be seen that the positioning accuracy is improved compared with the pseudorange only and pseudorange+TDCP methods after applying the total carrier phase in an integrated navigation system. The position estimated by the pseudorange+TDCP method seems to be smoother and less noisier than the pseudorange only method, since the TDCP can improve the relative position and velocity estimation accuracy. However, these two pseudorange based methods achieve a similar absolute positioning accuracy level. The total carrier phase based system is not convergent during the initial period, but the positioning accuracy enhancement is still very obvious.

Table 5.1: Performance difference among PR, PR+TDCP and PR+TCP methods in simulation

Methods	Position RMS (m)			Velocity RMS (m/s)			Yaw RMS (arcsecond)
	East	North	Up	East	North	Up	
PR	1.132	1.207	1.667	0.060	0.053	0.078	0.108
PR+TDCP	0.386	0.237	0.564	0.011	0.009	0.017	0.033
PR+TCP	0.009	0.010	0.023	0.0004	0.0005	0.0009	0.001

Table 5.2: Position difference among PR, PR+TDCP and PR+TCP methods in experiment

Methods	East RMS (m)	North RMS (m)	Height RMS (m)
PR	0.55	1.81	2.40
PR+TDCP	0.54	1.59	2.36
PR+TCP	0.53	1.01	0.84

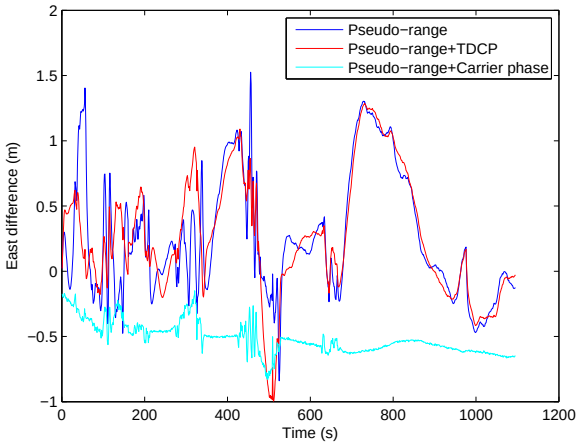

Figure 5.9: Eastern position comparison in the carrier phase experiment

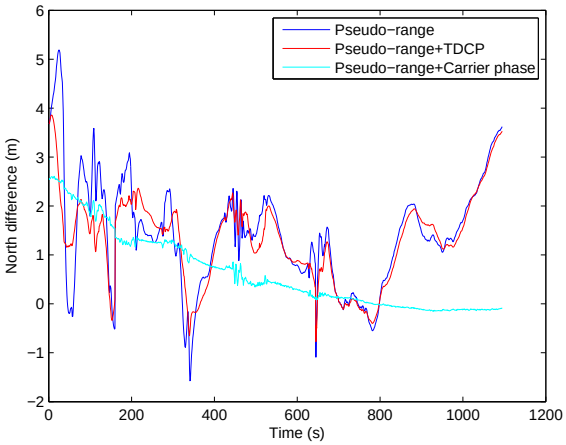

Figure 5.10: Northern position comparison in the carrier phase experiment

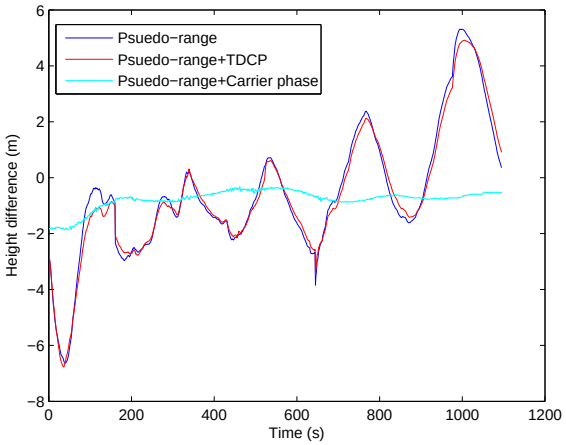

Figure 5.11: Height comparison in the carrier phase experiment

5.5 Conclusion

This chapter describes how to implement the GPS carrier phase (TDCP and TCP) in non-differential GPS/IMU tightly-coupled navigation systems. The TDCP is based on the property of carrier phase ambiguity remaining constant over a short period if there are no cycle slips. The TDCP can save the effort of fixing carrier phase ambiguities. The absolute positioning accuracy of the pseudorange+TDCP method is still determined by GPS pseudorange observations. The TCP method is based on the PPP technique. Carrier phase ambiguities are estimated as additional states in the navigation Kalman filter. The simulation and experiment results show that the application of the carrier phase observation can improve the position, velocity and attitude estimation accuracy compared with the pseudorange only method. The total carrier phase method shows a higher positioning accuracy than the TDCP method. However, according to the PPP working principle, the total carrier phase positioning method needs some time to become convergent. The initial positioning accuracy is not comparable to the final positioning accuracy, especially when the navigation time is short in kinematic cases. Nevertheless, realizing the benefits of carrier phase as a positioning accuracy improvement can still be expected in a TCP/IMU tightly-coupled navigation system. The TDCP based system can be applied to the applications when the high accuracy velocity is required, while the TCP based method is applicable to the high positioning accuracy applications.

6 Particle filter for TDCP/IMU tightly-coupled navigation

In this chapter, in order to improve the positioning accuracy of a KF-based PR+TDCP GPS/IMU tightly-coupled navigation system, a particle filter-based TDCP/IMU tightly-coupled strategy is proposed. The integration strategy includes two parts. The first part is a conventional KF-based PR+Doppler GPS/IMU tightly-coupled navigation system. The second part is a particle filter with modified TDCP measurements. The modified TDCP measurement is defined as the carrier phase difference between current and reference GPS time epochs, which can limit position drift caused by conventional TDCP, which is defined as the carrier phase difference between two successive GPS epochs. The modified TDCP measurement is then utilized to weight the particles generated from the *a posteriori* estimation of a KF-based PR+Doppler tightly-coupled navigation system. The positioning accuracy in both static and kinematic experiments can be improved to the sub-meter level, if initialised with an accurate reference position.

6.1 Introduction and background

As introduced in Chapter 5, directly implementing the TDCP measurements in a GPS/IMU tightly-coupled navigation Kalman filter will cause position drift because of the accumulation of position errors from previous epochs. In order to bound the position drift caused by the TDCP, pseudorange observations are usually introduced for the absolute position estimation (Han and Wang, 2012). However, due to the Kalman filter's working principle, the larger pseudorange noise will affect the TDCP position estimation through its effects on the measurement covariance matrix and subsequently the Kalman gain. Pseudorange noise will be further introduced to the *a posteriori* state estimation and covariance matrix. So the use of the pseudorange+TDCP as a navigation Kalman filter's measurements can only achieve the SPP accuracy as shown in Chapter 5.

Conventional Kalman filter-based PR+TDCP/IMU tightly-coupled navigation systems have two drawbacks: The first is the ignoring of Doppler measurements. Like the TDCP, Doppler is commonly used to estimate the velocity in conventional PR+Doppler tightly-coupled navigation systems (Yi, 2007; Zhou, 2013). If Doppler is tracked from the GPS receiver phase lock loop, the velocity estimation accuracy via Doppler should be comparable with the TDCP and with a simpler implementation form (Xu, 2007). The other is the TDCP measurement matrix computation. The TDCP expression in Chapter 5 is related to the velocity error integration from the former to the current epochs involving several adding and multiplying operations. Calculating the velocity error integration in a measurement matrix is time-consuming and difficult as introduced in Wendel and Trommer (2004); Wendel et al. (2006a); Han and Wang (2012); Zhao et al. (2015).

In order to improve the TDCP effect on a tightly-coupled navigation system, several enhancing methods are developed. In Tang et al. (2007), a reduced Kalman filter is applied to a TDCP/IMU integrated navigation system and provides some computation efficiency improvements. In Han and Wang (2012), the researchers design a dual-rate Kalman filter where the pseudorange and TDCP measurements work in one Kalman filter with different updating rates to reduce the pseudorange but improve the TDCP effects for position estimation, showing a relatively higher positioning accuracy than the pseudorange only method. The dual-rate Kalman filter tries to isolate the pseudorange observation noise from the TDCP. The high relative positioning accuracy of the TDCP can be kept by applying this strategy. According to the definition of the TDCP, Ding (2008) proposes the delta position aiding method and designs a two-step calibration scheme with one Kalman filter working in the inner loop with the TDCP for the IMU calibration and the other Kalman filter in the outer loop with pseudorange for the position bounding. Despite applying a dual-rate, reduced Kalman filter or two-step calibration scheme, the reported pseudorange+TDCP based system can only achieve SPP accuracy.

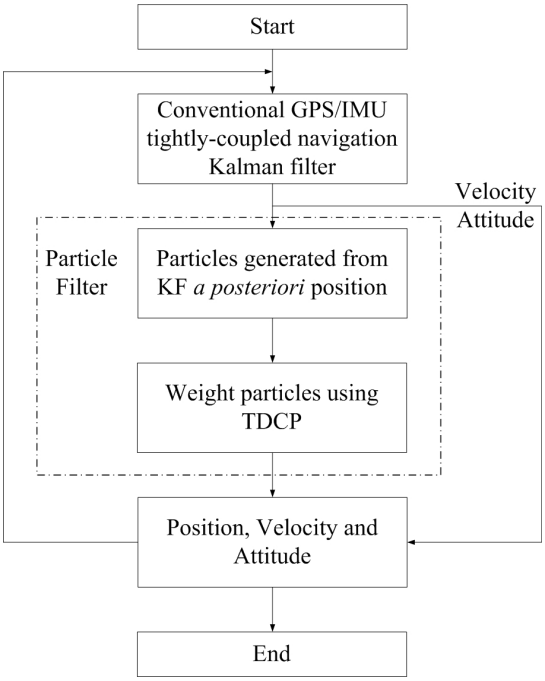

Figure 6.1: Flow chart of the particle filter based TDCP navigation strategy

In this chapter, the particle filter is implemented in TDCP/IMU tightly-coupled navigation systems to improve the positioning accuracy. The algorithm is divided into two parts as shown in Figure 6.1. In the first part, the GPS pseudorange and Doppler are implemented in a conventional GPS/IMU tightly-coupled navigation system as observations. The Kalman filter is used to estimate the position, velocity and attitude of the integrated navigation system as shown in Chapter 2. The velocity and attitude estimated in the conventional navigation Kalman filter are treated as the final velocity and attitude estimation and propagated to the next filtering loop, while the position is further updated with TDCP observations in the second part. In the second part (dashed box in Figure 6.1), several particles are generated around the *a posteriori* position estimated from the conventional navigation Kalman filter. A particle filter framework is then applied to weight these particles based on high-accuracy TDCP observations. Due to the better isolation between the TDCP and pseduo-range noises, after applying the integration strategy, the positioning accuracy can be improved greatly.

6.2 Modified TDCP observation

In a PF-based TDCP/IMU tightly-coupled navigation system, the TDCP measurement matrix is not necessary, which can save some efforts in solving the velocity error integration. However, an accurate TDCP measurement is still required to weight all the position particles. The more accurate the measurement, the better the positioning achievable accuracy is. In order to improve the effectiveness of the TDCP in weighting particles, two modifications are applied to the conventional TDCP measurement.

The receiver clock offset $c\delta t_r$ is estimated in the PR+Doppler GPS/IMU tightly-coupled navigation system, which appears to introduce some pseudorange noises to the TDCP observation if implemented as shown in equation (5.3). As a common error for all the observed satellites, the receiver clock offset can be eliminated by differencing between the carrier phase observations from the observed satellites and the reference satellite. The pseudorange noise can then be further isolated from the TDCP observation.

The application of the TDCP observation between two successive GPS epochs in weighting particles causes position drift, because position errors accumulate over time through this measurement. Differencing between two successive GPS epochs is helpful for the velocity estimation, at least the average

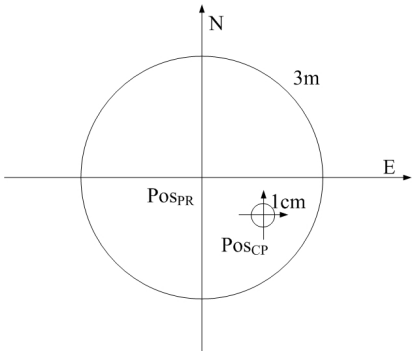

Figure 6.2: Sketch of the position uncertainty comparison between pseudorange and carrier phase positioning methods

velocity estimation. The velocity is estimated in a conventional Kalman filter with the Doppler observations in this proposed strategy. It is not necessary to apply the TDCP to estimate velocity again. Therefore, the TDCP measurement between two successive GPS epochs can be further modified as the TDCP between the current and the reference GPS epochs. If the reference epoch is initialised with a high accuracy position, the modified TDCP can help maintain the reference positioning accuracy. The cycle slip should be carefully detected in the navigation strategy. Once a cycle slip is detected, the current epoch with the new position estimation will be set as the new reference epoch. By avoiding introducing previous epochs' position errors to the current epoch, the position drift can be kept lower than conventional TDCP measurements. The modified TDCP observation can be expressed as

$$\begin{aligned} \Delta l_m &= (l_m(t_2) - l^{ref}(t_2)) - (l_m(t_1) - l^{ref}(t_1)) \\ &= \Delta r_m^{ref} + \Delta \varepsilon_{\delta,m} \end{aligned} \tag{6.1}$$

where t_1 represents the reference time epoch, t_2 is the current epoch and ref represents the reference satellite.

6.3 Particle filter

The particle filter is a sampling-based filtering method. It uses N independent samples from the *a priori* density to approximate the expectation of a system by sample average (Arulampalam et al., 2002). One of the most significant advantages of the particle filter is its capability in dealing with nonlinear and non-Gaussian problems, for example object-tracking, map-aided navigation, robot applications and so on (Arulampalam et al., 2002; Okuma et al., 2004; Hafner et al., 2014; Vlassis et al., 2002). However, the nonlinearity of tightly-coupled navigation systems is not so high, especially when the observation is always available and all the states become observable. The non-Gaussian property of pseudorange observations is only obvious in multi-path environments like building or forest surroundings. Besides this, most researchers implement Gaussian particle filter in GPS/IMU tightly-coupled navigation systems on the assumption that all the noises are Gaussian-distributed, due to the difficulty in obtaining the noise statistics of states and observations in real time. Therefore, the benefits of particle filtering methods in dealing with nonlinear and non-Gaussian problems cannot be fully shown in an integrated navigation system as shown in Chapter 3.

In this chapter, the sampling property of the particle filter is utilized. The idea is based on the position uncertainty from pseudorange being larger than carrier phase as illustrated in the sketch of Figure 6.2. So if some particles are generated around the position determined from pseudorange observations, one or several particles have the highest probability of being located close to the carrier phase position estimation. Once these particles are weighted according to the particle filter framework, the position

estimated by pseudorange will shift close to the carrier phase estimation. The positioning accuracy can be improved subsequently. There are two problems which need to be solved. The first is how to find or form a measurement with carrier phase accuracy. This can be accomplished by implementing the modified TDCP observation introduced in section 6.2. The second is how to generate and weight particles effectively to improve the positioning accuracy. The solution to the second problem is summarized below:

6.3.1 Particle generation

Based on the *a posteriori* position $\mathbf{p}_{k|k}$ estimated by the conventional PR+Doppler GPS/IMU tightly-coupled navigation Kalman filter, particles can be generated from the importance density distribution $N(0, \mathbf{P}_{k|k})$ as

$$\mathbf{X}_{k,i} = \mathbf{p}_{k|k} + \Delta\mathbf{p}_{k|k,i}, \Delta\mathbf{p}_{k|k,i} \sim N(0, \mathbf{P}_{k|k}) \tag{6.2}$$

where $i = 1, 2, ...N$, and N is the number of particles.

6.3.2 Weighting

Importance weights can be calculated as

$$w(\mathbf{X}_{k,i}) = \frac{p(\mathbf{z}_k|\mathbf{X}_{k,i}, \mathbf{R}_k) N(\mathbf{X}_{k,i}|\mathbf{p}_{k|k-1}, \mathbf{P}_{k|k-1})}{N(\mathbf{X}_{k,i}|\mathbf{p}_{k|k}, \mathbf{P}_{k|k})} \tag{6.3}$$

with

$$\begin{aligned}
p(\mathbf{z}_k|\mathbf{X}_{k,i}, \mathbf{R}_k) &= \frac{1}{\sqrt{(2\pi)^m \|\mathbf{R}_k\|}} \exp(-\frac{[\mathbf{z}_k - \mathbf{h}(\mathbf{X}_{k,i})]^T \mathbf{R}_k^{-1} [\mathbf{z}_k - \mathbf{h}(\mathbf{X}_{k,i})]}{2}) \\
N(\mathbf{X}_{k,i}^+|\mathbf{p}_{k|k-1}, \mathbf{P}_{k|k-1}) &= \frac{1}{\sqrt{(2\pi)^n \|\mathbf{P}_{k|k-1}\|}} \exp(-\frac{[\mathbf{X}_{k,i} - \mathbf{p}_{k|k-1}]^T (\mathbf{P}_{k|k-1})^{-1} [\mathbf{X}_{k,i} - \mathbf{p}_{k|k-1}]}{2}) \\
N(\mathbf{X}_{k,i}|\mathbf{p}_{k|k}, \mathbf{P}_{k|k}) &= \frac{1}{\sqrt{(2\pi)^n \|\mathbf{P}_{k|k}\|}} \exp(-\frac{[\mathbf{X}_{k,i} - \mathbf{p}_{k|k}]^T (\mathbf{P}_{k|k})^{-1} [\mathbf{X}_{k,i} - \mathbf{p}_{k|k}]}{2})
\end{aligned}$$

where m and n denote the dimensions of the observation and state vectors, $\mathbf{p}_{k|k-1}$ and $\mathbf{p}_{k|k}$ are the *a priori* and *a posteriori* positions estimated by the conventional GPS/IMU tightly-coupled navigation Kalman filter with the covariances $\mathbf{P}_{k|k-1}$ and $\mathbf{P}_{k|k}$. $\mathbf{z}_k$ is the modified TDCP with the covariance matrix $\mathbf{R}_k$ as shown in (6.1), while $\mathbf{h}(\mathbf{X}_{k,i})$ is the estimated TDCP with the position estimation at t_1 and the particles' position at t_2 expressed as (6.4). $p(\mathbf{z}_k|\mathbf{X}_{k,i}, \mathbf{R}_k)$ is the likelihood density function. Unlike the CPF in Chapter 3, the PF measurement is modified TDCP. The pseudorange and Doppler observations will not be used twice. $N(\mathbf{X}_{k,i}^+|\mathbf{p}_{k|k-1}, \mathbf{P}_{k|k-1})$ represents the *a priori* density function and $N(\mathbf{X}_{k,i}|\mathbf{p}_{k|k}, \mathbf{P}_{k|k})$ is the importance density function.

$$\begin{aligned}
\mathbf{h}(\mathbf{X}_{k,i}) = (&\sqrt{(x_{s,m}(t_2) - x_{k,i})^2 + (y_{s,m}(t_2) - y_{k,i})^2 + (z_{s,m}(t_2) - z_{k,i})^2} \\
&- \sqrt{(x_s^{ref}(t_2) - x_{k,i})^2 + (y_s^{ref}(t_2) - y_{k,i})^2 + (z_s^{ref}(t_2) - z_{k,i})^2}) \\
&- (\sqrt{(x_{s,m}(t_1) - x(t_1))^2 + (y_{s,m}(t_1) - y(t_1))^2 + (z_{s,m}(t_1) - z(t_1))^2} \\
&- \sqrt{(x_s^{ref}(t_1) - x(t_1))^2 + (y_s^{ref}(t_1) - y(t_1))^2 + (z_s^{ref}(t_1) - z(t_1))^2})
\end{aligned} \tag{6.4}$$

where $\mathbf{X}_{k,i}$ is a vector expressed in ECEF frame as $[x_{k,i}, y_{k,i}, z_{k,i}]^T$. In equation (6.4), the first term is the distance between the m-th satellite and the i-th position particle at time epoch t_2. The second term is the

distance between the reference satellite and the KF *a posteriori* position at time epoch t_2. The difference between the first and second terms eliminates the receiver clock offset at time epoch t_2. The third term is the distance between the m-th satellite and the KF *a posteriori* position at the reference time epoch t_1. The fourth term is the distance between the reference satellite and the KF *a posteriori* position at the reference time epoch t_1. The difference between the third and fourth terms eliminates the receiver clock offset at the reference time epoch t_1. As a nonlinear filtering method, there is no need in deriving Jacobian matrix for the particle filter applications.

The importance weights should be normalized as

$$w'(\mathbf{X}_{k,i}) = \frac{w(\mathbf{X}_{k,i})}{\sum_{i=1}^{N} w(\mathbf{X}_{k,i})} \tag{6.5}$$

6.3.3 Estimation

The *a posteriori* mean and covariance matrix can be computed as

$$\begin{aligned} \mathbf{p}_{k|k}^{+} &= \sum_{i=1}^{N} w'(\mathbf{X}_{k,i})\mathbf{X}_{k,i} \\ \mathbf{P}_{k|k}^{+} &= \sum_{i=1}^{N} w'(\mathbf{X}_{k,i})[\mathbf{X}_{k,i} - \mathbf{p}_{k|k}][\mathbf{X}_{k,i} - \mathbf{p}_{k|k}]^T \end{aligned} \tag{6.6}$$

The estimated position and its related covariance matrix will replace the position and covariance matrix estimated from the navigation Kalman filter and be fed back into the next filtering loop. Since the particles are regenerated in each filtering loop and will not be reused, there is no particles' impoverishment. The particles' resampling is not necessary, either.

6.4 Experiment

Some experiments are conducted to examine the performance of the PF-based TDCP/IMU tightly-coupled navigation strategy. A conventional KF-based PR+TDCP tightly-coupled navigation system is also implemented for a comparison. The starting position is initialized with the DGPS positioning result for the KF-based PR+TDCP integration strategy, which is also taken as the first reference position for the PF-based method. In order to better show the benefits of the PF-based method, the starting position is determined by the SPP technique. The parameters of the two systems are identical to those in Chapter 5 experiment, except that the standard deviation of the modified TDCP observation in the PF is 10 cm. A smaller standard deviation seems to cause the particles' impoverishment.

6.4.1 Particle propagation

In order to better show the benefits of the PF-based method in improving positioning accuracy, the particles' propagation after applying high accuracy TDCP measurements is shown in Figures 6.3 and 6.4. 1000 particles are sampled around the *a posteriori* position of the KF-based PR+Doppler GPS/IMU tightly-coupled navigation system. The red cycle is the position estimated in the PR+Doppler integrated navigation system. The blue points represent particles generated around the position estimated from the PR+Doppler tightly-coupled navigation system. The red cross is the true position from DGPS, while the green star is the position estimated after applying the PF-based method.

From Figure 6.3, it can be seen that the position estimated in the PR+Doppler GPS/IMU tightly-coupled navigation Kalman filter is far off from the true position. Therefore, only a few particles are located

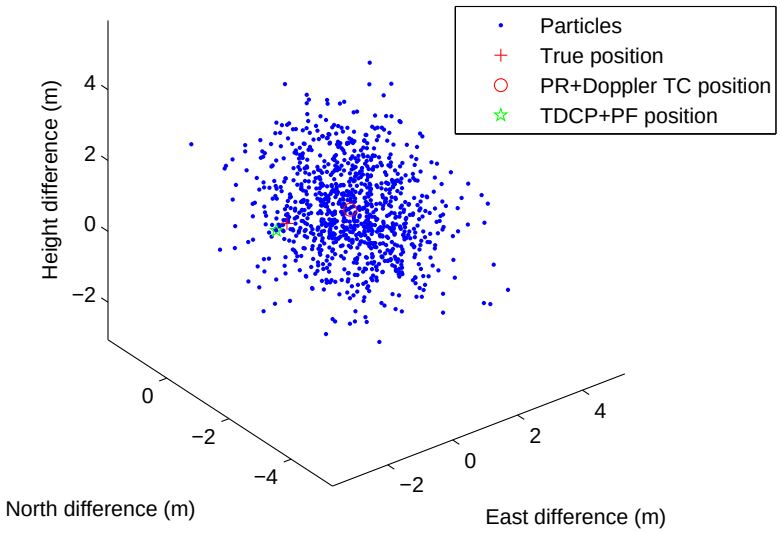

Figure 6.3: Particle propagation in initial stage

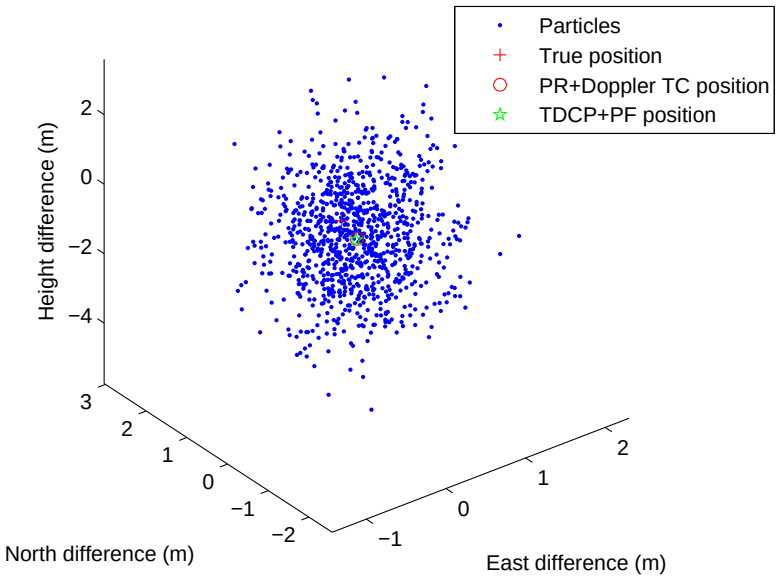

Figure 6.4: Particle propagation at the tenth GPS epoch

near the true position. However, when the high accuracy modified TDCP observations are applied, these particles are selected and highly weighted to improve the positioning accuracy. Figure 6.4 shows that the position estimated by the conventional PR+Doppler integrated navigation system is already close to the true position. Thus, most of the position particles generated around the estimated position are distributed around the true position. After applying the TDCP observation to propagate and weight particles, the position estimated by the particle filter is also near the true position. The high positioning accuracy of a conventional PR+Doppler GPS/IMU tightly-coupled navigation system benefits from the particle filter position correction. Actually, if the particle filter part is disabled, the positioning accuracy

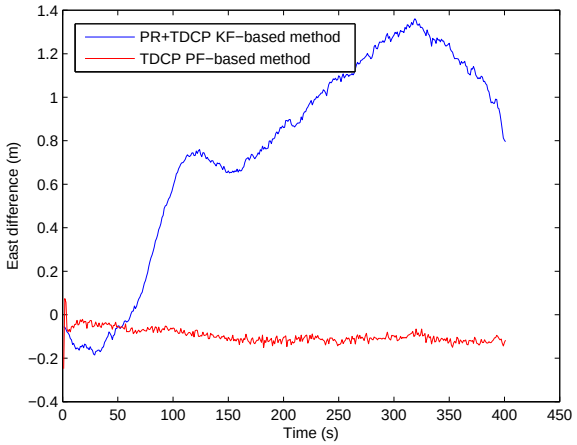

Figure 6.5: Eastern position error of the TDCP+PF method in static case

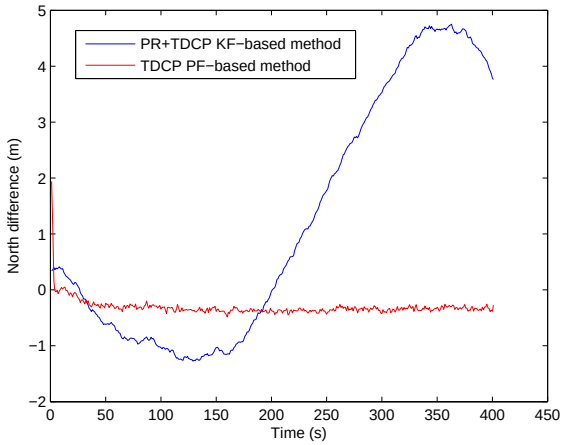

Figure 6.6: Northern position error of the TDCP+PF method in static case

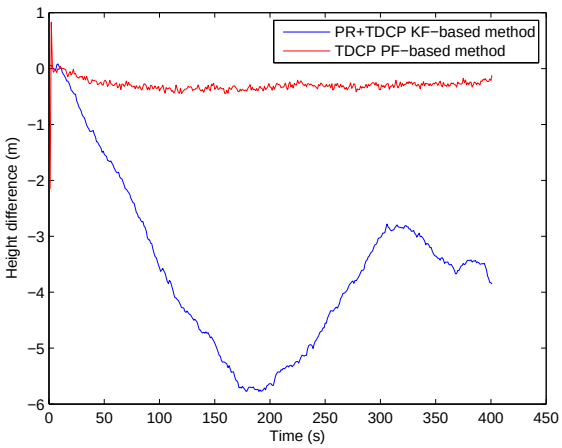

Figure 6.7: Height error of the TDCP+PF method in static case

Table 6.1: Position error of the TDCP+PF method in static case

Methods	East RMS (m)	North RMS (m)	Height RMS (m)	Horizontal RMS (m)	3D RMS (m)
pseudorange+TDCP	0.89	2.50	3.86	2.65	4.68
Particle filter+TDCP	0.10	0.35	0.33	0.36	0.49

will degrade again to SPP accuracy. From these two figures, it also can be seen that the particle filter-based method converges very fast, which allows it to be applied in real-time applications requiring high positioning accuracy without fixing ambiguities.

6.4.2 Static positioning accuracy

The performance comparison between the KF-based PR+TDCP/IMU and the PF-based TDCP/IMU tightly-coupled navigation systems in the static case is shown in Figures 6.5, 6.6, 6.7 and Table 6.1.

It can be seen that the PR+TDCP GPS/IMU tightly-coupled navigation system only achieves SPP accuracy in the static case, even if starting from an already known accurate position. The PF-based TDCP/IMU tightly-coupled navigation system makes use of the high accuracy TDCP observation to weight the par-

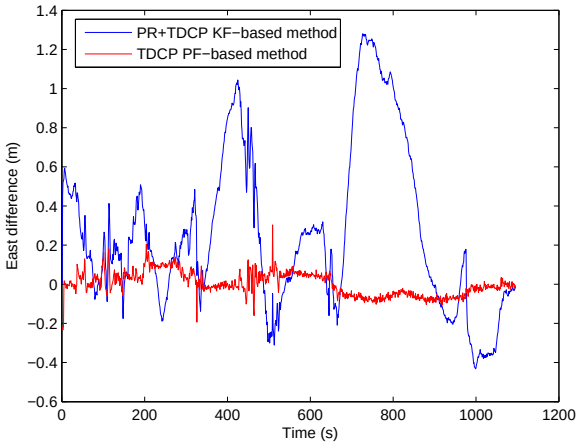

Figure 6.8: Eastern position error of the TDCP+PF method in kinematic case

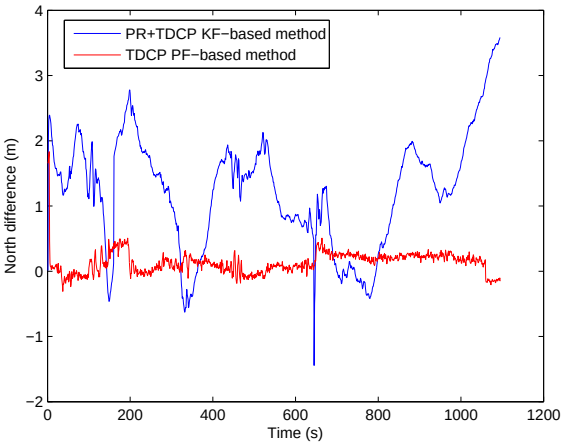

Figure 6.9: Northern position error of the TDCP+PF method in kinematic case

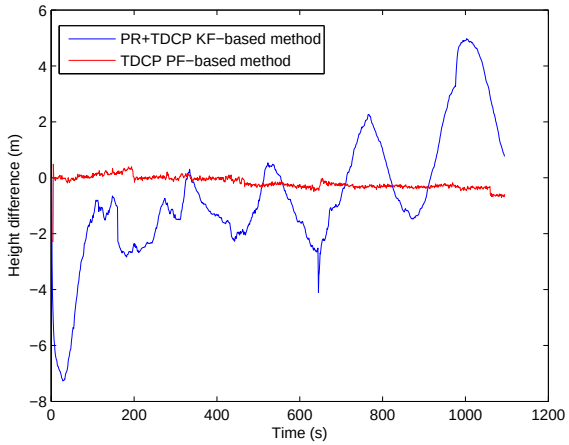

Figure 6.10: Height error of the TDCP+PF method in kinematic case

Table 6.2: Position error of the TDCP+PF method in kinematic case

Methods	East RMS (m)	North RMS (m)	Height RMS (m)	Horizontal RMS (m)	3D RMS (m)
pseudorange+TDCP	0.54	1.34	2.23	1.44	2.68
Particle filter+TDCP	0.06	0.22	0.30	0.22	0.37

ticles generated around the position estimation of the KF-based PR+Doppler GPS/IMU tightly-coupled navigation system. The positioning accuracy of the PF-based TDCP/IMU tightly-coupled navigation system can achieve the sub-meter level. From the static positioning results comparison, it can be seen that the PF-based method is helpful for position estimation.

6.4.3 Kinematic positioning accuracy

The trajectory of the kinematic experiment is shown in Figure 3.25. The navigation performance comparison between the PR+TDCP/IMU and the PF-based TDCP/IMU tightly-coupled navigation systems in kinematic case is shown in Figures 6.8, 6.9, 6.10 and Table 6.2.

It can be seen that the KF-based system can only achieve SPP accuracy in the kinematic case, while the PF-based system can achieve sub-meter positioning accuracy. The PF-based method can greatly enhance the positioning accuracy for the following reasons. The cascaded KF and PF working procedure isolates between the pseudorange and TDCP noises. Thus, the pseudorange noise is not introduced into the TDCP measurement. Using the KF *a posteriori* estimation to generate particles leads to most of the particles falling in the high likelihood area, which eases the curse of dimensionality. The modified TDCP measurement can bound the position error accumulation and is then used to weight position particles to achieve a higher positioning accuracy at the sub-meter level. However, this method's positioning accuracy is determined by the reference positioning accuracy since the modified TDCP is still a relative measurement between the current and the reference epochs. If the reference positioning accuracy is low, the final position result is smoothed with a higher relative positioning accuracy but with a lower absolute positioning accuracy.

6.5 Conclusion

In this chapter, a method of how to apply a particle filter to improve the positioning accuracy of a TDCP based GPS/IMU tightly-coupled navigation system is described. This integration strategy can be divided into two parts. The first part is a KF-based PR+Doppler GPS/IMU tightly-coupled navigation Kalman filter. The second part is a particle filter with the modified TDCP weighting position particles. This algorithm utilizes the high relative positioning accuracy property of TDCP measurements. If the initial reference position is taken from phase DGPS, the positioning accuracy of the tightly-coupled navigation system can reach sub-meter level as shown in the experimental results.

7 CKF+EKF hybrid filtering method for TCP/IMU tightly-coupled navigation

How to integrate total carrier phase observations with the IMU has been described in Chapter 5. The simulation and experiment results indicate that the positioning accuracy can be greatly improved after implementing GPS total carrier phase observations in the navigation Kalman filter. The total carrier phase introduces some additional states, such as ambiguities, to the system, which will increase the computational burden especially when a nonlinear filtering method is applied. In order to reduce the computational burden of the TCP/IMU tightly-coupled navigation system, one idea is to try to decrease the GPS time update rate. The GPS sampling rate (1Hz) is much lower than the IMU (100 Hz). Updating the GPS related states as frequently as the IMU in the Kalman filter time update part is not helpful for improving the navigation accuracy but can require a lot of computational time. The computational load can be expected to be reduced after applying multi-updating rates to different sensors in the integrated navigation system. The other idea to reduce the computational time is trying to use a linear filtering method to estimate the linear states in the state vector, mainly GPS related states, while a nonlinear filtering method estimates the nonlinear states like IMU related states. According to the estimation accuracy evaluation shown in Chapter 3, the implementation of nonlinear filtering methods in a linear system does not significantly improve the estimation accuracy because nonlinear filtering methods degrade into linear methods when implemented with a linear model. Both ideas can be accomplished through a dual estimation framework.

In a dual estimation framework, the state vector can be divided into two sub-vectors. These two sub-vectors are estimated separately in two parallel Kalman filters with identical measurements. One of these two sub-vectors is non-constant, and the other is constant. The non-constant sub-vector varies with time, usually referred as states, while the constant sub-vector stays as the same over time, usually referred as parameters. Based on dual estimation framework, it is possible to use different kinds of Kalman filters or different updating rates to estimate these two sub-vectors in parallel. As for TCP/IMU tightly-coupled navigation systems, the ambiguity always keeps as a constant if there is no cycle slip. The zenith path delay stays constant during a short period. Both of them can be treated as parameters. The others including IMU related states, receiver clock offset and drift change with time and can be defined as states. The state sub-vector sometimes suffers from nonlinear problems. For example, in TCP/IMU tightly-coupled navigation systems, the attitude related states are nonlinear as discussed in Chapter 3. In this chapter, based on the analysis above, a CKF+EKF hybrid filtering method will be developed by using the CKF to estimate the states (usually nonlinear) while using the EKF to estimate the parameters (linear) in a TCP/IMU tightly-coupled navigation system. The cross correlation aspect in a state covariance matrix will be estimated and propagated to improve the convergence speed. The performance of the hybrid filtering method will be examined through simulation and experiments.

7.1 Introduction and background

Dual estimation methods and related control approaches have been introduced and discussed in Nelson (2000); Marafioti (2010). In a dual estimation framework, the state vector can be divided into two sub-vectors (usually states and parameters). These two sub-vectors will be estimated separately in two parallel Kalman filters. Compared with joint estimation methods, conventional dual estimation methods do not estimate and propagate the cross correlation aspect of a covariance matrix, which yields some benefits in state estimation as shown in Nelson (2000); Wan and Nelson (1996); Wan et al. (1999); Wan and Nelson (1997).

The flow charts of the joint and dual estimation methods are shown in Figures 7.1 and 7.2, where $\mathbf{x}_k$, θ_k and $\mathbf{y}_k$ represent the state vector, parameter vector and mixed state/parameter vector.

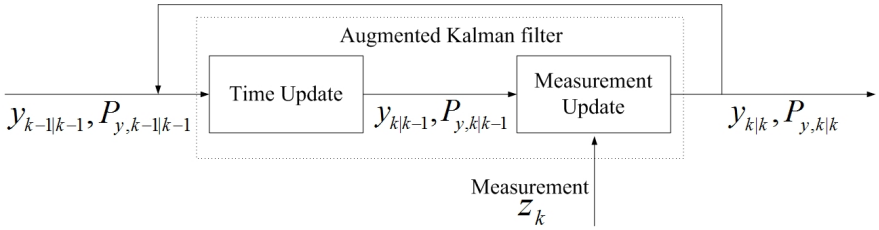

Figure 7.1: Flow chart of joint estimation method

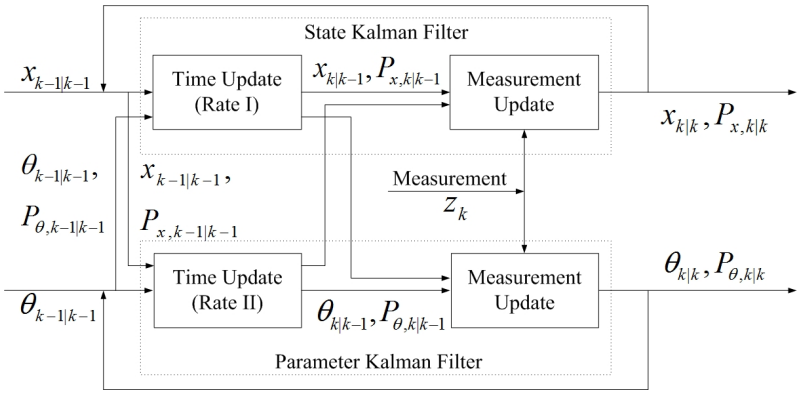

Figure 7.2: Flow chart of dual estimation method

From Figures 7.1 and 7.2, it can be seen that the states are augmented by the parameters and then estimated in the joint Kalman filter, while the state and parameter Kalman filters work in parallel in the dual estimation framework. The state and covariance matrix from the state Kalman filter are fed back to the parameter Kalman filter in the dual estimation framework and vice versa. In the dual estimation framework, it is also possible to use two different time update rates as shown in Figure 7.2.

According to the filter types implemented in the dual estimation framework, conventional dual estimation methods are roughly divided into two groups: dual EKF and dual UKF (Nelson, 2000; Van Der Merwe and Wan, 2001). The joint estimation method differs from the dual estimation method mainly in the cross correlation aspect of the covariance matrix with zero in the dual estimation methods and nonzero in the joint estimation methods (Wan and Nelson, 2001). The difference in the cross covariance matrix estimation will produce a state estimation difference. The application of an adaptive dual CKF to estimate vehicle states has been discussed in Chen (2012).

However, it is still difficult to state that dual estimation methods outperform the joint estimation methods, since they are more system specific (Nelson, 2000). For example, in respiratory system modelling (Saatci and Akan, 2009), autonomous terrain aided navigation system (Paul and Wan, 2005), damaging structures modelling (Azam, 2012) and hydrological models (Moradkhani et al., 2005), dual estimation methods are reported to provide satisfactory and even better results than joint estimation methods. Wankerl and Trommer (2014) discuss and evaluate the performance of a segmented filter in a GPS/IMU tightly-coupled navigation system, which is similar to the dual estimation method. In this work, the Kalman filter is segmented into two filters: position filter and dynamic filter including velocity, attitude and GPS related states, and navigation results can be improved after applying the segmentation, especially when the GPS signal is poor. Wendel et al. (2004) separate the correlated noise vector from the state vector of the standard Kalman filter in the rapid transfer alignment application. The computational load is expected to be reduced by applying the symmetry of the cross-correlation matrices.

In the dynamic modelling of neuronal responses in functional magnetic resonance imaging (fMRI) (Havlicek et al., 2011) and the estimation of biochemical dynamic pathways (Jia and Brownb, 2009), the researchers report a better performance of joint estimation methods. The performance difference

may be due to the correlation between parameters and states. A stronger correlation between states and parameters will enlarge the effect of parameter noise in the state estimation and vice versa. As mentioned in Nelson (2000), the higher sensitivity to inaccuracies in noise variances and model structure makes joint estimation methods the less robust alternative to dual estimation methods, while joint estimation methods are not seen to suffer from the convergence problem unlike dual estimation methods. Compared with the joint estimation method, the dual method is more flexible, because it allows different updating rates and Kalman filtering methods working simultaneously. In a TCP/IMU tightly-coupled navigation system, the direct implementation of the dual estimation method without the cross correlation part shows a lower convergence speed than the joint method. So the conventional dual estimation methods will be modified by estimating the cross covariance matrix simultaneously. The algorithm will be deduced in the following sections.

7.2 Modified dual estimation method

In order to deduce the dual estimation method by estimating the cross aspect of the covariance matrix, the working principle of the joint estimation method is investigated at first.

A system's state vector containing two sub-vectors (for better statement, states and parameters) is considered as

$$\mathbf{y}_k = \begin{bmatrix} \mathbf{x}_k \\ \theta_k \end{bmatrix} \tag{7.1}$$

where $\mathbf{x}_k$ represent states, and θ_k are parameters

In order to simplify the analysis, the EKF is taken as an example to analyse the effect of the parameters' estimation on the states' estimation. The system state space is,

$$\begin{aligned} \mathbf{y}_k &= \Phi \mathbf{y}_{k-1} + \mathbf{w}_{k-1} \\ \mathbf{z}_k &= \mathbf{H}\mathbf{y}_k + \mathbf{v}_k \end{aligned} \tag{7.2}$$

where

$$\Phi = \begin{bmatrix} \mathbf{A} & \mathbf{B} \\ \mathbf{0} & \mathbf{I} \end{bmatrix}, \mathbf{H} = \begin{bmatrix} \mathbf{C} & \mathbf{D} \end{bmatrix}, \mathbf{Q} = \begin{bmatrix} \mathbf{Q}_\mathbf{x} & \mathbf{0} \\ \mathbf{0} & \mathbf{Q}_\theta \end{bmatrix}$$

and the measurement covariance matrix is $\mathbf{R}_k$.

i) Measurement update

The following part will investigate how the parameters affect the states' estimation in the EKF measurement update part. Like the augmentation of the state transition matrix Φ and the measurement matrix $\mathbf{H}$, the Kalman gain and state covariance matrix can be written into block structures (Ljung, 1979, 1977)

$$\mathbf{K} = \begin{bmatrix} \mathbf{K}_\mathbf{x} \\ \mathbf{K}_\theta \end{bmatrix}, \mathbf{P}_{k|k-1} = \begin{bmatrix} \mathbf{P}_{\mathbf{xx},k|k-1} & \mathbf{P}_{\mathbf{x}\theta,k|k-1} \\ \mathbf{P}^T_{\mathbf{x}\theta,k|k-1} & \mathbf{P}_{\theta\theta,k|k-1} \end{bmatrix} \tag{7.3}$$

where $\mathbf{K}_\mathbf{x}$ and $\mathbf{K}_\theta$ are the states' and parameters' Kalman gain. $\mathbf{P}_{\mathbf{xx}}$ and $\mathbf{P}_{\theta\theta}$ represent the state and parameter covariance matrices. $\mathbf{P}_{\mathbf{x}\theta}$ is the cross correlation part in the covariance matrix.

The *a posteriori* states and parameters are calculated as,

$$\begin{aligned}\mathbf{x}_{k|k} &= \mathbf{A}\mathbf{x}_{k|k-1} + \mathbf{B}\theta_{k|k-1} + \mathbf{K}_{\mathbf{x}}(\mathbf{z}_k - \mathbf{H}\mathbf{y}_k)\\ \theta_{k|k} &= \theta_{k|k-1} + \mathbf{K}_{\theta}(\mathbf{z}_k - \mathbf{H}\mathbf{y}_k)\end{aligned} \tag{7.4}$$

The Kalman gain is

$$\begin{aligned}\mathbf{K}_{\mathbf{x}} &= (\mathbf{A}\mathbf{P}_{\mathbf{xx},k|k-1}\mathbf{C}^T + \mathbf{B}\mathbf{P}^T_{\mathbf{x}\theta,k|k-1}\mathbf{C}^T + \mathbf{A}\mathbf{P}^T_{\mathbf{x}\theta,k|k-1}\mathbf{D}^T + \mathbf{B}\mathbf{P}_{\mathbf{x}\theta,k|k-1}\mathbf{D}^T)\mathbf{S}^{-1}\\ \mathbf{K}_{\theta} &= (\mathbf{P}^T_{\mathbf{x}\theta,k|k-1}\mathbf{C}^T + \mathbf{P}^T_{\theta\theta,k|k-1}\mathbf{D}^T)\mathbf{S}^{-1}\end{aligned} \tag{7.5}$$

where

$$\mathbf{S} = \mathbf{C}\mathbf{P}_{\mathbf{xx},k|k-1}\mathbf{C}^T + \mathbf{C}\mathbf{P}_{\mathbf{x}\theta,k|k-1}\mathbf{D}^T + \mathbf{D}\mathbf{P}^T_{\mathbf{x}\theta,k|k-1}\mathbf{C}^T + \mathbf{D}\mathbf{P}_{\theta\theta,k|k-1}\mathbf{D}^T + \mathbf{R}_k \tag{7.6}$$

From equations (7.5) and (7.6), it can be found that the cross correlation part $\mathbf{P}_{\mathbf{x}\theta,k|k-1}$ affects the calculation of the state Kalman gain.

The *a posteriori* covariance matrices are

$$\begin{aligned}\mathbf{P}_{\mathbf{xx},k|k} &= \mathbf{A}\mathbf{P}_{\mathbf{xx},k|k-1}\mathbf{A}^T + \mathbf{A}\mathbf{P}_{\mathbf{x}\theta,k|k-1}\mathbf{B}^T + \mathbf{B}\mathbf{P}^T_{\mathbf{x}\theta,k|k-1}\mathbf{A}^T + \mathbf{B}\mathbf{P}_{\theta\theta,k|k-1}\mathbf{B}^T - \mathbf{K}_x\mathbf{S}\mathbf{K}_x^T + \mathbf{Q}_{\mathbf{x}}\\ \mathbf{P}_{\mathbf{x}\theta,k|k} &= \mathbf{A}\mathbf{P}_{\mathbf{x}\theta,k|k-1} + \mathbf{B}\mathbf{P}_{\theta\theta,k|k-1} - \mathbf{K}_x\mathbf{S}\mathbf{K}_{\theta}^T + \mathbf{Q}_{\mathbf{x}}\\ \mathbf{P}_{\theta\theta,k|k} &= \mathbf{P}_{\theta\theta,k|k-1} - \mathbf{K}_{\theta}\mathbf{S}\mathbf{K}_{\theta}^T + \mathbf{Q}_{\theta}\end{aligned} \tag{7.7}$$

After substituting (7.6) into $\mathbf{P}_{\mathbf{x}\theta,k|k}$ in equation (7.7), $\mathbf{P}_{\mathbf{x}\theta,k|k}$ can be rewritten as

$$\mathbf{P}_{\mathbf{x}\theta,k|k} = (\mathbf{A} - \mathbf{K}_x\mathbf{C})\mathbf{P}_{\mathbf{x}\theta,k|k-1} + (\mathbf{B} - \mathbf{K}_x\mathbf{D})\mathbf{P}_{\theta\theta,k|k-1} \tag{7.8}$$

Equation (7.8) indicates that $\mathbf{P}_{\mathbf{x}\theta,k|k-1}$ is mainly determined by the parameters' covariance matrix $\mathbf{P}_{\theta\theta,k|k-1}$.

The cross covariance matrix of the conventional dual estimation method is a zero matrix. The *a posteriori* state and covariance matrix of the conventional method can be deduced simply by setting the cross covariance matrices $\mathbf{P}_{\mathbf{x}\theta,k|k-1}$ and $\mathbf{P}_{\mathbf{x}\theta,k|k}$ to be zero as shown below.

$$\begin{aligned}\mathbf{K}_x &= \mathbf{A}\mathbf{P}_{\mathbf{xx},k|k-1}\mathbf{C}^T\mathbf{S}^{-1}\\ \mathbf{K}_{\theta} &= \mathbf{P}_{\theta\theta,k|k-1}\mathbf{D}^T\mathbf{S}^{-1}\end{aligned} \tag{7.9}$$

where

$$\mathbf{S} = \mathbf{C}\mathbf{P}_{\mathbf{xx},k|k-1}\mathbf{C}^T + \mathbf{D}\mathbf{P}_{\theta\theta,k|k-1}\mathbf{D}^T + \mathbf{R}_k \tag{7.10}$$

In this case, the *a posteriori* covariance matrix is

$$\begin{aligned}\mathbf{P}_{\mathbf{xx},k|k} &= \mathbf{A}\mathbf{P}_{\mathbf{xx},k|k-1}\mathbf{A}^T + \mathbf{B}\mathbf{P}_{\theta\theta,k|k-1}\mathbf{B}^T - \mathbf{K}_x\mathbf{S}\mathbf{K}_x^T + \mathbf{Q}_{\mathbf{x}}\\ \mathbf{P}_{\theta\theta,k|k} &= \mathbf{P}_{\theta\theta,k|k-1} - \mathbf{K}_{\theta}\mathbf{S}\mathbf{K}_{\theta}^T + \mathbf{Q}_{\theta}\end{aligned} \tag{7.11}$$

From equations (7.9) and (7.11), it can be found that the effect of the parameters on the states' estimation in the conventional dual estimation method is less than in the joint method, since the cross correlation part is neglected. The parameter covariance matrix $\mathbf{P}_{\theta\theta,k|k-1}$ in $\mathbf{S}$ and $\mathbf{P}_{\mathbf{xx},k|k}$ can be understood as follows: When estimating states, parameters are assumed to be already known in the dual estimation framework. The parameter noise is introduced to the measurement and system noises resulting in $\mathbf{P}_{\theta\theta,k|k-1}$ related terms in equation (7.10). These $\mathbf{P}_{\theta\theta,k|k-1}$ related terms are necessary in the conventional dual estimation method, which not only contributes a more accurate noise model but also reflects the true system property.

The measurement update part of the modified dual estimation method is the same as the analysis in the *a posteriori* estimation of the joint estimation method as shown in equations (7.4), (7.5) and (7.7). The time update of the modified dual estimation algorithm with the cross covariance matrix estimation is organised as shown below.

ii) Time update

The predicted states and parameters are

$$\begin{aligned} \mathbf{x}_{k|k-1} &= \mathbf{A}\mathbf{x}_{k-1|k-1} + \mathbf{B}\theta_{k-1|k-1} \\ \theta_{k|k-1} &= \theta_{k-1|k-1} \end{aligned} \tag{7.12}$$

The predicted covariance matrices are computed as

$$\begin{aligned} \mathbf{P}_{\mathbf{xx},k|k-1} &= \mathbf{A}\mathbf{P}_{\mathbf{xx},k-1|k-1}\mathbf{A}^T + \mathbf{B}\mathbf{P}^T_{\mathbf{x}\theta,k-1|k-1}\mathbf{A}^T + \mathbf{A}\mathbf{P}_{\mathbf{x}\theta,k-1|k-1}\mathbf{B}^T + \mathbf{B}\mathbf{P}_{\theta\theta,k-1|k-1}\mathbf{B}^T + \mathbf{Q}_{\mathbf{x}} \\ \mathbf{P}_{\mathbf{x}\theta,k|k-1} &= \mathbf{A}\mathbf{P}_{\mathbf{x}\theta,k-1|k-1} + \mathbf{B}\mathbf{P}_{\theta\theta,k-1|k-1} \\ \mathbf{P}_{\theta\theta,k|k-1} &= \mathbf{P}_{\theta\theta,k-1|k-1} + \mathbf{Q}_{\theta} \end{aligned} \tag{7.13}$$

In the time update part, parameters and states can work with two different updating rates. For example, GPS time updates with the GPS sampling rate and IMU time updates with the IMU sampling rate. In this case, parameters (GPS carrier phase ambiguities and zenith path delay) do not need to be updated as frequently as states (mainly IMU related states), saving some computational time. In this chapter, the modified dual EKF estimation method refers to the EKF+EKF filtering method, which uses two EKFs in parallel with one EKF estimating states and the other EKF estimating parameters.

7.3 CKF+EKF hybrid filtering method

As mentioned, the state vector of a TCP/IMU tightly-coupled navigation system is a mixture of states and parameters. The states, especially the IMU related states, show high nonlinearity in cases of unobservable, large misalignment and GPS outage, while the parameters are usually linear. The CKF is a second order approximation to a nonlinear system. According to the CKF working principle, the larger the state vector is, the more Cubature points are required to propagate states and covariance matrix. Therefore, the direct implementation of the CKF in a TCP/IMU tightly-coupled navigation system greatly increases the computational load. The increase in the computational load does not improve the estimation accuracy very much for the linear states' estimation, since the CKF degrades into the EKF when implemented with a linear system as suggested in Chapter 3. Based on the dual estimation framework, the CKF+EKF hybrid filtering method is proposed by applying the CKF to estimate the nonlinear states and the EKF for the linear parameters in parallel. The CKF+EKF can maintain the benefits of the CKF in nonlinear states' estimation without increasing the computational load, creating a balance between the computational load and the estimation accuracy. The algorithm of the CKF+EKF hybrid filtering method is summarized below.

Considering a system with a mixed state/parameter vector and a linear observation equation, which is

$$\begin{cases} \mathbf{x}_k = \mathbf{f}(\mathbf{x}_{k-1}) + \mathbf{B}\theta_{k-1} + \mathbf{w}_{\mathbf{x},k-1} \\ \theta_k = \theta_{k-1} + \mathbf{w}_{\theta,k-1} \\ \mathbf{z}_k = \mathbf{C}\mathbf{x}_k + \mathbf{D}\theta_k + \mathbf{v}_k \end{cases} \tag{7.14}$$

where $\mathbf{x}_k$ is the state vector with the covariance matrix $\mathbf{P}_{\mathbf{xx},k}$ and nonlinear state transition function $\mathbf{f}$. θ_k is the parameter vector with the covariance matrix $\mathbf{P}_{\theta\theta,k}$, $\mathbf{w}$ and $\mathbf{v}$ are Gaussian white noise with the covariance matrices $\mathbf{Q}$ and $\mathbf{R}$. $\mathbf{A}$ is defined as the first order Taylor term of the nonlinear function $\mathbf{f}$, which will be used to predict and propagate the cross covariance matrix $\mathbf{P}_{\mathbf{x}\theta,k}$.

According to the modified dual EKF estimation framework, the CKF+EKF hybrid filtering method is deduced as shown below.

7.3.1 State estimation

The CKF, a second order approximation to a nonlinear system, is implemented in the hybrid filtering method to estimate nonlinear states. In the CKF time update part, $2n$ Cubature points are calculated as

$$\begin{aligned} \mathbf{S}_{k-1|k-1} &= SVD(\mathbf{P}_{\mathbf{xx},k-1|k-1}) \\ \chi_{k-1|k-1} &= \mathbf{S}_{k-1|k-1}\xi + \mathbf{x}_{k-1|k-1} \end{aligned} \tag{7.15}$$

where n is the dimensionality of the state vector, SVD is the singular value matrix decomposition method.

After applying a nonlinear state transition function to propagate the Cubature points, the predicted Cubature points are

$$\chi^*_{k|k-1} = \mathbf{f}(\chi_{k-1|k-1}) \tag{7.16}$$

According to the CKF algorithm, the predicted state and relevant covariance matrix are calculated as

$$\begin{aligned} \mathbf{x}_{k|k-1} &= \frac{1}{m}\sum_{i=1}^{m}\chi^*_{i,k|k-1} \\ \mathbf{P}_{\mathbf{xx},k|k-1} &= \frac{1}{m}\sum_{i=1}^{m}\chi^*_{i,k|k-1}\chi^{*T}_{i,k|k-1} - \mathbf{x}_{k|k-1}\mathbf{x}^T_{k|k-1} + \mathbf{B}\mathbf{P}^T_{\mathbf{x}\theta,k-1|k-1}\mathbf{A}^T + \mathbf{A}\mathbf{P}_{\mathbf{x}\theta,k-1|k-1}\mathbf{B}^T + \mathbf{B}\mathbf{P}_{\theta\theta,k-1|k-1}\mathbf{B}^T + \mathbf{Q}_{\mathbf{x}} \end{aligned} \tag{7.17}$$

In the state covariance matrix prediction of equation (7.17), the linear parameters' covariance matrix is included to enlarge the states' system noise covariance matrix $\mathbf{Q}_{\mathbf{x}}$, because when states are estimated, parameters are assumed as known and their noise covariance matrix affects the system noise of states through the cross covariance matrix and the state transition matrix. This covariance matrix expression in equation (7.17) is a more general case, while in a TCP/IMU tightly-coupled navigation system, the state transition matrix $\mathbf{B}$ is a zero matrix. Therefore, equation (7.17) can be further simplified as

$$\mathbf{P}_{\mathbf{xx},k|k-1} = \frac{1}{m}\sum_{i=1}^{m}\chi^*_{i,k|k-1}\chi^{*T}_{i,k|k-1} - \mathbf{x}_{k|k-1}\mathbf{x}^T_{k|k-1} + \mathbf{Q}_{\mathbf{x}} \tag{7.18}$$

In the measurement update part, the Cubature points are regenerated using the predicted $\mathbf{x}_{k|k-1}$ and $\mathbf{P}_{\mathbf{xx},k|k-1}$ as

$$\begin{aligned}\mathbf{S}_{k|k-1} &= SVD(\mathbf{P}_{\mathbf{xx},k|k-1}) \\ \chi_{k|k-1} &= \mathbf{S}_{k|k-1}\xi + \mathbf{x}_{k|k-1}\end{aligned} \tag{7.19}$$

The predicted observations calculated with the Cubature points are

$$\begin{aligned}\mathbf{Z}_{k|k-1} &= \mathbf{C}\chi_{k|k-1} \\ \mathbf{z}_{k|k-1} &= \frac{1}{m}\sum_{i=1}^{m}\mathbf{Z}_{i,k|k-1}\end{aligned} \tag{7.20}$$

When only states are estimated, parameters are assumed as already known. Therefore, the measurement equation can be revised as

$$\mathbf{z}_k - \mathbf{D}\theta_{k|k-1} = \mathbf{C}\mathbf{x}_{k|k-1} + \mathbf{v}_k \tag{7.21}$$

After modifying the measurement equation, the estimation error $\tilde{\theta}$ of $\theta_{k|k-1}$ is introduced to be measurement noise. For a white noise, the following correlation equations are valid.

$$\begin{aligned}E\{\mathbf{v}_k\tilde{\theta}^T\} &= 0 \\ E\{\tilde{\theta}\mathbf{v}_k^T\} &= 0\end{aligned} \tag{7.22}$$

The measurement covariance matrix of the new measurement equation (7.21) is

$$\begin{aligned}\mathbf{R}_{k,\mathbf{x}} &= E\{(\mathbf{D}\tilde{\theta} + \mathbf{v}_k) * (\mathbf{D}\tilde{\theta} + \mathbf{v}_k)^T\} \\ &= E\{\mathbf{D}\tilde{\theta}\tilde{\theta}^T\mathbf{D}^T\} + E\{\mathbf{v}_k\mathbf{v}_k^T\} \\ &= \mathbf{D}\mathbf{P}_{\theta\theta,k|k-1}\mathbf{D}^T + \mathbf{R}_k\end{aligned} \tag{7.23}$$

This modified measurement equation is important for the hybrid filtering method, which significantly influences the estimation accuracy and convergence speed. Comparing equation (7.6) with equation (7.23), it is easy to find that if the cross correlation $\mathbf{P}_{\mathbf{x}\theta}$ is a zero matrix, without considering the state covariance matrix $\mathbf{P}_{\mathbf{xx}}$, these two equations have a same expression, indicating that it is correct to introduce the already known states' noise into the system and the measurement covariance matrices.

According to equation (7.5), the state Kalman gain is calculated as

$$\begin{aligned}\mathbf{P}_{\mathbf{zz},k|k-1} &= \frac{1}{m}\sum_{i=1}^{m}\mathbf{Z}_{i,k|k-1}\mathbf{Z}_{i,k|k-1}^T - \mathbf{z}_{k|k-1}\mathbf{z}_{k|k-1}^T + \mathbf{R}_{k,\mathbf{x}} + \mathbf{C}\mathbf{P}_{\mathbf{x}\theta,k|k-1}\mathbf{D}^T + \mathbf{D}\mathbf{P}_{\mathbf{x}\theta,k|k-1}^T\mathbf{C}^T \\ \mathbf{P}_{\mathbf{xz},k|k-1} &= \frac{1}{m}\sum_{i=1}^{m}\chi_{i,k|k-1}\mathbf{Z}_{i,k|k-1}^T - \mathbf{x}_{k|k-1}\mathbf{z}_{k|k-1}^T + \mathbf{B}\mathbf{P}_{\mathbf{x}\theta,k|k-1}^T\mathbf{C}^T + \mathbf{A}\mathbf{P}_{\mathbf{x}\theta,k|k-1}^T\mathbf{D}^T + \mathbf{B}\mathbf{P}_{\mathbf{x}\theta,k|k-1}\mathbf{D}^T \\ \mathbf{K}_{\mathbf{x}} &= \mathbf{P}_{\mathbf{xz},k|k-1}\mathbf{P}_{\mathbf{zz},k|k-1}^{-1}\end{aligned} \tag{7.24}$$

The *a posteriori* state and covariance matrix are estimated as

$$\begin{aligned}\mathbf{x}_{k|k} &= \mathbf{x}_{k|k-1} + \mathbf{K}_{\mathbf{x}}(\mathbf{z}_k - \mathbf{D}\theta_{k|k-1} - \mathbf{z}_{k|k-1}) \\ \mathbf{P}_{\mathbf{xx},k|k} &= \mathbf{P}_{\mathbf{xx},k|k-1} - \mathbf{K}_{\mathbf{x}}\mathbf{P}_{zz,k|k-1}\mathbf{K}_{\mathbf{x}}^T\end{aligned} \tag{7.25}$$

7.3.2 Parameter estimation

The EKF is implemented to estimate the parameter sub-vector. The state sub-vector is assumed as already known. The parameters and covariance matrix predicted by the EKF are

$$\begin{aligned} \theta_{k|k-1} &= \mathbf{A}\mathbf{x}_{k-1|k-1} + \mathbf{B}\theta_{k-1|k-1} \\ \mathbf{P}_{\theta\theta,k|k-1} &= \mathbf{B}\mathbf{P}_{\theta\theta,k-1|k-1}\mathbf{B}^T + \mathbf{A}\mathbf{P}_{\mathbf{xx},k-1|k-1}\mathbf{A}^T + \mathbf{Q}_\theta \end{aligned} \tag{7.26}$$

The *a priori* states $\mathbf{x}_{k-1|k-1}$ and covariance matrix $\mathbf{P}_{\mathbf{xx},k-1|k-1}$ are utilized to predict parameters. The states' estimation error affects the prediction of parameters and the relevant covariance matrix as shown in equation (7.26). Like states, the parameters' measurement equation is revised as

$$\mathbf{z}_k - \mathbf{C}\mathbf{x}_{k|k-1} = \mathbf{D}\theta_{k|k-1} + \mathbf{v}_k \tag{7.27}$$

The measurement covariance matrix is calculated as

$$\begin{aligned} \mathbf{R}_{k,\theta} &= E\{(\mathbf{C}\tilde{\mathbf{x}}_{k|k-1} + \mathbf{v}_k) * (\mathbf{C}\tilde{\mathbf{x}}_{k|k-1} + \mathbf{v}_k)^T\} \\ &= E\{\mathbf{C}\tilde{\mathbf{x}}_{k|k-1}\tilde{\mathbf{x}}_{k|k-1}^T\mathbf{C}^T\} + E\{\mathbf{v}_k\mathbf{v}_k^T\} \\ &= \mathbf{C}\mathbf{P}_{\mathbf{xx},k|k-1}\mathbf{C}^T + \mathbf{R}_k \end{aligned} \tag{7.28}$$

The Kalman gain, parameters and covariance matrix in the measurement update are calculated as

$$\begin{aligned} \mathbf{S} &= \mathbf{D}\mathbf{P}_{\theta\theta,k|k-1}\mathbf{D}^T + \mathbf{C}\mathbf{P}_{\mathbf{x}\theta,k|k-1}\mathbf{D}^T + \mathbf{D}\mathbf{P}_{\mathbf{x}\theta,k|k-1}^T\mathbf{C}^T + \mathbf{R}_{k,\theta} \\ \mathbf{K}_\theta &= (\mathbf{P}_{\mathbf{x}\theta,k|k-1}^T\mathbf{C}^T + \mathbf{P}_{\theta\theta,k|k-1}\mathbf{D}^T)/\mathbf{S} \\ \theta_{k|k} &= \theta_{k|k-1} + \mathbf{K}_\theta(\mathbf{z}_k - \mathbf{C}\mathbf{x}_{k|k} - \mathbf{D}\theta_{k|k-1}) \\ \mathbf{P}_{\theta\theta,k|k} &= \mathbf{P}_{\theta\theta,k|k-1} - \mathbf{K}_\theta\mathbf{D}\mathbf{P}_{\theta\theta,k|k-1} \end{aligned} \tag{7.29}$$

where $\mathbf{C}\mathbf{P}_{\mathbf{xx},k|k-1}\mathbf{C}^T$ is the measurement covariance matrix introduced by states' estimation error.

7.3.3 Cross covariance matrix estimation

Predicting and updating the cross covariance matrix is relatively simpler than the states' and parameters' estimation. The cross covariance matrix in the CKF is computed as

$$\mathbf{P}_{\mathbf{x}\theta} = \frac{1}{m}\sum_{i=1}^{m}(\chi_i - \mathbf{x})(\Theta_i - \theta)^T \tag{7.30}$$

The calculation of the cross covariance matrix using Cubature points also introduces an additional computational load. To further improve the filtering method's efficiency, in the CKF+EKF hybrid filtering method, the EKF is used to propagate the cross covariance matrix, consequently resulting in a suboptimal estimation.

The prediction of the cross covariance matrix is

$$\mathbf{P}_{\mathbf{x}\theta,k|k-1} = \mathbf{A}\mathbf{P}_{\mathbf{x}\theta,k-1|k-1} + \mathbf{B}\mathbf{P}_{\theta\theta,k-1|k-1} \tag{7.31}$$

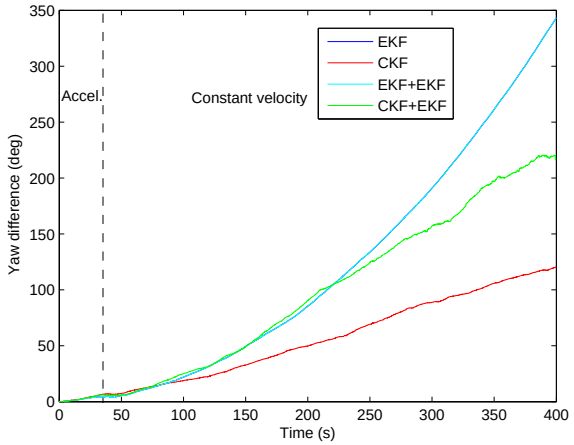

Figure 7.3: Yaw comparison of dual estimation methods in constant velocity simulation

The *a posteriori* cross covariance matrix is

$$\mathbf{P}_{\mathbf{x}\theta,k|k} = (\mathbf{A} - \mathbf{K}_x\mathbf{C})\mathbf{P}_{\mathbf{x}\theta,k|k-1} + (\mathbf{B} - \mathbf{K}_x\mathbf{D})\mathbf{P}_{\theta\theta,k|k-1} \tag{7.32}$$

From equations (7.31) and (7.32), it can be found that the cross covariance matrix is mainly related to the parameter covariance matrix in the model (7.14). The parameter covariance matrix $\mathbf{P}_{\theta\theta}$ affects the cross covariance matrix $\mathbf{P}_{\mathbf{x}\theta}$ and then affects the calculation of Kalman gain. Therefore, in a TCP/IMU tightly-coupled navigation system, the ignoring in the cross covariance matrix causes a smaller Kalman gain resulting in a slower convergence speed.

The CKF+EKF hybrid filtering method is a special case of the dual estimation methods, because it incorporates two different filtering methods for different states' estimation. From the hybrid filtering method, it can be seen that the dual estimation framework is much more flexible than the joint framework in that it allows multi-updating rates and different filtering methods for the estimation of different states, which not only can keep the estimation accuracy but also reduces the computational load. For example, according to the Cubature points generation, in a TCP/IMU tightly-coupled navigation system, $2 \times (17 + 1 + 8)$ Cubature points are needed to propagate states and the covariance matrix, assuming that 8 satellites are available by applying the joint CKF and each Cubature point should be propagated by the nonlinear state transition function once. In the hybrid filtering method, the number of Cubature points is 2×17. The extra Cubature points introduced by the linear states will not be used to propagate nonlinear states and the covariance matrix, meaning that the nonlinear state transition function is not executed as often as the joint CKF, which is helpful to reduce the computational burden.

7.4 Simulation

From the filtering performance comparison in Chapter 3, it has been shown that nonlinear filtering methods only show benefits when the nonlinearity of the system is high. For example, in non-accelerating cases when the yaw angle is totally unobservable, the CKF shows a slower yaw drift than the EKF. According to this property, to better compare and examine the performance differences among the EKF, CKF, EKF+EKF and CKF+EKF filtering methods, all four filtering methods are implemented with the constant velocity simulation data. The parameters are set identically to those in the constant velocity simulation in Chapter 3. The yaw angle comparison among the four methods is shown in Figure 7.3, which is the average of 20 filter runs' absolute error for each filtering method.

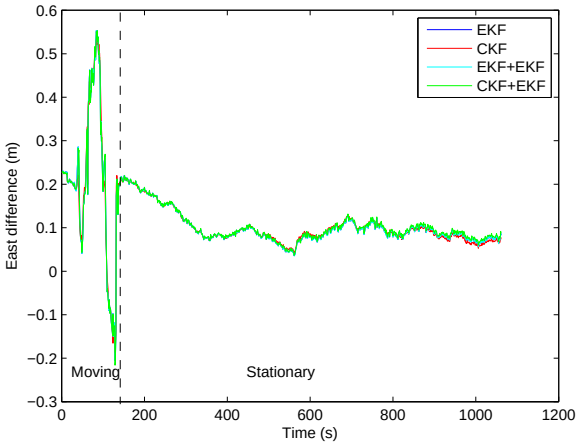

Figure 7.4: Eastern position error of dual estimation methods in stationary case

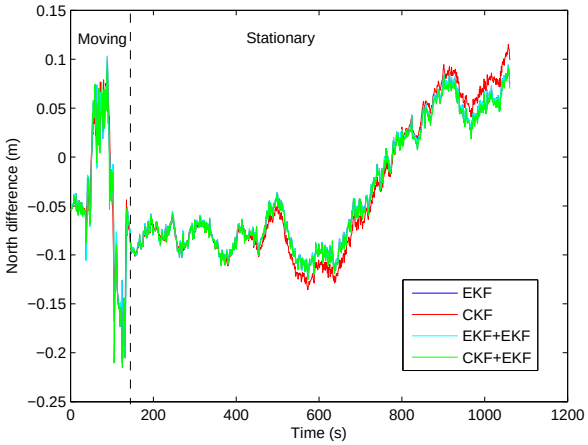

Figure 7.5: Northern position error of dual estimation methods in stationary case

From Figure 7.3, it can be seen that during a constant velocity period, the yaw estimation from the EKF based methods (EKF, EKF+EKF) drift much faster than the CKF based methods (CKF, CKF+EKF). In the accelerating stage, the four filtering methods show a similar performance because the acceleration renders the yaw angle observable. The nonlinearity of the system is accordingly reduced. In the constant velocity stage, the EKF+EKF has an identical performance to the EKF due to their being implemented with the same psi-angle expression, which yields invalid when the yaw angle error accumulates very quickly. The CKF+EKF can maintain the CKF's benefits in bounding the yaw angle drift better. But its yaw drift is larger than the CKF. When the computational load is considered, the CKF+EKF is superior to the CKF, since it needs less Cubature points to propagate the states and covariance matrix. So the CKF+EKF hybrid filtering method can balance computational load and estimation accuracy.

7.5 Experiments

In all the experiments, the EKF, CKF, EKF+EKF and CKF+EKF filtering methods are applied to a TCP/IMU tightly-coupled navigation system. A RLG IMU is used as the attitude reference, and the phase DGPS is the position reference. According to the filtering methods' comparison in Chapter 3, it is easy to find that the CKF outperforms the EKF, for example, in the unobservable case, large misalignment case and GPS outages. So the performance difference among the four filtering methods is only examined in these three cases.

7.5.1 Stationary case

In the stationary case, the yaw angle is totally unobservable. The observations have no benefits in the state estimation. The yaw error will accumulate very quickly in such a case, which causes the conventional psi-angle expression to become invalid and then introduces some nonlinearity to the tightly-coupled navigation system. And the CKF has a slower yaw drift than the EKF as shown in Chapter 3. To better show the performance difference among the four filtering methods in the stationary case, a good position and attitude initialisation is applied. The initial position is taken from the phase DGPS. The initial yaw angle is transferred from the RLG IMU. The initial ambiguities' standard deviation in $\mathbf{P}_0$ is set as 0.1 m due to the good position initialisation. The ambiguities' related parameters in $\mathbf{Q}$ are set to $1 \cdot 10^{-4}$ m to limit its change. The parameter setting helps maintaining initial positioning accuracy. The other parameters are the same as those in Chapter 5. The trajectory is shown in Figure 3.13. The position and yaw comparison are shown in Figures 7.4, 7.5, 7.6, 7.7 and Table 7.1.

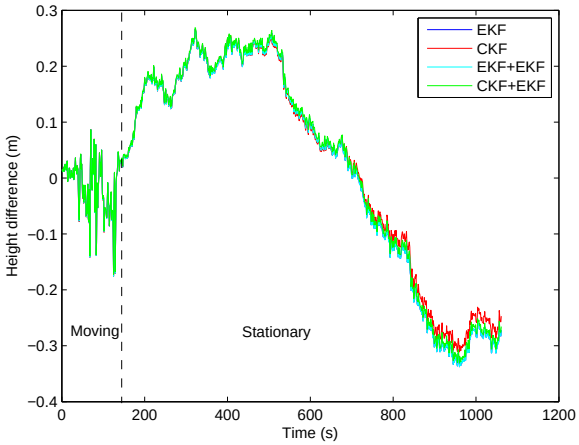

Figure 7.6: Height error of dual estimation methods in stationary case

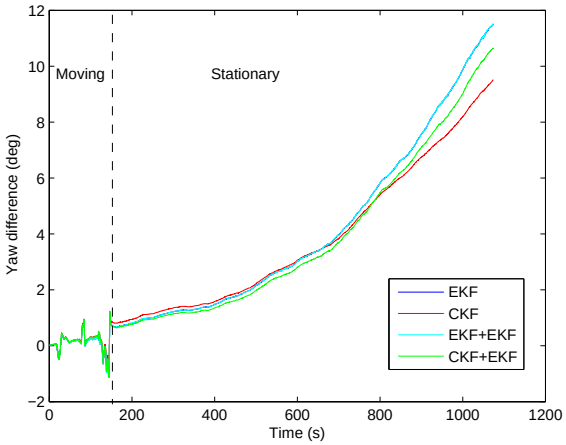

Figure 7.7: Yaw error of dual estimation methods in stationary case

Table 7.1: Position and attitude comparison of dual estimation methods in stationary case

Filtering methods	East RMS (m)	North RMS (m)	Height RMS (m)	Yaw RMS (deg)
EKF	0.142	0.074	0.184	4.886
CKF	0.142	0.081	0.176	4.330
EKF+EKF	0.142	0.074	0.184	4.887
CKF+EKF	0.143	0.075	0.183	4.540

From the position comparison as shown in Figures 7.4, 7.5 and 7.6, it can be seen that the positioning accuracy can reach the sub-meter level by applying the TCP in the integrated navigation system with a very accurate initial position. All four filtering methods show quite similar position estimation accuracy in the stationary case because position errors are always observable and can be determined directly from GPS observations. The CKF based methods (CKF and CKF+EKF) seem to have a relatively slower yaw drift than the EKF based methods as shown in Figure 7.7, due to the application of the nonlinear attitude error expression. Although it is difficult to get a very accurate initial position in a real application, it can be seen that using the carrier phase as observations in the Kalman filter can help to maintain initial positioning accuracy, which is impossible for a PR+Doppler tightly-coupled navigation system.

7.5.2 Large misalignment case

In the large misalignment case, a large initial yaw angle error renders the psi-angle expression implemented in the EKF invalid. As shown in Chapter 3, with the CKF, the nonlinear attitude error expression (3.33) can improve the convergence speed and the yaw estimation accuracy.

The trajectory is shown in Figure 3.25. The initial position is determined from the SPP method, whose positioning accuracy can only reach 3 m. Because of the high noise and bias of MEMS gyroscopes, if there are no other aiding sensors like magnetometers or GPS attitude systems, the initial yaw angle cannot be determined from MEMS gyroscope outputs during the fine alignment phase. The yaw angle calculated from the MEMS gyroscope outputs is arbitrary. The large misalignment problem occurs very easily in MEMS IMU applications, which can also be further used to examine the filtering methods' performance difference. The initial attitude standard deviations are set to 5 deg for roll and pitch, 17 deg for yaw

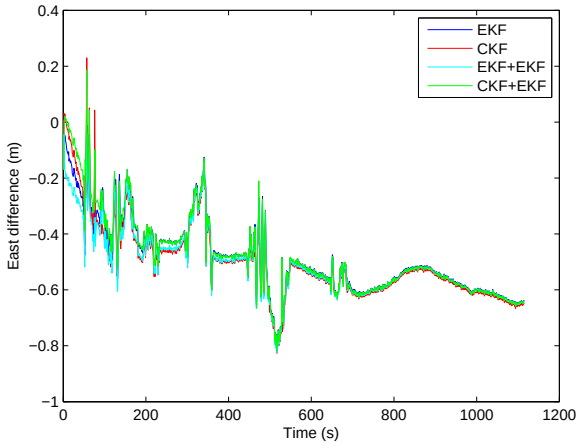

Figure 7.8: Eastern position error of dual estimation methods in large misalignment case

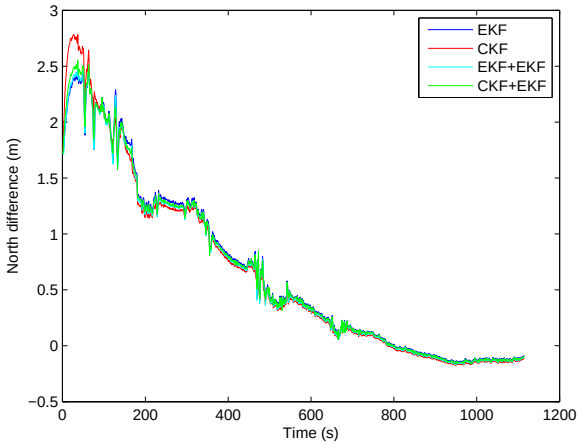

Figure 7.9: Northern position error of dual estimation methods in large misalignment case

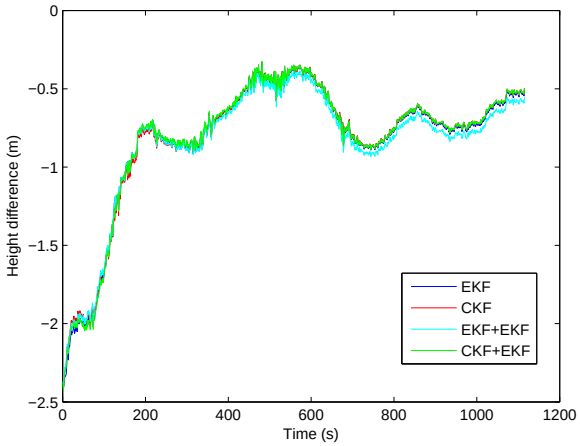

Figure 7.10: Height error of dual estimation methods in large misalignment case

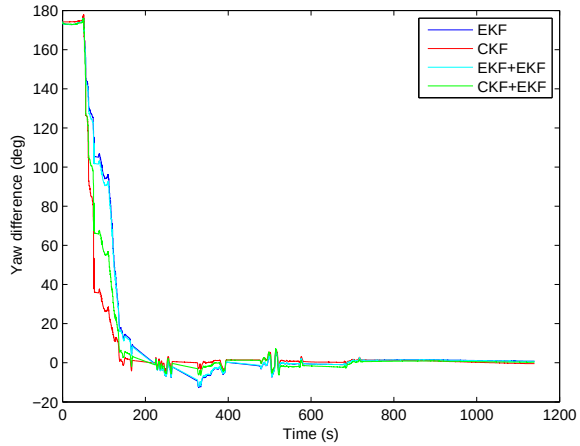

Figure 7.11: Yaw error of dual estimation methods in large misalignment case

as explained in Chapter 3. The other parameters are kept as same as the experiment in Chapter 5. The position and yaw comparisons are shown in Figures 7.8, 7.9, 7.10 and 7.11.

As presented in these figures, the four filtering methods (EKF, CKF, EKF+EKF, CKF+EKF) have similar positioning accuracy in eastern, northern and up directions. For the yaw angle estimation, due to the implementation of the nonlinear attitude expression, it can be seen that the CKF based methods have a higher estimation accuracy and faster convergence speed than the EKF based methods in the large misalignment case. The CKF also converges faster than the CKF+EKF filtering method. However, considering the computational load, dual estimation methods are superior to joint methods. For example, in the EKF+EKF filtering method, GPS related states do not need to be updated as frequently as IMU states, while in the CKF+EKF filtering method, linear GPS related states can be estimated using the EKF at a lower time updating rate and the number of Cubature points can also be reduced, indicating that the nonlinear state transition function does not need to be computed as frequently as the CKF. Thus, a decrease in the computational load can be expected with respect to the CKF. Due to the application of the carrier phase, the system positioning accuracy is much higher than the pseudorange based method, even though the carrier phase prolongs the convergence period.

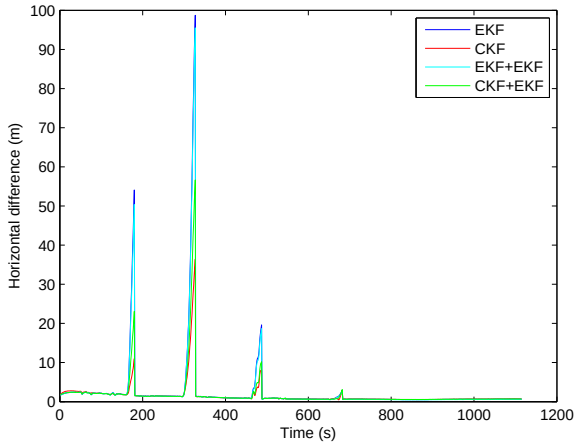

Figure 7.12: Horizontal position drift of dual estimation methods in coasting period

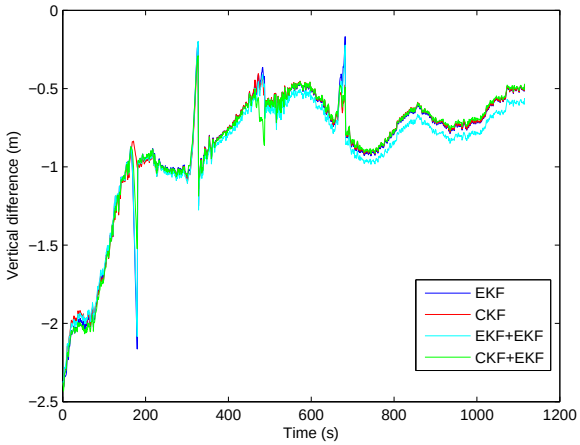

Figure 7.13: Vertical position drift of dual estimation methods in coasting period

7.5.3 Coasting performance

The filtering methods' performance comparison in Chapter 3 indicates that the GPS outages introduce nonlinearity to tightly-coupled navigation systems. To further examine the performance differences among the four filtering methods, four GPS outages are introduced by artificially blocking the GPS signal. During the coasting periods, the integrated navigation system performs IMU-only navigation. A low-cost MEMS IMU drifts very quickly without any aiding sensors. The CKF can help bound the position drift during GPS outages. The initial yaw angle is not well determined as well. Therefore, the integrated navigation system experiences a large misalignment problem. $\mathbf{P}_0$, $\mathbf{Q}$ and $\mathbf{R}$ are set to be the same as the values in the large misalignment case. The coasting performance comparisons among the four filtering methods are shown in Figures 7.12, 7.13 and Table 7.2.

It can be seen that the position drift in the first two coasting periods is much larger than the third and fourth coasting periods. The first two coasting periods are not only affected by GPS blockages but also

Table 7.2: Maximum position drift of dual estimation methods

Filters	1st GPS outage		2nd GPS outage	
	Horizontal drift (m)	Vertical drift (m)	Horizontal drift (m)	Vertical drift (m)
EKF	54.09	1.29	98.71	0.90
CKF	10.97	0.05	36.41	0.81
EKF+EKF	50.35	1.21	95.52	0.90
CKF+EKF	23.05	0.65	56.65	0.81
Filters	3rd GPS outage		4th GPS outage	
	Horizontal drift (m)	Vertical drift (m)	Horizontal drift (m)	Vertical drift (m)
EKF	19.60	0.18	2.97	0.51
CKF	8.16	0.12	2.92	0.21
EKF+EKF	18.66	0.17	2.91	0.50
CKF+EKF	10.21	0.25	3.02	0.22

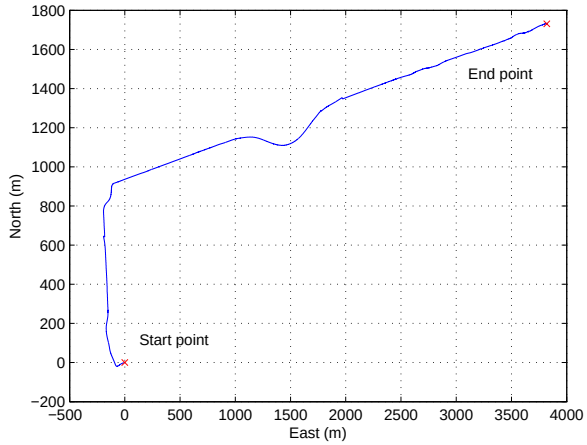

Figure 7.14: Trajectory of complex GPS case

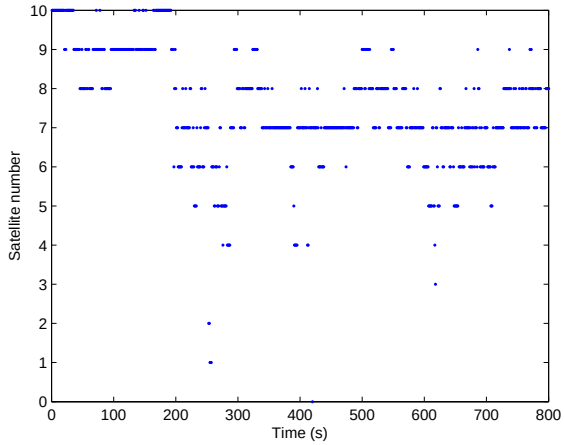

Figure 7.15: Satellite number change during experiment

the large misalignment, both of which contribute to the large position drift. During the third and fourth coasting periods, the yaw angle is already convergent and the position drift is only affected by the GPS blockage. Therefore, the position drift is much smaller. However, the CKF and CKF+EKF seem to drift more slowly than the EKF and EKF+EKF, because the nonlinear attitude expression implemented with these two filtering methods can deal with the large yaw angle error better and consequently bound the position drift.

The CKF has the smallest position drift among the four filtering methods. Compared with the CKF, the CKF+EKF filtering method maintains the CKF's benefits of a smaller position drift and reduces the computational load. However, the maximum position drift of the hybrid filtering method is still larger than the CKF, due to that the hybrid filtering framework reduces the effects of the cross correlation part to the state estimation. Since the EKF+EKF filtering method works in a dual framework, the IMU state and covariance matrix are directly fed back to the GPS related state and covariance matrix estimation, which can slightly bound the position drift. The EKF+EKF filtering method always seems to drift a little more slowly than the EKF during the four GPS outages with a smaller computational load.

7.5.4 Complex GPS case

The trajectory of the complex GPS environment trajectory is shown in Figure 7.14. The GPS signal is blocked by high buildings and trees from time to time. The satellite number change is shown in Figure 7.15. The performance of a TCP/IMU tightly-coupled navigation system with different filtering methods can be further examined in this case. The starting position is initialised with the DGPS result. The initial yaw angle is roughly determined from MEMS gyroscopes, again causing a large misalignment problem for the integrated navigation system. $\mathbf{P}_0$, $\mathbf{Q}$ and $\mathbf{R}$ are set to identical to the large misalignment case, except that the initial ambiguity standard devitation is set as 10 cm. The position and yaw angle comparisons are shown in Figures 7.16, 7.17, 7.18, 7.19 and Table 7.3.

From the figures and table, it can be seen that in a complex GPS environment when the GPS signal is blocked frequently, a TCP based integration strategy can only achieve SPP accuracy. On the contrary, during initial phase of the experiment when there are no GPS outages or satellite changes, the positioning accuracy of the TCP/IMU tightly-coupled navigation system is still much higher than that of the PR+Doppler GPS/IMU tightly-coupled navigation system. When the GPS signal meets the positioning requirements, the four filtering methods have a similar position estimation accuracy because the position is always observable and determined directly from GPS observations in the integrated navigation system.

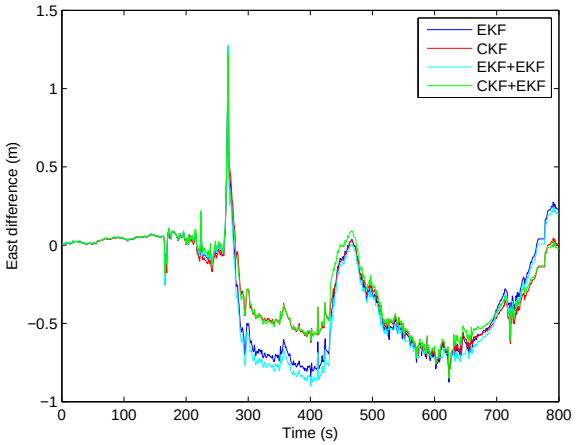

Figure 7.16: Eastern position error of dual estimation methods in complex GPS case

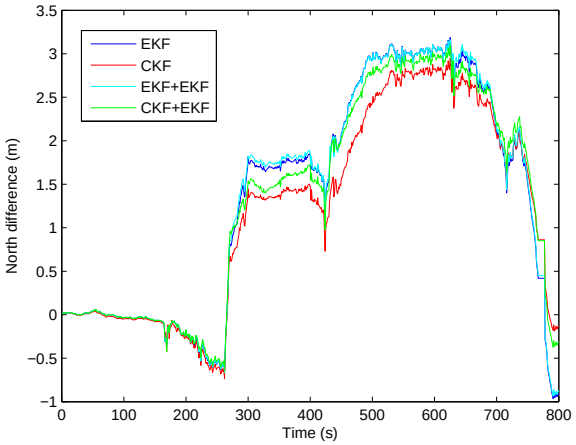

Figure 7.17: Northern position error of dual estimation methods in complex GPS case

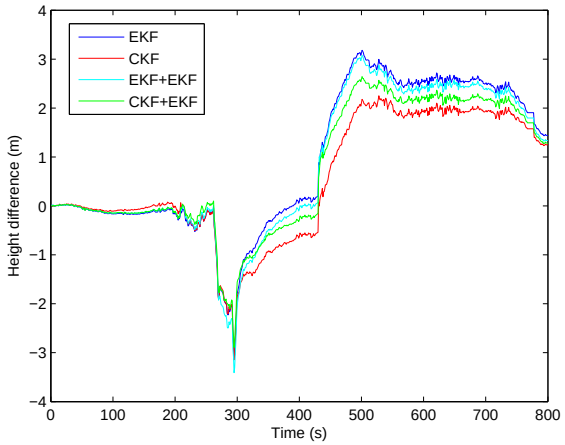

Figure 7.18: Height error of dual estimation methods in complex GPS case

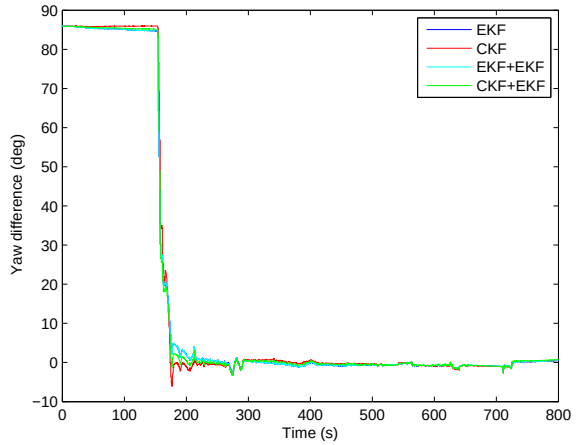

Figure 7.19: Yaw error of dual estimation methods in complex GPS case

Table 7.3: Performance comparison of dual estimation methods in complex GPS case

Filtering methods	East RMS (m)	North RMS (m)	Height RMS (m)	Yaw RMS (deg)
EKF	0.45	1.86	1.74	0.96
CKF	0.39	1.65	1.36	0.72
EKF+EKF	0.48	1.88	1.69	0.95
CKF+EKF	0.37	1.80	1.51	0.72

During GPS outages, the CKF based methods perform better than the EKF based methods with relatively smaller position drifts, coming to a similar conclusion as the coasting performance comparison.

From the yaw angle comparison shown in Figure 7.19, it can be seen that the CKF based methods converge faster than the EKF based methods in the large misalignment case, since the nonlinear attitude expression implemented with the CKF based methods can better deal with the large misalignment problem. Considering the CKF based methods only, the CKF converges faster than the CKF+EKF hybrid filtering method. However, the CKF+EKF has a lower computational load than the CKF. According to the

CKF working principle, the number of Cubature points is directly determined by the dimension of the state vector. The larger the state vector, the more Cubature points should be generated to propagate the states and covariance matrix. The CKF+EKF filtering method can help reduce the number of Cubture points required in the CKF, which consequently reduces the computational load.

7.6 Conclusion

In this chapter, according to the state vector property, a hybrid filtering method CKF+EKF is developed and implemented in a TCP/IMU tightly-coupled navigation system based on the dual estimation framework. From the attitude and position comparison, it can be seen that the hybrid filtering method has a superior performance to the EKF based methods such as the EKF and the EKF+EKF, with relatively lower computational load than the CKF, due to the application of the EKF to estimate linear states for mixed nonlinear/linear systems. The CKF+EKF filtering method can maintain the benefits of the CKF with a slower yaw drift than the EKF based methods in the stationary case, faster convergence speed in the large misalignment case and a smaller position drift during GPS outages as shown in the experiments.

8 Conclusion and future work

8.1 Summary and conclusion

8.1.1 Summary

This thesis investigates the methods of improving the navigation performance of a conventional non-differential GPS/MEMS IMU tightly-coupled navigation system from the viewpoint of filter design involving nonlinear filtering method application, stochastic error modelling and the implementation of GPS carrier phase observations. The Cubature Kalman filter is taken as an example to show the benefits of nonlinear filtering methods in a tightly-coupled navigation system. The CKF estimation accuracy is evaluated via the Taylor expansion at first, which proves that nonlinear filtering methods like the CKF show their own benefits only when implemented with a nonlinear system. In linear or linearised systems, the CKF will have similar or even worse estimation accuracy than the KF, because nonlinear filtering methods are suboptimal estimators. In order to better show the advantage of nonlinear filtering methods in integrated navigation systems, a nonlinear attitude expression using the direction cosine matrix to describe the misalignment between the true and estimated navigation frames, is described, which does not require any small attitude error approximation and is always valid.

According to observability analysis, the CKF's performance is further examined under different maneuvering with different degrees of observability. Simulation and experiment results show that the CKF has higher yaw angle accuracy than the EKF in unobservable cases such as constant velocity and stationary cases. In totally or weakly observable cases, the CKF has a similar estimation accuracy as the EKF. The CKF performance is further examined in large misalignment and GPS outage cases. Navigation results show that the CKF performs better than the EKF when the integrated navigation system shows some nonlinearity and the conventional psi-angle expression becomes invalid because of the large initial attitude error and the fast attitude error accumulation. Like the EPF and UPF, the CKF's *a posteriori* estimation and covariance matrix can also be implemented as the importance density function to generate particles for the particle filter. However, the non-Gaussian property of GPS observations is not so obvious. Although multipath effects can be treated as a non-Gaussian noise, its statistical property is difficult to describe. So the CPF and other particle filter extensions may not be the best choice for a GPS/IMU tightly-coupled navigation system design as shown in the comparison of the navigation results.

Accurately modelling the inertial sensors' stochastic errors in a navigation Kalman filter is helpful to improve the performance of an integrated navigation system. The coefficients of the inertial sensors' stochastic errors can be detected and then determined by an Allan variance plot. According to shaping filter theory, a stationary process can be generated by inputting a unit white noise to a system with the transfer function derived from its related PSD. For nonstationary processes, their shaping filter transfer functions should be approximated using mathematical methods. For example, bias instability, usually treated as a flicker noise, should be approximated as the summation of two independent 1st-order Markovian processes. Rate random walk behaving more like a Wiener process, can be generated by integrating a white noise, according to its sampled or generalized PSD analysis. Rate ramp is approximated as a 2nd-order Markovian process as shown in Chapter 4. The inertial sensors' coloured noises including bias instability, rate random walk and rate ramp, can be modelled together using one equivalent transfer function according to the equivalence theory. The state space of coloured noises in differential and difference equations are derived from the shaping filter transfer function through an inverse Laplace transformation or Z-transformation. The coasting performance comparison with the simulation and experiment data shows the effectiveness of the shaping filter based method, which has a similar or even smaller maximum position drift than conventional 1st-order Markovian process method during GPS outages.

The carrier phase observation is far more accurate than the pseudorange. The implementation of carrier phases as observations in a tightly-coupled navigation system is also beneficial for improving the navigation performance. Considering the difference in dealing with carrier phase ambiguities, the carrier phase related observations can be divided into TDCP and TCP. The TDCP method is based on carrier phase ambiguities staying constant if there is no cycle slip or GPS blockage, which makes it possible to eliminate carrier phase ambiguities by differencing between two GPS epochs, while the TCP method estimates the carrier phase ambiguities as extra states in a navigation Kalman filter. Due to the loss of positioning information, a KF-based PR+TDCP GPS/IMU tightly-coupled navigation system can only reach SPP accuracy. On the contrary, a TCP/IMU tightly-coupled navigation system can achieve sub-meter level positioning accuracy if it is convergent.

Based on the position uncertainty difference between pseudorange and carrier phase observations, a PF-based TDCP/IMU tightly-coupled integration strategy is proposed to achieve sub-meter positioning accuracy with an accurate reference position. A modified TDCP measurement, defined as difference between the reference and observation epochs with respect to the reference satellite, can further isolate the pseudorange noise from the carrier phase observation. Since position error accumulation is avoided, this measurement can bound the position drift caused by the TDCP. The modified TDCP is then implemented in the particle filter measurement update to weight particles generated from the *a posteriori* position of a conventional PR+Doppler GPS/IMU tightly-coupled navigation system. However, because the modified TDCP is a relative positioning measurement, the absolute positioning accuracy of this strategy is determined by the reference position. If the reference position is taken from, for example, DGPS, the positioning accuracy can reach the sub-meter level as shown in experiments. If the reference position is determined from SPP, the absolute position result will have a constant bias compared with the true position. But the position will be smoother than the KF-based PR+TDCP method, indicating a high relative accuracy.

Due to the introduction of carrier phase related states to the integrated navigation Kalman filter, the computational load of the TCP based tightly-coupled navigation system increases, especially when implemented with nonlinear filtering methods such as the CKF. The number of Cubature points required in the CKF increases with the size of the state vector according to the CKF working principle. However, the CKF shows no benefits when implemented with linear systems as indicated in the CKF theoretical analysis. Accordingly, applying the CKF in a linear system will only improve the computational burden without any accuracy enhancement. In order to reduce the computational load while maintaining the CKF's benefits, a CKF+EKF hybrid filtering method based on a dual estimation framework is introduced to the TCP/IMU tightly-coupled navigation system. In this method, the state vector is divided into nonlinear and linear states. The nonlinear states are estimated by the CKF, while the linear states are estimated by the EKF. The simulation and experiment results show that the CKF+EKF hybrid filtering method shows a better performance than the EKF filtering methods, i.e. the EKF and EKF+EKF methods, in the highly nonlinear cases. Compared with the CKF-only method, the hybrid filtering method can reduce the amount of Cubature points required in the CKF, which is also beneficial to improving the computational efficiency. So the CKF+EKF hybrid filtering method can keep the CKF's benefits but reduce the computational load as shown in experiment results.

8.1.2 Conclusion

From the summary above, the following conclusions can be drawn:

1. Implementing nonlinear filtering methods directly in a PR+Doppler GPS/IMU tightly-coupled navigation system in observable cases does not assist in improving attitude estimation accuracy even if a nonlinear attitude expression is applied.
2. The nonlinearity of tightly-coupled navigation systems is higher in the unobservable, large misalignment and GPS outage cases. The nonlinearity of integrated navigation systems is due to the

fast attitude error accumulation or large initial attitude error, which renders conventional psi-angle expression implemented in the EKF invalid. The CKF has no small attitude error requirement.

3. The particle filter and its extensions can be considered as a choice in designing integrated navigation systems, but its advantage in dealing with non-Gaussian noise cannot be fully shown in a conventional PR+Doppler GPS/IMU tightly-coupled navigation system.
4. The shaping filter theory is effective in modelling the inertial sensors' stochastic errors in a navigation Kalman filter. It has a similar or even better performance than the 1st-order Markovian process modelling method. All the coloured noises, including bias instability, rate random walk and rate ramp, can be modelled together as a single transfer function according to equivalence theory.
5. The non-stationary process can be approximated by stationary processes through certain mathematical transformations.
6. Both the differential equation and ARMA process can be deduced from the shaping filter transfer function. These two methods are equivalent in theory, and the simulation and experiment results show that they have a similar coasting performance during GPS outages.
7. The TDCP measurement does not help in improving the absolute positioning accuracy of a tightly-coupled navigation system, while the TCP based method can improve positioning accuracy to the sub-meter level.
8. The PF-based TDCP/IMU tightly-coupled strategy can improve the positioning accuracy to the sub-meter level if initialised with a high-accuracy position.
9. The CKF+EKF hybrid filtering method can help reduce the computational load of a TCP/IMU tightly-coupled navigation system but maintain the CKF's benefits in processing nonlinear problems. The hybrid filtering method can also be applied in other systems with mixed nonlinear/linear states.

8.2 Future work

In order to explore the full potential of GPS/IMU tightly-coupled navigation systems, some recommended future work is mentioned below.

1. The final target of this thesis is to use the techniques developed to construct a high-accuracy, robust and high-efficiency GPS/IMU tightly-coupled navigation system. For example, when the nonlinearity of the integrated navigation system is high, the nonlinear filtering methods and stochastic modelling method can be applied to improve the navigation performance. Otherwise, the linear filtering method should be implemented to keep the computation efficiency. During the fine alignment period, the TCP/IMU tightly-coupled navigation system can be executed to reach a higher initial positioning accuracy. The modified TDCP based navigation strategy can then be applied to keep the high initial positioning accuracy without solving ambiguities. A context-aware and adaptive strategy will be helpful for the changing-over among different navigation strategies.
2. Using the Allan variance technique to determine the stochastic errors' coefficients is time-consuming. Finding ways to reduce the sampling time will be beneficial in improving computational efficiency. Besides this, the stochastic errors' coefficients may change during different dynamics. The best way in modelling the inertial sensors' noise accurately is trying to determine and detect the relevant noise components in real time. Navigation performance can be improved if a real-time stochastic errors' coefficients determination technique is developed and applied.
3. The total carrier phase based method needs a relatively longer convergence time. Improving convergence speed is helpful to make this technique useful for real-time application when with the real-time precise orbit products from IGS.

4. For TDCP based methods, it is also worth researching how to make the best use of higher relative positioning accuracy to improve absolute positioning accuracy.
5. The CKF+EKF hybrid filtering method only roughly divides the state vector into IMU and GPS states. IMU states can be further divided, as for example, position states are linear. It is expected that the division will further help reduce the computational load.
6. In this thesis, only the GPS/IMU tightly-coupled navigation system is discussed. The integration with the other satellite navigation systems such as Glonass, Beidou and Galileo, will be also helpful for the navigation performance improvement. How to construct a multi-GNSS/IMU tightly-coupled navigation system is one of the main future works.

References

Abdel-Hamid, W. (2005). *Accuracy enhancement of integrated MEMS-IMU/GPS systems for land vehicular navigation applications*. PhD thesis, University of Calgary.

Ali, A. (2013). *Low-cost sensors-based attitude estimation for pedestrian Navigation in GPS-denied environments*. PhD thesis, University of Calgary.

Ali, J. and Ullah Baig Mirza, M. R. (2011). Initial orientation of inertial navigation system realized through nonlinear modeling and filtering. *Measurement*, 44(5):793–801.

Allan, D. (1966). Statistics of atomic frequency standards. *Proceedings of the IEEE*, 54(2):221–230.

Angrisano, A. (2010). *GNSS/INS integration methods*. PhD thesis, University of Naples.

Arasaratnam, I. (2009). *Cubature Kalman filtering: theory & applications*. PhD thesis, McMaster University.

Arasaratnam, I. and Haykin, S. (2009). Cubature Kalman filters. *Automatic Control, IEEE Transactions on*, 54(6):1254–1269.

Arasaratnam, I., Haykin, S., and Hurd, T. (2010). Cubature Kalman filtering for continuous-discrete systems: Theory and simulations. *Signal Processing, IEEE Transactions on*, 58(10):4977–4993.

Arulampalam, M. S., Maskell, S., Gordon, N., and Clapp, T. (2002). A tutorial on particle filters for online nonlinear/non-Gaussian Bayesian tracking. *Signal Processing, IEEE Transactions on*, 50(2):174–188.

Ascher, C., Roth, J., and Trommer, G. F. (2011). Performance analysis of tightly coupled precise point positioning with INS in urban areas. In *Proceedings of Gyro Technology Symposium*, volume 15.

Azam, S. E. (2012). *Reduced order modelling and dual estimation of damaging structures*. PhD thesis, Politecnico di Milano.

Bartosch, L. (2001). Generation of colored noise. *International Journal of Modern Physics C*, 12(06):851–855.

Becker, M., Bestmann, U., Schwithal, A., and Hecker, P. (2010). Observability of integrated navigation system states under varying dynamic conditions and aiding techniques. In *Proceedings of IEEE/ION Position Location and Navigation Symposium (PLANS)*, pages 632–638.

Bengtsson, T., Bickel, P., and Li, B. (2008). Curse-of-dimensionality revisited: Collapse of the particle filter in very large scale systems. In *Probability and statistics: Essays in honor of David A. Freedman*, pages 316–334. Institute of Mathematical Statistics.

Benson, D. O. (1975). A comparison of two approaches to pure-inertial and Doppler-inertial error analysis. *Aerospace and Electronic Systems, IEEE Transactions on*, (4):447–455.

Benzerrouk, H. M. (2014). *Modern approaches in nonlinear filtering theory applied to original problems of aerospace integrated navigation systems with non-Gaussian noises*. PhD thesis, Saint Petersburg State University.

Bistrovs, V. and Kluga, A. (2013). The analysis of the UKF-based navigation algorithm during GPS outage. *Elektronika ir Elektrotechnika*, 19(10):13–16.

Blake, S. J. (2007). *Heave compensation using time-differenced carrier observations from low cost GPS receivers*. PhD thesis, University of Nottingham.

Buschmann, M., Winkler, S., Kordes, T., Schulz, H.-W., and Vörsmann, P. (2001). A comparison of MEMS-based IMU calibration models for autonomous MAV navigation. In *Proceedings of the 16th International Technical Meeting of the Satellite Division of The Institute of Navigation (ION GPS/GNSS 2003)*, pages 2833–2839.

Carcanague, S. (2013). *Low-cost GPS/GLONASS precise positioning algorithm in aonstrained environment*. PhD thesis, University of Toulouse.

Chandra, K. P. B., Gu, D., and Postlethwaite, I. (2011). Cubature Kalman filter based localization and mapping. In *Proceedings of 18th International Federation of Automatic Control (IFAC) World Congress*, volume 18, pages 2121–2125.

Chandra, K. P. B., Gu, D., and Postlethwaite, I. (2014). A cubature H infinity filter and its square-root version. *International Journal of Control*, 87(4):764–776.

Chen, H. (2012). Adaptive cubature Kalman filter for nonlinear state and parameter estimation. In *Proceedings of 15th International Conference on Information Fusion (FUSION)*, pages 1413–1420.

Chiang, K., Noureldin, A., and El-Sheimy, N. (2003). Multisensor integration using neuron computing for land-vehicle navigation. *GPS Solutions*, 6(4):209–218.

Choi, M., Kong, S., and Song, S. (2014). In-motion alignment algorithm of the low-grade IMU using inexpensive multisensor measurements. In *Proceedings of the 27th International Technical Meeting of The Satellite Division of the Institute of Navigation (ION GNSS+ 2014)*.

Crassidis, J. L. (2006). Sigma-point Kalman filtering for integrated GPS and inertial navigation. *Aerospace and Electronic Systems, IEEE Transactions on*, 42(2):750–756.

de Jong, P. and Penzer, J. (2004). The ARMA model in state space form. *Statistics & probability letters*, 70(1):119–125.

Ding, W. (2007). Integration of MEMS INS with GPS carrier phase derived velocity: A new approach. In *Proceedings of the 20th International Technical Meeting of The Satellite Division of the Institute of Navigation (ION GNSS 2007)*, pages 2085–2093.

Ding, W. (2008). *Optimal integration of GPS with inertial sensors: modelling and implementation*. PhD thesis, University of New South Wales.

Ding, W. and Wang, J. (2011). Precise velocity estimation with a stand-alone GPS receiver. *Journal of Navigation*, 64(02):311–325.

Du, S. (2010). Integration of precise point positioning and low cost MEMS IMU. Master's thesis, University of Calgary.

Du, S. (2011). An inertial aided cycle slip detection and identification method for integrated PPP GPS/MEMS IMU system. In *Proceedings of the 24th International Technical Meeting of The Satellite Division of the Institute of Navigation (ION GNSS 2011)*, page 3183.

Du, S. and Gao, Y. (2010). Integration of PPP GPS and low cost IMU. In *Proceedings of Canadian Geomatics Conference*.

Du, S. and Gao, Y. (2012). Inertial aided cycle slip detection and identification for integrated PPP GPS and INS. *Sensors*, 12(11):14344–14362.

Du, S., Sun, W., and Gao, Y. (2014). An investigation on MEMS IMU error mitigation using rotation modulation technique. In *Proceedings of the 27th International Technical Meeting of The Satellite Division of the Institute of Navigation (ION GNSS+ 2014)*.

El-Diasty, M. Development of a PPP-based GPS/INS integration system for hydrographic surveys.

El-Sheimy, N., Chiang, K., and Noureldin, A. (2006). The utilization of artificial neural networks for multisensor system integration in navigation and positioning instruments. *Instrumentation and Measurement, IEEE Transactions on*, 55(5):1606–1615.

El-Sheimy, N., Hou, H., and Niu, X. (2008). Analysis and modeling of inertial sensors using Allan variance. *Instrumentation and Measurement, IEEE Transactions on*, 57(1):140–149.

Farrell, J. (2008). *Aided navigation: GPS with high rate sensors*. McGraw-Hill New York.

Figueiredo e Silva, P. (2012). Cycle slip detection and correction using low cost IMU measurements. Master's thesis, Technical Unviersity of Lisbon.

Flenniken, W., Wall, J., and Bevly, D. (2005). Characterization of various IMU error sources and the effect on navigation performance. In *Proceedings of the 18th International Technical Meeting of The Satellite Division of the Institute of Navigation (ION GNSS 2005)*, pages 967–978.

Freda, P., Angrisano, A., Gaglione, S., and Troisi, S. (2014). Time-differenced carrier phases technique for precise GNSS velocity estimation. *GPS Solutions*, 19(2):335–341.

Geist, M. and Pietquin, O. (2011). Kalman filtering & colored noises: the (autoregressive) moving-average case. In *Proceedings of the IEEE Workshop on Machine Learning Algorithms, Systems and Applications (MLASA 2011)*, pages 1–4.

Georgy, J., Noureldin, A., Korenberg, M., and Bayoumi, M. (2010). Low-cost three-dimensional navigation solution for RISS/GPS integration using mixture particle filter. *Vehicular Technology, IEEE Transactions on*, 59(2):599–615.

Giremus, A., Tourneret, J., and Djuric, P. (2005). An improved regularized particle filter for GPS/INS integration. In *Proceedings of IEEE 6th Workshop on Signal Processing Advances in Wireless Communication*, pages 1013–1017.

Godha, S. (2006). *Performance evaluation of low cost MEMS-based IMU integrated with GPS for land vehicle navigation application*. PhD thesis, University of Calgary.

Goshen-Meskin, D. and Bar-Itzhack, I. (1990). Observability analysis of piece-wise constant systems with application to inertial navigation. In *Proceedings of the 29th IEEE Conference on Decision and Control*, pages 821–826.

Goshen-Meskin, D. and Bar-Itzhack, I. (1992). Observability analysis of piece-wise constant systems. i. Theory. *Aerospace and Electronic Systems, IEEE Transactions on*, 28(4):1056–1067.

Granger, C. and Morris, M. (1976). Time series modelling and interpretation. *Journal of the Royal Statistical Society. Series A (General)*, pages 246–257.

Groves, P. D. (2008). *Principles of GNSS, inertial, and multisensor integrated navigation systems*. Artech House.

Guerrier, S. (2013). *Two essays in statistics: a prediction divergence criterion for model selection & wavelet variance based estimation of latent time series models*. PhD thesis, University of Geneva.

Guerrier, S., Stebler, Y., Skalud, J., and Victoria-Feser, M. (2013). Limits of the Allan variance and optimal tuning of wavelet variance based estimators. Technical report, Research Center for Statistics, University of Geneva.

Gustafsson, F. and Hendeby, G. (2012). Some relations between extended and unscented kalman filters. *Signal Processing, IEEE Transactions on*, 60(2):545–555.

Hafner, P., Huber, K., and Moder, T. (2014). Development of a positioning tool for the navigation of visually impaired people. In *Proceedings of the 27th International Technical Meeting of The Satellite Division of the Institute of Navigation (ION GNSS+ 2014)*.

Hall, J., Williams II, R., and van Graas, F. (2000). Inertial measurement unit calibration platform. *Journal of Robotic Systems*, 17(11):623–632.

Hammon, R. (1960). An application of random process theory to gyro drift analysis. *Aeronautical and Navigational Electronics, IRE Transactions on*, (3):84–91.

Han, S. and Rizos, C. (1996). GPS network design and error mitigation for real-time continuous array monitoring systems. In *Proceedings of the 9th International Technical Meeting of The Satellite Division of the Institute of Navigation (ION GPS 1996)*.

Han, S. and Wang, J. (2008). Monitoring degree of observability in GPS/INS integration. In *Proceedings of International symposium on GPS/GNSS, Yokohama, Japan*, pages 25–28.

Han, S. and Wang, J. (2011). Quantization and colored noises error modeling for inertial sensors for GPS/INS integration. *Sensors Journal, IEEE*, 11(6):1493–1503.

Han, S. and Wang, J. (2012). Integrated GPS/INS navigation system with dual-rate Kalman filter. *GPS solutions*, 16(3):389–404.

Havlicek, M., Friston, K., Jan, J., Brazdil, M., and Calhoun, V. (2011). Dynamic modeling of neuronal responses in fMRI using cubature Kalman filtering. *Neuroimage*, 56(4):2109–2128.

Hong, S., Lee, M., Chun, H., Kwon, S., and Speyer, J. (2005). Observability of error states in GPS/INS integration. *Vehicular Technology, IEEE Transactions on*, 54(2):731–743.

Hou, H. (2004). Modeling inertial sensors errors using Allan variance. Master's thesis, University of Calgary.

IEEE Std 952TM-1997, R. (2008). IEEE standard specification format guide and test procedure for single-axis interferometric fiber optic gyros. *IEEE-SA Standards Board*.

Itô, K. (1974). *Diffusion Processes*. Wiley Online Library.

Jia, B., Xin, M., and Cheng, Y. (2013). High-degree cubature Kalman filter. *Automatica*, 49(2):510–518.

Jia, Z. and Brownb, M. (2009). Joint state and parameter estimation for biochemical dynamic pathways with iterative extended Kalman filter: comparison with dual state and parameter estimation. *Open Automation and Control Systems Journal*, 2(1):69–77.

Jiang, Z. (2010). *Digital route model aided integrated satellite navigation and low-cost inertial sensors for high-performance positioning on the railways*. PhD thesis, Univeristy College London.

Julier, S. and Uhlmann, J. (1997). New extension of the Kalman filter to nonlinear systems. In *Proceedings of AeroSense'97*, pages 182–193.

Julier, S. and Uhlmann, J. (2002). Reduced sigma point filters for the propagation of means and covariances through nonlinear transformations. In *Proceedings of the American Control Conference*, volume 2, pages 887–892.

Julier, S. and Uhlmann, J. (2004). Unscented filtering and nonlinear estimation. *Proceedings of the IEEE*, 92(3):401–422.

Julier, S., van der Merwe, R., and Wan, E. (2007). Navigation system applications of sigma-point Kalman filters for nonlinear estimation and sensor fusion.

Kalman, R. E. (1960). A new approach to linear filtering and prediction problems. *Journal of basic Engineering*, 82(1):35–45.

Kaplan, E. D. and Hegarty, C. (2005). *Understanding GPS: principles and applications*. Artech house.

Karaim, M., Karamat, T., and Noureldin, A. (2013). Real-time cycle-slip detection and correction for land vehicle navigation using inertial aiding. In *Proceedings of the 26th International Technical Meeting of The Satellite Division of the Institute of Navigation (ION GNSS+ 2013)*.

Karamat, T. (2014). *Improved land vehicle navigation and GPS integer ambiguity resolution using enhanced reduced-IMU/GPS integration*. PhD thesis, Queen's University.

Kasdin, J. (1995). Discrete simulation of colored noise and stochastic processes and $1/f^{\alpha}$ power law noise generation. *Proceedings of the IEEE*, 83(5):802–827.

Kerr, T. (1991). Streamlining measurement iteration for EKF target tracking. *Aerospace and Electronic Systems, IEEE Transactions on*, 27(2):408–421.

Keshner, M. (1982). 1/f noise. *Proceedings of the IEEE*, 70(3):212–218.

Kong, X., Nebot, E., and Durrant-Whyte, H. (1999). Development of a nonlinear psi-angle model for large misalignment errors and its application in INS alignment and calibration. In *Proceedings of IEEE International Conference on Robotics and Automation*, volume 2, pages 1430–1435.

Kotecha, J. and Djuric, P. (2003a). Gaussian particle filtering. *Signal Processing, IEEE Transactions on*, 51(10):2592–2601.

Kotecha, J. and Djuric, P. (2003b). Gaussian sum particle filtering. *Signal Processing, IEEE Transactions on*, 51(10):2602–2612.

Kubo, Y., Fujioka, S., Nishiyama, M., and Sugimoto, S. (2006). Nonlinear filtering methods for the INS/GPS in-motion alignment and navigation. *International Journal of Innovative Computing, Information and Control*, 2(5):1137–1151.

Lee, D. (2005). *Nonlinear Bayesian filtering with applications to estimation and navigation*. PhD thesis, Texas A&M University.

Li, B., Bengtsson, T., and Bickel, P. (2005). Curse-of-dimensionality revisited: collapse of importance sampling in very large scale systems. Technical Report 696, Department of Statistics, UC-Berkeley.

Li, T. (2012). *Ultra-tightly coupled high sensitivity GPS receiver for on-road vehicle applications*. PhD thesis, University of Calgary.

Li, W. and Jia, Y. (2012). Location of mobile station with maneuvers using an IMM-based cubature Kalman filter. *Industrial Electronics, IEEE Transactions on*, 59(11):4338–4348.

Li, W., Wang, J., Lu, L., and Wu, W. (2013). A novel scheme for DVL-aided SINS in-motion alignment using ukf techniques. *Sensors*, 13(1):1046–1063.

Li, Y., Hu, B., Qin, F., and Li, K. (2014). Online estimation of ARW coefficient of fiber optic gyro. *Mathematical Problems in Engineering*, 2014:Article ID 768590.

Li, Y., Li, Y., Rizos, C., and Xu, X. (2012a). Observability analysis of SINS/GPS during in-motion alignment using singular value decomposition. *Advanced Materials Research*, 433:5918–5923.

Li, Y., Niu, X., Zhang, Q., Zhang, H., and Shi, C. (2012b). An in situ hand calibration method using a pseudo-observation scheme for low-end inertial measurement units. *Measurement Science and Technology*, 23(2012):105104.

Li, Y., Wang, J., Rizos, C., Mumford, P., and Ding, W. (2006). Low-cost tightly coupled GPS/INS integration based on a nonlinear Kalman filtering design. In *Proceedings of ION National Technical Meeting (ION NTM 2006)*, pages 18–20.

Liu, J., Cai, B., Tang, T., and Wang, J. (2010). A CKF based GNSS/INS train integrated positioning method. In *Proceedings of International Conference on Mechatronics and Automation (ICMA)*, pages 1686–1689.

Ljung, L. (1977). Analysis of recursive stochastic algorithms. *Automatic Control, IEEE Transactions on*, 22(4):551–575.

Ljung, L. (1979). Asymptotic behavior of the extended Kalman filter as a parameter estimator for linear systems. *Automatic Control, IEEE Transactions on*, 24(1):36–50.

Marafioti, G. (2010). *Enhanced model predictive control: Dual control approach and state estimation issues*. PhD thesis, Norwegian Univerisyt of Science and Technology.

Martin, I. (2013). *GNSS precise point positioning: the enhancement with GLONASS*. PhD thesis, Newcastle University.

Miller, I., Schimpf, B., Campbell, M., and Leyssens, J. (2008). Tightly-coupled GPS/INS system design for autonomous urban navigation. In *Proceedings of IEEE/ION Position, Location and Navigation Symposium*, pages 1297–1310.

Miller, R. (1983). A new strapdown attitude algorithm. *Journal of Guidance, Control, and Dynamics*, 6(4):287–291.

Misra, P. and Enge, P. (2006). *Global Positioning System: Signals, Mesurements, and Performance (2nd Edition)*. Ganga-Jamuna Press.

Moafipoor, S., Grejner-Brzezinska, D., and Toth, C. (2004). Tightly coupled GPS/INS integration based on GPS carrier phase velocity update. In *Proceedings of ION National Technical Meeting (ION NTM 2004)*.

Moradkhani, H., Sorooshian, S., Gupta, H., and Houser, P. (2005). Dual state-parameter estimation of hydrological models using ensemble Kalman filter. *Advances in Water Resources*, 28(2):135–147.

Moritz, H. (1980). Geodetic reference system 1980. *Journal of Geodesy*, 54(3):395–405.

Nelson, A. T. (2000). *Nonlinear estimation and modeling of noisy time-series by dual Kalman filtering methods*. PhD thesis, Oregon Health & Science University.

Ninness, B. (1998). Estimation of 1/f noise. *Information Theory, IEEE Transactions on*, 44(1):32–46.

Niu, X., Chen, Q., Zhang, Q., Zhang, H., Niu, J., Chen, K., Shi, C., and Liu, J. (2014). Using Allan variance to analyze the error characteristics of GNSS positioning. *GPS solutions*, 18(2):231–242.

Niu, X., Li, Y., and Zhang, Q. (2012). Observability analysis of non-holonomic constraints for land-vehicle navigation systems. *Journal of Global Positioning Systems*, 11(1):80–88.

Ogata, K. and Yang, Y. (1970). Modern control engineering.

Okuma, K., Taleghani, A., De Freitas, N., Little, J., and Lowe, D. (2004). A boosted particle filter: Multitarget detection and tracking. In *Proceedings of European Conference Computer Vision (ECCV)*, pages 28–39.

Park, M. (2004). Error analysis and stochastic modeling of MEMS based inertial sensors for land vehicle navigation applications. Master's thesis, University of Calgary.

Park, M. and Gao, Y. (2008). Error and performance analysis of MEMS-based inertial sensors with a low-cost GPS receiver. *Sensors*, 8(4):2240–2261.

Paul, A. and Wan, E. (2005). Dual Kalman filters for autonomous terrain aided navigation in unknown environments. In *Proceedings of IEEE International Joint Conference on Neural Networks*, volume 5, pages 2784–2789.

Pham, T. (1991). Kalman filter mechanization for INS airstart. In *Proceedings of IEEE/AIAA 10th Conference on Digital Avionics Systems*, pages 516–525.

Pittelkau, M. E. (2013). Attitude determination Kalman filter with a 1/f flicker noise gyro model. In *Proceedings of the 26th International Technical Meeting of the ION Satellite Division (ION GNSS+ 2013)*, pages 2143–2160.

Quang, P., Musso, C., and Le Gland, F. (2010). An insight into the issue of dimensionality in particle filtering. In *Proceedings of 13th Conference on Information Fusion (FUSION)*, pages 1–8.

Quinchia, A. (2014). *Performance enhancement MEMS based INS/GPS integrated system implemented on a FPGA for terrestrial applications*. PhD thesis, Universitat Autònoma de Barcelona.

Quinchia, A., Ferrer, C., Falco, G., and Dovis, F. (2013). Constrained non-linear fitting for stochastic modeling of inertial sensors. In *Proceedings of Conference on Design and Architectures for Signal and Image Processing (DASIP)*, pages 119–125.

Rabbou, M. (2014). Non-linear filtering for precise point positioning GPS/INS integration. In *Proceedings of ISPRS Technical Commission II Symposium, Toronto, Canada*.

Rabbou, M. and El-Rabbany, A. (2014a). Tightly coupled integration of GPS-PPP and MEMS-based inertial system using EKF and UKF. In *Proceedings of FIG Congress 2014 Engaging the Challenges, Enhancing the Relevance Kuala Lumpur, Malaysia*.

Rabbou, M. and El-Rabbany, A. (2014b). Tightly coupled integration of GPS precise point positioning and MEMS-based inertial systems. *GPS Solutions*, 19(4):601–609.

Rahim, K. A. (2012). *Heading drift mitigation for low-cost inertial pedestrian navigation*. PhD thesis, University of Nottingham.

Ramanandan, A. (2011). *High accuracy sensor aided inertial navigation systems*. PhD thesis, University of California Riverside.

Rhee, I., Abdel-Hafez, M., and Speyer, J. (2004). Observability of an integrated GPS/INS during maneuvers. *Aerospace and Electronic Systems, IEEE Transactions on*, 40(2):526–535.

Rhudy, M. (2013). *Sensitivity and stability analysis of nonlinear Kalman filters with application to aircraft attitude estimations*. PhD thesis, West Virginia University.

Rhudy, M., Gu, Y., Gross, J., Gururajan, S., and Napolitano, M. (2013). Sensitivity analysis of extended and Unscented kalman filters for attitude estimation. *Journal of Aerospace Information Systems*, 10(3):131–143.

Rizos, C. (2003). Network RTK research and implementation-a geodetic perspecti. *Journal of Global Positioning Systems*, 1(02).

Rizos, C. and Han, S. (2003). Reference station network based RTK systems-concepts and progress. *Wuhan University Journal of Natural Sciences*, 8(2):566–574.

Roesler, G. and Martell, H. (2009). Tightly coupled processing of precise point position (PPP) and INS data. In *Proceedings of the 22nd International Technical Meeting of the ION Satellite Division (ION GNSS 2009)*, number 1898–1905.

Roscoe, K. (2001). Equivalency between strapdown inertial navigation coning and sculling integrals/algorithms. *Journal of Guidance, Control, and Dynamics*, 24(2):201–205.

Rothman, Y., Klein, I., and Filin, S. (2014). Analytical observability analysis of INS with vehicle constraints. *Navigation, Journal of Institute of Navigation*, 61(3):227–236.

Saatci, E. and Akan, A. (2009). Dual Unscented Kalman filter and its applications to respiratory system modelling. *Kalman Filter: Recent Advances and Applications*, pages 205–228.

Sadeghi, B. and Moshiri, B. (2007). Second-order EKF and unscented Kalman filter fusion for tracking maneuvering targets. In *Proceedings of IEEE International Conference on Information Reuse and Integration*, pages 514–519.

Saini, V., Rana, S., and Kuber, M. (2010). Online estimation of state space error model for MEMS IMU. *Journal of Modelling and Simulation of Systems*, 1(4):219–225.

Särkkä, S. (2006). *Recursive bayesian inference on stochastic differential equations*. PhD thesis, Helsinki University of Technology.

Savage, P. G. (1998a). Strapdown inertial navigation integration algorithm design part 1: Attitude algorithms. *Journal of Guidance, Control, and Dynamics*, 21(1):19–28.

Savage, P. G. (1998b). Strapdown inertial navigation integration algorithm design part 2: Velocity and position algorithms. *Journal of Guidance, Control, and Dynamics*, 21(2):208–221.

Savage, P. G. (2002). Analytical modeling of sensor quantization in strapdown inertial navigation error equations. *Journal of Guidance, Control, and Dynamics*, 25(5):833–842.

Scherzinger, B. (1996). Inertial navigator error models for large heading uncertainty. In *Proceedings of IEEE/ION Position Location and Navigation Symposium*, pages 477–484.

Schmidt, G. (2011). INS/GPS technology trends. Technical report, DTIC Document.

Schwarz, K. and Wei, M. (2001). INS/GPS integration for geomatics. Technical report, Department of Geomatics, University of Calgary.

Seong, S., Lee, J., and Park, C. (2000). Equivalent ARMA model representation for RLG random errors. *Aerospace and Electronic Systems, IEEE Transactions on*, 36(1):286–290.

Serrano, L., Kim, D., Langley, R., Itani, K., and Ueno, M. (2004). A GPS velocity sensor: how accurate can it be?–A first look. In *Proceedings of ION National Technical Meeting (ION NTM 2004)*, pages 875–885.

Shin, E. and El-Sheimy, N. (2004). An unscented Kalman filter for in-motion alignment of low-cost IMUs. In *Proceedings of IEEE/ION Position Location and Navigation Symposium (PLANS)*, pages 273–279.

Soon, B., Scheding, S., Lee, H., Lee, H., and Durrant-Whyte, H. (2008). An approach to aid INS using time-differenced GPS carrier phase (TDCP) measurements. *GPS Solutions*, 12(4):261–271.

Stebler, Y. (2013). *Modeling and processing approaches for integrated inertial navigation*. PhD thesis, Ecole polytechnique federale de Lausanne.

Stebler, Y., Guerrier, S., Skaloud, J., and Victoria-Feser, M. (2012). A framework for inertial sensor calibration using complex stochastic error models. In *Proceedings of IEEE/ION Position Location and*

Navigation Symposium (PLANS), pages 849–861.

Steinhardt, N. (2014). *Eine Architektur zur Schaetzung kinematischer Fahrzeuggroessen mit integrierter Qualitaetsbewertung durch Sensordatenfusion*. PhD thesis, Technischen Universitaet Darmstadt.

Sun, D. (2010). *Ultra-tight GPS/Reduced IMU for land vehicle navigation*. PhD thesis, University of Calgary.

Syed, Z. (2009). *Design and implementation issues of a portable navigation system*. PhD thesis, University of Calgary.

Syed, Z., Aggarwal, P., Goodall, C., Niu, X., and El-Sheimy, N. (2007). A new multi-position calibration method for MEMS inertial navigation systems. *Measurement Science and Technology*, 18(7):1897.

Tang, X., Wei, J., and Chen, K. (2012). Square-root adaptive cubature Kalman filter with application to spacecraft attitude estimation. In *Proceedings of 15th International Conference on Information Fusion (FUSION)*, pages 1406–1412.

Tang, Y., Lian, J., Wu, M., and Shen, L. (2007). Reduced kalman filter for RDSS/INS integration based on time differenced carrier phase. In *Proceedings of 2nd IEEE Conference on Industrial Electronics and Applications*, pages 11–14.

Tang, Y., Wu, Y., Wu, M., Wu, W., Hu, X., and Shen, L. (2009). INS/GPS integration: global observability analysis. *Vehicular Technology, IEEE Transactions on*, 58(3):1129–1142.

Teräsvirta, T. (1977). The invertibility of sums of discrete MA and ARMA processes. *Scandinavian Journal of Statistics*, pages 165–170.

Titterton, D. and Weston, J. (2004). *Strapdown inertial navigation technology*, volume 17. Peter Peregrinus Ltd.

Torge, W. (1991). *Geodesy (2nd Edition)*. de Gruyter.

Ueno, M., Nimura, T., Fujiwara, T., and Nonaka, K. (1997). Evaluation of RTK-OTF positioning system for free running manoeuvrability test of a model ship. In *Proceedings of MTS/IEEE Conference Proceedings*, volume 2, pages 1120–1125.

Vágner, M., Benes, P., and Havránek, Z. (2012). Experience with Allan variance method for MEMS gyroscope performance characterization. In *Proceedings of IEEE International Instrumentation and Measurement Technology Conference (I2MTC)*, pages 1343–1347.

Van Der Merwe, R. (2004). *Sigma-point Kalman filters for probabilistic inference in dynamic state-space models*. PhD thesis, Oregon Health & Science University.

Van Der Merwe, R., Doucet, A., De Freitas, N., and Wan, E. (2000). The unscented particle filter. Technical report, Cambridge University Engineering Department.

Van Der Merwe, R. and Wan, E. (2001). The square-root unscented Kalman filter for state and parameter-estimation. In *Proceedings of IEEE International Conference on Acoustics, Speech, and Signal Processing*, volume 6, pages 3461–3464.

Van Dierendonck, A., McGraw, J., and Brown, R. (1984). Relationship between Allan variances and Kalman filter parameters. Technical report, DTIC Document.

Vlassis, N., Terwijn, B., and Krose, B. (2002). Auxiliary particle filter robot localization from high-dimensional sensor observations. In *Proceedings of IEEE International Conference on Robotics and Automation*, volume 1, pages 7–12.

Wan, E. and Nelson, A. (1996). Dual Kalman filtering methods for nonlinear prediction, smoothing, and estimation. In *Advances in Neural Information Processing Systems 9 (NIPS 1996)*, volume 9, pages 793–799.

Wan, E. and Nelson, A. (1997). Neural dual extended Kalman filtering: applications in speech enhancement and monaural blind signal separation. In *Proceedings of IEEE Conference on Neural Networks for Signal Processing*, pages 466–475.

Wan, E. and Nelson, A. (2001). *Dual extended Kalman filter methods*. New York: Wiley.

Wan, E., Van Der Merwe, R., and Nelson, A. (1999). Dual estimation and the unscented transformation. In *Advances in Neural Information Processing Systems 12 (NIPS 1999)*, pages 666–672. Citeseer.

Wang, K., Li, Y., and Rizos, C. (2009). The feasibility of MEMS inertial sensors for deep integration of GPS and INS. In *Proceedings of the 21st International Technical Meeting of the Satellite Division of The Institute of Navigation (ION GNSS 2009)*, pages 22–25.

Wang, K., Xiong, S., and Li, Y. (2012). Modeling with noises for inertial sensors. In *Proceedings of IEEE/ION Position Location and Navigation Symposium (PLANS)*, pages 625–632.

Wang, Q., Li, Y., Rizos, C., and Li, S. (2008). The UKF and CDKF for low-cost SDINS/GPS in-motion alignment. In *Proceedings of International Symposium on GPS/GNSS*, pages 441–448.

Wankerl, M. and Trommer, G. F. (2014). Evaluation of a segmented navigation filter approach for vehicle self-localization in urban environment. *Gyroscopy and Navigation*, 5(2):98–107.

Wendel, J., Maier, A., Metzger, J., and Trommer, G. F. (2005). Comparison of extended and sigma-point Kalman filters for tightly coupled GPS/INS integration. In *Proceedings of AIAA Guidance, Navigation, and Control Conference and Exhibit*, volume 6055.

Wendel, J., Meister, O., Monikes, R., and Trommer, G. F. (2006a). Time-differenced carrier phase measurements for tightly coupled GPS/INS integration. In *Proceedings of IEEE/ION Position, Location and Navigation Symposium*, pages 54–60.

Wendel, J., Metzger, J., Moenikes, R., Maier, A., and Trommer, G. F. (2006b). A performance comparison of tightly coupled GPS/INS navigation systems based on extended and sigma point Kalman filters. *Navigation, Journal of Institute of Navigation*, 53(1):21–31.

Wendel, J., Metzger, J., and Trommer, G. F. (2004). Rapid transfer alignment in the presence of time correlated measurement and system noise. In *Proceedings of AIAA Guidance, Navigation, and Control Conference and Exhibit*, pages 1–12.

Wendel, J. and Trommer, G. F. (2004). Tightly coupled GPS/INS integration for missile applications. *Aerospace Science and Technology*, 8(7):627–634.

Xing, Z. and Gebre-Egziabher, D. (2008). Modeling and bounding low cost inertial sensor errors. In *Proceedings of IEEE/ION Position, Location and Navigation Symposium*, pages 1122–1132.

Xu, G. (2007). *GPS theory, algorithms and applications (2nd Edition)*. Springer.

Xu, P., Shi, C., Fang, R., Liu, J., Niu, X., Zhang, Q., and Yanagidani, T. (2013). High-rate precise point positioning (PPP) to measure seismic wave motions: an experimental comparison of GPS PPP with inertial measurement units. *Journal of Geodesy*, 87(4):361–372.

Yi, Y. (2007). *On improving the accuracy and reliability of GPS/INS-based direct sensor georeferencing*. PhD thesis, Ohio State University.

Yi, Y. and Grejner-Brzezinska, D. (2006). Tightly-coupled GPS/INS integration using unscented Kalman filter and particle filter. In *Proceedings of the 19th International Technical Meeting of the Satellite Division of The Institute of Navigation (ION GNSS 2006)*, pages 2182–2191.

Zelinker, G. and Taylor, F. (1994). *Advanced digital signal processing: theory and applications*. CRC Press.

Zhan, R. and Wan, J. (2007). Iterated unscented Kalman filter for passive target tracking. *Aerospace and Electronic Systems, IEEE Transactions on*, 43(3):1155–1163.

Zhang, N. (2008). Allan variance of time series models for measurement data. *Metrologia*, 45(5):549.

Zhang, Q., Meng, X., Zhang, S., and Wang, Y. (2014a). Singular value decomposition-based robust Cubature Kalman filter for an integrated GPS/SINS navigation system. *ISPRS-International Archives of the Photogrammetry, Remote Sensing and Spatial Information Sciences*, 1(1):149–155.

Zhang, Q., Niu, X., Chen, Q., Zhang, H., and Shi, C. (2013a). Using Allan variance to evaluate the relative accuracy on different time scales of GNSS/INS systems. *Measurement Science and Technology*,

24(8):085006.

Zhang, Q., Niu, X., Zhang, H., and Shi, C. (2013b). Algorithm improvement of the low-end GNSS/INS systems for land vehicles navigation. *Mathematical Problems in Engineering*, 2013:Article ID 435286.

Zhang, X., Li, Y., Mumford, P., and Rizos, C. (2008). Allan variance analysis on error characters of MEMS inertial sensors for an FPGA-based GPS/INS system. In *Proceedings of International Symposium on GPS/GNSS*, pages 127–33.

Zhang, Y. and Gao, Y. (2004). Design and analysis of a tightly coupled Kalman filter for point GPS/INS system: preliminary results. In *Proceedings of International Symposium on GPS/INS*.

Zhang, Y. and Gao, Y. (2005a). Performance analysis of a tightly-coupled Kalman filter for the integration of undifferenced GPS and inertial data. In *Proceedings of ION National Technical Meeting (ION NTM 2005)*.

Zhang, Y. and Gao, Y. (2005b). Performance comparison between between point and differential GPS/INS systems. In *Proceedings of the 18th International Technical Meeting of the Satellite Division of The Institute of Navigation (ION GNSS 2005)*.

Zhang, Y. and Gao, Y. (2008). Integration of INS and un-differenced GPS measurements for precise position and attitude determination. *Journal of Navigation*, 61(01):87–97.

Zhang, Y., Huang, Y., Wu, Z., and Li, N. (2014b). Moving state marine SINS initial alignment based on high degree CKF. *Mathematical Problems in Engineering*, 2014:Article ID 546107.

Zhao, Y. (2013). *Key technologies in low-cost integrated vehicle navigation systems*. PhD thesis, Royal Institute of Technology (KTH).

Zhao, Y., Becker, M., Becker, D., and Leinen, S. (2015). Improving the performance of tightly-coupled GPS/INS navigation by using time-differenced GPS-carrier-phase measurements and low-cost MEMS IMU. *Gyroscopy and Navigation*, 6(2):133–142.

Zhao, Y., Horemuz, M., and Sjöberg, L. (2011). Stochastic modeling and analysis of IMU sensor errors. *Archives of Photogrammetry, Cartography and Remote Sensing*, 22:437–449.

Zhou, J. (2013). *Low-cost MEMS-INS/GPS integration using nonlinear filtering approaches*. PhD thesis, University of Siegen.

Zhou, J., Edwan, E., Knedlik, S., and Loffeld, O. (2010). Low-cost INS/GPS with nonlinear filtering methods. In *Proceedings of 13th Conference on Information Fusion (FUSION)*, pages 1–8.

Zhou, J., Yang, Y., Zhang, J., and Edwan, E. (2011). Applying quaternion-based unscented particle filter on INS/GPS with field experiments. In *Proceedings of the 24th International Technical Meeting of The Satellite Division of the Institute of Navigation (ION GNSS 2011)*, pages 3842–3855.

List of Acronyms

ANN	Artificial Neural Network
AR	Auto-Regressive
ARMA	Auto-Regressive Moving Average
AV	Allan Variance
CDKF	Central Difference Kalman Filter
CDMA	Code Division Multiple Access
CKF	Cubature Kalman Filter
CP	Carrier Phase
CPF	Cubature Particle Filter
DCM	Direction Cosine Matrix
DGPS	Differential GPS
ECEF	Earth Centred Earth Fixed
ECI	Earth Centred Inertial
EKF	Extended Kalman Filter
ENU	East North Up
EWL	Extra Wide Lane
fMRI	Functional Magnetic Resonance Imaging
FOG	Fibre Optic Gyroscope
GM	Gauss Markovian process
GMWM	Generalized Method of Wavelet Moments
GNSS	Global Navigation Satellite System
GPF	Gaussian Particle Filter
GPS	Global Positioning System
GSPF	Gaussian Sum Particle Filter
IEEE	Institute of Electrical and Electronics Engineers
IEKF	Iterated Extended Kalman Filter
IGS	International GNSS Service
IMU	Inertial Measurement Unit
IMM	Iterative Multi Model
INS	Inertial Navigation System
KF	Kalman Filter
LLH	Longitude, Latitude, Height
LTI	Linear Time Invariant
MA	Moving Average
MEMS	MicroElectroMechanical Systems
NCO	Numerical Controller Oscillator
NED	North East Down
OTF	On The Fly
PDR	Pedestrian Dead Reckoning
PEM	Prediction Error Method
PF	Particle Filter
PPP	Precise Point Positioning
PR	Pseudo-Range

PSD	Power Spectral Density
PWCS	Piece Wise Constant System
RLG	Ring Laser Gyroscope
RMS	Root Mean Square
RTK	Real-Time Kinematic
SLAM	Simultaneous Localisation And Mapping
SPKF	Sigma-Point Kalman Filter
SPP	Single Point Positioning
SVD	Singular Value Decomposition
TCP	Total Carrier Phase
TDCP	Time Difference Carrier Phase
UKF	Unscented Kalman Filter
UPF	Unscented Particle Filter
WGS	World Geodetic System
WL	Wide Lane
WV	Wavelet Variance
ZUPT	Zero Velocity Update

List of Symbols

Kalman filter

$\mathbf{F}$	System matrix
$\mathbf{H}$	Measurement matrix
$\mathbf{K}$	Kalman gain
$\mathbf{N}$	Gaussian density
$\mathbf{P}$	State covariance matrix
$\mathbf{Q}$	System noise covariance matrix
$\mathbf{R}$	Measurement noise covariance matrix
$\mathbf{X}$	Particle
$\mathbf{f}$	State transition function
$\mathbf{h}$	Measurement function
$\mathbf{v}$	Measurement noise
$\mathbf{w}$	System noise
$\mathbf{x}$	State vector
$\mathbf{y}$	Mixed nonlinear/linear state vector
$\mathbf{z}$	Measurements
Φ	State transition matrix
χ	Cubature points
θ	Parameters
$(.)_{k-1\|k-1}$	*a priori* estimation
$(.)_{k\|k-1}$	Predicted estimation
$(.)_{k\|k}$	*a posteriori* estimation

GPS

$\mathbf{C}^a$	Derivative of transformation from ECEF frame to LLH frame
$\mathbf{C}^e$	Transformation from ECEF frame to LLH frame
$\mathbf{C}_n^e$	Transformation from navigation frame to ECEF frame
C/N_0	Carrier-to-noise ratio
I	Ionospheric delay
N	Carrier phase ambiguity
R_m	Normal radius
R_n	Median radius
$\overrightarrow{R_m}$	The m-th GPS satellite position vector
T	Tropospheric delay
$\overrightarrow{b}$	The receiver position vector
c	Speed of light
e	Earth eccentricity
$\overrightarrow{e_m}$	Line of sight respect to the m-th satellite
f_1	L1 frequency

f_2	L2 frequency
δf	Doppler frequency correction
$\overrightarrow{g_m}$	Derivative of line of sight respect to the m-th satellite
l	Carrier phase observation
l_I	Estimated carrier phase observation
r	True range
$\dot{r}$	True range rate
δt_s	Satellite clock offset
δt_r	Receiver clock offset
$\delta \dot{t}_s$	Satellite clock drift
$\delta \dot{t}_r$	Receiver clock drift
x, y, z	Receiver position in ECEF frame
x_s, y_s, z_s	Satellite position in ECEF frame
$\dot{x}, \dot{y}, \dot{z}$	Receiver velocity in ECEF frame
$\dot{x}_s, \dot{y}_s, \dot{z}_s$	Satellite velocity in ECEF frame
Δ	Time difference operator
ρ	Pseudo-range observation
ρ_I	Estimated pseudo-range observation
$\dot{\rho}$	Doppler/Range rate observation
$\dot{\rho}_I$	Estimated Doppler/range rate observation
$\overrightarrow{\rho}$	Range vector
λ, φ, h	Longitude, Latitude, Height
ε_ρ	Pseudo-range error
ε_l	Carrier phase error
$\varepsilon_{\dot{\rho}}$	Doppler error
$theta_{ele}$	Elevation angle

IMU

$\mathbf{C}_b^n$	Direction cosine matrix from body frame to navigation frame
$\mathbf{C}_{\tilde{n}}^n$	Direction cosine matrix from estimated navigation frame to true navigation frame
$\mathbf{M}$	Magnetometer output
$\mathbf{f}$	Specific force
$\mathbf{g}$	Gravity
$\mathbf{p}$	Position
$\mathbf{v}$	Velocity
v_e, v_n, v_u	Eastern velocity, Northern velocity and Up velocity
$\delta v_e, \delta v_n, \delta v_u$	Velocity error in ENU frame
α	Roll angle
β	Pitch angle
γ	Yaw angle
Ψ	Attitude error

$\delta\alpha$	Roll angle error
$\delta\beta$	Pitch angle error
$\delta\gamma$	Yaw angle error
$\delta\lambda, \delta L, \delta h$	Position error expressed in longitude, latitude, height
ϵ	Gyroscope bias
∇	Accelerometer bias
ω_{in}^{n}	Turn rate of navigation frame with respect to inertial frame expressed in navigation frame
ω_{ie}^{n}	Turn rate of the Earth with respect to inertial frame expressed in navigation frame
ω_{en}^{n}	Turn rate of navigation frame with respect to Earth frame expressed in navigation frame

Noise

B	Bias instability
$C(\tau)$	Auto-correlation function
$H(j\omega)$	Transfer function in frequency domain
$H(s)$	Continuous transfer function
$H(z)$	Discrete transfer function
K	Rate random walk
N	Angle/Velocity random walk
Q	Quantization noise
R	Rate ramp
$R(t, \tau)$	Auto-correlation function of nonstationary process
$S(f)$	Power spectral density
T_c	Time constant of 1st-order Markovian process
$a_i, b_i, c_i, c_i, d_i, e_i, f_i$	Coefficients
q_c	Covariance of 1st-order Markovian process
$w(t)$	White noise
$\sigma^2(\tau)$	Allan variance
Ω	Discrete data

Appendix

The direct implementation of conventional ARMA process state space form in Kalman filter sometimes causes a degraded performance and even numerical instability, due to that the discretion introduces an inconsistency between continuous and discrete transfer functions as shown in Figure A.1.

From Figure A.1, it can be found that the continuous and discrete transfer functions' magnitude frequency characteristic properties differ mainly in the very low frequency domain. The coefficients of ARMA process deduced from shaping filter transfer function are related with the power of time interval T_s, for example e_6. If time interval is very small, the contribution of other coefficients like b_6, b_5, b_4, b_3 to e_6 is also limited, and e_6 will be dominated by b_1, b_2. This property is the main reason of the inconsistency between continuous and discrete transfer functions, which further degrades the filtering performance when implemented in navigation Kalman filter. To avoid this, in this part, a modified state space of ARMA process is introduced according to the internal relationship between its coefficients in the specific application.

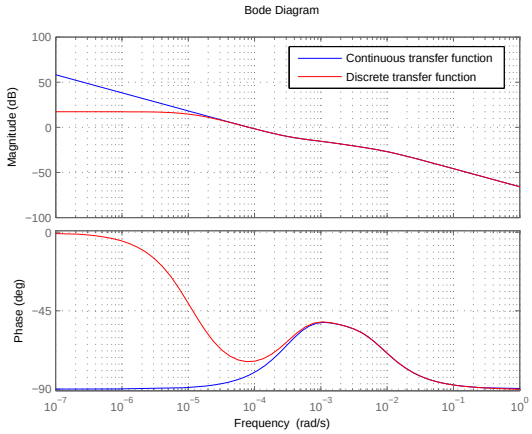

Figure A.1: Bode diagram comparison between continuous and discrete transfer function

Constructing the following states as

$$
\begin{aligned}
z_{5,k} &= y_k \\
z_{4,k} &= \frac{y_k - y_{k-1}}{T_s} + \frac{b_2}{b_1} y_k - \frac{a_1}{b_1} x_k \\
z_{3,k} &= \frac{y_k - 2y_{k-1} + y_{k-2}}{T_s^2} + \frac{b_2}{b_1} \frac{y_k - y_{k-1}}{T_s} + \frac{b_3}{b_1} y_k - \frac{a_1}{b_1} \frac{x_k - x_{k-1}}{T_s} - \frac{a_2}{b_1} x_k \\
z_{2,k} &= \frac{y_k - 3y_{k-1} + 3y_{k-2} - y_{k-3}}{T_s^3} + \frac{b_2}{b_1} \frac{y_k - 2y_{k-1} + y_{k-2}}{T_s^2} + \frac{b_3}{b_1} \frac{y_k - y_{k-1}}{T_s} \\
&\quad + \frac{b_4}{b_1} y_k - \frac{a_1}{b_1} \frac{x_k - 2x_{k-1} + x_{k-2}}{T_s^2} - \frac{a_2}{b_1} \frac{x_k - x_{k-1}}{T_s} - \frac{a_3}{b_1} x_k \\
z_{1,k} &= \frac{y_k - 4y_{k-1} + 6y_{k-2} - 4y_{k-3} + y_{k-4}}{T_s^4} + \frac{b_2}{b_1} \frac{y_k - 3y_{k-1} + 3y_{k-2} - y_{k-3}}{T_s^3} \\
&\quad + \frac{b_3}{b_1} \frac{y_k - 2y_{k-1} + y_{k-2}}{T_s^2} + \frac{b_4}{b_1} \frac{y_k - y_{k-1}}{T_s} + \frac{b_5}{b_1} y_k \\
&\quad - \frac{a_1}{b_1} \frac{x_k - 3x_{k-1} + 3x_{k-2} - x_{k-3}}{T_s^3} - \frac{a_2}{b_1} \frac{x_k - 2x_{k-1} + x_{k-2}}{T_s^2} \\
&\quad - \frac{a_3}{b_1} \frac{x_k - x_{k-1}}{T_s} - \frac{a_4}{b_1} x_k
\end{aligned}
\tag{A.1}
$$

Equation (A.1) is deduced from Z-transformation of shaping filter transfer function. The first term of the last equation of (A.1) can be calculated from $\frac{(1-z^{-1})}{T_s^4} Y(z)$ using inverse Z transformation.

If $z_{i,k}$ is differenced as $\frac{z_{i,k} - z_{i,k-1}}{T_s}$, the relationship in equation (A.2) meets. Substituting $z_{i,k}$ into $z_{i+1,k}$ and computing it iteratively, the final coefficients of this expression is same as ARMA process equation (4.54). So in this sense, the expression is equivalent to the conventional one.

$$
\begin{aligned}
\frac{z_{5,k} - z_{5,k-1}}{T_s} &= z_{4,k} - \frac{b_2}{b_1} z_{5,k} + \frac{a_1}{b_1} x_k \\
\frac{z_{4,k} - z_{4,k-1}}{T_s} &= z_{3,k} - \frac{b_3}{b_1} z_{5,k} + \frac{a_2}{b_1} x_k \\
\frac{z_{3,k} - z_{3,k-1}}{T_s} &= z_{2,k} - \frac{b_4}{b_1} z_{5,k} + \frac{a_3}{b_1} x_k \\
\frac{z_{2,k} - z_{2,k-1}}{T_s} &= z_{1,k} - \frac{b_5}{b_1} z_{5,k} + \frac{a_4}{b_1} x_k \\
\frac{z_{1,k} - z_{1,k-1}}{T_s} &= -\frac{b_6}{b_1} z_{5,k} + \frac{a_5}{b_1} x_k
\end{aligned}
\tag{A.2}
$$

If $\mathbf{z}_k = \begin{bmatrix} z_{5,k} & z_{4,k} & z_{3,k} & z_{2,k} & z_{1,k} \end{bmatrix}^T$, the following state space form can be constructed for ARMA process according to the relationship (A.2)

$$
\begin{cases}
\mathbf{z}_k = \mathbf{T}_k \mathbf{z}_{k-1} + \mathbf{G}_k \mathbf{w}_k \\
\mathbf{y}_k = \mathbf{H}_k \mathbf{z}_k
\end{cases}
\tag{A.3}
$$

where

$$\mathbf{T}_k = \begin{bmatrix} 1-\frac{b_2 T_s}{b_1} & T_s & 0 & 0 & 0 \\ -\frac{b_3 T_s}{b_1} & 1 & T_s & 0 & 0 \\ -\frac{b_4 T_s}{b_1} & 0 & 1 & T_s & 0 \\ -\frac{b_5 T_s}{b_1} & 0 & 0 & 1 & T_s \\ -\frac{b_6 T_s}{b_1} & 0 & 0 & 0 & 1 \end{bmatrix}, \mathbf{G}_k = \begin{bmatrix} \frac{a_1}{b_1} T_s \\ \frac{a_2}{b_1} T_s \\ \frac{a_3}{b_1} T_s \\ \frac{a_4}{b_1} T_s \\ \frac{a_5}{b_1} T_s \end{bmatrix}, \mathbf{H}_k = \begin{bmatrix} 1 \\ 0 \\ 0 \\ 0 \\ 0 \end{bmatrix}^T$$

This state space is applicable to the specific application only when the internal relationship of ARMA process's coefficients are very clear. Due to avoiding to use discrete coefficients directly, the numerical instability problem will not happen. So compared with conventional expression, this state space is more robust. This state space can also be treated as the discretion of continuous state space. The differential equation and ARMA process expression are equivalent by using the modified state space.